Histone H2A Mono-Ubiquitination in Neurodevelopmental Disorders: Molecular Insights from Rare Genetic Variants

by

Brian T. McGrath

A dissertation submitted in partial fulfillment
of the requirements for the degree of
Doctor of Philosophy
(Cellular and Molecular Biology)
in the University of Michigan
2021

Doctoral Committee:

Associate Professor Stephanie Bielas, Chair
Professor Yali Dou, University of Southern California
Professor Gregory Dressler
Assistant Professor Jacob Kitzman
Professor Donna Martin

Brian T. McGrath

btmcg@umich.edu

ORCID ID: 0000-0001-6224-560X

I dedicate this thesis to individuals with BRS and their families.

Acknowledgements

I first want to thank my family for all their love and support throughout this whole process. My parents Jean and Marty for providing a great home to grow up in. I appreciate all the sacrifices you made for me and the many ways that you have cared for me. My sisters Elizabeth, Bridget and Meghan. Thank you for making it easy to be a brother with three sisters. Each of you did more than you know to help get me here. To all my family, I will cherish our many fun times in Ann Arbor together.

I want to thank the Cellular and Molecular Biology program for their support throughout graduate school. I especially want to thank Margarita, Pat, and Lauren who helped make my life easier in so many ways. I want to also thank the members of my committee for the fruitful discussions that helped shape my project.

This thesis could not have been completed without the help of a team of people. I especially want to thank Peijun Wu, Shachi Salvi, and Navjit Girgla. Your dedication to these projects helped me in so many ways and I appreciate all of your efforts.

I would like to recognize all past and present members of the Bielas lab, Amanda Moccia, Yao Tsan, Shachi Salvi, Anshika Srivastava, Ritesh KC, Liz Werren, Sadie Marlow, Navjit Girgla, and Jacob Ogle. Thank you for helping me grow as a scientist and for all the lab memories we created.

A huge thank you to my friends and family for supporting me throughout college and graduate school. I appreciated the many visits and questions on how my mice were

doing. Your friendship and support is unwavering and I am forever grateful for your friendship.

I especially want to thank my mentor, Dr. Stephanie Bielas. Thank you for allowing me to join your lab and supporting me through the highs and lows of my graduate career. Your dedication throughout this process meant so much to me. I appreciate all of the scientific training you provided me but even more so for the many life lessons I learned from you. You have helped shape who I have become and I will always be grateful for that. Thank you also for making Abigail and I feel like family and exposing us to many unique experiences.

Lastly, I want to thank my fiancée Abigail. Thank you for your unending support with graduate school and with life. Without you I would not have been able to accomplish my PhD. I am so thankful for the times we have enjoyed in Ann Arbor together, but I look so forward to beginning this next journey with you.

Table Of Contents

List of Figures

ABSTRACT

De novo dominant *ASXL3* frameshift variants are the genetic basis of Bainbridge-Ropers Syndrome (BRS) and syndromic autism spectrum disorder (ASD), emphasizing the importance of this gene in development. ASXL3 is a component of the Polycomb repressive deubiquitination (PR-DUB) complex that is critical for Polycomb-mediated transcriptional repression. PR-DUB catalyzes the removal of ubiquitin from Histone 2A (H2AUb1), a repressive histone modification catalyzed by Polycomb repressive complex 1 (PRC1). The molecular mechanism of H2AUb1 and the cellular processes it regulates during normal development and disease remain largely unexplored. To investigate the role of ASXL3 in development we generated a mouse model that carries a clinically relevant *Asxl3* frameshift variant (*Asxl3*^{fs}). Genetic inactivation of *Asxl3* leads to perinatal lethality, multi-organ developmental defects, and increased levels of H2AUb1. *Asxl3*$^{fs/fs}$ mice exhibit highly penetrant congenital heart defects, primarily hypoplastic right ventricles. Our structural, molecular, and transcriptomic analysis of cardiogenesis revealed that defects in extracellular matrix (ECM) composition and associated signaling underlie the *Asxl3*^{fs} dependent heart defects. Within the developing cerebral cortex, loss of ASXL3 perturbs the composition of excitatory neurons and fidelity of cortical layer deposition. We carried out single-cell RNA sequencing at three developmental stages during neurogenesis to characterize the cellular composition and transcriptomic changes. The emerging pathogenic model based on analysis of multiple cell types, at sequential developmental timepoints, implicates overactivation of Notch signaling that alters NPCs proliferation and timing of differentiation. These early developmental defects lead to altered composition of excitatory neurons with aberrant expression of proneural genes responsible for layer specificity at later timepoints. Across cortical development, dysregulated genes were enriched for high confidence ASD risk genes, implicating a convergent pathological mechanism. Together our findings underscore the importance of ASXL3 in Polycomb transcriptional repression during development and provide insight into developmental mechanisms altered by ASD risk genes.

Chapter 1[1]

Introduction

Development of multicellular organisms depends on their capacity to produce and maintain different cell types while sharing genomic DNA. Expression of cell type specific transcriptional programs governs acquisition of cell fate. Cells utilize epigenetic regulation to coordinate these expression programs that instruct cell-identity and cell fate choices. Within the nucleus, chromosomal DNA wraps around a nucleosome and organizes into chromatin fibers. Each nucleosome octamer is composed of two of each evolutionarily conserved histones H2A, H2B, H3 and H4 [1, 2]. The chromatin can then be packaged into higher order structures and compartments of heterochromatin and euchromatin. The N-terminal and C-terminal tails of histones undergo numerous post-translational modifications (PTMs), including acetylation, ubiquitination, phosphorylation, and methylation of specific amino acid residues. These marks throughout the genome demarcate genomic elements like promoters, enhancers, and gene bodies. Histone PTMs also influence chromatin compaction, transcriptional regulation and interaction with protein complexes. The genome-wide histone PTM landscape requires active maintenance to accommodate changing transcriptional profiles that allow for differentiation of diverse cell types and tissues from pluripotent stem cells during development [3]. PTMs are dynamically modified and interpreted by chromatin readers, writers and erasers. Throughout development, chromatin complexes can respond to

---

[1] This chapter represents a published manuscript. Srivastava A, **McGrath B**, Bielas SL. Histone H2A Monoubiquitination in Neurodevelopmental Disorders. Trends in Genetics. 2017;33(8):566-578.

internal and external cues to reshape the histone PTM landscape and allow for activation of certain networks and repression of others. Understanding how the patterns of histone modifications are deciphered and changed by cells is critical for our understanding of development and disease.

Polycomb transcriptional regulation

Among the most well conserved family of chromatin modifiers are the Polycomb group genes (PcG). PcGs were initially identified in a genetic screen that detected homeotic transformations of the *Drosophila* sex comb [4]. Within these mutants ectopic expression of Hox genes due to a loss of Polycomb repression caused the observed homeotic transformations during body segmentation [5]. These early studies underscore a fundamental role of Polycomb transcriptional repression specification and maintenance of cell fate during body patterning. Since these drosophila studies, PcG proteins have emerged as central players in epigenetic programming events during mammalian development. At the center of this evolutionarily conserved PcG system are three multiprotein complexes namely Polycomb repressive complex 1 (PRC1), Polycomb repressive complex 2 (PRC2), and Polycomb repressive deubiquitination complex (PR-DUB). PRC2 mono, di, or tri methylate histone H3 lysine 27 (H3K27me3). Meanwhile, PRC1 and PR-DUB work antagonistically to monoubiquitinate or deubiquitinate histone H2A lysine 119 (H2AUb1) respectively. These three complexes undergo complex cross-regulation mediated by their respective histone modifications. Work in invertebrates and vertebrates are uncovering differences between these organisms in the mechanisms of PcG transcriptional repression and the composition of PRC2 and PRC1.

Composition of polycomb complexes

Polycomb repressive complex 1

While the PcG complexes are evolutionarily conserved, the diversity of the mammalian complexes has increased [6]. Functional diversity of the PRC1, PR-DUB, and PRC2 is generated by distinct subunit compositions. The catalytic core of PRC1 includes one of six Polycomb group factor (PCGF) proteins assembled around an E3 ubiquitin ligase, Ring1A or Ring1B. The presence of different PCGF defines the enzymatic activity and localization of PRC1 [7-9]. Biochemical characterization has revealed distinct PRC1 complexes classified as either canonical (cPRC1) or non-canonical (ncPRC1). cPRC1components include Ring1A/B associated with either PCGF2 (MEL18) or PCGF4 (BMI1), CBX2/6/4/8, which can bind H3K27me3, and PHC1/2/3. ncPRC1 complexes possess Ring1A/B, RYBP or YAF2, and either PCGF1,3,5,or 6 with additional binding partners. PRC1 can compact chromatin and mediate higher-order chromatin structure independent of its H2AUb1 catalytic activity [10-12]. The contribution and necessity of each function in initiation and maintenance of Polycomb gene regulation has been heavily debated. Research suggests the compaction and catalytic activities are split between canonical and variant PRC1 complexes respectively. *In vitro* analysis of E3 ligase activity demonstrated variant PRC1 complexes have the greatest H2A monoubiqutination activity [7]. Systemic analysis of canonical and variant PRC1 complexes in ESCs, revealed canonical PRC1 contributes very little to H2AUb1 whereas variant complexes synergize to coordinate H2AUb1 levels throughout the genome [8, 9]. The CBX containing canonical PRC1 complexes are responsible for shaping the nuclear landscape by mediating long range interactions [12].

Polycomb repressive deubiquitination complex

PR-DUB was initially identified in Drosophila, as a complex between the ubiquitin hydrolase, calypso, and additional sex combs (ASX) [13]. In mammals, PR-DUB contains of one of three ASXL family members (ASXL1/2/3) and BAP1, the ortholog of calypso. ASXL family members share a common domain structure which includes an ASX N-terminal (ASXN), ASX homology (ASXH), two ASX-middle (ASXM1, ASXM2), and a PHD finger domain [14]. Together these domains grant ASXL proteins epigenetic protein-protein interactions, DNA binding, and histone reader capabilities. ASXL proteins associate with BAP1 through a conserved region of ASXH termed the DEUBiquitinase Adaptor Domain (DEUBAD) [15-17]. Mechanistically, BAP1 deubiquitinase activity requires a stable interaction with the conserved DEUBAD domain in ASXL proteins [18-20]. This mandatory interaction is not only required for BAP1 enzymatic activity but also its stability [20]. Proteomics based studies have reported that additional BAP1 interactions with a variety of other proteins including transcription factors, chromatin factors, cell cycle regulator and DNA repair proteins [21, 22]. Given that the interactions between BAP1 and ASXL occur in a mutually exclusive fashion, further analysis will need to dissect PR-DUB complex composition for each ASXL1/2/3 across development [20]. Depletion of Bap1 or any ASXL family members results in increased H2AUb1 [16, 22, 23]. In BAP1 knockout mESCs, the excess H2AUb1 accumulates across the genome which leads to widespread reduction in gene expression [23]. Notably, transcriptional defects and increased H2AUb1 can be rescued by inactivation of PRC1 [22, 23]. This highlights a need for balanced PRC1 and PR-DUB activity and controlled levels of H2AU1 to regulate transcription.

Polycomb repressive complex 2

In Eukaryotic cells, PRC2 is responsible for all mono-, di-, and trimethylation of histone H3 lysine 27 [24, 25]. Biochemically, the PRC2 core is comprised of a histone methyltransferase, EZH1/2, bound to EED, SUZ12 and RBP4/7. Additional accessory proteins further define PRC2.1 and PRC2.2 by regulating its enzymatic activity and chromatin localization [26, 27]. PRC2.1 mutually exclusively incorporates one of three Polycomb-like homologs PHF1, MTF2, or PHF19 [21]. Meanwhile, PRC2.2 interacts with AEBP2 and Jarid2 which recognizes H2AUB1 deposited by PRC1 [21, 28-30]. Recent biochemical analysis with mouse embryonic stem cells suggests that the combined actions of PRC2.1 and PRC2.2 direct the deposition of H3K7me3 [31].

Mono-ubiquitinated histone H2A

Reversible H2AUb1 has diverse roles in a complex transcriptional milieu comprised of multiple chromatin modifications, DNA methylation, and chromatin remodeling molecules. Recent genome wide analysis has demonstrated the H2AUb1 is found broadly throughout the genome [8, 32, 33]. Polycomb chromatin domains have high levels of H2AUb1, H3K27me3 and Polycomb complexes [34, 35]. Within ESCs, bivalent promoters are signature of developmentally important genes that establish cell identity [34, 36, 37]. H2AUb1 serves to prevent elongation of RNA polymerase machinery at bivalent loci, while RNA polymerase initiation remains unhindered [38, 39]. This poised state allows for dynamic transition between a transcriptionally active or repressed state required for normal development. Ubiquitinating and deubiquitinating components of the H2AUb1 regulatory axis reflect a similar genome-wide binding pattern implicating developmental modulation of this modification as an important regulatory mechanism [19, 35, 40]. Resolution of bivalent promoters at developmentally regulated genes towards active or fully repressed involves the concerted activity of various chromatin-modifying complexes [41, 42]. The emerging mechanisms suggest they can interact. The compounding effect among histone modifications due to alteration of a single histone modification can complicate interpreting the resulting molecular and transcriptional impacts.

H2AUb1 plays an important role in epigenetic establishment of mature cell fates by protecting CpG islands against DNA methylation required for constitutive repression of the corresponding genes [43, 44]. It still remains mechanistically unclear how developmental redistribution of H2AUb1 contributes to this diversity of transcriptional functions. Nevertheless, it underscores the diversity of clinical features and syndromic nature of inherited neurodevelopmental disorders that impact the H2AUb1 regulatory axis.

Mechanisms of polycomb repression

Several studies have characterized the recruitment of PRC1 and PRC2 to target genes for Polycomb gene silencing and the importance of H3K27me3 and H2AUb1 in this process [45-47]. In Drosophila, the dynamic functions of PRC1 and PRC2 are coordinated in a sequential manner at Polycomb repressive elements (PREs) to mediate transcriptional repression and chromatin compaction, with PRC2 initiating this molecular cascade [45]. The E3 ubiquitin ligase and chromatin compaction activities are conserved between vertebrates and invertebrates, yet the composition of PRC1 complexes are more heterogenous in vertebrates [18]. Likewise, in vertebrates PREs are not the functional genomic element that provides the platform for PcG repression and coordination of PRC1 and PRC2 activities exhibits more diversity. Rather in mammals, the majority of gene promoters are encompassed by CpG islands, that correspond to contiguous non-methylated segments of the genome with a higher than average level of CpG dinucleotides [48]. DNA methylation of CpG islands acts as a stable and heritable repressive epigenetic mark essential for development and generating a diversity of cell fates from multipotent progenitor cells. PcG have been demonstrated to be enriched at CpG islands [34, 37]. The PRC1.1 component KDM2B can bind DNA at CpG islands and recruit variant PRC. However, KDM2B does not recruit variant PRC1 to all CpG islands it binds [35]. There are additional accessory proteins in PRC1 complexes with DNA binding function, however their contribution to PcG recruitment is unclear.

Initial genome-wide mapping studies in vertebrate models revealed a strong overlap between H3K27me3 and H2AUb1 at the promoters of many repressed gene loci [36, 49-52]. Cross talk between PcG complexes was further supported by data that showed H3K27me3 increases the affinity of CBX-bound PRC1 complexes to chromatin [45, 46]. Together this data implicated a hierarchical recruitment model of PcG gene repression with initial recruitment of PRC2 to deposit H3K27me3. Sequentially, PRC1 gets recruited to the chromatin by CBX recognition of H3K27me3 followed by monoubiquitination of H2A. However, H2AUb1 can also be found at chromatin loci without H3K27me3, implicating an H3K27me3 independent PRC1 role [32]. Additional studies demonstrating RING1B and H2AUb1 continue to be recruited to target sites in PRC2-deficient mouse ESCs further substantiate an alternative recruitment mechanism [47].

Lastly, removal of PRC1 in mESCs drives a reduction in PRC2 binding and H3K27me3 at Polycomb target sites [7, 28]. However the PRC1 function responsible for this loss was not investigated.

Given the two functionally distinct PRC1 activities, the initial model of Polycomb recruitment questions the necessity of H2AUb1 in Polycomb regulation. This precipitated a series of studies designed to isolate their functional impacts on Polycomb regulation and development. Ring1A and Ring1B (Ring1A/B) are the central E3 ubiquitin ligases of all PRC1 complexes. Complete deletion of *Ring1A/B* in mESCs leads to loss of both PRC1 complex stability, essential for compaction function, and H2AUb1 ligase activity [11]. Consequently, *Ring1A/B*$^{-/-}$ mESCs spontaneously differentiate and de-repress many developmentally regulated genes [49]. In drosophila, an I48A mutation in *Sex Combs Extra* (S*ce*), the Ring1 homolog, ablates the E3 ligase enzymatic activity and results in decreased H2AUb1 levels [10]. *Sce*$^{I48a/I48a}$ maintain repression of many classical PCG target genes and show less severe phenotypes than *Sce*$^{-/-}$, but *Sce*$^{I48a/I48a}$ arrest development at the end of embryogenesis due to undefined causes [53]. Introduction of a catalytically inactive *Ring1B* I53A variant allowed for the H2AUb1 ligase activity of PRC1 to be evaluated independent of chromatin compaction [54, 55]. Unexpectedly, these genetic manipulations revealed that formation of a stable multimeric PRC1 complex could target developmental genes and compact chromatin independent of H2AUb1. This highlighted the dual functions of PRC1 and questioned the requirement for H2AUb1 in development. While *Ring1B*$^{-/-}$ mice are embryonic lethal by ~E10.5, *Ring1B*$^{I53A/I53A}$ embryos complete gastrulation, but are unable to survive past ~E15.5 emphasizing an essential function for H2AUb1 later in development [55]. It's important to note Ring1A was still present in *Ring1B*$^{I53A/I53A}$ and may compensate for decreased Ring1b catalytic activity. Additional work showed the I53A variant does not sufficiently abolish E3 ligase activity and instead acts as a hypomorph [56].

Two recent studies investigated the conditional inactivation of Ring1B catalytic activity by introducing the RING1B$^{I53A/D56K}$ and RING1B$^{I53S/I53S}$ alleles into mESCs [57, 58] Compared to the I53A allele alone, RING1B$^{I53A/D56K}$ and RING1B$^{I53S/ I53S}$ cause a complete loss of bulk H2AUb1. Upon complete depletion of H2AUb1, PRC2 and H3K27me3 across the genome are greatly reduced. Inactivation of PRC1 catalytic activity affected occupancy of both PRC2.1 and PRC2.2 at target sites. However PRC2.2, which contains the H2AUb1 binding subunit Jarid2, was reduced to a greater extent than PRC2.1. Consistent with these changes in PRC2 activity, localization of canonical PRC1 which depends on recognition of H3K27me3 through CBX binding, was compromised. As a consequence, long range interactions between classical Polycomb target sites were disrupted. On the contrary, binding of variant PRC1 remained largely intact in the absence of PRC1 catalytic activity. These results are contrary to the initial PRC2 led Polycomb recruitment model. Instead, the emerging model (Fig. 1.2) suggests variant PRC1 targets Polycomb sites independent of catalytic activity to deposit H2AUb1. In response, PRC2 is recruited to H2AUb1 chromatin sites to methylate H3K27. This drives accumulation of canonical PRC1 complex which promotes long-range interactions and chromatin compaction. This new model recognizes the importance of both PRC1 functions, but argues that PRC1 catalytic activity and H2AUb1 is central to Polycomb transcriptional regulation. As the function and mechanism of PcG transcriptional repression continues to unravel, it will be important to determine how variant PRC1 recognizes target sites.

Considering these studies were performed with ESCs, it will be important to conduct studies on the role H2AUb1 in more differentiated cell types and across development.

Together these studies demonstrate the vital requirement for proper regulation of H2AUb1 during development and emphasize that H2AUb1 can regulate non-canonical PCG target genes. The essential nature of H2AUb1 in development is further emphasized when viewed from the perspective of the H2AUb1 regulatory axis, representing a number of complexes and single molecules with a primary function of H2AUb1 modification (Fig. 1.3). Genes encoding axis components have been implicated as the genetic basis of many different diseases including cancers, congenital heart defects, and neurodevelopmental disorders. Likewise, recurrent pathogenic variants in genes that encode H2A monoubiquitination or deubiquitination components in neurodevelopmental disorders bolster this argument and will be discussed.

Histone H2A Monoubiquitination in Neurodevelopmental Disorders

Developmental decisions during lineage commitment are precisely coordinated at the genome level by gene expression programs that jointly activate or repress transcription [59]. Brain development requires the concurrent differentiation of neuronal cell types that must be organized into a complex organ [60, 61]. This process involves specification of pluripotent cells to ectoderm and neural precursors prior to terminal differentiation. Thus, brain development depends on precise temporal control of gene expression patterns, and disruption of transcriptional networks in brain development underlies neurodevelopmental disorders. It is not known how groups of genes are co-regulated during fate specification of neural lineages. Modification of histone marks is fundamentally important in specifying different cell types during embryonic development and pathogenic variants in genes that encode a broad-set of molecules that mediate chromatin modifications, including mono-ubiquitination of histone H2A lysine 119 (H2AUb1), are emerging as a prominent contribution to the genetic and molecular etiology of neurodevelopmental disorders [62-64].

H2AUb1 has historically been associated with the E3 ubiquitin ligase activity of Polycomb repressive complex 1 (PRC1) and Polycomb transcriptional repression, yet a variety of molecules that ubiquitinate or deubiquitinate H2A comprised of components of the H2AUb1 regulatory axis [65-68]. The components that decorate H2A with ubiquitin include canonical PRC1, variant PRC1, and TRIM37. Among the deubiquitinating components are the Polycomb repressive deubiquitinating complexes (PR-DUB) and USP16 [69, 70] (Fig. 1.3). Dynamic exchange of this histone modification reflect the succession of transcriptional profile changes required to produce the cellular diversity from pluripotent cells during development.

Large scale sequencing studies and widespread use of clinical exome sequencing are identifying inherited and *de novo* germline variants enriched in the H2AUb1 regulatory axis as important molecular pathology of syndromic neurodevelopmental disorders with features of autism and intellectual disability. Pathogenic human variants observed in *Really interesting new gene* (*Ring1), Autism susceptibility candidate 2 (AUTS2*), *Polyhomeotic-like 1* (*PHC1*), *Additional sex combs like* family members (*ASXl1,2,3*), *Tripartite motif-containing protein 37 (TRIM37)*, *BCL6 corepressor* (*BCOR*) and *Ubiquitin-specific protease 16* (*USP16*) are components of the histone H2A ubiquitination regulatory axis. In this review, we will summarize the confluence of human neurogenetic findings around this important area of histone modification critical for brain development (Table 1.1).

Histone H2A ubiquitination syndromes

Ring1 in syndromic neurodevelopmental disorder

Whole exome sequencing revealed a likely damaging de novo *RING1* missense mutation in a 13 year old girl with a syndromic neurodevelopmental disorder [71]. She was born with mild growth retardation and microcephaly. While early motor and language development was normal, she later displayed delay in acquisition of language, cognitive, and social skills. By 13, she began to show symptoms of schizophrenia including hallucinations, delusions and disorganized thinking. RING1 is one of two E3-ubiquitin ligases in the catalytic core of PRC1. In vitro ubiquitination analysis revealed the patient missense mutation disrupts ubiquitination of H2A. Likewise, decreased levels of H2AUb1 were observed in patient lymphoblast cells compared to control indicating a loss of protein function. When this variant was introduced in a *C. elegan* model, H2AUb1 was reduced and neuronal migration and axon guidance were disrupted.

Ring1A is the mouse ortholog to human *RING1*. Ring1a null mice have skeletal abnormalities due to homeotic transformations [72]. However, no other overt phenotypes were observed. Combinatorial loss of both *Ring1a* and *Ring1b* has a greater effect on development. The level of H2AUb1 in the telencephalic wall was greatly reduced upon double knockout compared to *Ring1A* null alone [73]. Together, Ring1A and Ring1B govern mouse telencephalic regionalization by regulating the spatial expression patterns of morphogens along the dorsal ventral axis [73].Inactivation of Ring1B catalytic activity in Ring1a deficient neural progenitor cells activates ectopically activates neurogenic genes [56]. This result implicates an H2AUb1 dependent role in repression of neurogenic transcriptional programs. Investigations into how clinically associated Ring1a variants disrupt patterning or transcriptional maintenance remains unexplored.

PHC1 in autosomal recessive primary microcephaly

Autosomal recessive primary microcephaly (MCPH) is clinically characterized as a small head circumference that reflects a correspondingly small brain. This genetically heterogeneous disorder is largely attributed to defects in neural progenitor cell (NPC) proliferation, neurogenesis and apoptosis, which reduce the size of the NPC pool available to build a brain. PHC1 is a core component of the canonical PRC1. Homozygous missense *PHC1* variants were identified as a genetic basis for MCPH11 in a family with reported consanguinity (OMIM; 615414) [64]. This inherited rare variant in *PHC1* is noteworthy based on the loss-of-function (LOF) intolerance and high constraint for homozygous variants calculated for this gene by Exome Aggregation Consortium (ExAC) [74] (Table 1.1). The clinical presentation of MCPH11 includes primary microcephaly, low-normal cognitive function and short stature. Functional analysis of this pathogenic variant in patient cells revealed reduced PHC1 expression with lower H2AUb1 levels genome-wide and impaired recruitment of PHC1 to loci of DNA damage and repair. These defects were also accompanied by increased expression of GMNN (Geminin), which was previously shown to cooperate with PcG transcriptional repression to achieve germinal differentiation, lineage commitment and early specification of neural cell fate [75]. Differential expression of GMNN was not linked to alterations in H2AUb1 at the *GMNN* locus, but is consistent with decreased progenitor proliferation and differentiation implicated in the pathogenic mechanisms of MCPH.

Phc1 null mice display diverse and severe phenotypes, including cephalic neural crest defect, microcephaly, abnormal facies, parathyroid and thymic hypoplasia together with skeletal and cardiac abnormalities [76-79]. These phenotypes are consistent with constitutive disruption of both canonical PRC1 chromatin folding and E3 ligase activities. In comparison to the *Phc1* knockout phenotype, the MCPH11 phenotype suggests the *PHC1* missense variants function as a hypomorphic allele. As the defective protein is expressed at normal levels, PRC1 formation, and thus chromatin compaction properties, may not be altered. We instead speculate that the MCPH11 phenotypes may be explained as a defect in PRC1 E3 ligase activity, which alone has been shown generate a milder phenotype in animal models. Interestingly, the MCPH11 *PHC1* variant predominantly impacted neural development in affected individuals, potentially highlighting a sensitivity of the developing brain to dysregulation of developmental H2AUb1 exchange kinetics.

AUTS2 in autism spectrum and neurodevelopmental disorders

AUTS2 was originally identified as a candidate for neurodevelopmental disorders by resolution of a translocation-breakpoint in twins with autism spectrum disorder (ASD), developmental delay (DD), and epilepsy [80]. Following this initial description, *AUTS2* structural variants and *de novo* dominant variants were identified by recent large-scale WES studies [81-85]. AUTS2 is a component of variant the PRC1 complex PRC1.5. PRC1.5 is sufficient for H2A ubiquitination *in vivo* and *in vitro, a* finding confirmed in the

PCGF5 knockout mouse that disrupts the formation of PRC1.5 and is accompanied by a reduction of H2AUb1 levels [86]. In 293T-REx cells, AUTS2 stably recruits casein kinase 2 (CK2) to PRC1.5. In an *in vitro* nucleosomal assay CK2 suppresses PRC1.5 H2A mono-ubiquitination activity through a RING1B phosphorylation event [62]. This reduction in H2AUb1 corresponds to transcriptional activation associated with the recruitment of P300. While direct experimental evidence is needed to confirm this molecular mechanism in the developing brain, it highlights the importance of modulating H2AUb1 activity, in this scenario by RING1B phosphorylation, for proper neural development. Of note, heterozygous *de novo* mutations in *EP300* (*E1A binding protein p300*), which encodes the histone H3 acetyltransferase P300, is a genetic basis for Rubinstein-Taybi syndrome (RSTS1 MIM: 180849), an neurodevelopmental disorder that shares clinical features AUTS2-ASD. AUTS2 associated chromatin biology exemplifies the complexity and interconnected nature of coordinated histone modifications, the molecular mechanisms of which will need to be elucidated to fully appreciate their role in brain development and neuropathology.

Homozygous *Auts2* knockout mice exhibit reduced intrauterine and postnatal growth, altered motor control and reduced vocalizations relative to controls [62]. While these findings corroborate human genetic findings associated with *AUTS2* and implicate an important role in neuropathology, the molecular function of AUTS2 in neural development and cortical neuron fate specification are yet to explored. AUTS2 exhibits highest expression in the developing cortex [87]. During cortical development, neural progenitor cells (NPCs) produce mature neuronal subtypes and glial cells in a defined temporal order. The timing of fate switches that determine the number of neuronal subtypes that will make up the composition of the six-layer cortex is governed by dynamic changes in NPC chromatin. Abnormal productions of cortical progeny have been shown to underlie ASD neuropathology. Uncovering the epigenomic role of AUTS2 and H2AUb1 dysregulation within the pathogenic PRC1.5 mechanism and more generally in normal development will be an important direction for future research.

TRIM37 in Mulibrey nanism

Mulibrey nanism (MUL; OMIM: 253250) is a rare autosomal recessive genetic disorder. The acronym “mu–li–br–ey” reflects the “muscle–liver–brain–eye” involvement in this syndrome. MUL is characterized by prenatal-onset growth retardation, short stature, craniofacial features, hepatomegaly, enlarged ventricles and dysarthria. Cardiac involvement is illustrated by progressive constrictive pericarditis, myocardial hypertrophy, and variable myocardial fibrosis. Pathogenic variants in *TRIM*37 are the genetic basis of MUL [88]. *TRIM37* encodes a RING finger domain like the hallmark E3 ubiquitin ligases RING1A/B, but functions independent of and of the multimeric PRC1 complexes. Thus, TRIM37 does not exhibit chromatin compaction properties conveyed by PRC1 complexes, highlighting the critical role of H2AUb1 in development [89]. While the H2A ubiquitin ligase activity of TRIM37 has been experimentally demonstrated in vitro and in vivo, the molecular pathology associated with pathogenic TRIM37 variants has not been explored. Likewise, further studies are needed to confirm the dynamics of H2A ubiquitination in primary cells from individuals with MUL. The spectrum of phenotypes described for the *Trim37*$^{-/-}$ mouse model recapitulates many clinical features of MUL and thus provides a good model to study pathogenesis related to TRIM37 deficiency [90].

Despite the prominent neurological features of MUL, the role of TRIM37 in neural development has not been investigated.

***BCL6 corepressor* (*BCOR*) in syndromic microphthalmia 2**

Syndromic microphthalmia 2 (MCOPS2, MIM 300166) is a rare, X-linked disorder characterized by microphthalmia, congenital cataracts, dysmorphic facial features, congenital heart defects, malformed ears, dental, skeletal, renal and urogenital anomalies. Neurologically, MCOPS2 is associated with ID, microcephaly and structural brain abnormalities. Pathogenic variants in X-linked *BCOR* (*BCL6 interacting corepressor*) are the genetic basis of this disorder that presents with a broad phenotypic spectrum consistent with hemizygosity in males and random X inactivation in females [91, 92]. These phenotypes also encompass those associated with reported copy number variants of *BCOR* reported. Pathogenic variants in BCOR are associated with a significant reduction in genome-wide H2AUb1 levels in mesenchymal stem cells isolated from an individual with MCOPS2 compared to control, implicating H2AUb1 dysregulation in the molecular pathology [92, 93].

BCOR is a transcriptional corepressor that was originally identified by its ability to interact with the site-specific transcriptional repressor BCL6 [94]. BCOR, KDM2B (lysine demethylase 2B) and PCGF1 are PcG-associated proteins that characterize the composition of variant PRC1.1 [67, 95]. *PCGF1* knockdown experiments exhibit a dramatic reduction of H2AUb1, mirroring H2AUb1 deposition activity of PRC1.1 [96]. A role for KDM2B in the BCOR MCOPS2 molecular pathology has not been investigated, but KDM2B binds DNA and is critical for recruiting PRC1.1 E3 ligase activity to unmethylated CpG islands to protect against *de novo* methylation and constitutive repression (Fig. 1.1) [43]. Such PRC1.1 functions would allow genome-wide epigenetic changes during development required to maintain the balance between proliferation and differentiation, and the subsequent emergence of cellular diversity defined by unique genome-wide DNA methylation patterns [97].

A role of H2AUb1 dysregulation has not been described for the neural developmental defects described for the *Bcor* conditional knockout mouse where BCOR is required for Sonic Hedgehog (SHH) signaling suppression by BCL6 in cerebellar development [98]. The epigenetic changes that mediate transcriptional repression of SHH signaling effectors in association with BCOR have not been elucidated, but recruitment of the histone deacetylation SIRT1 by BCOR to BCL6 target genes has been shown to be important. This again emphasizes a role for co-regulation of histone modifications in H2AUb1 associated transcriptional regulation. A similar SHH mechanism could contribute to the pathogenesis of medulloblastoma tumorigenesis associated with somatic variants in *BCOR* and cardiac laterality defects observed in individuals with MCOPS2 [99].

H2AUb1 deubiquitination syndromes

Ubiquitin-specific protease 16 (USP16) in Down syndrome

Down Syndrome (DS; OMIM: 190685) results from full or partial trisomy of chromosome 21 and is characterized by reduced growth, facial dysmorphisms, ID, motor deficits and early onset Alzheimer's disease. The constellations of DS phenotypes are attributed to the overexpression of a number of dosage-sensitive genes on chromosome 21. Among the genes that have been evaluated is *Usp16* [100]. USP16 can independently remove ubiquitin moieties from histone H2A and exhibits high expression in stem cell populations. The Ts65Dn mouse model that has a third copy of approximately two-thirds of the murine genes homologous to genes on human chromosome 21, including *Usp16,* recapitulates several traits of the human disorder. Ts65Dn mice have 1.5-fold increase in Usp16 expression and a 40% decrease in H2AUb1. This molecular defect is proposed to account for decreased stem cell proliferation and increased senescence. Restoring Usp16 expression to disomy levels by reducing the USP16 dosage or reducing Usp16 expression by shRNA knockdown, rescues the stem cell proliferation and premature senescence phenotypes. These experiments suggest the third copy of *Usp16* in Ts65Dn mice disrupt maintenance of stem cell multipotency contributing to DS pathology. A survey of tissues from individuals with DS confirmed reduced self-renewal of hematopoietic stem cells and premature senescence of mammary epithelial cells, NPCs, and fibroblasts [40, 101]. Molecularly, this highlights the role of histone H2AUb1 in pluripotency, differentiation and cell lineage commitment.

Usp16 knockout mice are early embryonic lethal and further implicate an essential role for USP16 in development and lineage commitment. *Usp16* knockout mESCs exhibit elevated H2AUb1 unlike Ts65Dn mice, proliferate normally and maintain pluripotency. Upon differentiation high H2AUb1 levels persist at transcriptional start sites of many pluripotency and developmentally regulated genes. This molecular defect corresponds to persistent expression of pluripotency genes, delayed expression of germinal layer markers and an impediment to differentiation. A role for USP16 H2A deubiquitination in neural development has not been explored. We speculate that the epigenomic functions of USP16 may underlie the highly dynamic disruption of gene expression in the brains of individuals with DS spanning mid-fetal development to adulthood [102]. These transcriptomic findings implicate cell-autonomous deficits in oligodendrocyte differentiation and the production of neocortical myelin in DS pathogenesis, molecular and developmental biology consistent with UPS16 H2AUb1 hydrolase activity.

Developmental disorders: additional sex combs-like (ASXL1, ASXL2 and ASXL3)

ASXL1, ASXL2 and ASXL3 are mammalian homologs of Drosophila *Additional sex combs* (*Asx*) and share a conserved domain structure [13]. The paralogs interact with *BRCA1 Associated Protein-1* (*BAP1*) in a mutually exclusive fashion to form three separate PR-DUB complexes. BAP1 provides the H2AUb1 ubiquitin hydrolase activity for the PR-DUBs represented by each ASXL family member. BAP1 is a critical tumor suppressor that has attracted medical interest in the past years since its loss leads to a variety of cancers due to somatic variants, but no pathogenic germline variants have been identified as the genetic basis of a developmental disorder to date [103-106]. Conversely, *de novo* heterozygous germline variants have been detected in all three family members by research and clinical sequencing efforts, for multi-organ developmental disorders with shared features of hypotonia, ID, craniofacial dysmorphisms, white matter loss and skeletal manifestations. Despite these overlapping features, each gene is associated with its own distinct neurodevelopmental syndrome that differ based on their constellation of partially penetrant clinical features, molecular pathology and associated cancer risk. *De novo* variants in ASXL1 are the genetic basis of Bohring–Opitz syndrome (BOS; MIM 605039) [107, 108]. BOS is distinctive among ASXL family member disorders based on severe and highly penetrant skeletal abnormalities, facial nevus flammeus, microcephaly, persistent feeding difficulties and delays in speech and gross motor skills. ASXL2 is the genetic basis of Shashi-Pena syndrome (SPS; MIM 617190), which is the least severe of the ASXL associated disorders and distinctive because of mild neonatal feeding difficulties, complete penetrance of macrocephaly, partially penetrant facial nevus flammeus, variability in severity of ID, normal height and weight and bone density abnormalities [109]. Pathogenic *ASXL3* variants have been discovered in Bainbridge Ropers syndrome (BRS; MIM 615485). BRS is characterized by persistent severe feeding difficulties, partially penetrant microcephaly, highly penetrant severe hypotonia, failure to meet developmental milestones including walking and highly penetrant nonverbal outcomes [16, 110]. Comprehensively, these findings suggest an important role for H2AUb1 exchange kinetics in development, with prominent and distinct neurological defects.

The *Asxl1* and *Asxl2* knockout mice exhibit both posterior and an anterior homeotic skeletal transformation, suggesting their role in Hox regulation is conserved in vertebrates [111, 112]. Both genotypes were born at less than Mendelian ratio, demonstrated perinatal lethality with the null animals proportionally smaller than control littermates [112, 113]. Besides skeletal transformations, *Asxl1*$^{-/-}$ mice exhibit microphthalmia, craniofacial dysmorphisms and myelodysplasia but have not been described as microcephalic [47, 54, 113, 114]. *Asxl2*$^{-/-}$ mice showed enlarged hearts with interstitial fibrosis and cardiomyocyte disarray and do not exhibit macrocephaly [112, 115]. This discrepancy in brain size phenotypes between mice and humans is an interesting observation that warrants further analysis, as the role for PR-DUB function in brain development has not yet been described.

Between analysis of mouse models and primary cells established from affected individuals, dysregulation of H2AUb1 DUB activity is a key molecular defect of ASXL pathogenic variants [16]. However, molecular differences may also contribute to their phenotypic differences. In addition to H2AUb1, ASXL1 molecular pathology is also impacted by dysregulation of H3K27me3 [116]. ASXL3 molecular pathology has been linked primarily to defects in H2AUb1 DUB activity and elevated genome-wide levels of H2AUb1 [16]. Pathogenic variants in *ASXL2* have been implicated to function in a dominant-negative manner in the PR-DUB complex, a finding that will need to be confirmed [109]. Additionally, *Asxl2*$^{-/-}$ mice demonstrate elevated levels of H2AUb1 presumably due to an absence of PR-DUB activity [117]. Further investigating these pathogenic mechanisms in affected tissue will provide insight into the tissue-specific H2AUb1 modification exchange in fate specification of distinct cell lineages.

Gene dosage in neurodevelopmental disorders

Advanced genomic sequencing and clinical genetic testing tools have significantly added to the list of *de novo* variants contributing to neurological syndromes. Pathogenic *de novo* dominant heterozygous variants can act through dominant negative, toxic gain-of-function or LOF genetic mechanisms. A large proportion of heterozygous variants are predicted to result in LOF and haploinsufficiency, yet only a fraction are experimentally confirmed. What underlies the vulnerability to haploinsufficiency is unclear, however, it accentuates the importance of gene dosage and the pathogenicity that results from such changes of dosage-sensitive genes. Chromatin modifying genes are an important group of disease-associated genes that are contributing to the recent expansion of early-onset reproductively lethal neurodevelopmental disorders attributed to pathogenic *de novo* variants. The molecular mechanisms that underlie the phenotypic spectrum of dosage-sensitive genes have been largely unexplored. Through comprehensive genetic testing and research sequencing the SNVs and CNVs will be important to define dosage sensitive genes and the corresponding spectrum of phenotypic outcomes.

Reciprocal dosage of *Usp16* that results in opposing phenotypes is an example of the relationship of dosage and phenotypic outcomes for dosage sensitive genes. Located on chromosome 21, triplicate copies of USP16 are present in Down syndrome [100]. Reduced dosage of USP16 has not been described in human pathogenesis. Yet, early embryonic lethality of the *Usp16* knockout suggests USP16 may be essential for development in humans as well. An evaluation of different cell types, including differentiation of mESCs towards a germinal fate showed that knockout of *Usp16* results in increased H2AUb1 levels at key developmental regulators and persistent multipotency, while an extra functional copy of *USP16* promotes H2AUb1 deubiquitination, progenitor proliferation, accelerated differentiation and senescence. For most cases of dosage the resulting phenotypic outcomes and proposed molecular mechanisms are more variable than this direct relationship between gene dosage and phenotype. For many of the neurodevelopmental disorder genes that encode components of the histone H2A ubiquitination regulatory axis, in depth molecular studies will be required to understand how a gene dosage alters tissue- and developmental- specific expression and how the altered amount of a single subunit of a multi-subunit protein complex leads to recognizable phenotypes. These two criteria are particularly relevant given the variability in subunit composition of PRC1.

Coincidence of variants in cancers and neurodevelopmental disorders

A decidedly unexpected finding from comprehensive analysis of data from large scale sequencing efforts and routine clinical genome-wide genetic tests was the coincidence of variants in chromatin modifying genes that are attributed to both neurodevelopmental disorders and cancer. Similar to germline variants in components of the histone H2AUb1 regulatory axis detected for neurodevelopmental disorders, somatic variants are being identified as potential drivers of a variety of tissue malignancies. Individually mutated genes can be preferentially associated with individual tumor types, as well as overlapping contributions to a broad range of cancers including neural, epithelial and hematopoietic malignancies. The ASXL family members are an example of this complex interconnectedness. Pathogenic germline variants in *ASXL1*, *ASXL2* and *ASXL3* are each associated with distinct neurodevelopmental disorders that share some overlapping phenotypes. Likewise, somatic variants in *ASXL1*, *ASXL2* and *ASXL3* are detected in many malignancies, but each is also associated prominently with AML, breast cancer and melanoma respectively [14]. These cases highlight the importance of tissue- and developmental- specific expression to pathogenesis and suggest shared molecular mechanisms conveyed by germline and somatic variants in the same gene. An outstanding question is how variants in different subunits of the same complex can generate divergent phenotypes and susceptibility to tumorigenesis. Thus, the context of genetic variations, including timing, genetic background and cell type, may contribute to the differing disease phenotypes, despite similar protein defects. The cell and tissue choices for investigating the molecular mechanisms of pathogenesis will be critically important to uncover the pathogenic mechanism of neurodevelopmental defects and generation of cancer.

Concluding remarks

Convergence of neurogenetics findings on genes that encode components of the H2AUb1 regulatory axis provides genetic evidence for the important function of this histone PTM in normal development and pathogenesis. The diversity of syndromic features that define these neurodevelopmental disorders belies the dosage sensitivity and molecular complexity that accompanies developmental H2AUb1 exchange. Divergent phenotypes exhibited by pathogenic variants in genes that encode components of overlapping protein complexes with H2AUb1 modifying activity also suggests tissue- and developmental- specific expression. These genetic observations will be critical for designing experimental approaches to understand the fundamental epigenetic mechanisms of H2AUb1. More mechanistic studies will be needed to translate these genetic perturbations into a better understanding of the Polycomb histone modifications required for the generation and maintenance of cellular diversity of different organ systems, including the brain. These genetic findings provide a strong foundation on which to base these future research goals.

REFERENCES:

1. Kornberg, R.D., *Chromatin structure: a repeating unit of histones and DNA.* Science, 1974. **184**(4139): p. 868-71.
2. Thomas, J.O. and R.D. Kornberg, *An octamer of histones in chromatin and free in solution.* Proc Natl Acad Sci U S A, 1975. **72**(7): p. 2626-30.
3. Tee, W.W. and D. Reinberg, *Chromatin features and the epigenetic regulation of pluripotency states in ESCs.* Development, 2014. **141**(12): p. 2376-90.
4. Kassis, J.A., J.A. Kennison, and J.W. Tamkun, *Polycomb and Trithorax Group Genes in Drosophila.* Genetics, 2017. **206**(4): p. 1699-1725.
5. Lewis, E.B., *A gene complex controlling segmentation in Drosophila.* Nature, 1978. **276**(5688): p. 565-70.
6. Schuettengruber, B., et al., *Genome Regulation by Polycomb and Trithorax: 70 Years and Counting.* Cell, 2017. **171**(1): p. 34-57.
7. Rose, N.R., et al., *RYBP stimulates PRC1 to shape chromatin-based communication between Polycomb repressive complexes.* Elife, 2016. **5**.
8. Fursova, N.A., et al., *Synergy between Variant PRC1 Complexes Defines Polycomb-Mediated Gene Repression.* Mol Cell, 2019. **74**(5): p. 1020-1036 e8.
9. Scelfo, A., et al., *Functional Landscape of PCGF Proteins Reveals Both RING1A/B-Dependent-and RING1A/B-Independent-Specific Activities.* Mol Cell, 2019. **74**(5): p. 1037-1052 e7.
10. Pengelly, A.R., et al., *Transcriptional repression by PRC1 in the absence of H2A monoubiquitylation.* Genes Dev, 2015. **29**(14): p. 1487-92.
11. Francis, N.J., R.E. Kingston, and C.L. Woodcock, *Chromatin compaction by a polycomb group protein complex.* Science, 2004. **306**(5701): p. 1574-7.
12. Boyle, S., et al., *A central role for canonical PRC1 in shaping the 3D nuclear landscape.* Genes Dev, 2020. **34**(13-14): p. 931-949.
13. Scheuermann, J.C., et al., *Histone H2A deubiquitinase activity of the Polycomb repressive complex PR-DUB.* Nature, 2010. **465**(7295): p. 243-7.
14. Katoh, M., *Functional and cancer genomics of ASXL family members.* Br J Cancer, 2013. **109**(2): p. 299-306.
15. Scheuermann, J.C., et al., *Histone H2A deubiquitinase activity of the Polycomb repressive complex PR-DUB.* Nature, 2010. **465**(7295): p. 243-7.
16. Srivastava, A., et al., *De novo dominant ASXL3 mutations alter H2A deubiquitination and transcription in Bainbridge-Ropers syndrome.* Hum Mol Genet, 2016. **25**(3): p. 597-608.
17. Sanchez-Pulido, L., L. Kong, and C.P. Ponting, *A common ancestry for BAP1 and Uch37 regulators.* Bioinformatics, 2012. **28**(15): p. 1953-6.
18. Barbour, H., et al., *Polycomb group-mediated histone H2A monoubiquitination in epigenome regulation and nuclear processes.* Nat Commun, 2020. **11**(1): p. 5947.
19. Sahtoe, D.D., et al., *BAP1/ASXL1 recruitment and activation for H2A deubiquitination.* Nat Commun, 2016. **7**: p. 10292.
20. Daou, S., et al., *The BAP1/ASXL2 Histone H2A Deubiquitinase Complex Regulates Cell Proliferation and Is Disrupted in Cancer.* J Biol Chem, 2015. **290**(48): p. 28643-63.

21. Hauri, S., et al., *A High-Density Map for Navigating the Human Polycomb Complexome.* Cell Rep, 2016. **17**(2): p. 583-595.
22. Campagne, A., et al., *BAP1 complex promotes transcription by opposing PRC1-mediated H2A ubiquitylation.* Nat Commun, 2019. **10**(1): p. 348.
23. Fursova, N.A., et al., *BAP1 constrains pervasive H2AK119ub1 to control the transcriptional potential of the genome.* Genes Dev, 2021. **35**(9-10): p. 749-770.
24. Holoch, D. and R. Margueron, *Mechanisms Regulating PRC2 Recruitment and Enzymatic Activity.* Trends Biochem Sci, 2017. **42**(7): p. 531-542.
25. Laugesen, A., J.W. Hojfeldt, and K. Helin, *Molecular Mechanisms Directing PRC2 Recruitment and H3K27 Methylation.* Mol Cell, 2019. **74**(1): p. 8-18.
26. Pasini, D., et al., *JARID2 regulates binding of the Polycomb repressive complex 2 to target genes in ES cells.* Nature, 2010. **464**(7286): p. 306-10.
27. Ciferri, C., et al., *Molecular architecture of human polycomb repressive complex 2.* Elife, 2012. **1**: p. e00005.
28. Blackledge, N.P., et al., *Variant PRC1 complex-dependent H2A ubiquitylation drives PRC2 recruitment and polycomb domain formation.* Cell, 2014. **157**(6): p. 1445-59.
29. Kalb, R., et al., *Histone H2A monoubiquitination promotes histone H3 methylation in Polycomb repression.* Nat Struct Mol Biol, 2014. **21**(6): p. 569-71.
30. Cooper, S., et al., *Jarid2 binds mono-ubiquitylated H2A lysine 119 to mediate crosstalk between Polycomb complexes PRC1 and PRC2.* Nat Commun, 2016. **7**: p. 13661.
31. Healy, E., et al., *PRC2.1 and PRC2.2 Synergize to Coordinate H3K27 Trimethylation.* Mol Cell, 2019. **76**(3): p. 437-452 e6.
32. Lee, H.G., et al., *Genome-wide activities of Polycomb complexes control pervasive transcription.* Genome Res, 2015. **25**(8): p. 1170-81.
33. Kahn, T.G., et al., *Interdependence of PRC1 and PRC2 for recruitment to Polycomb Response Elements.* Nucleic Acids Res, 2016. **44**(21): p. 10132-10149.
34. Mikkelsen, T.S., et al., *Genome-wide maps of chromatin state in pluripotent and lineage-committed cells.* Nature, 2007. **448**(7153): p. 553-60.
35. Ku, M., et al., *Genomewide analysis of PRC1 and PRC2 occupancy identifies two classes of bivalent domains.* PLoS Genet, 2008. **4**(10): p. e1000242.
36. Bernstein, B.E., et al., *A bivalent chromatin structure marks key developmental genes in embryonic stem cells.* Cell, 2006. **125**(2): p. 315-26.
37. Boyer, L.A., et al., *Polycomb complexes repress developmental regulators in murine embryonic stem cells.* Nature, 2006. **441**(7091): p. 349-53.
38. Stock, J.K., et al., *Ring1-mediated ubiquitination of H2A restrains poised RNA polymerase II at bivalent genes in mouse ES cells.* Nat Cell Biol, 2007. **9**(12): p. 1428-35.
39. Zhou, W., et al., *Histone H2A monoubiquitination represses transcription by inhibiting RNA polymerase II transcriptional elongation.* Mol Cell, 2008. **29**(1): p. 69-80.
40. Yang, W., et al., *The histone H2A deubiquitinase Usp16 regulates embryonic stem cell gene expression and lineage commitment.* Nat Commun, 2014. **5**: p. 3818.

41. Voigt, P., W.W. Tee, and D. Reinberg, *A double take on bivalent promoters.* Genes Dev, 2013. **27**(12): p. 1318-38.
42. Piunti, A. and A. Shilatifard, *Epigenetic balance of gene expression by Polycomb and COMPASS families.* Science, 2016. **352**(6290): p. aad9780.
43. Boulard, M., J.R. Edwards, and T.H. Bestor, *FBXL10 protects Polycomb-bound genes from hypermethylation.* Nat Genet, 2015. **47**(5): p. 479-85.
44. Wu, X., J.V. Johansen, and K. Helin, *Fbxl10/Kdm2b recruits polycomb repressive complex 1 to CpG islands and regulates H2A ubiquitylation.* Mol Cell, 2013. **49**(6): p. 1134-46.
45. Fischle, W., Y. Wang, and C.D. Allis, *Histone and chromatin cross-talk.* Curr Opin Cell Biol, 2003. **15**(2): p. 172-83.
46. Min, J., Y. Zhang, and R.M. Xu, *Structural basis for specific binding of Polycomb chromodomain to histone H3 methylated at Lys 27.* Genes Dev, 2003. **17**(15): p. 1823-8.
47. Tavares, L., et al., *RYBP-PRC1 complexes mediate H2A ubiquitylation at polycomb target sites independently of PRC2 and H3K27me3.* Cell, 2012. **148**(4): p. 664-78.
48. Blackledge, N.P. and R. Klose, *CpG island chromatin: a platform for gene regulation.* Epigenetics, 2011. **6**(2): p. 147-52.
49. Endoh, M., et al., *Histone H2A mono-ubiquitination is a crucial step to mediate PRC1-dependent repression of developmental genes to maintain ES cell identity.* PLoS Genet, 2012. **8**(7): p. e1002774.
50. Endoh, M., et al., *Polycomb group proteins Ring1A/B are functionally linked to the core transcriptional regulatory circuitry to maintain ES cell identity.* Development, 2008. **135**(8): p. 1513-24.
51. Brookes, E., et al., *Polycomb associates genome-wide with a specific RNA polymerase II variant, and regulates metabolic genes in ESCs.* Cell Stem Cell, 2012. **10**(2): p. 157-70.
52. Schoenfelder, S., et al., *Polycomb repressive complex PRC1 spatially constrains the mouse embryonic stem cell genome.* Nat Genet, 2015. **47**(10): p. 1179-86.
53. Gutiérrez, L., et al., *The role of the histone H2A ubiquitinase Sce in Polycomb repression.* Development, 2012. **139**(1): p. 117-27.
54. Eskeland, R., et al., *Ring1B compacts chromatin structure and represses gene expression independent of histone ubiquitination.* Mol Cell, 2010. **38**(3): p. 452-64.
55. Illingworth, R.S., et al., *The E3 ubiquitin ligase activity of RING1B is not essential for early mouse development.* Genes Dev, 2015. **29**(18): p. 1897-902.
56. Tsuboi, M., Y. Hirabayashi, and Y. Gotoh, *Diverse gene regulatory mechanisms mediated by Polycomb group proteins during neural development.* Curr Opin Neurobiol, 2019. **59**: p. 164-173.
57. Tamburri, S., et al., *Histone H2AK119 Mono-Ubiquitination Is Essential for Polycomb-Mediated Transcriptional Repression.* Mol Cell, 2020. **77**(4): p. 840-856 e5.
58. Blackledge, N.P., et al., *PRC1 Catalytic Activity Is Central to Polycomb System Function.* Mol Cell, 2020. **77**(4): p. 857-874 e9.

59. Davidson, E.H., *Emerging properties of animal gene regulatory networks.* Nature, 2010. **468**(7326): p. 911-20.
60. Azevedo, F.A., et al., *Equal numbers of neuronal and nonneuronal cells make the human brain an isometrically scaled-up primate brain.* J Comp Neurol, 2009. **513**(5): p. 532-41.
61. Greig, L.C., et al., *Molecular logic of neocortical projection neuron specification, development and diversity.* Nat Rev Neurosci, 2013. **14**(11): p. 755-69.
62. Gao, Z., et al., *An AUTS2-Polycomb complex activates gene expression in the CNS.* Nature, 2014. **516**(7531): p. 349-54.
63. Srivastava, A., et al., *De novo dominant ASXL3 mutations alter H2A deubiquitination and transcription in Bainbridge-Ropers syndrome.* Hum Mol Genet, 2015.
64. Awad, S., et al., *Mutation in PHC1 implicates chromatin remodeling in primary microcephaly pathogenesis.* Hum Mol Genet, 2013. **22**(11): p. 2200-13.
65. Gil, J. and A. O'Loghlen, *PRC1 complex diversity: where is it taking us?* Trends Cell Biol, 2014. **24**(11): p. 632-41.
66. Di Croce, L. and K. Helin, *Transcriptional regulation by Polycomb group proteins.* Nat Struct Mol Biol, 2013. **20**(10): p. 1147-55.
67. Gao, Z., et al., *PCGF homologs, CBX proteins, and RYBP define functionally distinct PRC1 family complexes.* Mol Cell, 2012. **45**(3): p. 344-56.
68. Vidal, M. and K. Starowicz, *Polycomb complexes PRC1 and their function in hematopoiesis.* Exp Hematol, 2017. **48**: p. 12-31.
69. Vissers, J.H., et al., *The many faces of ubiquitinated histone H2A: insights from the DUBs.* Cell Div, 2008. **3**: p. 8.
70. He, M., et al., *The emerging role of deubiquitinating enzymes in genomic integrity, diseases, and therapeutics.* Cell Biosci, 2016. **6**: p. 62.
71. Pierce, S.B., et al., *De novo mutation in RING1 with epigenetic effects on neurodevelopment.* Proc Natl Acad Sci U S A, 2018. **115**(7): p. 1558-1563.
72. del Mar Lorente, M., et al., *Loss- and gain-of-function mutations show a polycomb group function for Ring1A in mice.* Development, 2000. **127**(23): p. 5093-100.
73. Eto, H., et al., *The Polycomb group protein Ring1 regulates dorsoventral patterning of the mouse telencephalon.* Nat Commun, 2020. **11**(1): p. 5709.
74. Lek, M., et al., *Analysis of protein-coding genetic variation in 60,706 humans.* Nature, 2016. **536**(7616): p. 285-91.
75. Sankar, S., et al., *Gene regulatory networks in neural cell fate acquisition from genome-wide chromatin association of Geminin and Zic1.* Sci Rep, 2016. **6**: p. 37412.
76. Ohta, H., et al., *Polycomb group gene rae28 is required for sustaining activity of hematopoietic stem cells.* J Exp Med, 2002. **195**(6): p. 759-70.
77. Takihara, Y., et al., *Targeted disruption of the mouse homologue of the Drosophila polyhomeotic gene leads to altered anteroposterior patterning and neural crest defects.* Development, 1997. **124**(19): p. 3673-82.
78. Tokimasa, S., et al., *Lack of the Polycomb-group gene rae28 causes maturation arrest at the early B-cell developmental stage.* Exp Hematol, 2001. **29**(1): p. 93-103.

79. Nomura, M., Y. Takihara, and K. Shimada, *Isolation and characterization of retinoic acid-inducible cDNA clones in F9 cells: one of the early inducible clones encodes a novel protein sharing several highly homologous regions with a Drosophila polyhomeotic protein.* Differentiation, 1994. **57**(1): p. 39-50.
80. Sultana, R., et al., *Identification of a novel gene on chromosome 7q11.2 interrupted by a translocation breakpoint in a pair of autistic twins.* Genomics, 2002. **80**(2): p. 129-34.
81. Talkowski, M.E., et al., *Sequencing chromosomal abnormalities reveals neurodevelopmental loci that confer risk across diagnostic boundaries.* Cell, 2012. **149**(3): p. 525-37.
82. Beunders, G., et al., *Exonic deletions in AUTS2 cause a syndromic form of intellectual disability and suggest a critical role for the C terminus.* Am J Hum Genet, 2013. **92**(2): p. 210-20.
83. Nagamani, S.C., et al., *Detection of copy-number variation in AUTS2 gene by targeted exonic array CGH in patients with developmental delay and autistic spectrum disorders.* Eur J Hum Genet, 2013. **21**(3): p. 343-6.
84. Oksenberg, N. and N. Ahituv, *The role of AUTS2 in neurodevelopment and human evolution.* Trends Genet, 2013. **29**(10): p. 600-8.
85. Jolley, A., et al., *De novo intragenic deletion of the autism susceptibility candidate 2 (AUTS2) gene in a patient with developmental delay: a case report and literature review.* Am J Med Genet A, 2013. **161A**(6): p. 1508-12.
86. Si, S., et al., *Loss of Pcgf5 Affects Global H2A Monoubiquitination but Not the Function of Hematopoietic Stem and Progenitor Cells.* PLoS One, 2016. **11**(5): p. e0154561.
87. Bedogni, F., et al., *Autism susceptibility candidate 2 (Auts2) encodes a nuclear protein expressed in developing brain regions implicated in autism neuropathology.* Gene Expr Patterns, 2010. **10**(1): p. 9-15.
88. Avela, K., et al., *Gene encoding a new RING-B-box-Coiled-coil protein is mutated in mulibrey nanism.* Nat Genet, 2000. **25**(3): p. 298-301.
89. Bhatnagar, S., et al., *TRIM37 is a new histone H2A ubiquitin ligase and breast cancer oncoprotein.* Nature, 2014. **516**(7529): p. 116-20.
90. Kettunen, K.M., et al., *Trim37-deficient mice recapitulate several features of the multi-organ disorder Mulibrey nanism.* Biol Open, 2016. **5**(5): p. 584-95.
91. Hilton, E., et al., *BCOR analysis in patients with OFCD and Lenz microphthalmia syndromes, mental retardation with ocular anomalies, and cardiac laterality defects.* Eur J Hum Genet, 2009. **17**(10): p. 1325-35.
92. Ng, D., et al., *Oculofaciocardiodental and Lenz microphthalmia syndromes result from distinct classes of mutations in BCOR.* Nat Genet, 2004. **36**(4): p. 411-6.
93. Fan, Z., et al., *BCOR regulates mesenchymal stem cell function by epigenetic mechanisms.* Nat Cell Biol, 2009. **11**(8): p. 1002-9.
94. Sánchez, C., et al., *Proteomics analysis of Ring1B/Rnf2 interactors identifies a novel complex with the Fbxl10/Jhdm1B histone demethylase and the Bcl6 interacting corepressor.* Mol Cell Proteomics, 2007. **6**(5): p. 820-34.
95. Gearhart, M.D., et al., *Polycomb group and SCF ubiquitin ligases are found in a novel BCOR complex that is recruited to BCL6 targets.* Mol Cell Biol, 2006. **26**(18): p. 6880-9.

96. Wu, X., et al., *Cooperation between EZH2, NSPc1-mediated histone H2A ubiquitination and Dnmt1 in HOX gene silencing.* Nucleic Acids Res, 2008. **36**(11): p. 3590-9.
97. Mo, A., et al., *Epigenomic Signatures of Neuronal Diversity in the Mammalian Brain.* Neuron, 2015. **86**(6): p. 1369-84.
98. Tiberi, L., et al., *A BCL6/BCOR/SIRT1 complex triggers neurogenesis and suppresses medulloblastoma by repressing Sonic Hedgehog signaling.* Cancer Cell, 2014. **26**(6): p. 797-812.
99. Pennekamp, P., et al., *Situs inversus and ciliary abnormalities: 20 years later, what is the connection?* Cilia, 2015. **4**(1): p. 1.
100. Adorno, M., et al., *Usp16 contributes to somatic stem-cell defects in Down's syndrome.* Nature, 2013. **501**(7467): p. 380-4.
101. Joo, H.Y., et al., *Regulation of cell cycle progression and gene expression by H2A deubiquitination.* Nature, 2007. **449**(7165): p. 1068-72.
102. Olmos-Serrano, J.L., et al., *Down Syndrome Developmental Brain Transcriptome Reveals Defective Oligodendrocyte Differentiation and Myelination.* Neuron, 2016. **89**(6): p. 1208-22.
103. Carbone, M., et al., *BAP1 and cancer.* Nat Rev Cancer, 2013. **13**(3): p. 153-9.
104. Wiesner, T., et al., *Germline mutations in BAP1 predispose to melanocytic tumors.* Nat Genet, 2011. **43**(10): p. 1018-21.
105. Testa, J.R., et al., *Germline BAP1 mutations predispose to malignant mesothelioma.* Nat Genet, 2011. **43**(10): p. 1022-5.
106. Harbour, J.W., et al., *Frequent mutation of BAP1 in metastasizing uveal melanomas.* Science, 2010. **330**(6009): p. 1410-3.
107. Hoischen, A., et al., *De novo nonsense mutations in ASXL1 cause Bohring-Opitz syndrome.* Nat Genet, 2011. **43**(8): p. 729-31.
108. Dangiolo, S.B., et al., *Bohring-Opitz syndrome (BOS) with a new ASXL1 pathogenic variant: Review of the most prevalent molecular and phenotypic features of the syndrome.* Am J Med Genet A, 2015. **167A**(12): p. 3161-6.
109. Shashi, V., et al., *De Novo Truncating Variants in ASXL2 Are Associated with a Unique and Recognizable Clinical Phenotype.* Am J Hum Genet, 2017. **100**(1): p. 179.
110. Bainbridge, M.N., et al., *De novo truncating mutations in ASXL3 are associated with a novel clinical phenotype with similarities to Bohring-Opitz syndrome.* Genome Med, 2013. **5**(2): p. 11.
111. Kloet, S.L., et al., *The dynamic interactome and genomic targets of Polycomb complexes during stem-cell differentiation.* Nat Struct Mol Biol, 2016. **23**(7): p. 682-90.
112. Morey, L., et al., *Nonoverlapping functions of the Polycomb group Cbx family of proteins in embryonic stem cells.* Cell Stem Cell, 2012. **10**(1): p. 47-62.
113. Endoh, M., et al., *PCGF6-PRC1 suppresses premature differentiation of mouse embryonic stem cells by regulating germ cell-related genes.* Elife, 2017. **6**.
114. He, J., et al., *Kdm2b maintains murine embryonic stem cell status by recruiting PRC1 complex to CpG islands of developmental genes.* Nat Cell Biol, 2013. **15**(4): p. 373-84.

115. Wong, S.J., et al., *KDM2B Recruitment of the Polycomb Group Complex, PRC1.1, Requires Cooperation between PCGF1 and BCORL1.* Structure, 2016. **24**(10): p. 1795-1801.
116. Abdel-Wahab, O., et al., *Deletion of Asxl1 results in myelodysplasia and severe developmental defects in vivo.* J Exp Med, 2013. **210**(12): p. 2641-59.
117. Lai, H.L. and Q.T. Wang, *Additional sex combs-like 2 is required for polycomb repressive complex 2 binding at select targets.* PLoS One, 2013. **8**(9): p. e73983.

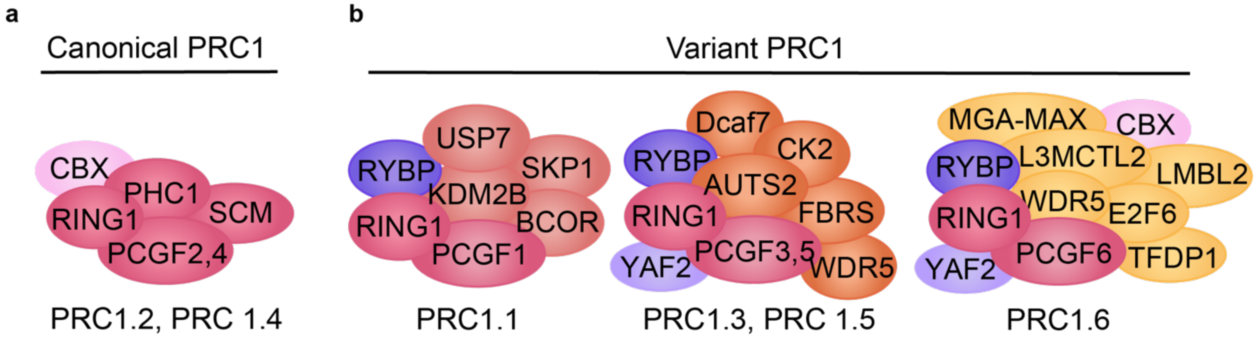

Fig. 1.1. Canonical versus variant PRC1 There are two categories of PRC1 complexes, **A,** canonical and **B,** variant, which are distinguished by the mutually exclusive incorporation of one of six PCGF paralogs. This family of complexes is biochemically defined by the presence of RING1A/B. Components of canonical PRC1 include RING1A/B, PHC1, and CBX family members and are labeled as either PRC1.2 or PRC1.4 based on incorporation of PCGF2 or PCGF4 respectively. RYBP/YAF2, PCGF and RING1A/B are shared core components of variant PRC1, that are characterized by accessory binding partners, including BCOR, KDM2B, E2F6, RYBP, and AUTS2, and labeled according to the PCGF1, PCGF3, PCGF5 or PCGF6 subunits (PRC1.1, PRC1.3, PRC1.5 and PRC1.6)

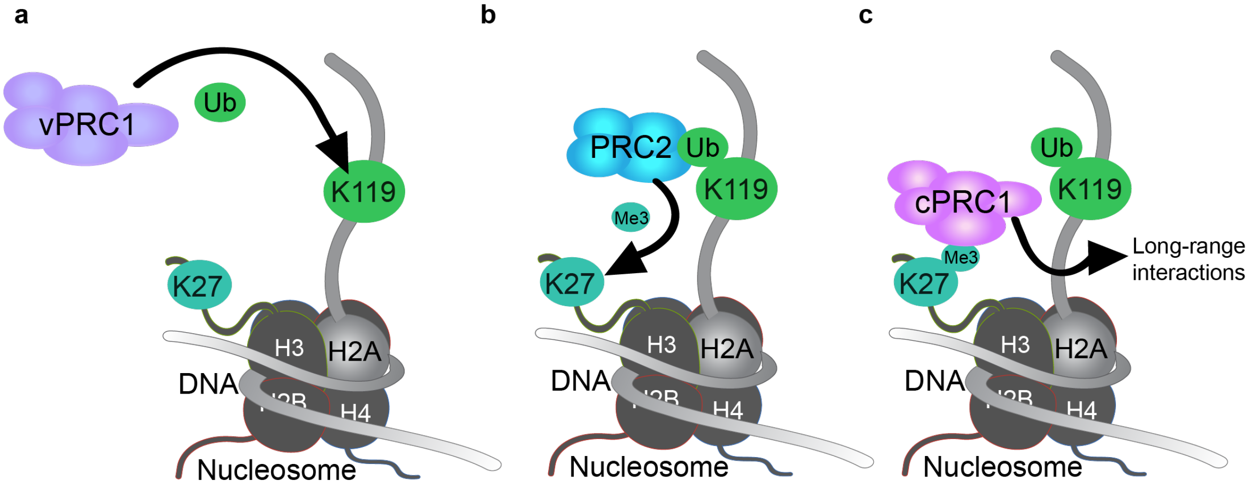

Figure 1.2. Polycomb recruitment model. Schematic summarizing the emerging model of Polycomb transcriptional regulation. **A,** Variant PRC1 monoubiquinates H2AK119. **B,** PRC2 is recruited by H2AUb1 and deposits H3K27me3. **C,** Canonical PRC1 recognizes H3K27me3 and promotes long-range interactions.

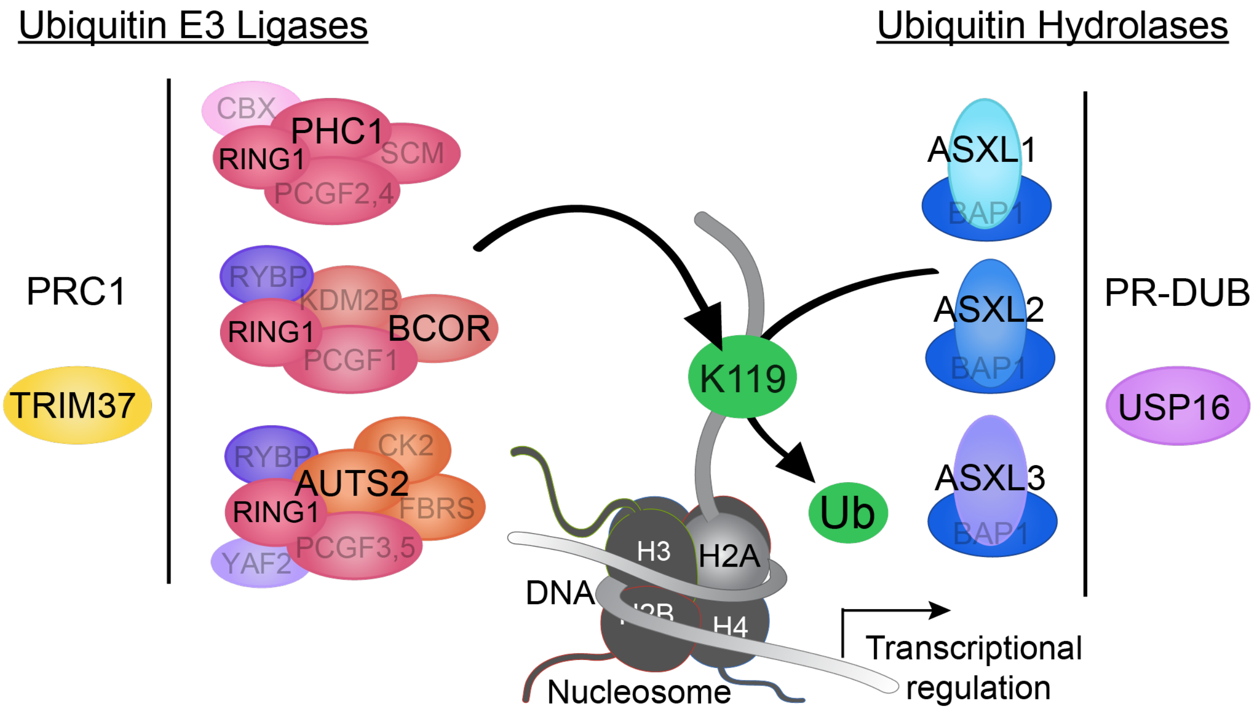

Fig. 1.3. Histone H2A monoubiquitination regulatory axis. Occurrence of genetic variants in the components that mediate H2AUb1 either independently or in association with Polycomb complexes. AUTS2, BCOR, and PHC1 are components of different PRC1 complexes that mediate the ubiquitination of lysine 119 on H2A. TRIM37 also functions as a ubiquitin E3 ligase but has not been shown to directly bind to a PRC1 complex. Along the right side, enzymes with H2AUb1 hydrolase activity are depicted. Individual ASXL family members form mutually exclusive PR-DUB complexes that mediate the deubiquitination of lysine 119 on H2A. The three PR-DUB complexes have overlapping and unique tissue and cell specificity. USP16 deubiquitinates H2AUb1 but does not interact with Polycomb complexes. Abbreviations: ASXL, additional sex comb-like; AUTS2, autism susceptibility candidate 2; BCOR, BCL6 corepressor; H2AUb1, monoubiquitination of histone H2A; PHC1, polyhomeotic-like 1; PRC1, Polycomb repressive complex 1; PR-DUB, Polycomb repressive deubiquitination complex; TRIM37, tripartite motif-containing protein 37; USP16, ubiquitin-specific protease 16.

Table 1.1. Clinical features and model organism phenotypes implicated in H2AUb1 remodeling and Neurodevelopmental Disorders[a,b]

Gene/Disorder	Human Phenotypes	pLI[c]	Z score[d]	Model system: phenotypes	Refs
ASXL1/BOS	Developmental delays, ID, hypotonia, hypoplastic/agenesis corpus callosum, delayed myelination, microcephaly, craniofacial dysmorphisms, feeding difficulties, skeletal manifestations, VSD, ASD	0.00	0.08	Mouse: craniofacial dysmorphism, skeletal transformations, myeloid dysplasia	[58, 59]
ASXL2/SPS	Delayed psychomotor development and speech, ID, ventriculomegaly, white matter volume loss, enlarged extra axial spaces, macrocephaly craniofacial dysmorphisms, feeding difficulties, skeletal manifestations, ASD	0.99	-0.01	Mouse: abnormal heart morphology, skeletal transformations	[60]
ASXL3/BRS, autism	Global psychomotor development delay, profound ID, microcephaly, craniofacial dysmorphisms, feeding difficulties, skeletal manifestations	1.00	-0.94	Mouse: abnormal heart development	[16]
USP16/Down Syndrome	ID, ventriculomegaly, hypotonia, skeletal manifestations, CHD, AVC	0.01	-0.89	Mouse: Embryonic lethal < E7.5 Xenopus laevis: homeotic transformation	[40, 61]
AUTS2/autism	Delayed psychomotor development and speech, learning difficulties, microcephaly, ID, hypertonia, craniofacial dysmorphisms, feeding difficulties, skeletal manifestations	1.00	3.09	Mouse: developmental delay in sensorimotor, cognition, and communication Zebrafish: craniofacial dysmorphism	[62, 63]
PHC1/microcephaly	Low-normal intelligence, microcephaly, craniofacial dysmorphisms	1.00	4.01	Mouse: congenital heart defects, homeotic transformations, craniofacial dysmorphisms	[62, 64]
Trim37/Mulibrey Nanism	Large cerebral ventricles and cisternae, dysarthria, craniofacial dysmorphisms, dolichocephaly, skeletal manifestations, myocardial fibrosis, congestive heart failure, pericardial constriction, globular-shaped heart	0.17	1.42	Mouse: cardiomyopathy, reproductive organ defects	[65]
BCOR/syndromic micropthalamia 2	Mild ID, delayed motor development, hypoplastic or absent optic chiasm, spastic paraparesis, hypoplastic corpus callosum, microcephaly, craniofacial dysmorphisms, skeletal manifestations, ASD, VSD, aortic valve stenosis, pulmonary valve stenosis, pentalogy of Fallot, DORV, dextrocardia, mitral valve prolapse, tricuspid valve inefficiency	1.00	1.06	Mouse: heart defects, craniofacial dysmorphism, abnormal forebrain development, decreased cerebellar size	[66]
Ring1/Schizophrenia	Intrauterine growth retardation, microcephaly, delayed acquisition of language, cognitive, and social skills, mild scoliosis, schizophrenic sypmtoms	0.92	3.42	Mouse: Abnormalities of axial skeleton patterning. Defects in dorsal ventral patterning of telencephalon.	[67]

[a] Both Z score and pLI values have been obtained from the ExAC browser (http://exac.broadinstitute.org).

[b] Abbreviations: ASD, atrial septal defect; AVC, atrioventricular canal; BOS, Bohring–Opitz syndrome; BRS, Bainbridge–Ropers syndrome; CHD, congenital heart disease; DORV, double outlet right ventricle; SPS, Shashi–Pena syndrome; VSD, ventricular septal defect.

[c] pLI is the probability of being LOF intolerant (pLI). The closer pLI is to one, the more LOF intolerant the gene appears to be.

[d] For synonymous and missense, Z score has been created. Z score is the deviation of observed counts from the expected number. Positive Z scores indicate increased constraint (intolerance to variation) and therefore the gene had fewer variants than expected. Negative Z scores are given to genes that had more variants than expected.

Chapter 2[2]

Aberrant Extracellular Matrix and Cardiac Development in Models Lacking the PR-DUB Component ASXL3

ABSTRACT

Clinical and research based genetic testing has uncovered genes that encode chromatin modifying complex components required for organogenesis. Covalent histone modifications play a key role in establishing transcriptional plasticity during development, required for cell fate specification, and have been implicated as a developmental mechanism that accounts for autism spectrum disorder (ASD) and CHD co-occurrence. *ASXL3* has been identified as a high confidence ASD gene. ASXL3 is a component of the Polycomb Repressive Deubiquitination (PR-DUB) complex, which deubiquitinates histone H2A. However, the role of ASXL3 in cardiac development remains unknown. We used CRISPR/Cas9 gene editing to generate clinically relevant *Asxl3* frameshift alleles in a mouse model and human embryonic stem cells (hESCs). To evaluate ASXL3 function in developing hearts, we performed structural, molecular, immunostaining and histological analyses. Transcriptomic and cellular compositional changes were assessed with bulk RNA sequencing of mouse hearts and single-cell RNA sequencing (scRNA-seq) of human cardiac tissue differentiated from isogenic hESC lines. Biallelic genetic inactivation of *Asxl3* leads to perinatal lethality and increased levels of histone H2A mono-ubiquitination, which are regulated by PR-DUB. *Asxl3*$^{+/fs}$ and *Asxl3*$^{fs/fs}$ mice display cardiac abnormalities including ventricular hypoplasia, septal defects, and bifid cardiac apex with variable penetrance. The presence of underdeveloped ventricles is preceded

---

[2] This chapter represents a submitted manuscript. McGrath B, Tsan YC, Salvi S, Ghali N, Martin DM, Hannibal M, Keegan CP, Helms A, Bielas SL, Srivastava A. Aberrant extracellular matrix and cardiac development in models lacking the PR-DUB component ASXL3. *Under Review Circulation*

by increased progenitor proliferation in the ventricles, as determined by EdU incorporation. Differential gene expression, assessed by bulk RNA sequencing implicates extracellular matrix dysfunction as a pathogenic mechanism. This correlates with a reduction in vimentin-positive cardiac fibroblasts. scRNA-seq of cardiac cultures differentiated from human *ASXL3*$^{fs/fs}$ ESC lines exhibit altered ratios of cardiac fibroblasts and cardiomyocytes. Similar to the mouse data, genes essential for extracellular matrix composition and signaling are differentially expressed between *ASXL3*$^{+/+}$ and *ASXL3*$^{fs/fs}$ human *in vitro* differentiated cardiac tissue. The observed transcriptomic changes predict diminished cell-cell signaling interactions between cardiac fibroblasts and cardiomyocyte progenitors in *ASXL3* cultures. Collectively, our data implicates species-specific roles for ASXL3 in both human and mouse cardiac development. These results highlight the role of extracellular matrix gene programs by cardiac fibroblast during cardiomyocyte development and provide insight into mechanisms of altered cardiogenesis by autism risk genes.

INTRODUCTION

Heart development requires exquisite orchestration of cardiac progenitor proliferation, migration, differentiation, morphogenesis and developmental remodeling to form four chambers. Disruption of this complex process is the basis of congenital heart defects, the most prevalent birth defect. Investigating the genetic and molecular mechanisms underlying cardiac development will unveil the transcriptomic and regulatory networks essential for normal and abnormal cardiogenesis.

Transformation of the embryonic heart tube into the mammalian four chambered heart requires coordinated proliferation of cardiac progenitor cell (CPC) pools and differentiation toward diverse cardiac lineages. Analysis of cardiogenesis in model organisms has allowed the developmental origin of the mature structural heart features to be traced back to one of the two mesoderm derived cardiac primordia, the first (FHF) and second heart fields (SHF), or neural crest lineages [1]. The left ventricle and atria are a product of FHF progenitors and the SHF contributes to the right ventricle, atria, outflow and inflow tracks. Single-cell transcriptomics studies along heart organogenesis have defined the shared and distinct expression profile of CPCs progressing through a series of intermediate cardiac-cell states to mature endocardial and cardiomyocyte cardiac lineages, in mouse and human model systems [2-5].

Within the embryonic heart, the extracellular matrix (ECM) plays an active role in governing the spatial programs of cardiac organogenesis[6]. Beyond structural support for cardiac cells, the ECM influences cardiomyocyte migration during cardiac tube expansion, looping, ventricular trabeculation and compaction and regulation of cell proliferation and differentiation [7-16]. The influence of the ECM on these developmental processes depends on the coordinated synthesis and degradation of ECM secreted factors and expression of corresponding ECM receptors [6]. For instance, cardiac fibroblasts, which comprise a large cell population in the heart, secrete high levels of developmental stage-specific extracellular matrix and growth factors, including fibronectin (FN) [17].Cell surface expression of β1 Integrin by cardiomyocytes binds FN in the ECM, promoting CPC proliferation and expansion of ventricular chambers during cardiogenesis [14, 18, 19]. ECM composition varies across cardiac structures and development. Independent of the stage of heart development, ECM composition is transcriptionally regulated across various cardiac cell lineages and can be disrupted by epigenetic mechanisms that alter chromatin remodeling or genome wide post-translational modifications[12, 20, 21].

During cardiogenesis, epigenetic mechanisms establish transcriptional plasticity that generates distinct transcriptional profiles for development. The evolutionarily conserved Polycomb group (PcG) complexes contribute to establishing this transcriptional plasticity by regulating transcriptional repression [22]. The PcG complexes, Polycomb repressive complex 1 (PRC1), complex 2 (PRC2) and PR-DUB, are subdivided on the basis of associated enzymatic activities[23]. Histone H3 lysine 27 trimethylation (H3K27me3) is catalyzed by PRC2. PRC1 catalyzes mono-ubiquitylation of H2A (H2AUb1), while PR-DUB hydrolyzes H2AUb1 deubiquitination. The core components of the PR-DUB complex are the ubiquitin hydrolase BAP1 (BRCA1 associated protein 1) and one of three ASXL family members, ASXL1, ASXL2 or ASXL3 [24]. Individual ASXL family members function as the mutually exclusive obligate regulatory subunits of the PR-

DUB complex, as BAP1 does not exhibit histone H2A deubiquitination activity (DUB) in the absence of an ASXL protein [25, 26]. While all ASXL family members were expressed in the embryonic mouse heart, the role of *Asxl3* during cardiac development has not been investigated [27].

Monoallelic frameshift *ASXL3* variants are the genetic basis of Bainbridge-Ropers Syndrome (BRS) and syndromic autism spectrum disorder (ASD), characterized by repetitive and social features of ASD, global developmental delay, intellectual disability, hypotonia, craniofacial dysmorphism, reduced gastrointestinal motility and altered sleep cycle [28, 29]. While congenital heart defects are not enriched in this cohort, they have been described as a feature of ultra-rare biallelic recessive *ASXL3* missense variants [30]. We investigated the role of ASXL3 in cardiac development by using a biallelic frameshift *Asxl3* mouse model and cardiac tissue differentiated from biallelic frameshift *ASXL3* human embryonic stem cell (hESC) lines. Constitutive loss of *Asxl3* exhibit highly penetrant CHDs and perinatal lethality, with less severe cardiac phenotypes observed in heterozygous animals. Altered composition of cardiac cell lineages and ECM components were observed in models from both species. Transcriptomics implicate species-specific genetic and molecular features of these shared pathogenic mechanisms. Correlation between these biallelic models highlight a dosage-sensitive role for *ASXL3* in cardiogenesis and underscores the differential expressivity of CHDs in BRS/ASD.

RESULTS

H2AUb1 elevated in Asxl3 frameshift mouse model

To investigate the role of ASXL3 in development, we generated a mouse model with a two base-pair deletion in *Asxl3*, corresponding to homologous nucleotides classified as pathogenic *ASXL3* BRS/ASD variants. Single guide RNAs (sgRNAs) were designed to target a region of mouse exon 12, which is homologous to human exon 11 (Fig. 2.1A). CRISPR/Cas9 editing created an *Asxl3* c.990_992delCA:993T > G;p.T484Afs*5 frameshift (*Asxl3fs*) allele through non-homologous end joining in B6SJL hybrid blastocyst after pronuclear injection (Fig. 2.1B). Expression of full-length *Asxl3* and its protein product was not detected by RT-qPCR and Western blot in *Asxl3*$^{fs/fs}$ mice (Fig. 2.1C and 2.1D). ASXL3 interacts with BAP1 to form the PR-DUB complex, which mediates histone H2A deubiquitylation [29]. We measured the levels of Histone H2A mono-ubiquitination in E13.5 hearts by western blot. Consistent with findings from patient derived fibroblasts, we found a 1.5 fold increase of H2AUb1 relative to histone H3 in *Asxl3*$^{fs/fs}$ mice (Fig. 2.1E and 2.1F).

Asxl3 null mouse exhibits Polycomb transcriptional repression phenotypes

Heterozygous intercrosses yielded *Asxl3*$^{fs/fs}$ at standard Mendelian ratios till birth at P0.5 (Fig. 2.1G). Consistent with neonatal lethality, *Asxl3*$^{fs/fs}$ pups are underrepresented from P0.5 to P5. At birth, *Asxl3*$^{fs/fs}$ mice weigh less than both *Asxl3*$^{+/fs}$ and *Asxl3*$^{+/+}$ littermates which are comparable in weight (Fig. 2.1H). Given the important role for Polycomb transcriptional repression on Hox gene expression, we performed skeletal Alcian blue staining to assess evidence of skeletal homeotic transformations [23]. No defects were observed in the vertebral column of 8 *Asxl3*$^{+/+}$ pups, while a low penetrant cervical rib homeotic transformation of cervical vertebrae C7 was observed for 1 in 10 *Asxl3*$^{+/fs}$, and 1 of 11 *Asxl3*$^{fs/fs}$ pups. Small ossified rib anlagen at cervical vertebra C7 are observed at very low penetrance in wild-type mice of some hybrid mouse strains [31]. This phenotype has not been described for a B6SJL hybrid mouse strain, implicating a nonredundant role of ASXL3 in Hox gene regulation of axial skeleton segmentation.

Asxl3 mutant neonates exhibit severe congenital heart defects

Phenotypic evaluation of multiple organ systems was performed to determine an etiology of neonatal lethality. Stomach milk is externally observed in P0.5 *Asxl3*$^{fs/fs}$ pups, suggesting that suckling reflexes are intact. Hematoxylin and eosin (H&E) histological evaluation of whole mount P0.5 *Asxl3*$^{+/+}$, *Asxl3*$^{+/fs}$ and *Asxl3*$^{fs/fs}$ neonates depicted normal gross anatomy of liver, lungs, kidneys, small intestine, colon, testis, and stomach for all three genotypes (Supplemental Fig. 2.1) No structural brain defects were observed by cresyl violet staining, but distinct borders defining cortical layers are diminished (Chapter 3). These defects are not predicted to result in neonatal lethality.

Conversely, *Asxl3*$^{fs/fs}$ neonates exhibit congenital cardiac defects by H&E staining and gross organ structural defects. Hearts of P0.5 mice displayed congenital morphological abnormalities ranging from cardiac bifida to separated ventricles in *Asxl3*$^{+/fs}$ and *Asxl3*$^{fs/fs}$ mice at increasing penetrance, respectively (Fig. 2.2A and 2.2B). Bifida cardiac apex was observed in 16.7% of *Asxl3*$^{fs/fs}$ mice and separated ventricles were observed in 4.5% of *Asxl3*$^{+/fs}$ and 16.7% of *Asxl3*$^{fs/fs}$ mice. Out of 39 *Asxl3*$^{fs/fs}$ neonatal hearts serially sectioned and analyzed by H&E staining, 11 (28%) showed right ventricular hypoplasia, with 4 presenting with almost complete loss of the ventricular lumen, making this the most penetrant heart phenotype in this *Asxl3* mouse model. Apical muscular ventricular septal defects were also detected in 5.1% of *Asxl3*$^{fs/fs}$ mice. The ventricles in hypoplastic ventricular hearts appeared incomplete with reduced luminal space throughout the entirety of serial sections (Fig. 2.2 and Supplemental Fig. 2.3). Such cardiac defects have been observed in transgenic mouse models of genes that encode components of Polycomb complexes and are predicted to be the basis of neonatal lethality [27].

Right ventricular hypoplasia in *Asxl3*$^{+/fs}$ and *Asxl3*$^{fs/fs}$ P0.5 hearts correlates to increased heart weight and heart to body weight ratios, consistent with increased cardiac tissue. We independently weighed P0.5 pups as well as dissected hearts with extra-cardiac tissue removed. *Asxl3*$^{fs/fs}$ hearts weigh significantly more than *Asxl3*$^{+/+}$ hearts, with a corresponding increase in heart to body-weight ratio (Fig. 2.2D and 2.2E). No significant difference was observed in heterozygous mice. Quantitative morphometric analysis of H&E stained heart sections were performed to characterize the ventricular tissue changes in hypoplastic hearts. Morphometric analysis included interventricular septum (IVS), left ventricle internal diameter (LVID), left wall thickness (LWT), right ventricular internal diameter (RVID), and right wall thickness (RWT) (Fig. 2.2F). This analysis revealed a decrease in LVID and RVID in *Asxl3*$^{fs/fs}$ mice consistent with ventricular hypoplasia (Fig. 2.2G). The absence of a significant increase in RWT, LWT, or IVS length could be due to the variable penetrance of hypoplastic hearts since the septum and ventricular walls of hypoplastic hearts appear thicker (Supplemental Fig. 2.3).

Increased proliferation during heart development

Several pathogenic mechanisms of cardiac development including fibrosis, increased cardiomyocyte size (hypertrophy) or altered cardiac progenitor proliferation (hyperplasia) could account for an increased ventricular chamber wall thickness. Masson trichrome staining performed on P0.5 paraffin-embedded heart sections did not show evidence of fibrosis in ventricular or septum tissue from mice of any genotype (Fig. 2.3A and 2.3B). To investigate the possibility of cardiomyocyte hypertrophy, the cross-sectional area of cardiomyocytes was quantified from P0.5 coronal cardiac sections stained with Alexa 488 conjugated wheat germ agglutinin (WGA). No significant difference in cardiomyocyte size was observed in *Asxl3*$^{+/fs}$ or *Asxl3*$^{fs/fs}$ tissue relative to controls across corresponding structural areas (Supplemental Fig. 2.3).

CPC proliferation during development was interrogated using a 24hr pulse of EdU, to label mitotically active cells undergoing DNA replication. Timed-pregnant dames were administered EdU, by intraperitoneal injection at embryonic day 13.5 (E13.5) (Fig. 2.3C). A day later, hearts from E14 littermates were fixed, cryosectioned and EdU was detected through a Click-it reaction (Fig. 2.3F and 2.3G). No appreciable changes in EdU positive cells were noted in the septum between genotypes (Fig. 2.3E). In the left ventricle of *Asxl3*$^{+/fs}$ and *Asxl3*$^{fs/fs}$ hearts, EdU was detected in more cells relative to wild type littermates (Fig. 2.3E). EdU-positive cells were also increased in the right ventricle of *Asxl3*$^{+/fs}$ and *Asxl3*$^{fs/fs}$ hearts, however, significance was achieved in only *Asxl3*$^{fs/fs}$ tissue relative to controls (Fig. 2.3E). Overall, *Asxl3*$^{fs/fs}$ hearts tend to show increased levels of EdU incorporation in both the left and right ventricles at E14. This is consistent with a model of cardiac progenitor hyperplasia, with a secondary reduction in ventricular luminal size.

RNA Seq uncovers distinct gene expressions in E18.5 Asxl3 mutants

De novo and CRISPR-edited *ASXL3* genetic variants disrupt ASXL3-dependent PR-DUB H2AUb1 deubiquitination and transcriptional regulation (Fig. 2.1E). To analyze transcriptional changes correlated with elevated H2AUb1 in *Asxl3*$^{+/fs}$ and *Asxl3*$^{fs/fs}$ hearts, we performed bulk-RNA sequencing of E18.5 ventricles isolated from closely associated aorta, left atrium and right atrium from four sets of *Asxl3*-littermates. Highly reproducible transcriptomic changes were observed in the ventricular samples from both *Asxl3*$^{+/fs}$ and *Asxl3*$^{fs/fs}$ samples. 333 differentially expressed genes (DEGs; false discovery rate adjusted *p*-values defined by DESeq2, $q < 0.05$ and $\log_2$ fold change of ≥0.4) were identified in *Asxl3*$^{+/fs}$ ventricles, with 170 (51.05%) downregulated and 163 (48.95%) upregulated (Fig. 2.4A). Similarly, 366 DEGs were observed in *Asxl3*$^{fs/fs}$ ventricular tissue with 161 (43.99%) downregulated and 205 (56.01%) upregulated (Fig. 2.4B).

Comparison of all *Asxl3*$^{+/fs}$ and *Asxl3*$^{fs/fs}$ DEGs revealed that ~30% of DEGs were represented in both genotypes (Supplemental Fig. 2.4A and 2.4B). Kyoto Encyclopedia of Genes and Genomes (KEGG) pathway enrichment analysis of *Asxl3*$^{+/fs}$ and *Asxl3*$^{fs/fs}$ transcriptomics revealed overlapping pathways for downregulated DEGs including ‘ECM-receptor interactions’, ‘focal adhesion’, and ‘PI3K-AKT signaling pathway’ (Fig. 2.4C). Similar findings were detected with GO analysis (Supplemental Fig.2.4C). Together these altered pathways implicate disrupted extracellular matrix (ECM) function in *Asxl3*$^{+/fs}$ and *Asxl3*$^{fs/fs}$ ventricles. The ECM provides both signaling and structural functions in the developing heart that are critical for the heart organogenesis [6]. Downregulated DEGs enriched in *Asxl3*$^{+/fs}$ and *Asxl3*$^{fs/fs}$ shared pathways include important cardiac ECM components like *Col1a1, Col5a1, Fbln2, Fbn1, Eln, Ltbp4, and Fn1*, (Fig. 2.4A and 2.4B).

Of note, while *Asxl3*$^{+/fs}$ and *Asxl3*$^{fs/fs}$ shared a similar number of upregulated (55) and downregulated (52) genes, upregulated DEGs enriched in KEGG pathways were not shared between *Asxl3*$^{+/fs}$ and *Asxl3*$^{fs/fs}$ datasets (Fig. 2.4D). ECM involvement in *Asxl3*$^{fs/fs}$ cardiac phenotype was also implicated by gene set enrichment analysis (GSEA) of the C5 ontology gene set from the molecular signature database (MSigDB), which also identified significant DEG transcript enrichment in GO Extracellular Matrix Assembly and GO Collagen Fibril Organization (Fig. 2.4E and 2.4F). While negative normalized enrichment scores (NESs) quantified the correlation of downregulated DEGs for both *Asxl3*$^{+/fs}$ and *Asxl3*$^{fs/fs}$ samples, this analysis also reveals the intermediate transcriptional changes for *Asxl3*$^{+/fs}$ relative to *Asxl3*$^{fs/fs}$ samples, for both the rank order DEGs and negative NES. An *Asxl3*$^{+/fs}$ NES of -1.2 and -1.23 versus *Asxl3*$^{fs/fs}$ NES of -1.89 and -2.13 for GO Extracellular Matrix Assembly and GO Collagen Fibril Organization pathways respectively quantify the difference of enriched hits from bottom-ranked genes in the pathway. This data does not differentiate between timing of the onset of differential expression across cardiac development, both of which may be required to describe the discrepancy in the severity of cardiac phenotypes between *Asxl3*$^{+/fs}$ and *Asxl3*$^{fs/fs}$ animals.

Reduced cardiac fibroblasts in ventricles of *Asxl3* mutants

Cardiac fibroblasts are a prominent source of ECM deposition, degradation, and remodeling in the developing heart [17]. Embryonic cardiac fibroblasts are also a source of integrin ligands, including fibronectin and collagen, that promote cardiomyocyte proliferation through integrin signaling pathways [14]. Given the differential expression of ECM components we detected in *Asxl3*$^{+/fs}$ and *Asxl3*$^{fs/fs}$ ventricles and increased proliferation observed at E14, cardiac fibroblasts distribution and ECM deposition was evaluated. Coronal sections of fixed P0.5 heart were immunostained for vimentin, an intermediate filament protein marker of cardiac fibroblasts. Vimentin-positive cells were quantified in each ventricle separately and the septum (Fig. 2.5C). An equivalent number of fibroblasts were observed in the septum between all three genotypes (Fig. 2.5B). A significant reduction in vimentin-positive cells were quantified in *Asxl3*$^{+/fs}$ and *Asxl3*$^{fs/fs}$ samples relative to controls (Fig. 2.5D and 2.5F). This decrease in cardiac fibroblasts is a mechanism that would account for downregulation of ECM gene signatures by RNA sequencing.

Given, *Collagen1A1* (*COL1A1*) and *Collagen3A1* (*Col3A1*) expression was downregulated by RNA-seq, ECM deposition in E15.5 and P0.5 heart were validated by immunohistochemistry. Surprisingly, minimal collagen differences were observed at P0.5 in any heart region (Supplemental Fig. 2.5). At E15 *Col3A1* appeared comparable in the left ventricle of Asxl3+/+ and *Asxl3*$^{fs/fs}$ mice, but it appeared slightly increased in the right ventricle of *Asxl3*$^{fs/fs}$ littermates. Evaluation of other ECM components and/or additional developmental time points would provide greater insights into the disrupted ECM dynamics. Together these findings suggest that inactivation of *Asxl3* in cardiac development may have downstream consequences such as the disrupted collagen and decreased number of cardiac fibroblasts as is observed in the heterozygous and null hearts.

ASXL3-dependent *in vitro* human cardiac differentiation

Given the *Asxl3*$^{fs/fs}$ mouse cardiac phenotype, and congenital heart defects attributed to biallelic *ASXL3* missense variants, a human *in vitro* model of cardiac differentiation was used to explore the function of *ASXL3* in normal physiology and pathology. CRISPR/cas9 gene-editing was used to create isogenic H9 human embryonic stem cell (hESC) lines carrying biallelic *ASXL3* c.1393dupT;p.C465LfsX4; and c.1390_1393del;p.E464AfsX19 (*ASXL3*$^{fs/fs}$) variants in exon 11 an *ASXL3* exon enriched for variants clinically classified as pathogenic [29] (Fig 2.6A and Supplemental Fig. 2.6). Isogenic control and *ASXL3*$^{fs/fs}$ hESC lines were differentiated to a cardiac lineage using an established protocol, but lactate selection or magnetic beads assisted cell sorting was omitted to preserve non-cardiomyocyte lineages in the culture, thus enhancing the cellular heterogeneity of tissue differentiated from the common cardiogenic mesodermal lineage [32]. Differentiation of monolayer cultured hESC towards cardiomyocyte lineage is induced by modulating components of the WNT signaling pathway over first 5 successive days to establish cardiogenic mesoderm and transition into CPCs. By omitting cardiomyocyte selection at day 10, differentiation proceeds to generate NKX2-5 cardiomyocytes lineages and non-contractile cardiac derivatives (Fig. 2.6B). Single-cell RNA sequencing was performed on *ASXL3*$^{+/+}$ control and *ASXL3*$^{fs/fs}$ cultures at 12 days of differentiations to characterize the progeny of cardiac lineages. A total of 18,577 cells (9,379 *ASXL3*$^{+/+}$ and 9,198 *ASXL3*$^{fs/fs}$ cells) with an average of 1001.73 genes detected per cell that met our data quality control and filtering parameters, were captured from three *ASXL3*$^{+/+}$ and two *ASXL3*$^{fs/fs}$ independent cardiac differentiations. The filtered dataset was analyzed using our pipeline based on Seurat version 3 [33].

By performing dimensionality reduction and unsupervised clustering with uniform manifold approximation and projection (UMAP) we identified 11 unique cell populations (Fig 2.6C and 2.6D). Clusters were manually annotated according to expression of cell type markers described by various experimental approach, and each set of cluster-specific marker genes were cross-referenced against published scRNAseq studies (Fig. 2.6C and 2.6E) [2-4]. The cell populations identified correlated to major cell-types present in *in vivo* cardiogenesis and *in vitro* cardiac differentiation, including cardiomyocyte progenitors, cardiomyocytes, fibroblast progenitors, and cardiac fibroblasts. The TTN+ cardiomyocyte clusters, clusters 8, 9, 10, and 11 express high levels of sarcomere genes *MYH6*, *MYL3*, *TNNT2*, *TTN*. While we observe three NKX2-5 positive cardiomyocyte progenitor populations, cluster 5, 6, and 7, only cluster 5 actively expressed cell proliferation marker *MKI67*. Interestingly first heart field marker *TBX5* and second heart field marker *MEF2C* shared similar expression patterns among all cardiomyocyte progenitor clusters, suggesting these are still early-stage progenitors. We identified three Decorin (*DCN*)-positive fibroblast clusters cardiac fibroblast populations, clusters 1, 2, and 3 that contain cells expressing high levels of extracellular matrix genes such as *DCN*, *COL3A1* and *COL1A1*. We further classified cluster 1 (DCN+MKI67+ Proliferating Fibroblast) as proliferating fibroblast progenitors based on their expression of *MKi67*. Lastly, we detected an ID1+ non-cardiomyocyte progenitor cluster. In the developing heart, *ID1* is exclusively expressed by non-cardiomyocyte cells in the epicardium and endocardium [34].

Comparable cell-type clusters were detected in control and *ASXL3*$^{fs/\mathrm{fs}}$ samples when clustered independently and in aggregate. In the combined analysis, *ASXL3*$^{fs/fs}$ cells are distributed across all clusters (Fig. 2.6C). The reproducibility of scRNA-seq transcriptomics allows the cellular composition of heterogeneous differentiating tissue to be determined between control and *ASXL3*$^{fs/fs}$ samples (Fig. 2.6F). The ratio of non-cardiomyocytes fated cell progeny (+/+ 20.3%, *fs/fs* 25.5%) relative to cardiomyocytes fated lineages (+/+ 79.7%, *fs/fs* 74.5%) was similar in samples from both genotypes (Fig. 2.6F). A slight increase in *ASXL3*$^{fs/fs}$ cardiac fibroblasts, differentiating along a *DCN* defined lineage, was observed relative to control sample (+/+ 17.8%, fs/fs 24.9%). Additional days of cardiac differentiation are required to determine if this composition difference resolves or results in a *ASXL3*$^{fs/fs}$ cardiac differentiation phenotype.

To identify transcriptomic changes that occur during cardiac differentiation, *ASXL3*$^{fs/fs}$ DEG were determined for each cluster (supplemental data). An average of 367 DEGs were detected per cluster (Min. 184; Max. 749). KEGG pathway analysis of DEGs showed overlapping dysregulation of ECM receptor interaction, signaling pathways, cardiomyopathy, and cell function related pathways (Fig. 2.6G). These aberrant pathways were enriched for both up- and down-regulated genes across multiple clusters. Notably, three of the top KEGG pathways focused on ECM receptor interaction showed DEG enrichment, specifically "Focal Adhesion", "ECM-receptor interaction" and "PI3K-AKT signaling pathway" (Fig. 2.4C and 2.6G). These findings suggest pathologic mechanisms are shared between mice and humans. In addition, DEGs from three NKX2-5 positive, cardiomyogenic progenitor clusters (NKX2-5+MKI67+ Progenitor, NKX2-5+MKI67- Progenitor 1, and NKX2-5+MKI67- Progenitor 2) were similarly enriched in the Focal adhesion KEGG pathway. Of the 184, 235, and 467 DEGs identified in each cluster respectively *MAP2K1*, *ACTB*, and *MYLK* were differentially expressed among all 3 clusters from the Focal adhesion KEGG pathway. Interestingly the majority of these DEGs were down-regulated DEGs (168, 228, 259, respectively). ECM deposited by the stromal fibroblast populations acts non-autonomously to influence cardiomyogenic progenitor proliferation (Fig. 2.7H). Coalescence of cardiomyogenic progenitor DEGs in the focal adhesion KEGG pathway implicates that imbalanced expression of ECM ligand components and/or receptors in cardiomyogenic progenitor cells impacts proliferation and differentiation.

To assess defects in cell-cell communication, due to a cell-specific imbalance of ligand-receptor expression, we processed our scRNA-seq dataset using CellphoneDB, an analysis tool developed to objectively quantify potential cell signaling between clusters based on single-cell transcriptomics [35]. The averaged expression intensity of each ligand-receptor pair was calculated and compared to the random permuted null distribution to calculate *p* values, which are based on unbiased identification of cell-cell interactions and active signaling pathways. 129 and 217 active molecular signaling pathways were identified in *ASXL3*$^{+/+}$ and *ASXL3*$^{fs/fs}$ cells respectively (Fig. 2.7A and 2.7B) by the CellphoneDB algorithm. Interestingly regardless of genotype, DCN+ fibroblast 1 was the most "communicative" population of cells, interacting within itself and robustly with both cardiomyogenic progenitors (NKX2-5+MKI67+ Progenitor, and NKX2-5+MKI67- Progenitor 1 clusters), and non-cardiomyogenic progenitors (DCN+MKI67+ Proliferating and Fibroblast, ID1+ Progenitor) (Fig. 2.7A and 2.7B). This piece of evidence again strongly favors the hypothesis that the fibroblasts support and regulate progenitors in the developing heart through both laying down the ECM environment and secreting other signaling cue molecules. Conversely in comparison mature cardiomyocytes are "quieter" and less communicative in general (Fig. 2.7A), although in the *ASXL3*$^{fs/fs}$ condition the mature TTN+ cardiomyocyte populations were more communicative compared to their *ASXL3*$^{+/+}$ counterparts with the progenitor populations (Fig. 2.7B). However, we also identified a group of cardiomyogenic progenitors (NKX2-5+MKI67-

Progenitor 2) that had very little communication with other cells (Fig. 2.7A). The importance and function of this group of cells remain to be further investigated.

We next compared the changes in cell-cell signaling pathways between the *ASXL3*$^{+/+}$ and *ASXL3*$^{fs/fs}$ cells. Active cell-cell communication lines between each cell populations in *ASXL3*$^{+/+}$ and *ASXL3*$^{fs/fs}$ cells were generated and then cross-referenced. While changes in total of 183 different cell-cell signaling communication lines were detected, 143 were strengthened and only 40 communication lines were weakened in *ASXL3*$^{fs/fs}$ compared to *ASXL3*$^{+/+}$ control cells (Fig. 2.7D and 2.7E). Strikingly, among the 40 weakened communication lines, DCN+ Fibroblast 1 was involved in 28 among the 40, suggesting an important role this group of fibroblasts play in the biology of *ASXL3*$^{fs/fs}$ defects (Fig. 2.7C). Fibronectin 1 (FN1) was one of the most important ECM proteins downregulated by ASXL3 loss of function identified in our mouse model (Fig. 2.4). Similarly in our human in vitro model, FN1 was highly expressed in the DCN+ Fibroblast 1 cells while the different heterodimer combinations between Integrin A5/AV (ITGA5/ITGAV) and Integrin B1/B5 (ITGB1/ITGB5) were expressed by the cardiomyogenic progenitor clusters NKX2-5+MKI67+ Progenitor and NKX2-5MKI67- Progenitor 1 (Supplemental Fig. 2.8). FN1 expression was downregulated among all fibroblast clusters (Supplemental Fig. 2.8) while the integrin receptor genes were mostly downregulated in the NKX2-5+MKI67+ Progenitor and NKX2-5MKI67- Progenitor 1 (Supplemental Fig. 2.8). CellphoneDB hence predicted a weakening of the Fibronectin (DCN+ Fibroblast 1) - Integrin (NKX2-5+MKI67+ Progenitor/NKX2-5MKI67- Progenitor 1) signaling in our *ASXL3*$^{fs/fs}$ model compared to the *ASXL3*$^{+/+}$ controls (Fig. 2.7F and 2.7H). Conversely, BMP signaling was among the signaling pathways strengthened in the

ASXL3$^{fs/fs}$ cells. BMP signaling plays a crucial role and regulates cardiogenesis during heart development and loss of one of the BMP receptor genes BMPR1A leads to decrease in cell proliferation in the developing heart [36]. Interestingly we observed that multiple BMP signaling communication lines were strengthened between and within the cardiomyogenic progenitor clusters (Fig 2.7F and 2.7I). Although we did not observe an increase in proliferating cardiomyogenic progenitors in our in vitro model, increased BMP signaling pathways may implicate proliferation defects as observed in the *Asxl3*$^{fs/fs}$ animal model (Fig 3).

DISCUSSION

In this study, we demonstrate that pathogenic frameshift variants in *Asxl3* cause increased levels of H2AUb1, neonatal lethality, and an array of partially penetrant congenital heart defects (CHD). Hypoplasia of the right ventricle, the most prevalent *Asxl3*-associated CHD, was observed together with cellular composition changes within the heart. While different genes are dysregulated in mouse and human *ASXL3* models, both showed suppression of ECM gene sets indicating disruption of a conserved regulatory mechanism. Corresponding disruption to key signaling pathways and proliferation were detected in mouse ventricular development and human cardiac differentiation. Our findings provide an evidence for how chromatin biology can influence heart development through ECM regulation, and more broadly, a mechanism for co-occurrence of CHDs with ASD due to pathogenic variants in chromatin genes.

ASXL1, ASXL2 and *ASXL3* are the genetic basis of Bohring-Optiz (BOS), Sashsi-Pena (SPS) and Bainbridge-Ropers syndromes (BRS) respectively [28, 37, 38], developmental disorders with multiorgan involvement. Despite a shared H2AUb1 deubiquitination molecular mechanism, each ASXL1-, ASXL2- and ASXL3-PR-DUB complex conveys non-redundant functions based on the unique constellation of clinical features attributed to each disorder. CHDs have been described in association with *de novo* monoallelic pathogenic variants in *ASXL1* (BOS) and *ASXL2* (SPS), but not *de novo* monoallelic frameshift *ASXL3* (BRS/ASD) variants. CHDs observed in individuals with BOS include ventricular and atrial septal defects with minor incidence of cardiac hypertrophy and bradycardia. SPS is characterized by atrial septal defects, patent ductus arteriosus (PDA) and left ventricular dysfunction. While the pathogenicity of monoallelic

ASXL3 missense variants is difficult to classify, CHDs were recently reported for biallelic *ASXL3* missense variants, providing evidence of the pathogenicity of *ASXL3* missense variants [30]. Distinct CHDs detected in loss-of-function (knockout or frameshift) *Asxl1*, *Asxl2* and *Asxl3* mouse models, support non-redundant roles for ASXL family members in heart development, while highlighting the discrepancy in dosage-sensitivity between the species [27, 39].

Cardiac phenotypes of biallelic loss-of-function *Asxl* mouse models mirror the diversity of clinical features observed across the ASXL-related developmental disorders. Highly penetrant severe inlet ventricular septal defects, with interventricular septum (IVS) involvement are observed in *Asxl1* knockout mouse model, reminiscent of cardiovascular features of BOS [27]. Minor membranous VSDs were detected in *Asxl2*, while muscular VSDs were found in *Asxl1* and *Asxl3* mice. The severe *Asxl1* VSD phenotype can also be distinguished from *Asxl2*$^{-/-}$ and *Axsl3*$^{fs/fs}$ heart phenotypes by normal ventricular wall and valve thickness. Partially penetrant ventricular hypoplasia is observed in both *Asxl2*$^{-/-}$ and *Asxl3*$^{fs/fs}$ mouse models, but exhibit distinct ventricular laterality involvement. *Asxl2*$^{-/-}$ animals are characterized by hypoplastic left ventricle and IVS with corresponding thickening of the compact myocardium, while *Asxl3*$^{fs/fs}$ animals present with right ventricular hypoplasia. The general contribution of FHF and SHF cardiac primordia, to the left versus right ventricles respectively, highlight the spatiotemporal specificity of the individual *Asxl2* and *Asxl3* family members. Identifying the non-redundant genome-wide H2A deubiquitination functions of individual PR-DUB complexes will be critical future studies to correlate direct genomic targets of individual PR-DUB complexes to mechanisms of heart development.

Based on the cardiac involvement in the *Asxl3*$^{fs/fs}$ mouse, we analyzed echocardiograms of three individuals clinically diagnosed with BRS based on *de novo* frameshift *ASXL3* variants, which revealed a single case of bicuspid aortic valve. Furthermore, review of published case reports revealed one additional BRS case displaying cardiac phenotypes as pulmonary artery stenosis, small patent foramen ovale and PDA [38, 40]. This analysis did not investigate digenic or co-occurrence of a second pathogenic coding variants in these cases, yet the incidence of these CHDs is insufficient evidence to conclude a direct link between *de novo* monoallelic frameshift *ASXL3* variants and CHDs. Individuals with biallelic missense *ASXL3* variants present with Tetralogy of Fallot (TOF) [30]. TOF refers to the combination of four congenital abnormalities; VSD, pulmonary valve stenosis, misplaced aorta and thickened right ventricular wall. Thickened right ventricular wall and VSD phenotypes phenocopy the CHDs detected in *Asxl3*$^{fs/fs}$ mouse alluding to a consistent genotype-phenotype correlation. The developmental mechanism implicated by transcriptomic analysis of a biallelic missense *Asxl3* mouse model implicated involvement of the PI3K/AKT KEGG pathway, also detected in our *Asxl3*$^{fs/fs}$ model, and altered expression of components of the PRC2 complex, a phenotype shared with the *Asxl2*$^{-/-}$ mouse model [27, 30, 39]. These phenotypic outcomes provide further evidence for the importance of chromatin biology and Polycomb transcriptional repression in heart development.

The occurrence of heart defects in mouse models that disrupt genes encoding PRC1, PR-DUB, and PRC2 components demonstrates the importance of Polycomb transcriptional plasticity during cardiogenesis [22]. Phenotypic overlap between PR-DUB and PRC1 models, as compared to PRC2, implicates dynamic exchange of distinct

Polycomb histone PTMs as central to the cardiac morphogenesis phenotypes [27, 41-43]. Similar to the *Asxl3*$^{fs/fs}$ mouse model, right ventricular hypoplasia was detected in the knockout mouse model of *Phc1* (also known as *Rae28)*, which encodes canonical PRC1 complex (PRC1.2 and PRC1.4) component PHC1 [42]. VSDs, reminiscent of the cardiac phenotype observed in the *Asxl1*$^{-/-}$ mouse model, have been described in *Phc1* and the noncanonical PRC1 (PRC1.1) complex component *Bcor* knockout mouse models [44, 45]. While dynamic exchange of H2A mono-ubiquitination by PRC1 and PR-DUB complexes are clearly essential for cardiac development, careful evaluation of cardiac morphogenesis for defects associated with a comprehensive representation of PRC1 complexes is required to assign non-redundant roles in heart development and complementary PR-DUB phenotypes. Alternatively, PRC2 heart phenotypes are distinct from those shared between mouse models of PRC1 and PR-DUB components, highlighting the paucity of data detailing how H2AUb1 and H3K27Me3 dependent transcriptional plasticity is coordinated. Knockout mouse models of PRC2 components *Ezh2* or *Jarid2* present with a spectrum of cardiac structural malformations including hyper-trabeculation and hypoplasia of the compact myocardium, which is characterized by thinning of the ventricular wall [21, 46-48]. Neither do PRC2 associated heart phenotypes exhibit phenotypic laterality, by preferentially disrupting morphogenesis of a single ventricle.

Genetic and functional studies have contributed to our current understanding of the pathogenic mechanisms that give rise to single ventricular disorders (SVDs), namely hypoplastic left heart syndrome (HLHS) and hypoplastic right heart syndrome (HRHS). HRHS is a phenotype shared with the *Asxl3*$^{fs/fs}$ mouse model. Both HLHS and HRHS are characterized by underdeveloped or malformed structures of a single ventricle. Human and mouse genetic studies of SVDs have identified chromatin regulators, transcription factors, and signaling pathway components as the basis of these developmental defects [42, 49-62]. The convergence of the human genetics and animal models on these common molecular pathways implicate a shared pathogenic mechanism that impinges on CPC proliferation and ECM composition [52-54, 63, 64]. The left and right ventricle have distinct FHF versus SHF origins. Nevertheless, mouse HLHS- relative to HRHS ventricular transcriptomics not only reveal DEGs enriched in similar signaling pathways, but implicated altered ECM based mechanisms. The enriched KEGG pathways include ECM receptor interaction, Calcium signaling pathway, Focal adhesion, TGF-Beta signaling, Dilated cardiomyopathy, Hypertrophic cardiomyopathy, and Arrhythmogenic RV cardiomyopathy [54]. Consistent with these findings, analysis of ECM content in left and right ventricles of HLHS post-mortem and myocardial biopsy samples revealed reduced collagen levels compared to age-matched controls [64, 65]. Together these results suggest altered ECM dynamics contribute to laterality of ventricular hypoplastic heart phenotypes, but does not provide a mechanism for how asymmetric expressivity is established.

Genes that encode ECM components are differentially expressed in both ASXL3 mouse and human models. Developmentally, the ECM functions as a substrate for cell migration and promotes CPC proliferation, differentiation and maturation, chamber formation, and valve development [66]. ECM composition is tailored, spatially and temporally to promote chamber-specific signaling pathways and structural integrity to direct these morphogenetic events. ECM coordination of cell-cell communication in cardiac development is well established, and exemplified by the influence of FN1, expressed by cardiac fibroblasts, on proliferation of CPCs through $\beta 1$ integrin receptor binding to FN1 and PI3K/Akt pathway signaling. The importance of dynamic remodeling of ECM composition for organogenesis has been acknowledged, where disrupting either synthesis or degradation of the ECM results in CHDs attributed to disorganization of the dynamic tissue morphogenesis [15, 16, 66, 67]. More recent studies have described the network of transcription factors and chromatin-based regulatory mechanisms complexes that spatially and temporally coordinate expression of ECM genes [21, 68, 69]. For instance, conditional endocardial specific knockout of *Brg1*, a chromatin remodeler, allows for increased expression of the matrix metalloproteinase ADAMTS1, which results in premature degradation of the cardiac jelly and excessive trabeculation [12]. Our data provides additional evidence to link chromatin biology to the regulation of ECM components during cardiogenesis.

Expression of *Asxl3* at single-cell resolution during cardiac development has not been determined. *Asxl3* expression has been documented, from single-cell transcriptomics, in intermediate cell types along the Nkx2-5 cardiomyocyte lineage, and in cardiac fibroblasts of fetal mouse heart [5, 70]. Cardiac fibroblasts are an important source of diverse secreted components of the ECM [71]. In the *Asxl3* model, we detect fewer vimentin-positive fibroblasts in P0.5 $Asxl3^{+/fs}$ and $Asxl3^{fs/fs}$ ventricles and reduced expression of genes that encode ECM. We hypothesize that dysregulation of ECM during heart development contributes to E13.5 CPC reduced proliferation, that across development preferentially impinges on right ventricular development. Our analysis does not allow us to predict the initial source of this molecular pathology; we cannot preclude that loss of Asxl3 alters the differentiation of cardiac lineages that disrupts ECM composition and/or Asxl3-dependent ECM composition changes alter production of CPCs during development. We discovered extensive overlap between KEGG pathways enriched in our mouse model and other HLHS mouse models that centered around ECM composition, signaling, and cardiac defects [54]. The pathways included ECM receptor interaction, calcium signaling pathway, focal adhesion, TGF-Beta signaling, dilated cardiomyopathy, Hypertrophic cardiomyopathy, and Arrhythmogenic RV cardiomyopathy. Similar disrupted pathways are also observed in the biallelic *Asxl3* missense mouse [30]. Two models for SVDs have been proposed to explain this phenotype. One attributes decreased blood flow during a critical period of ventricular development to the reduced ventricular size [72]. The second model suggests CPC hyperplasia as the driving force for underdeveloped ventricles [51]. The increased proliferation we observe in *Asxl3*$^{fs/fs}$ ventricles provides further evidence for the second model, but cannot rule out a role for hemodynamics as it was not assessed.

Interestingly, molecular mechanisms implicated from the *Asxl3* mouse model were generally corroborated by *in vitro* human cardiac differentiation of bi-allelic *ASXL3* frameshift hESC lines. In both species, phenotypic differences were attributed to changes in the ratio of CPC subtypes and ECM mediated signaling defects, while the distinct genetic and molecular details of each pathogenic mechanism are species-specific. In the human *in vitro* model system, the ratio of cardiac fibroblast lineages, relative to NKX2-5 cardiomyocyte fated lineages were greater in *ASXL3*$^{fs/fs}$ cultures relative to controls. This is opposite to the trend observed in the *Asxl3* mouse model where a reduction in cardiac fibroblasts were observed. The significance of the opposing observation is difficult to conclude due to differences between species, in the stage of differentiation/development, and *in vitro* culture relative to *in vivo* development. Conversely, ECM components, such as members of the collagen super family and FN1 were prominently differentially expressed in both models. While assessment of cell-cell interaction, using single cell transciptomics, specifically indicated weakened cardiac fibroblast FN1 signaling interaction via cardiomyocyte progenitor expressed $\alpha_v\beta_1$, $\alpha_5\beta_1$, and $\alpha_v\beta_5$ integrin, a reduction in FN1 expression was also detected in bulk RNA sequencing results from the mouse model (Fig. 2.4A and 2.7I). Reduced FN1 expression has also been reported upon loss of HLHS associated genes ETS1, CHD7, and KMT2D in endocardial cells and may represent shared pathology among chromatin modifying genes [20].The influence of FN1 on the mitotic behavior of cardiomyocytes depends upon FN1/β1 integrin signaling through the PI3K/Akt pathway, a features shared by all ASXL3 models to date [14, 20].Collagen subtypes also fulfill structural and signaling cohesiveness to ECM functions and fall into broad functional groups. Four collagen subfamilies were downregulated in the mouse (COL1,4,5 &6), while substantially more subfamilies were differentially expressed in the human model (COL1,4,5,6,8,9,11,12, 13, 14, 18 & 25) (Fig 2.4A and 2.4B and 2.6G). This evidence suggests that ASXL3 has a conserved role in regulating ECM cardiac biology and highlights the importance of this cell biology for normal and pathogenic cardiogenesis. Nevertheless, it will be important to resolve if altered differentiation of cardiac lineages initiate a cascade of ECM composition changes and cell-cell signaling defects, or if chromatin changes directly alter expression of ECM components.

Human genetic studies have described the high incidence of pathogenic de novo variants in chromatin genes that are the genetic basis of syndromic ASD with partially penetrant CHDs [50, 73, 74]. *ASXL3* is a high confidence ASD gene [75]. *De novo* monoallelic frameshift *ASXL3* alleles, also the genetic basis of BRS, are also recognized as the genetic basis of ASD. The low to high penetrance of CHDs between $Asxl3^{+/fs}$ to $Asxl3^{fs/fs}$ genotypes harkens the co-occurrence of ASD and CHDs and suggests that reduced penetrance of CHDs in ASD may reflect increased vulnerability of developing brain relative to heart to de novo pathogenic variants in chromatin genes. Future studies will be required to determine if this is due to organ-specific differences in dosage sensitivity of chromatin genes and/or represents differences in organ-specific thresholds at which altered histone modifications genome-wide impact organ development.

METHODS

All sequencing data sets in this article are deposited in international public repository, Gene Expression Omnibus (GEO), under accession IDs for mouse and human cardiomyocytes bulk RNA sequencing and GSE for single cell RNA Sequencing from human cardiomyocyte.

Animals

All experiments were performed in accordance with animal protocols approved by the Unit for Laboratory Animal Medicine (ULAM), University of Michigan. Briefly, CRISPR/cas9 was used to edit a region in *Asxl3* exon 12. The differential *Asxl3* expression was validated by qRT-PCR and western blot. *Asxl3*$^{+/fs}$ mice were maintained on a C57BL/6 background. Heterozygous breeding was used for experiments with E0.5 established as the day of vaginal plug.

Statistics

We analyzed data using GraphPad Prism with values being represented as means±SEM. Student's 2-tailed *t* test was used to generate *p*-values. Chi square analysis was used for statistical analysis of Mendelian ratios. *p*-values <0.05 were considered significant. Benjamini-Hochberg multiple hypothesis corrections of the *p* values was used to test significance after DAVID analysis. Wilcoxon rank-sum test was used to identify differentially expressed genes from our scRNA-seq.

Single-guide RNA (sgRNA) design

Potential sgRNAs for the target sequence in *Asxl3* gene were identified by a previously published scoring algorithm (http://crispr.mit.edu). Selection was made on the basis of a qualitative balance of specificity scores, distance to desired mutation/insertion and manual assessment of the off-target list. A total of three sgRNAs were selected. Bicistronic expression vector px330 expressing Cas9 and sgRNA [77] was used for cloning the sgRNAs (Addgene) as described previously [78].

Genotyping

A product size of ~850 bp flanking the *Asxl3* mutation is generated by PCR using primer pair, forward: TCACATGGCTTAGTGGTTGT, reverse: CTGTTCTTCGGGGTCACTCT. Sanger sequencing and ligation detection reaction are used for genotyping of CRISPR/Cas9 edited *Asxl3* alleles [79].

Off-target mutation analysis

In the off-target list assessment, we considered the preference to avoid sgRNAs with potential hits in coding regions, sgRNAs with off-target hits on the same chromosome as the intended target, and, when possible, any sgRNAs that had many predicted off-targets lacking mismatches in the seed region (10–12 nucleotide proximal to the protospacer-adjacent motif (PAM), as well as whether off-targets had NGG or NAG PAMs. Predicted off-target sites included regions in *Sdc* and *Gsta1.* Two approaches were used to validate the on-target and off-target CRISPR/Cas9 genome-editing. One, Sanger sequencing of the predicted on-target and off-target regions and two, whole genome sequencing (WGS) were performed. No predicted pathogenic single nucleotide polymorphisms, indels or structural variants such as inversions, rearrangements, duplications and major deletions were detected (Supplemental Fig. 2.1).

Pronuclear injection

Sexually immature female C57BL/6 mice (4 weeks old) were superovulated by intraperitoneal injection of 5 IU Pregnant mare serum gonadotropin (PMSG) followed by

5 IU human chorionic gonadotropin (hCG) at an interval of 48 h and mated overnight with C57BL/6 male mice that were >12 weeks old. Fertilized eggs were collected after 20 hours of hCG injection by oviductal flashing, and pronuclei-formed zygotes were put into the M2 medium. Microinjection was performed using a microinjector (Narishige) equipped microscope. The injected eggs were cultivated overnight in potassium simplex optimization medium (KSOM) at 37C 5% CO2 humidified incubator. Two-cell stage embryos were transferred into the oviducts of 0.5 days pseudopregnant C57BL/6 X DBA/2 F1 females. After birth, ~1 mm tail biopsy from 2–4-day-old pups was used as a source of DNA for *Asxl3* genotyping (forward: TCACATGGCTTAGTGGTTGT, reverse: CTGTTCTTCGGGGTCACTCT).

Western blot analysis

Complete hearts from E13.5 *Asxl3*$^{+/+}$ and *Asxl3*$^{fs/fs}$ mice were homogenized in RIPA buffer supplemented with protease inhibitor cocktail and phosphatase inhibitor cocktail 3 obtained from Sigma-Aldrich (P8340 and P0044; St Louis, MO, USA). Protein levels were normalized after BCA analysis (Pierce). Cell lysates were separated using electrophoresis on 4-20% SDS-polyacrylamide gels and transferred to PVDF membrane (Millipore, Billerica, MA, USA). For western blot, after the transfer, the PVDF membrane was blocked with 5% milk and incubated with following antibodies overnight. Primary antibodies used: anti-ASXL3 (Bielas Lab, 1 to 200), anti-ubiquityl-Histone H2A (Cell Signaling Technology, 8240, 1 to 2000), anti-Histone H3 (Abcam, Ab10543, 1 to 5000). Donkey anti-rabbit HRP-conjugated (Cytiva, NA9340V, 1 to 5000) and goat anti-mouse HRP-conjugated (Invitrogen, 32430, 1 to 10000) were used for 1h incubation at room temperature. Antibody incubation and chemiluminescence detection were performed according to manufacturer's instruction [ThermoFisher Scientific (Waltham, MA, USA) cat no. 34095].

Skeletal preparations

For skeletal preparations, newborn animals were skinned and fixed in 95% ethanol. Fixed skeletons were stained with Alcian Blue (76% ethanol:20% acetic acid) at 37°C for 48 h, rinsed in 95% ethanol, treated with 1% KOH for 4-5 h and stained with Alizarin Red in 2% KOH for 1 h. Stained skeletons were cleared successively in 20% glycerol:1% KOH, 50% glycerol:1% KOH and 100% glycerol (n = 7 for each genotype). Forelimbs were removed and imaged on a Leica MZ125 stereomicroscope.

H&E and Masson's Trichrome staining

Newborn mice were sacrificed and the whole body was fixed for 24 h in 4% paraformaldehyde, dehydrated, and embedded in paraffin. Paraffin blocks were serially sectioned at 5 μm thickness and stained with Hematoxylin/Eosin and Masson's trichrome.

Immunohistochemistry

Hearts were dissected and removed from mice at E14 or P0.5 and then kept in 4% PFA at 4℃ overnight. Hearts were cryopreserved by submersion in 20% then 30% sucrose solutions and embedded in OCT cryosectioning media (Tissue-Tek, Torrance, CA). 13 μm cryosections were obtained. After thawing, sections were incubated with PBS for 15 min to wash away OCT. For antibodies that required antigen retrieval, cryosections were heated in 10 mM sodium citrate for 20 minutes at 95℃ followed by incubation at room temperature for 20 minutes and 3 PBS washes. Sections were then incubated with a normal donkey serum (NDS) blocking buffer [5% NDS (Jackson ImmunoResearch), 0.1% Triton X-100, 5% BSA] for 1 hour. Subsequently, they were incubated with primary antibodies diluted in NDS blocking buffer at 4℃ overnight, washed with PBS, and stained with secondary antibodies at room temperature for 1 hour. Slides were washed with PBS, incubated with DAPI for 5 minutes and coverslipped with MOWIOL. The following antibodies and dilutions were used: COL1A1 (Novus Biologicals, NB600-408, 1 to 500), COL3A1 (Abcam, ab7778, 1 to 100), VIM (Abcam, ab195878, 1 to 500). AlexaFluor-conjugated secondaries were: donkey anti-rabbit 647 (Invitrogen, A31573, 1 to 400), anti-rabbit 555 (Invitrogen, A31572, 1 to 400), donkey anti-mouse 555 (Invitrogen, A31570, 1 to 400), donkey anti-mouse 647 (Invitrogen, A31571, 1 to 400).

Image analysis and quantification

Images of immunostained slides were acquired with a Nikon A1 confocal microscope and processed with LAS X software. Positively stained cells from anatomically-matched serial sections were quantified with ImageJ software. Scaled images were segmented using the grid function in ImageJ with the area per point set to 50000 pixels^2 for each image. Positively stained cells within a segment were counted using the ImageJ Cell Counter plugin. To measure the cross-sectional area of cardiomyocytes we used wheat germ agglutinin Alexa Fluor™ 488 Conjugate (Abcam, W11261, 1 to 100). ImageJ software was used to calculate the cross-sectional area of the cardiomyocyte.

EdU birth-dating analysis

Females from timed-pregnant matings were injected with EdU (20 mg/kg) at embryonic day 13.5 24 hours later, hearts were dissected and removed from EdU injected embryos then kept in 4% PFA at 4℃ overnight. EdU labeling was detected in cryosections by using the Click-IT EdU imaging kit (Invitrogen, Carlsbad, CA) according to the manufacturer's instructions. After sections were incubated with Click-IT reaction cocktail, they were washed with normal donkey serum blocking buffer and then additional antibody staining was performed.

E18.5 heart ventricular RNA sequencing

Total RNA from E18.5 ventricles was extracted from *ASXL3*$^{+/+,}$ *ASXL3*$^{+/fs}$, and *ASXL3*$^{fs/fs}$ littermates. Transcriptome libraries were prepared using 200–1000 ng of total RNA. PolyA + RNA isolation, cDNA synthesis, end-repair, A-base addition and ligation of the Illumina indexed adapters were performed according to the TruSeq RNA protocol (Illumina). Libraries were size selected for 250–300 bp cDNA fragments on a 3% Nusieve 3:1 (Lonza) gel, recovered using QIAEX II reagents (QIAGEN) and PCR amplified using Phusion DNA polymerase (New England Biolabs). Total transcriptome libraries were prepared as above, omitting the poly A selection step and captured using Agilent SureSelect Human All Exon V4 reagents and protocols. Library quality was measured on an Agilent 2100 Bioanalyzer for product size and concentration. Single-end libraries were sequenced with the Illumina HiSeq 2500 with sequence coverage to 100-150 m reads. Single-end sequenced reads were aligned to the mouse reference genome (mm10) using Tophat2 (Tophat 2.0.4) with default settings. Fragment quantification was computed using feature Counts and annotated according to RefSeq genes. DESeq2 was used to calculate estimates of dispersion and logarithmic fold changes to perform the expression normalization and differential expression analysis. Further genes and isoforms were annotated with NCBI Entrez GeneIDs and text descriptions. We used gene ontology consortium (http://geneontology.org) and the DAVID database (https://david.ncifcrf.gov/)

for the enrichment analysis of the set of DEGs to identify significantly enriched functional categories. Benjamini-Hochberg multiple hypothesis corrections of the *p*-values was used, and *p*-values less than 0.05 were called to be significant changes.

hESC CRISPR/Cas9 editing

Human embryonic stem cell line H9 (WiCell) was maintained in mTeSR1 media (Stemcell Technology) on matrigel coated tissue culture dishes. Undifferentiated human Embryonic Stem Cells (hESCs) hESCs were passaged three times every two weeks with daily media change. To generate the patient equivalent variants identified by our lab [29] in hESCs, we designed the sgRNAs flanking the *ASXL3* variant (c.1443dupT). Pluripotent H9 cells were electroporated with PX330 plasmids (described above) with Amaxa electroporator using manufacturers protocol (Lonza). After electroporation single cells were plated in 96 wells and viable healthy colonies were then sequenced to confirm the gene editing in *ASXL3*.

Cardiac differentiation of hESCs

We modified previously described small-molecule protocols to differentiate hESCs toward a cardiac lineage [32, 80]. In brief, $1x10^6$ hESCs were seeded per well in matrigel coated 6-well tissue culture plates. Once the culture reached 100% confluence within 3 days the media was changed to RPMI 1640 with 1X B27 supplement minus Insulin (RPMI/B27- media) with 6 uM CHIR99021 and the day marked as differentiation day 0. 24 hours later the media was changed back RPMI/B27- media without CHIR99021 for another 24 hours. Afterwards CHIR99021 was added back for another 24 hours. On day 3 the old media was removed and washed once with PBS. The cells were then incubated in RPMI/B27- with 5 uM Wnt inhibitor IWP-4 for additional 48 hours. At the conclusion of

Wnt inhibition the media was changed back to RPMI/B27- and replaced every other day until day 10. After day 10, the media was changed to RPMI 1640 with 1X regular B27 Supplement (RPMI/B27+ media) with media replacement every other day. Cardiomyocytes typically start contracting between day 7 and day 12. If no contracting cardiomyocytes were observed by day 12, the cells were discarded, otherwise the cells were dissociated and subject to single cell RNA sequencing.

Seq-Well single-cell RNA-sequencing

Seq-Well was performed as described [81, 82]. Briefly, functionalized Seq-Well arrays, containing 90,000 picowells, were loaded with barcoded beads (ChemeGenes, Wilmington, MA). 20,000 cells were loaded onto the arrays and incubated for 15 minutes. To remove residual BSA and excess cells, arrays were washed with PBS. Functionalized membranes were applied to the top of arrays, sealed in an Agilent clamp, and incubated at 37° for 45 minutes. Sealed arrays were incubated in a lysis buffer (5M guanidine thiocynate, 1 mM EDTA, 0.5% sarkosyl, 1% BME) for 20 minutes followed by a 45 minute incubation with hybridization buffer (2M NaCl, 1X PBS, 8% PEG8000). Beads were removed from arrays by centrifuging at 2000xg for 5 minutes in wash buffer (2M NaCl, 3mM $MgCl_2$, 20mM Tris-HCl pH 8.0, 8% PEG8000). To perform reverse transcription, beads were incubated with the Maxima Reverse Transcriptase (Thermo Scientific) for 30 minutes at room temperature followed by overnight incubation at 52℃. Reactions were treated with Exonuclease 1 (New England Biolabs) for 45 minutes at 37℃. Following we performed a second strand synthesis reaction with the Maxima Reverse Transcriptase (Thermo Scientific) for 1 hour at 37℃ as described (Hughes et al. 2020). Whole transcriptome amplification was performed using the 2X KAPA Hifi Hotstart Readymix

(KAPA Biosystems). Beads were split to 1,500-2,000 per reaction and run under the following conditions 4 Cycles (98℃, 20s; 65℃, 45s; 72℃, 3m) 12 Cycles (98℃, 20s; 67℃, 20s; 72℃, 3m) final extension (72℃, 3m, 4℃, hold). Products were purified with Ampure SPRI beads (Beckman Coulter) at a 0.6X volumetric ratio then a 1.0X volumetric ratio. Libraries were prepared using the Nextera XT kit (Illumina) and libraries were sequenced on an Illumina NextSeq 75 cycle instrument.

Seq-Well data preprocessing

Sequencing reads were processed into a digital gene expression matrix using Drop-seq software as described [83]. FASTQ files were converted into bam files before being tagged with cell and molecular barcodes and trimmed. After converting back to FASTQs, reads were aligned to hg19 with STAR. BAM files are then sorted, merged, and tagged with gene exons. Bead synthesis errors were corrected as described and digital gene expression matrices were generated. For downstream analysis Cells with fewer than 300 detectable genes, greater than 5000 genes or greater than 10% mitochondrial genes were removed. Genes that were detected in less than 5 cells were also excluded. A total of 9,379 cells captured from *ASXL3*$^{+/+}$ and 9,198 cells captured from *ASXL3*$^{fs/fs}$ cultures passed the quality control and were used in the final analysis.

UMAP dimensionality reduction and cluster annotation

We used the Seurat package (v3.1.2) to perform dimensionality reduction. We used the integrated and normalized data as the input to the RunPCA function of Seurat (v3.1.2) in order to compute the first 100 PCs. After that, we used the elbow algorithm to find the optimal number of PCs to construct Uniform Manifold Approximation and Projection (UMAP) plots. Visualizations in a two-dimensional space were done using

RunUMAP function of Seurat (v3.1.2) for the integrated data using previous dimensional reduction data and predetermined best PC number. We performed a graph-based clustering approach using FindNeighbors and FindClusters functions of Seurat (v3.1.2). A K-nearest neighbor graph was constructed based on the Euclidean distance in the predetermined PCA dimension with drawn edges between cells with similar expression levels and then refined the edge weights between any two cells. We then clustered the cells based on modularity optimization technique: Louvain algorithm with resolution parameter 0.5 and partitioned the graph constructed before into communities. We then collected cluster marker genes using the Wilcoxon rank-sum test which is a nonparametric test between the cells in a single cluster and all other cells with log fold change threshold as 0.2. To assign identities to clusters, we cross-referenced the marker genes with previously described cardiac subtype markers [2-4].

Single-Cell differential gene expression and pathway enrichment analysis

We used the FindMarkers function in Seurat and performed a Wilcoxon rank-sum test (logFC.threshold=0.15) to compute differentially expressed genes between *ASXL3*$^{+/+}$ and *ASXL3*$^{fs/fs}$ cells within each cluster. A p-value cut-off < 0.05 was used to identify differentially expressed genes. DAVID analysis (https://david.ncifcrf.gov/tools.jsp) was performed with the up-, down-regulated, and combined genes to identify enriched KEGG pathways.

CellPhoneDB analysis

CellPhoneDB V2 was used to predict changes between genotypes in cell-to-cell communication. *ASXL3*$^{+/+}$ and *ASXL3*$^{fs/fs}$ were analyzed individually using the metadata from the integrated Seurat object as described [35]. Ligand-receptor pair expression means and p-values were calculated. For comparison between $ASXL3^{+/+}$ and $ASXL3^{fs/fs}$ p-values of each ligand-receptor pair expression score in both genotypes have to be below 0.05 to be considered. Significant ligand-receptor pair signaling communication line changes in $ASXL3^{fs/fs}$ were identified as gained if $ASXL3^{+/+}$ mean=0 and $ASXL3^{fs/fs}$ mean >0; lost if $ASXL3^{+/+}$ mean>0 and $ASXL3^{fs/fs}$ mean =0; strengthened if ($ASXL3^{fs/fs}$ mean/$ASXL3^{+/+}$ mean) >1.5; or weakened if ($ASXL3^{+/+}$ mean/$ASXL3^{fs/fs}$ mean) >1.5.

REFERNCES:

1. Buijtendijk, M.F.J., P. Barnett, and M.J.B. van den Hoff, *Development of the human heart.* Am J Med Genet C Semin Med Genet, 2020. **184**(1): p. 7-22.
2. Friedman, C.E., et al., *Single-Cell Transcriptomic Analysis of Cardiac Differentiation from Human PSCs Reveals HOPX-Dependent Cardiomyocyte Maturation.* Cell Stem Cell, 2018. **23**(4): p. 586-598 e8.
3. Cui, Y., et al., *Single-Cell Transcriptome Analysis Maps the Developmental Track of the Human Heart.* Cell Rep, 2019. **26**(7): p. 1934-1950 e5.
4. Churko, J.M., et al., *Defining human cardiac transcription factor hierarchies using integrated single-cell heterogeneity analysis.* Nat Commun, 2018. **9**(1): p. 4906.
5. Jia, G., et al., *Single cell RNA-seq and ATAC-seq analysis of cardiac progenitor cell transition states and lineage settlement.* Nat Commun, 2018. **9**(1): p. 4877.
6. Del Monte-Nieto, G., et al., *Basic Biology of Extracellular Matrix in the Cardiovascular System, Part 1/4: JACC Focus Seminar.* J Am Coll Cardiol, 2020. **75**(17): p. 2169-2188.
7. George, E.L., et al., *Defects in mesoderm, neural tube and vascular development in mouse embryos lacking fibronectin.* Development, 1993. **119**(4): p. 1079-91.
8. Linask, K.K. and J.W. Lash, *A role for fibronectin in the migration of avian precardiac cells. I. Dose-dependent effects of fibronectin antibody.* Dev Biol, 1988. **129**(2): p. 315-23.
9. Trinh, L.A. and D.Y. Stainier, *Fibronectin regulates epithelial organization during myocardial migration in zebrafish.* Dev Cell, 2004. **6**(3): p. 371-82.
10. Linask, K.K., et al., *Cardiac morphogenesis: matrix metalloproteinase coordination of cellular mechanisms underlying heart tube formation and directionality of looping.* Dev Dyn, 2005. **233**(3): p. 739-53.
11. Le Garrec, J.F., et al., *A predictive model of asymmetric morphogenesis from 3D reconstructions of mouse heart looping dynamics.* Elife, 2017. **6**.
12. Stankunas, K., et al., *Endocardial Brg1 represses ADAMTS1 to maintain the microenvironment for myocardial morphogenesis.* Dev Cell, 2008. **14**(2): p. 298-311.
13. Zhou, Z., et al., *The cerebral cavernous malformation pathway controls cardiac development via regulation of endocardial MEKK3 signaling and KLF expression.* Dev Cell, 2015. **32**(2): p. 168-80.
14. Ieda, M., et al., *Cardiac fibroblasts regulate myocardial proliferation through beta1 integrin signaling.* Dev Cell, 2009. **16**(2): p. 233-44.
15. Camenisch, T.D., et al., *Disruption of hyaluronan synthase-2 abrogates normal cardiac morphogenesis and hyaluronan-mediated transformation of epithelium to mesenchyme.* J Clin Invest, 2000. **106**(3): p. 349-60.
16. Hatano, S., et al., *Versican/PG-M is essential for ventricular septal formation subsequent to cardiac atrioventricular cushion development.* Glycobiology, 2012. **22**(9): p. 1268-77.
17. Tallquist, M.D., *Developmental Pathways of Cardiac Fibroblasts.* Cold Spring Harb Perspect Biol, 2020. **12**(4).
18. Shai, S.Y., et al., *Cardiac myocyte-specific excision of the beta1 integrin gene results in myocardial fibrosis and cardiac failure.* Circ Res, 2002. **90**(4): p. 458-64.

19. Civitarese, R.A., et al., *Role of integrins in mediating cardiac fibroblast-cardiomyocyte cross talk: a dynamic relationship in cardiac biology and pathophysiology.* Basic Res Cardiol, 2017. **112**(1): p. 6.
20. Miao, Y., et al., *Intrinsic Endocardial Defects Contribute to Hypoplastic Left Heart Syndrome.* Cell Stem Cell, 2020. **27**(4): p. 574-589 e8.
21. Cho, E., et al., *Cardiac-specific developmental and epigenetic functions of Jarid2 during embryonic development.* J Biol Chem, 2018. **293**(30): p. 11659-11673.
22. Wang, Q.T., *Epigenetic regulation of cardiac development and function by polycomb group and trithorax group proteins.* Dev Dyn, 2012. **241**(6): p. 1021-33.
23. Schuettengruber, B., et al., *Genome Regulation by Polycomb and Trithorax: 70 Years and Counting.* Cell, 2017. **171**(1): p. 34-57.
24. Barbour, H., et al., *Polycomb group-mediated histone H2A monoubiquitination in epigenome regulation and nuclear processes.* Nat Commun, 2020. **11**(1): p. 5947.
25. Sahtoe, D.D., et al., *BAP1/ASXL1 recruitment and activation for H2A deubiquitination.* Nat Commun, 2016. **7**: p. 10292.
26. Daou, S., et al., *The BAP1/ASXL2 Histone H2A Deubiquitinase Complex Regulates Cell Proliferation and Is Disrupted in Cancer.* J Biol Chem, 2015. **290**(48): p. 28643-63.
27. McGinley, A.L., et al., *Additional sex combs-like family genes are required for normal cardiovascular development.* Genesis, 2014. **52**(7): p. 671-86.
28. Bainbridge, M.N., et al., *De novo truncating mutations in ASXL3 are associated with a novel clinical phenotype with similarities to Bohring-Opitz syndrome.* Genome Med, 2013. **5**(2): p. 11.
29. Srivastava, A., et al., *De novo dominant ASXL3 mutations alter H2A deubiquitination and transcription in Bainbridge-Ropers syndrome.* Hum Mol Genet, 2016. **25**(3): p. 597-608.
30. Fu, F., et al., *Compound heterozygous mutation of the ASXL3 gene causes autosomal recessive congenital heart disease.* Hum Genet, 2021. **140**(2): p. 333-348.
31. Kessel, M., *Respecification of vertebral identities by retinoic acid.* Development, 1992. **115**(2): p. 487-501.
32. Burridge, P.W., A. Holmstrom, and J.C. Wu, *Chemically Defined Culture and Cardiomyocyte Differentiation of Human Pluripotent Stem Cells.* Curr Protoc Hum Genet, 2015. **87**: p. 21 3 1-21 3 15.
33. Stuart, T., et al., *Comprehensive Integration of Single-Cell Data.* Cell, 2019. **177**(7): p. 1888-1902 e21.
34. Fraidenraich, D., et al., *Rescue of cardiac defects in id knockout embryos by injection of embryonic stem cells.* Science, 2004. **306**(5694): p. 247-52.
35. Efremova, M., et al., *CellPhoneDB: inferring cell-cell communication from combined expression of multi-subunit ligand-receptor complexes.* Nat Protoc, 2020. **15**(4): p. 1484-1506.
36. Yang, L., et al., *Isl1Cre reveals a common Bmp pathway in heart and limb development.* Development, 2006. **133**(8): p. 1575-85.

37. Aggarwal, M., et al., *Three-dimensional diffusion tensor microimaging for anatomical characterization of the mouse brain.* Magn Reson Med, 2010. **64**(1): p. 249-61.
38. Shashi, V., et al., *De Novo Truncating Variants in ASXL2 Are Associated with a Unique and Recognizable Clinical Phenotype.* Am J Hum Genet, 2017. **100**(1): p. 179.
39. Lai, H.L., et al., *Maintenance of adult cardiac function requires the chromatin factor Asxl2.* J Mol Cell Cardiol, 2012. **53**(5): p. 734-41.
40. Dinwiddie, D.L., et al., *De novo frameshift mutation in ASXL3 in a patient with global developmental delay, microcephaly, and craniofacial anomalies.* BMC Med Genomics, 2013. **6**: p. 32.
41. Andricovich, J., et al., *Histone demethylase KDM2B regulates lineage commitment in normal and malignant hematopoiesis.* J Clin Invest, 2016. **126**(3): p. 905-20.
42. Takihara, Y., et al., *Targeted disruption of the mouse homologue of the Drosophila polyhomeotic gene leads to altered anteroposterior patterning and neural crest defects.* Development, 1997. **124**(19): p. 3673-82.
43. Cox, B.J., et al., *Phenotypic annotation of the mouse X chromosome.* Genome Res, 2010. **20**(8): p. 1154-64.
44. Hamline, M.Y., et al., *OFCD syndrome and extraembryonic defects are revealed by conditional mutation of the Polycomb-group repressive complex 1.1 (PRC1.1) gene BCOR.* Dev Biol, 2020. **468**(1-2): p. 110-132.
45. Shirai, M., et al., *The Polycomb-group gene Rae28 sustains Nkx2.5/Csx expression and is essential for cardiac morphogenesis.* J Clin Invest, 2002. **110**(2): p. 177-84.
46. Chen, L., et al., *Conditional ablation of Ezh2 in murine hearts reveals its essential roles in endocardial cushion formation, cardiomyocyte proliferation and survival.* PLoS One, 2012. **7**(2): p. e31005.
47. Mysliwiec, M.R., E.H. Bresnick, and Y. Lee, *Endothelial Jarid2/Jumonji is required for normal cardiac development and proper Notch1 expression.* J Biol Chem, 2011. **286**(19): p. 17193-204.
48. He, A., et al., *PRC2 directly methylates GATA4 and represses its transcriptional activity.* Genes Dev, 2012. **26**(1): p. 37-42.
49. Giannakou, A., et al., *Copy number variants in hypoplastic right heart syndrome.* Am J Med Genet A, 2018. **176**(12): p. 2760-2767.
50. Jin, S.C., et al., *Contribution of rare inherited and de novo variants in 2,871 congenital heart disease probands.* Nat Genet, 2017. **49**(11): p. 1593-1601.
51. Grossfeld, P., et al., *Hypoplastic Left Heart Syndrome: A New Paradigm for an Old Disease?* J Cardiovasc Dev Dis, 2019. **6**(1).
52. Trivedi, C.M., et al., *Hopx and Hdac2 interact to modulate Gata4 acetylation and embryonic cardiac myocyte proliferation.* Dev Cell, 2010. **19**(3): p. 450-9.
53. Montgomery, R.L., et al., *Histone deacetylases 1 and 2 redundantly regulate cardiac morphogenesis, growth, and contractility.* Genes Dev, 2007. **21**(14): p. 1790-802.
54. Liu, X., et al., *The complex genetics of hypoplastic left heart syndrome.* Nat Genet, 2017. **49**(7): p. 1152-1159.

55. Lickert, H., et al., *Baf60c is essential for function of BAF chromatin remodelling complexes in heart development.* Nature, 2004. **432**(7013): p. 107-12.
56. Ashraf, H., et al., *A mouse model of human congenital heart disease: high incidence of diverse cardiac anomalies and ventricular noncompaction produced by heterozygous Nkx2-5 homeodomain missense mutation.* Circ Cardiovasc Genet, 2014. **7**(4): p. 423-433.
57. Sakata, Y., et al., *The spectrum of cardiovascular anomalies in CHF1/Hey2 deficient mice reveals roles in endocardial cushion, myocardial and vascular maturation.* J Mol Cell Cardiol, 2006. **40**(2): p. 267-73.
58. Rajagopal, S.K., et al., *Spectrum of heart disease associated with murine and human GATA4 mutation.* J Mol Cell Cardiol, 2007. **43**(6): p. 677-85.
59. van Walree, E.S., et al., *Germline variants in HEY2 functional domains lead to congenital heart defects and thoracic aortic aneurysms.* Genet Med, 2021. **23**(1): p. 103-110.
60. Kitamura, K., et al., *Mouse Pitx2 deficiency leads to anomalies of the ventral body wall, heart, extra- and periocular mesoderm and right pulmonary isomerism.* Development, 1999. **126**(24): p. 5749-58.
61. Marguerie, A., et al., *Congenital heart defects in Fgfr2-IIIb and Fgf10 mutant mice.* Cardiovasc Res, 2006. **71**(1): p. 50-60.
62. McCright, B., J. Lozier, and T. Gridley, *A mouse model of Alagille syndrome: Notch2 as a genetic modifier of Jag1 haploinsufficiency.* Development, 2002. **129**(4): p. 1075-82.
63. Gaber, N., et al., *Fetal reprogramming and senescence in hypoplastic left heart syndrome and in human pluripotent stem cells during cardiac differentiation.* Am J Pathol, 2013. **183**(3): p. 720-34.
64. Davies, B., et al., *Differences in extra-cellular matrix and myocyte homeostasis between the neonatal right ventricle in hypoplastic left heart syndrome and truncus arteriosus.* Eur J Cardiothorac Surg, 2008. **34**(4): p. 738-44.
65. Salih, C., K.P. McCarthy, and S.Y. Ho, *The fibrous matrix of ventricular myocardium in hypoplastic left heart syndrome: a quantitative and qualitative analysis.* Ann Thorac Surg, 2004. **77**(1): p. 36-40.
66. Derrick, C.J. and E.S. Noel, *The ECM as a driver of heart development and repair.* Development, 2021. **148**(5).
67. Kern, C.B., et al., *Versican proteolysis mediates myocardial regression during outflow tract development.* Dev Dyn, 2007. **236**(3): p. 671-83.
68. Liu, Y., et al., *Spatiotemporal Gene Coexpression and Regulation in Mouse Cardiomyocytes of Early Cardiac Morphogenesis.* J Am Heart Assoc, 2019. **8**(15): p. e012941.
69. Moore-Morris, T., et al., *Role of Epigenetics in Cardiac Development and Congenital Diseases.* Physiol Rev, 2018. **98**(4): p. 2453-2475.
70. Han, X., et al., *Mapping the Mouse Cell Atlas by Microwell-Seq.* Cell, 2018. **172**(5): p. 1091-1107 e17.
71. Silva, A.C., et al., *Bearing My Heart: The Role of Extracellular Matrix on Cardiac Development, Homeostasis, and Injury Response.* Front Cell Dev Biol, 2020. **8**: p. 621644.

72. deAlmeida, A., T. McQuinn, and D. Sedmera, *Increased ventricular preload is compensated by myocyte proliferation in normal and hypoplastic fetal chick left ventricle.* Circ Res, 2007. **100**(9): p. 1363-70.
73. Homsy, J., et al., *De novo mutations in congenital heart disease with neurodevelopmental and other congenital anomalies.* Science, 2015. **350**(6265): p. 1262-6.
74. Zaidi, S., et al., *De novo mutations in histone-modifying genes in congenital heart disease.* Nature, 2013. **498**(7453): p. 220-3.
75. Satterstrom, F.K., et al., *Large-Scale Exome Sequencing Study Implicates Both Developmental and Functional Changes in the Neurobiology of Autism.* Cell, 2020. **180**(3): p. 568-584 e23.
76. Subramanian, A., et al., *Gene set enrichment analysis: a knowledge-based approach for interpreting genome-wide expression profiles.* Proc Natl Acad Sci U S A, 2005. **102**(43): p. 15545-50.
77. Cong, L., et al., *Multiplex genome engineering using CRISPR/Cas systems.* Science, 2013. **339**(6121): p. 819-23.
78. Ran, F.A., et al., *Genome engineering using the CRISPR-Cas9 system.* Nat Protoc, 2013. **8**(11): p. 2281-308.
79. Kc, R., et al., *Detection of nucleotide-specific CRISPR/Cas9 modified alleles using multiplex ligation detection.* Sci Rep, 2016. **6**: p. 32048.
80. Lian, X., et al., *Directed cardiomyocyte differentiation from human pluripotent stem cells by modulating Wnt/beta-catenin signaling under fully defined conditions.* Nat Protoc, 2013. **8**(1): p. 162-75.
81. Aicher, T.P., et al., *Seq-Well: A Sample-Efficient, Portable Picowell Platform for Massively Parallel Single-Cell RNA Sequencing.* Methods Mol Biol, 2019. **1979**: p. 111-132.
82. Gierahn, T.M., et al., *Seq-Well: portable, low-cost RNA sequencing of single cells at high throughput.* Nat Methods, 2017. **14**(4): p. 395-398.
83. Macosko, E.Z., et al., *Highly Parallel Genome-wide Expression Profiling of Individual Cells Using Nanoliter Droplets.* Cell, 2015. **161**(5): p. 1202-1214.

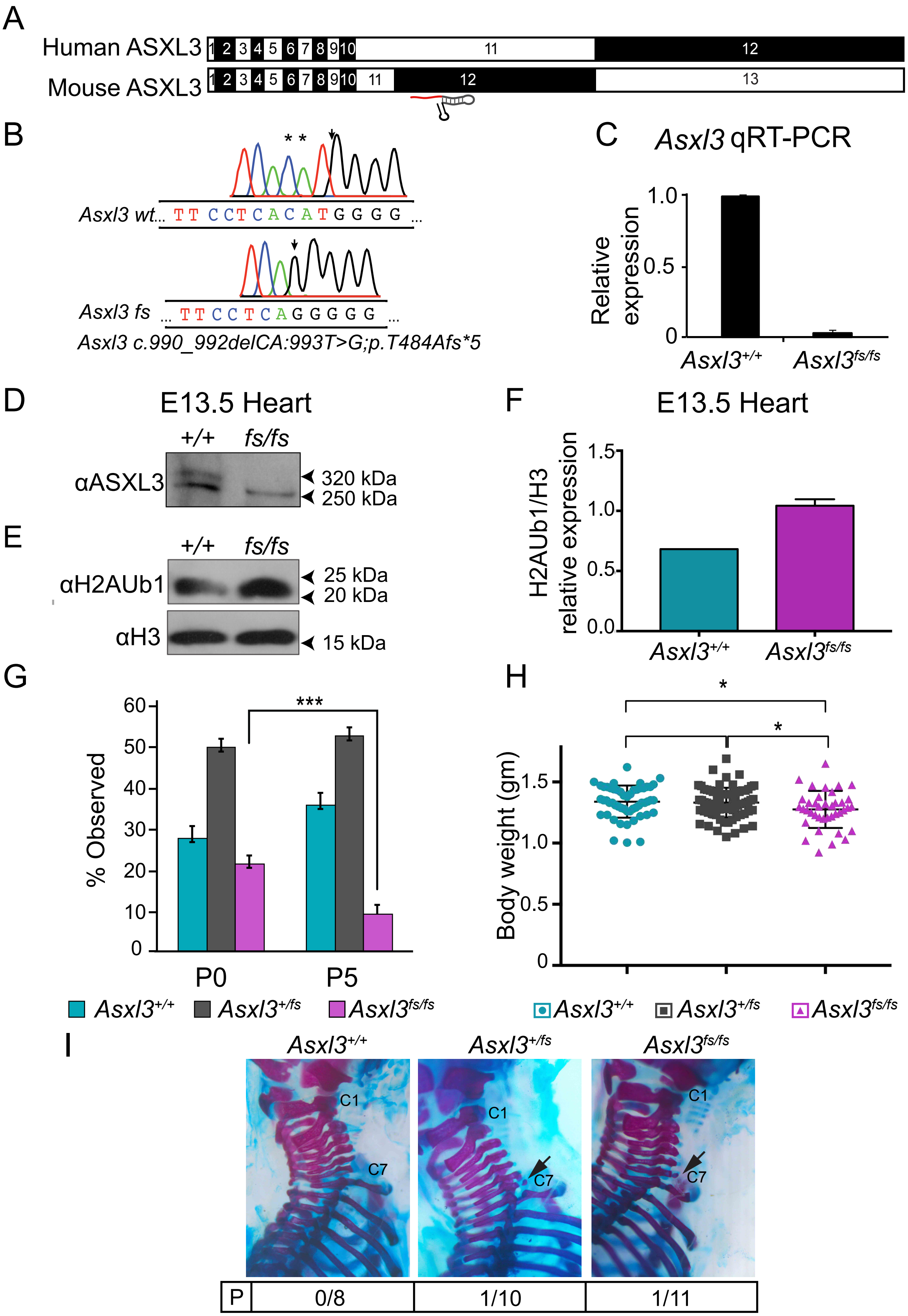
A
Human ASXL3
1 2 3 4 5 6 7 8 9 10 11 12
Mouse ASXL3
1 2 3 4 5 6 7 8 9 10 11 12 13
B
* *
Asxl3 wt... TTCCTCACATGGGG ...
Asxl3 fs ... TTCCTCAGGGGG ...
Asxl3 c.990_992delCA:993T>G;p.T484Afs*5
C
Asxl3 qRT-PCR
Relative expression
1.0
0.5
0
Asxl3+/+
Asxl3fs/fs
D
E13.5 Heart
+/+
fs/fs
αASXL3
320 kDa
250 kDa
E
+/+
fs/fs
αH2AUb1
25 kDa
20 kDa
αH3
15 kDa
F
E13.5 Heart
H2AUb1/H3 relative expression
1.5
1.0
0.5
0.0
Asxl3+/+
Asxl3fs/fs
G
% Observed
60
50
40
30
20
10
0
***
P0
P5
Asxl3+/+
Asxl3+/fs
Asxl3fs/fs
H
Body weight (gm)
1.5
1.0
0.5
0
*
*
Asxl3+/+
Asxl3+/fs
Asxl3fs/fs
I
Asxl3+/+
Asxl3+/fs
Asxl3fs/fs
C1
C7

P	0/8	1/10	1/11

Fig. 2.1. Generation of Asxl3$^{fs/fs}$ mice A, Depiction of CRISPR/Cas9 genome editing strategy for *Asxl3*^{fs} mouse generation. The sgRNA targets a loci of mouse *Asxl3* exon 12 that is homologous to a region of human *ASXL3* exon 11 that contains clinically relevant variants. **B,** Representative indel sequences from Sanger sequencing of targeted *Asxl3* loci. **C,** RT-qPCR analysis of Asxl3 mRNA levels in Embryonic day 13.5 (E13.5) *Asxl3*^{fs} edited neural progenitor cells. **D,** Western blot analysis shows the expression of full length ASXL3 is lost in E13.5 *Asxl3*$^{fs/fs}$ hearts. **E,** Western blot analysis of H2AK119Ub1 (H2AUb1) and H3 acid extracted histones from *Asxl3*$^{+/+}$ and *Asxl3*$^{fs/fs}$ E13.5 hearts. **F,** Quantification of H2AUb1 relative to H3 control levels revealed a 2-fold increase in *Asxl*$^{fs/fs}$ E13.5 hearts compared to control. **G,** Percentage of observed *Asxl3*$^{+/+}$*, Asxl3*$^{+/fs}$*,* and *Asxl3*$^{fs/fs}$ mice at P0 and P5. Chi square analysis showed a reduction in *Asxl3fs/fs* mice based on normal mendelian distribution. **H,** Student's *t* test shows a significant reduction in body weight of *Asxl3*$^{fs/fs}$ P0 mice relative to wild type and heterozygous mice (n=53 for *Asxl3*$^{+/+}$, n=75 for *Asxl3*$^{+/fs}$ and n=39 for *Asxl3*$^{fs/fs}$). **I,** Alcian blue and Alizarin red staining of P0.5 embryos. Arrows indicate cervical ribs observed in *Asxl3*$^{+/fs}$*,* and *Asxl3*$^{fs/fs}$ mice. Penetrance of cervical ribs by genotype displayed below. Values are mean±SEM. *$P<0.05$, **$P<0.01$, ***$P<0.001$.

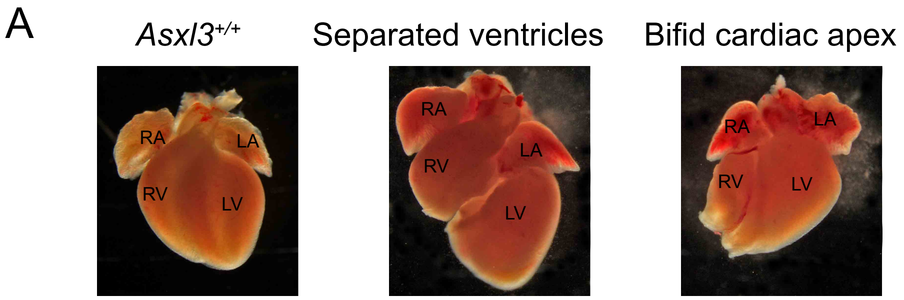

B

	Asxl3$^{+/+}$	*Asxl3*$^{+/fs}$	*Asxl3*$^{fs/fs}$
Separated ventricles	0/10 (0%)	1/22 (4.5%)	2/12 (16.7%)
Bifid cardiac apex	0/10 (0%)	0/22 (0%)	2/12 (16.7%)
Septal defects	0/38 (0%)	0/16 (0%)	2/39 (5.1%)
Ventricular hypoplasia	0/38 (0%)	2/16 (12.5%)	11/39 (28%)

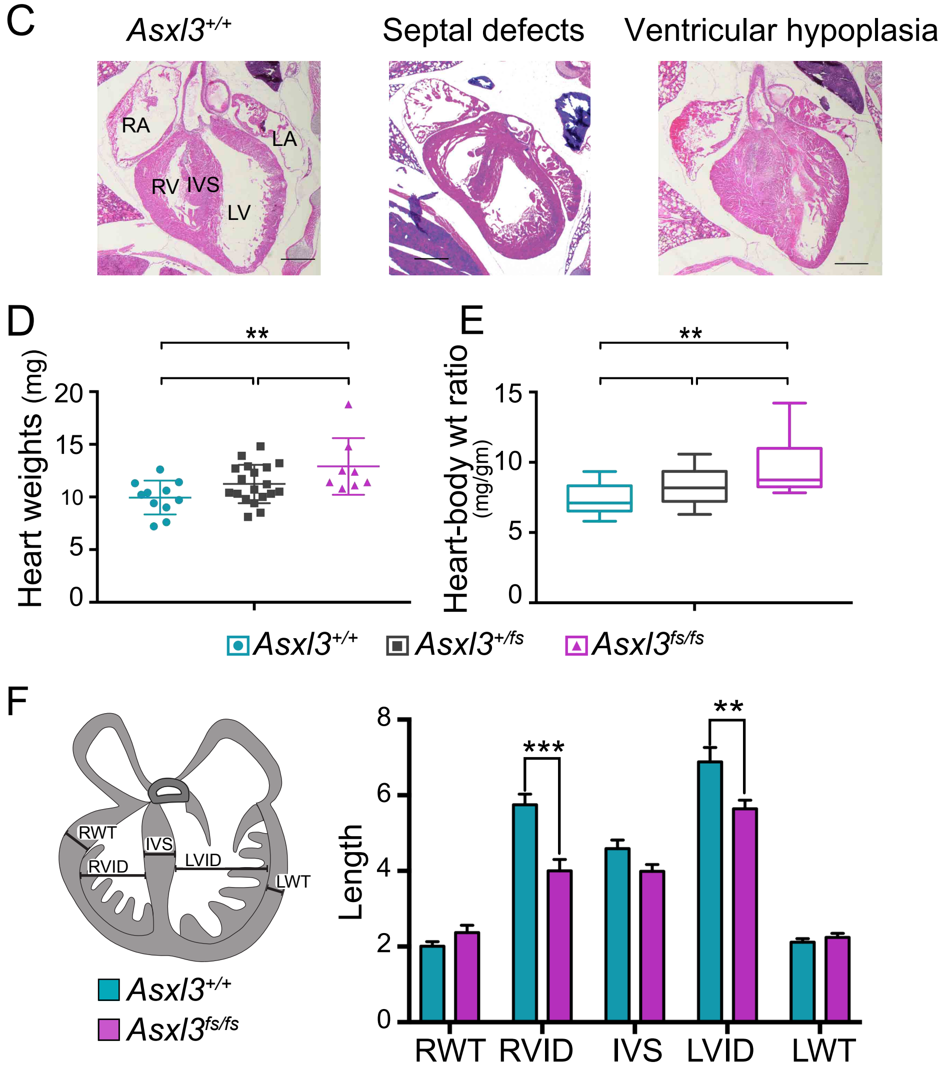

Fig. 2.2. Representative *Asxl3*^{fs}-associated cardiac anomalies A, Whole mount images of P0.5 dissected hearts displaying separated ventricles and bifid cardiac apex. **B,** Table summarizing cardiac anomalies observed in *Asxl3*$^{+/+}$, *Asxl3*$^{+/fs}$, and *Asxl3*$^{fs/fs}$ P0.5 mice. **C,** Hematoxylin and eosin staining of P0.5 hearts shows representative images of the *Asxl3*^{fs}-associated septal defects and ventricular hypoplasia. Scale bars, 500 µm. Student's *t* test analysis of P0.5 **D,** heart weights and **E,** heart to body weight ratio between genotypes (n=11 for *Asxl3*$^{+/+}$, n=18 for *Asxl3*$^{+/fs}$ and n=8 for *Asxl3*$^{fs/fs}$). Data are presented as mean±SEM. **F,** P0.5 heart Illustration detailing morphometric measurements for right wall thickness (RWT), right ventricular free wall (RVFW), interventricular septum (IVS), left ventricular free wall (LVFW), left wall thickness (LWT). **G,** Student's *t* test analysis of P0.5 morphometric measurements shows increased RVFW and LVFW in *Asxl3*$^{fs/fs}$ mice compared to *Asxl3*$^{+/+}$ (n=4 for *Asxl3*$^{+/+}$, n=5 for *Asxl3*$^{fs/fs}$). *$p<0.05$, **$p<0.01$, ***$p<0.001$.

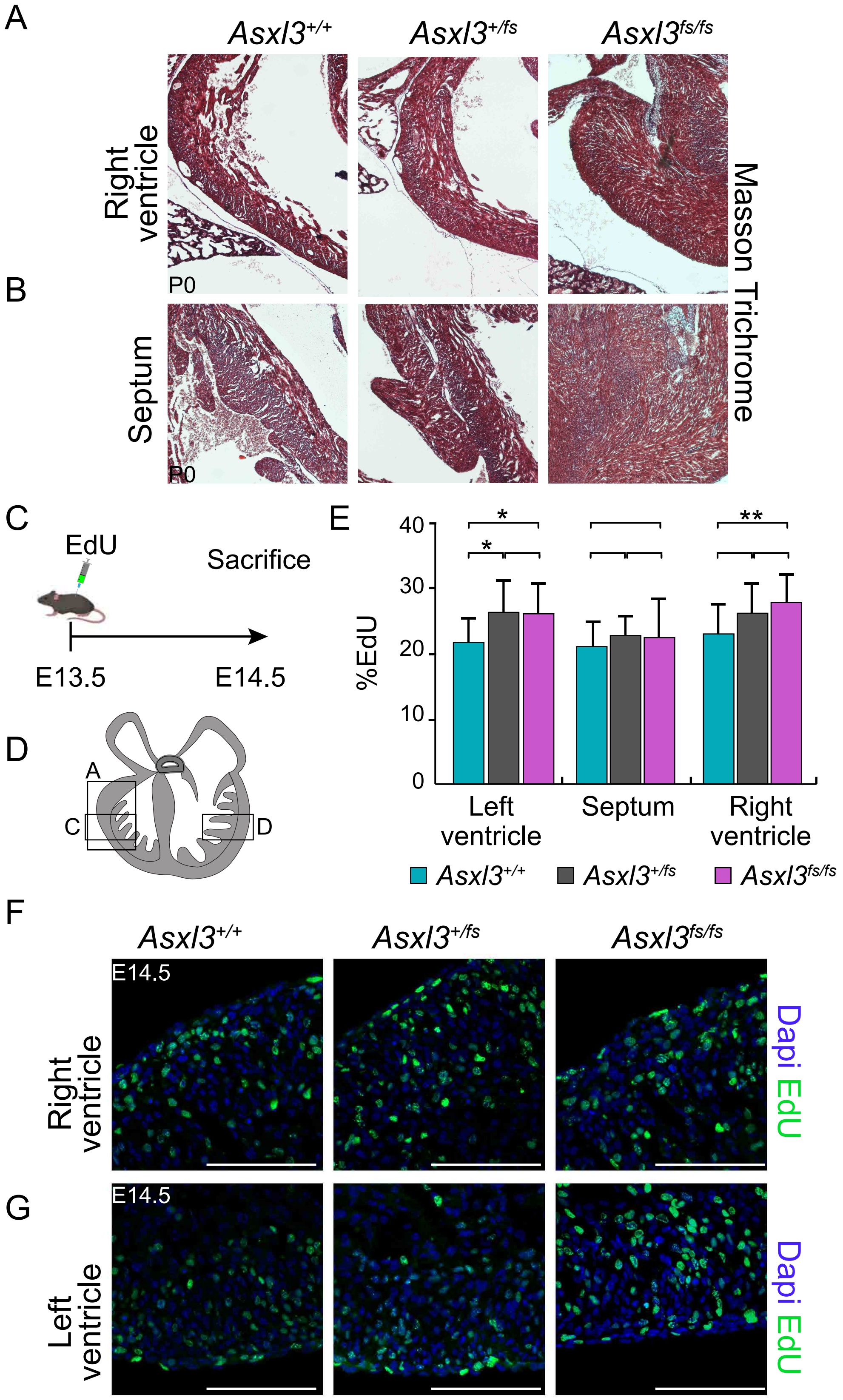
A
Asxl3+/+
Asxl3+/fs
Asxl3fs/fs
Right ventricle
P0
Masson Trichrome
B
Septum
P0
C
EdU
Sacrifice
E13.5
E14.5
D
A
C
D
E
%EdU
40
30
20
10
0
*
*
**
Left ventricle
Septum
Right ventricle
Asxl3+/+
Asxl3+/fs
Asxl3fs/fs
F
Asxl3+/+
Asxl3+/fs
Asxl3fs/fs
E14.5
Right ventricle
Dapi EdU
G
E14.5
Left ventricle
Dapi EdU

Fig. 2.3. Increased proliferation during heart development Representative images of the **A,** right ventricular walls and **B,** septums from *Asxl3*$^{+/+}$, *Asxl3*$^{+/fs}$, and *Asxl3*$^{fs/fs}$ P0.5 hearts stained with Masson trichrome. Scale bars, 500 µm. No difference in Masson trichrome staining was observed between genotypes. **C,** Experimental timeline showing EdU labeling at E13.5 and collection 24 hours later. **D,** Schematic depicting representative regions of images used for quantifications in transverse heart section **E,** Student's *t* test analysis of EdU-positive proliferative cells in E14.5 hearts between genotypes (n=4 for Asxl3$^{+/+}$, n=10 for Asxl3$^{+/fs}$ and n=5 for Asxl3$^{fs/fs}$). Representative images of E14.5 **F,** right and **G,** left ventricles from *Asxl3*$^{+/+}$, *Asxl3*$^{+/fs}$ and *Asxl3*$^{fs/fs}$ hearts after EdU incorporation. Scale bars, 100 µm. Values are mean±SEM. *$p<0.05$, **$p<0.01$, ***$p<0.001$.

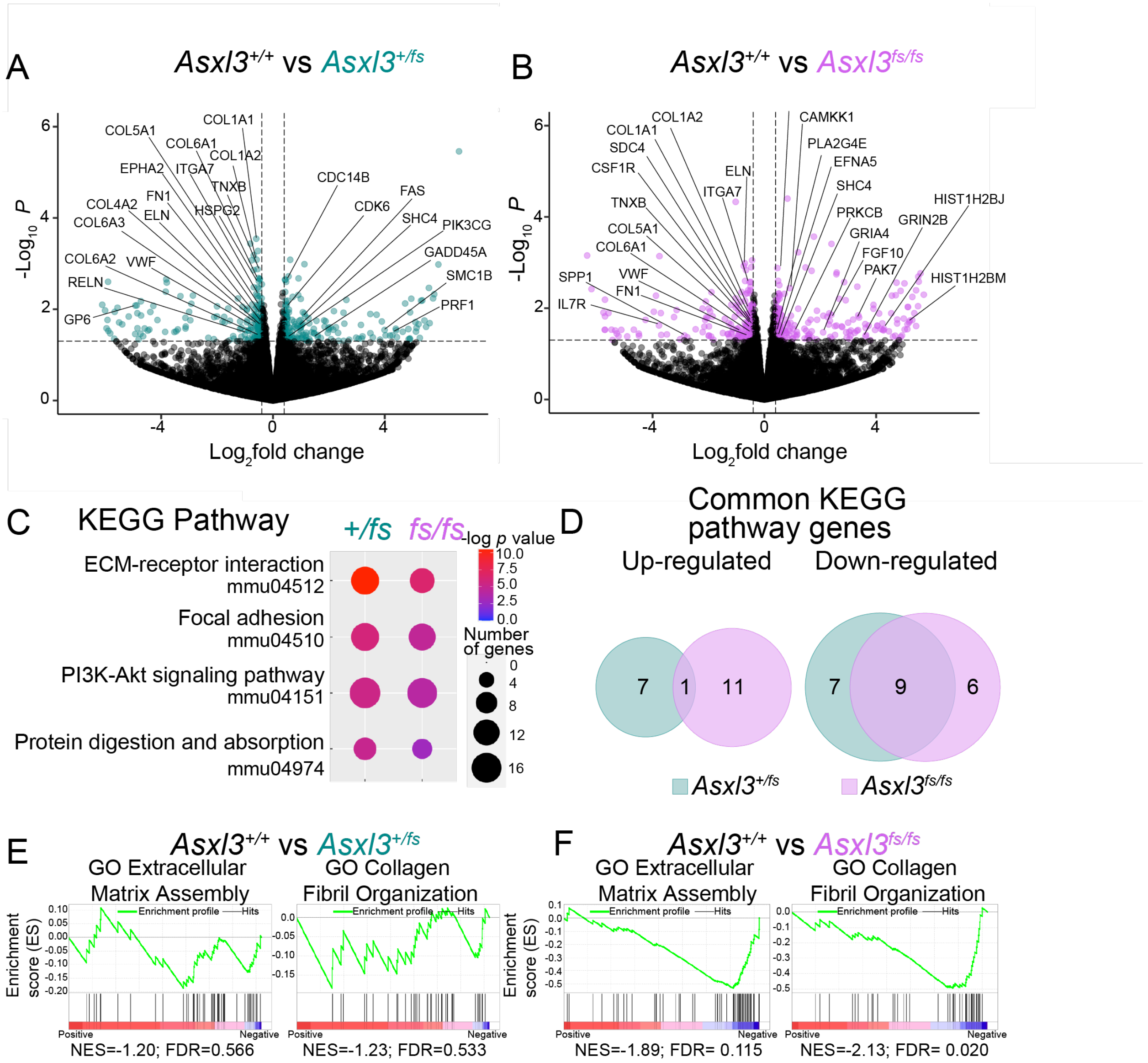

Fig. 2.4. Loss of *Asxl3* leads to altered expression of extracellular matrix components Volcano plots exhibiting gene expression changes in **A,** *Asxl3*$^{+/fs}$ vs. *Asxl3*$^{+/+}$ and **B,** *Asxl3*$^{fs/fs}$ vs. *Asxl3*$^{+/+}$ E18.5 hearts. Genes with a p-value > 0.05 and log fold change > 0.4 are highlighted. GSEA enrichment plots for GO:Extracellular Matrix Assembly and GO:Collagen Fibril Organization from **C,** *Asxl3*$^{+/fs}$ vs. *Asxl3*$^{+/+}$ and **D,** *Asxl3*$^{fs/fs}$ vs. *Asxl3*$^{+/+}$ analysis. Gene set enrichment analysis (GSEA) was performed with the ontology gene sets in GSEA molecular signature database. **E,** KEGG pathway enrichment analysis for *Asxl3*$^{+/fs}$ and *Asxl3*$^{fs/fs}$ downregulated genes. The top 4 KEGG pathways for both *Asxl3*$^{+/fs}$ and *Asxl3*$^{fs/fs}$ are shown. The size of each dot represents the gene number and the shading represents the $-\log_{10}$ p-value. **F,** The Venn diagram illustrates the overlap of unique upregulated (left) or downregulated (right) genes contributing to common KEGG pathways.

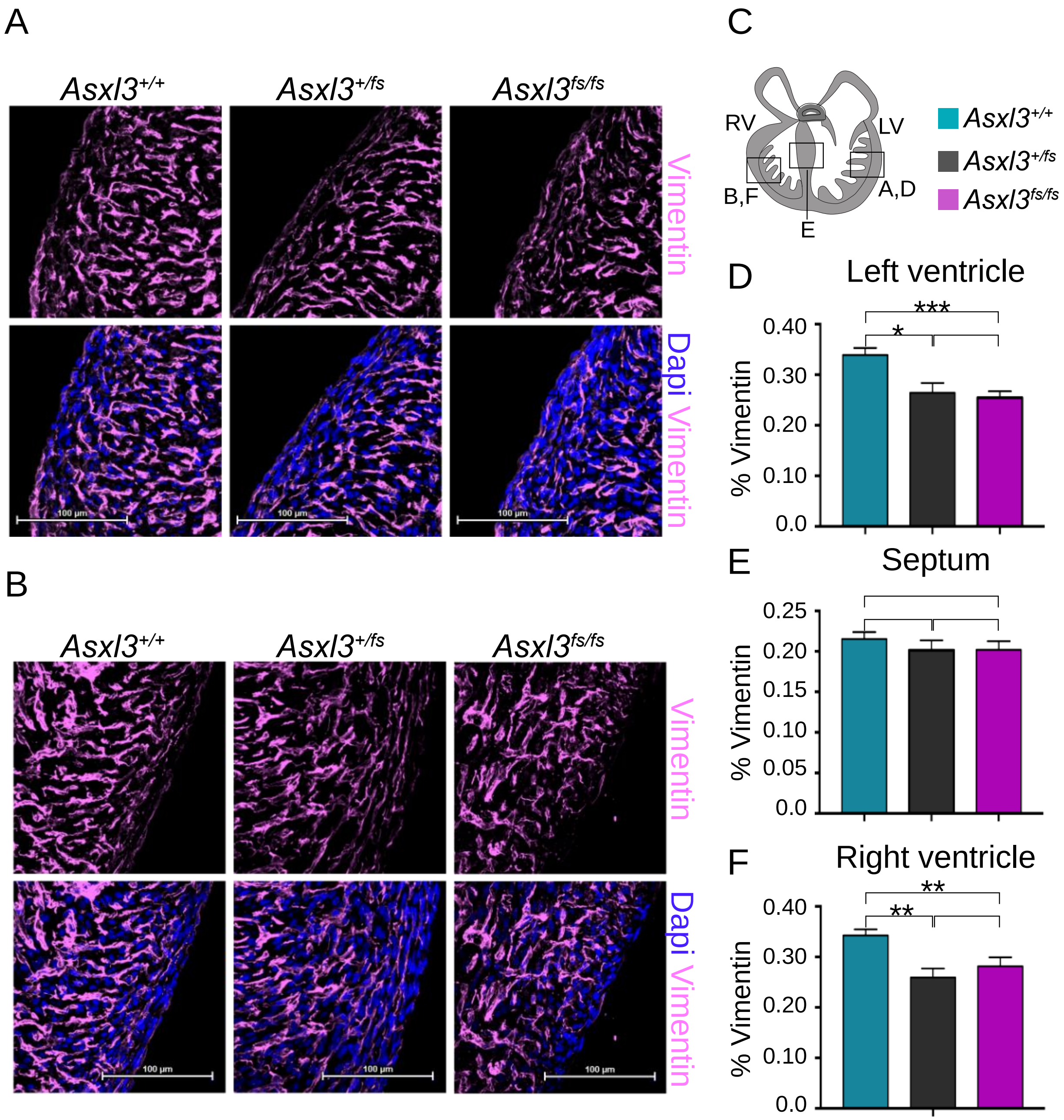

Fig 2.5. Reduction in vimentin-positive cardiac fibroblasts Immunostaining of P0.5 **A,** left ventricular free wall and **B,** right ventricular free wall with vimentin to mark cardiac fibroblasts and nuclei stained with DAPI (n=6 for Asxl3$^{+/+}$, n=3 for Asxl3$^{+/fs}$ and n=5 for Asxl3$^{fs/fs}$). **C,** Schematic of P0.5 transverse heart sections depicting representative regions of images used for quantifications. Statistical analysis of vimentin-positive cells detected in the **D,** left ventricular free wall, **E,** interventricular septum, and **F,** right ventricular free wall of *Asxl3*$^{+/+}$, *Asxl3*$^{+/fs}$ and *Asxl3*$^{fs/fs}$ P0.5 hearts. Values are mean± SEM. RV indicates right ventricle; LV, left ventricle. *p<0.05, **p<0.01, ***p<0.001.

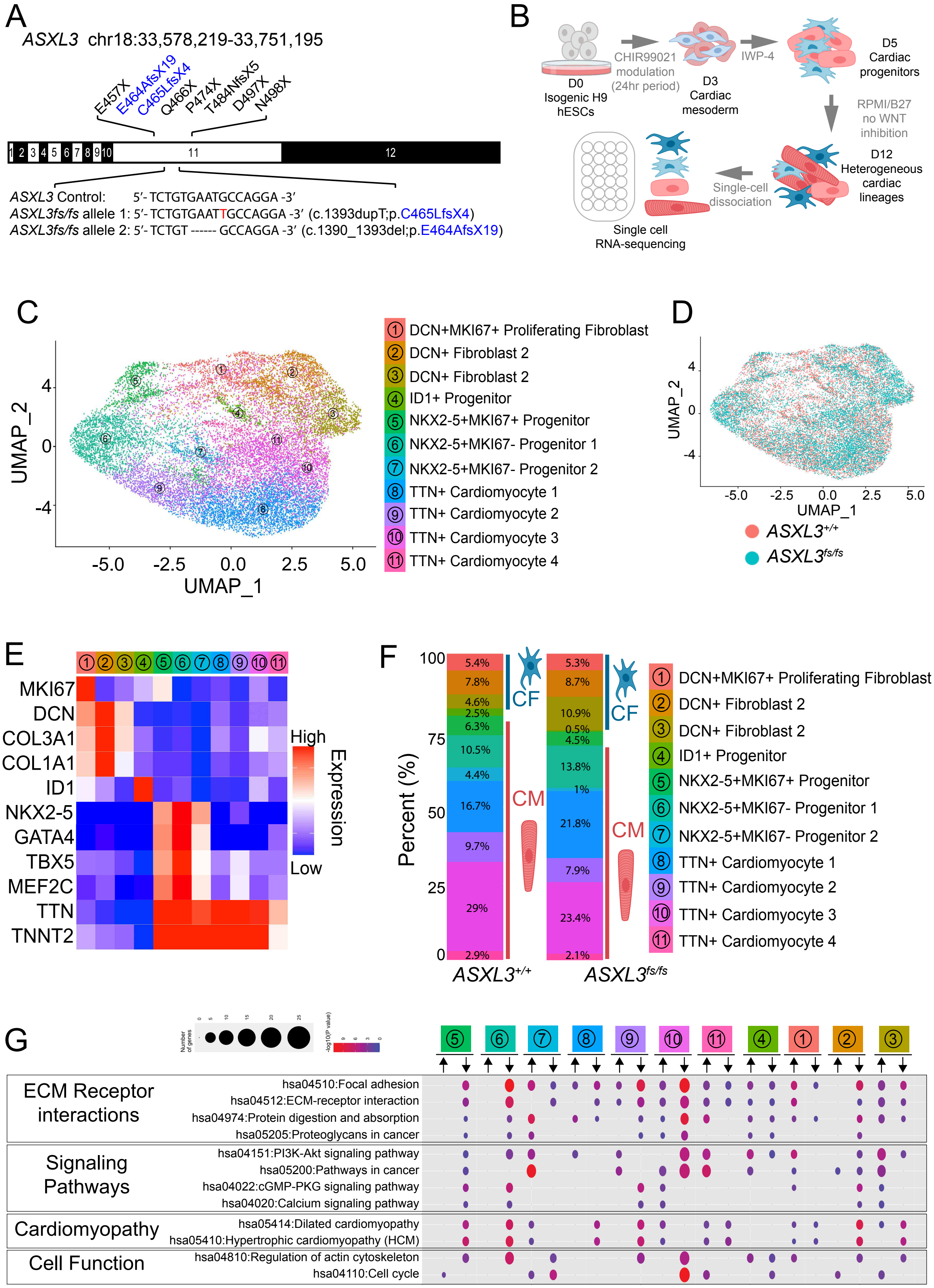
A
ASXL3 chr18:33,578,219-33,751,195
E457X
E464AfsX19
C465LfsX4
Q466X
P474X
T484NfsX5
D497X
N498X
1 2 3 4 5 6 7 8 9 10
11
12
ASXL3 Control: 5′- TCTGTGAATGCCAGGA -3′
ASXL3fs/fs allele 1: 5′- TCTGTGAATTGCCAGGA -3′ (c.1393dupT;p.C465LfsX4)
ASXL3fs/fs allele 2: 5′- TCTGT ------ GCCAGGA -3′ (c.1390_1393del;p.E464AfsX19)
B
D0
Isogenic H9
hESCs
CHIR99021
modulation
(24hr period)
D3
Cardiac
mesoderm
IWP-4
D5
Cardiac
progenitors
RPMI/B27
no WNT
inhibition
D12
Heterogeneous
cardiac
lineages
Single-cell
dissociation
Single cell
RNA-sequencing
C
UMAP_2
UMAP_1
4
0
-4
-5.0
-2.5
0.0
2.5
5.0
① DCN+MKI67+ Proliferating Fibroblast
② DCN+ Fibroblast 2
③ DCN+ Fibroblast 2
④ ID1+ Progenitor
⑤ NKX2-5+MKI67+ Progenitor
⑥ NKX2-5+MKI67- Progenitor 1
⑦ NKX2-5+MKI67- Progenitor 2
⑧ TTN+ Cardiomyocyte 1
⑨ TTN+ Cardiomyocyte 2
⑩ TTN+ Cardiomyocyte 3
⑪ TTN+ Cardiomyocyte 4
D
UMAP_2
UMAP_1
4
0
-4
-5.0
-2.5
0.0
2.5
5.0
ASXL3+/+
ASXL3fs/fs
E
① ② ③ ④ ⑤ ⑥ ⑦ ⑧ ⑨ ⑩ ⑪
MKI67
DCN
COL3A1
COL1A1
ID1
NKX2-5
GATA4
TBX5
MEF2C
TTN
TNNT2
High
Low
Expression
F
Percent (%)
100
75
50
25
0
5.4%
7.8%
4.6%
2.5%
6.3%
10.5%
4.4%
16.7%
9.7%
29%
2.9%
5.3%
8.7%
10.9%
0.5%
4.5%
13.8%
1%
21.8%
7.9%
23.4%
2.1%
CF
CM
ASXL3+/+
ASXL3fs/fs
① DCN+MKI67+ Proliferating Fibroblast
② DCN+ Fibroblast 2
③ DCN+ Fibroblast 2
④ ID1+ Progenitor
⑤ NKX2-5+MKI67+ Progenitor
⑥ NKX2-5+MKI67- Progenitor 1
⑦ NKX2-5+MKI67- Progenitor 2
⑧ TTN+ Cardiomyocyte 1
⑨ TTN+ Cardiomyocyte 2
⑩ TTN+ Cardiomyocyte 3
⑪ TTN+ Cardiomyocyte 4
G
Number of genes
-log10(P value)
⑤ ⑥ ⑦ ⑧ ⑨ ⑩ ⑪ ④ ① ② ③
↑ ↓
ECM Receptor interactions
hsa04510:Focal adhesion
hsa04512:ECM-receptor interaction
hsa04974:Protein digestion and absorption
hsa05205:Proteoglycans in cancer
Signaling Pathways
hsa04151:PI3K-Akt signaling pathway
hsa05200:Pathways in cancer
hsa04022:cGMP-PKG signaling pathway
hsa04020:Calcium signaling pathway
Cardiomyopathy
hsa05414:Dilated cardiomyopathy
hsa05410:Hypertrophic cardiomyopathy (HCM)
Cell Function
hsa04810:Regulation of actin cytoskeleton
hsa04110:Cell cycle

Fig. 2.6. scRNA-seq analysis of *ASXL3*$^{+/+}$ and *ASXl3*$^{fs/fs}$ cardiac directed differentiation A, *ASXL3* Frameshift mutations (blue) introduced in control H9 human embryonic stem cells via CRISPR gene editing and representative mutations identified in Bainbridge-Ropers syndrome patients (black). The introduced frameshift mutations (*c.1393dupT; p.C465LfsX4* and *c.1390_1393del; p.E464AfsX19*) are within the same genomic region as the patients mutations **B**, Schematic representation of human embryonic stem cell cardiac directed differentiation. Differentiation day 12 cells were collected for single-cell RNA sequencing analysis. **C**, Uniform Manifold Approximation and Projection (UMAP) analysis of *ASXL3*$^{+/+}$ (n=9,379) and *ASXL3*$^{fs/fs}$ (n=9,198) cells across the cardiac lineage. 11 clusters were identified. **D**, UMAP from C colored by genotype. **E**, Heatmap of marker genes used for cell identity. **F**, Stacked barplot displaying the proportion of clustered cells detected from *ASXL3*$^{+/+}$ and *ASXL3*$^{fs/fs}$ cultures within each phenotypic clusters. **G**, Highlights of KEGG analysis of differentially expressed genes in each cluster in the human *ASXL3*$^{fs/fs}$ ESC *in vitro* cardiac differentiation.

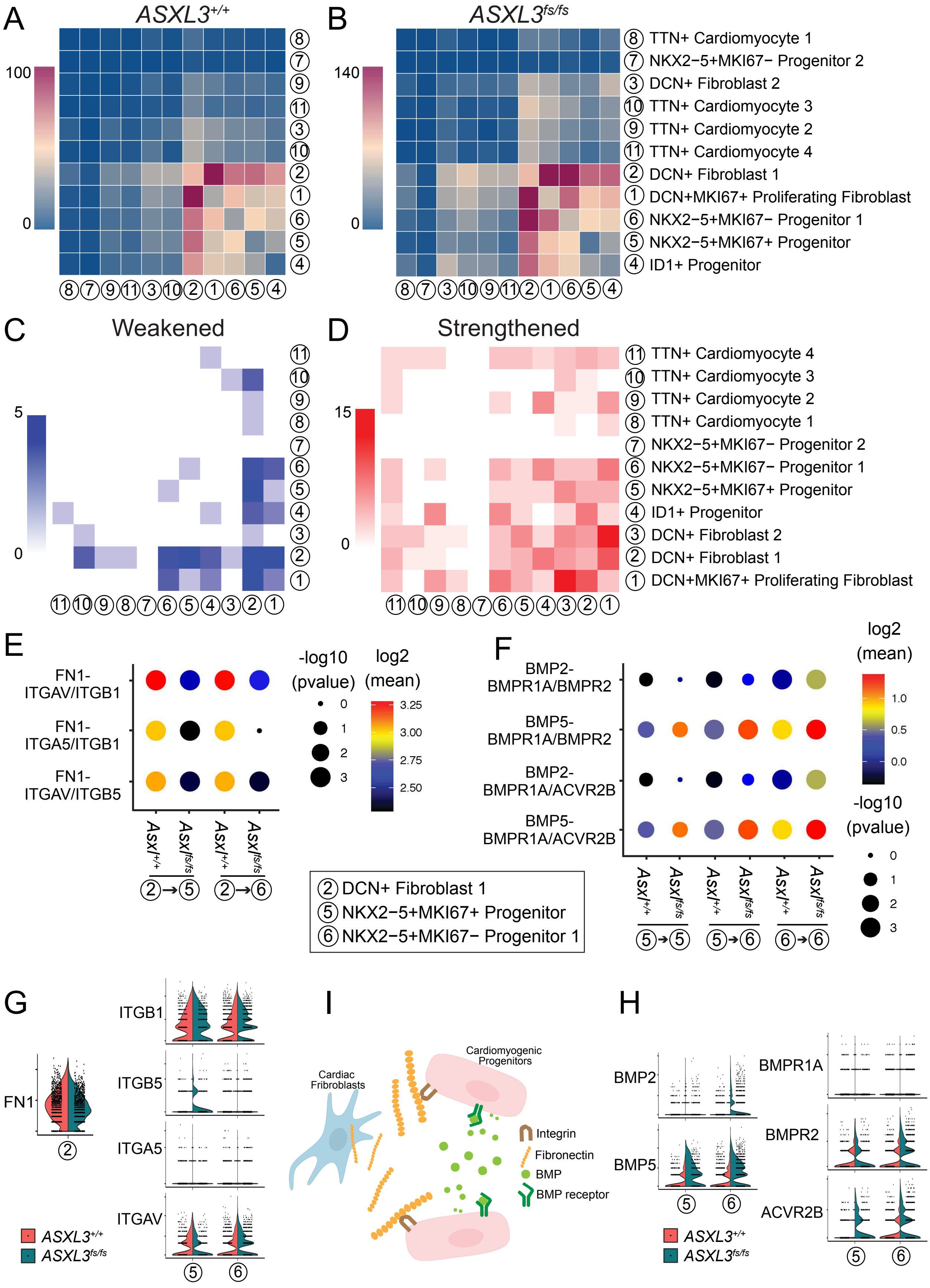
A
ASXL3+/+
100
0
B
ASXL3fs/fs
140
0
⑧ TTN+ Cardiomyocyte 1
⑦ NKX2−5+MKI67− Progenitor 2
③ DCN+ Fibroblast 2
⑩ TTN+ Cardiomyocyte 3
⑨ TTN+ Cardiomyocyte 2
⑪ TTN+ Cardiomyocyte 4
② DCN+ Fibroblast 1
① DCN+MKI67+ Proliferating Fibroblast
⑥ NKX2−5+MKI67− Progenitor 1
⑤ NKX2−5+MKI67+ Progenitor
④ ID1+ Progenitor
C
Weakened
5
0
D
Strengthened
15
0
E
FN1-ITGAV/ITGB1
FN1-ITGA5/ITGB1
FN1-ITGAV/ITGB5
Asxl+/+
Asxlfs/fs
②→⑤
②→⑥
-log10 (pvalue)
0
1
2
3
log2 (mean)
3.25
3.00
2.75
2.50
② DCN+ Fibroblast 1
⑤ NKX2−5+MKI67+ Progenitor
⑥ NKX2−5+MKI67− Progenitor 1
F
BMP2-BMPR1A/BMPR2
BMP5-BMPR1A/BMPR2
BMP2-BMPR1A/ACVR2B
BMP5-BMPR1A/ACVR2B
⑤→⑤
⑤→⑥
⑥→⑥
log2 (mean)
1.0
0.5
0.0
-log10 (pvalue)
0
1
2
3
G
FN1
ITGB1
ITGB5
ITGA5
ITGAV
ASXL3+/+
ASXL3fs/fs
I
Cardiac Fibroblasts
Cardiomyogenic Progenitors
Integrin
Fibronectin
BMP
BMP receptor
H
BMP2
BMP5
BMPR1A
BMPR2
ACVR2B
ASXL3+/+
ASXL3fs/fs

Fig. 2.7. Loss of ASXL3 leads to disruptions in ECM and cell-cell communication in hESC in vitro cardiac differentiation Heatmap of significant cell-cell signaling pathways between identified clusters in *ASXL3*$^{+/+}$ cells **A**, and *ASXL3*$^{fs/fs}$ cells **B**, predicted by CellPhoneDB. Note that the active communications occurred between the fibroblast clusters and the progenitor populations. Heatmap of weakened **C**, and strengthened **D**, cell-cell communication lines in *ASXL3*$^{fs/fs}$ cells compared to *ASXL3*$^{+/+}$ cells. **E,** Dotplots of Fibronectin-Integrin pathways intensities between DCN+ Fibroblast 1 and the NKX2-5+ cardiomyogenic progenitors. Fibronectin (FN1) was expressed by DCN+ Fibroblast 1 and the NKX2-5+ cardiomyogenic progenitors expressed the Integrin receptors. CellphoneDB predicted a decrease in the *ASXL*$^{fs/fs}$ cells. **F,** Dotplots of BMP pathways intensities between cardiomyogenic progenitor cells. Both BMP ligands and BMP receptors were expressed in cardiomyogenic progenitor populations. CellphoneDB predicted an increase in the *ASXL*$^{fs/fs}$ cells. Gene expression violin plots of **G,** fibronectin-integrin and **I,** BMP signaling genes FN1, ITGA5, ITGAV, ITGB1, ITGB5, BMP2, BMP5, BMPR1A, BMPR2, and ACVR2B in clusters discussed in **E** and **F**. **H**, Our proposed model. From our scRNA-Seq data CellphoneDB predicted that cardiac fibroblasts expressed fibronectin, which is an important ECM substrate that supports the cardiomyogenic progenitors while the autocrine and paracrine BMP signaling occurred between the cardiomyogenic progenitors. Defects in ASXL3 led to disruptions of these cell-cell communications.

A

Asxl3 -chr18: 22515929-22515951

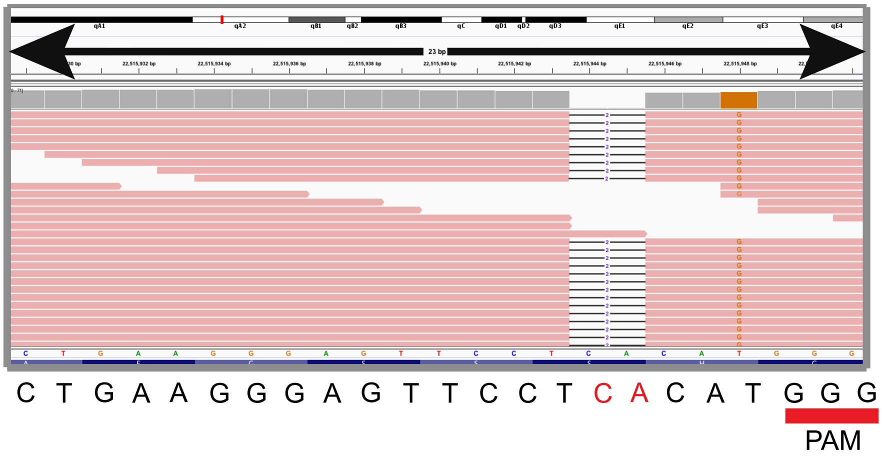

B

Gsta1 - chr9: 78242481-78242503

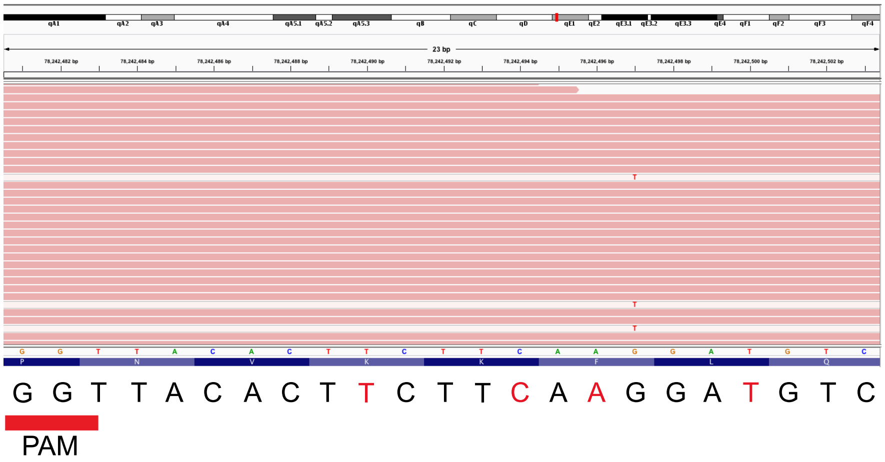

C

Sdc3- chr4:130818697-130818719

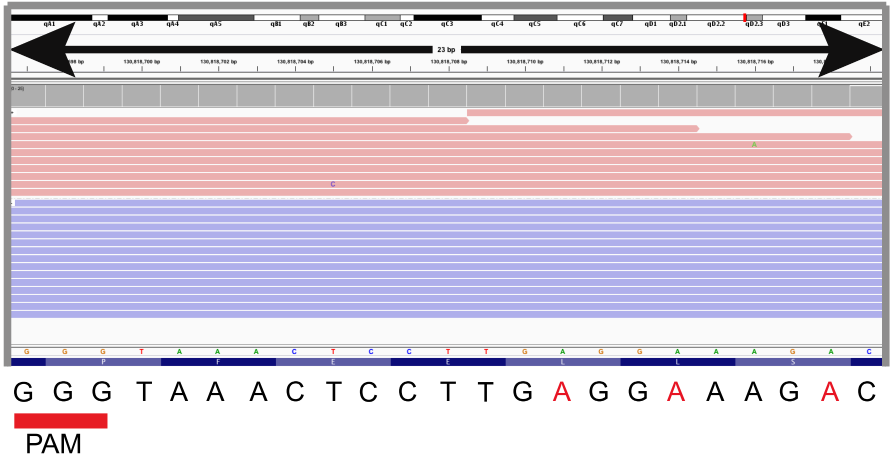

Supplemental Fig. 2.1. Whole genome sequencing to confirm CRISPR editing of *Asxl3* IGV viewer windows of whole genome sequencing results from Asxl3$^{fs/fs}$ mice. Displayed are sgRNA target site regions for **A,** *Asxl3*, **B,** *Gsta1*, and **C,** *Sdc3.*

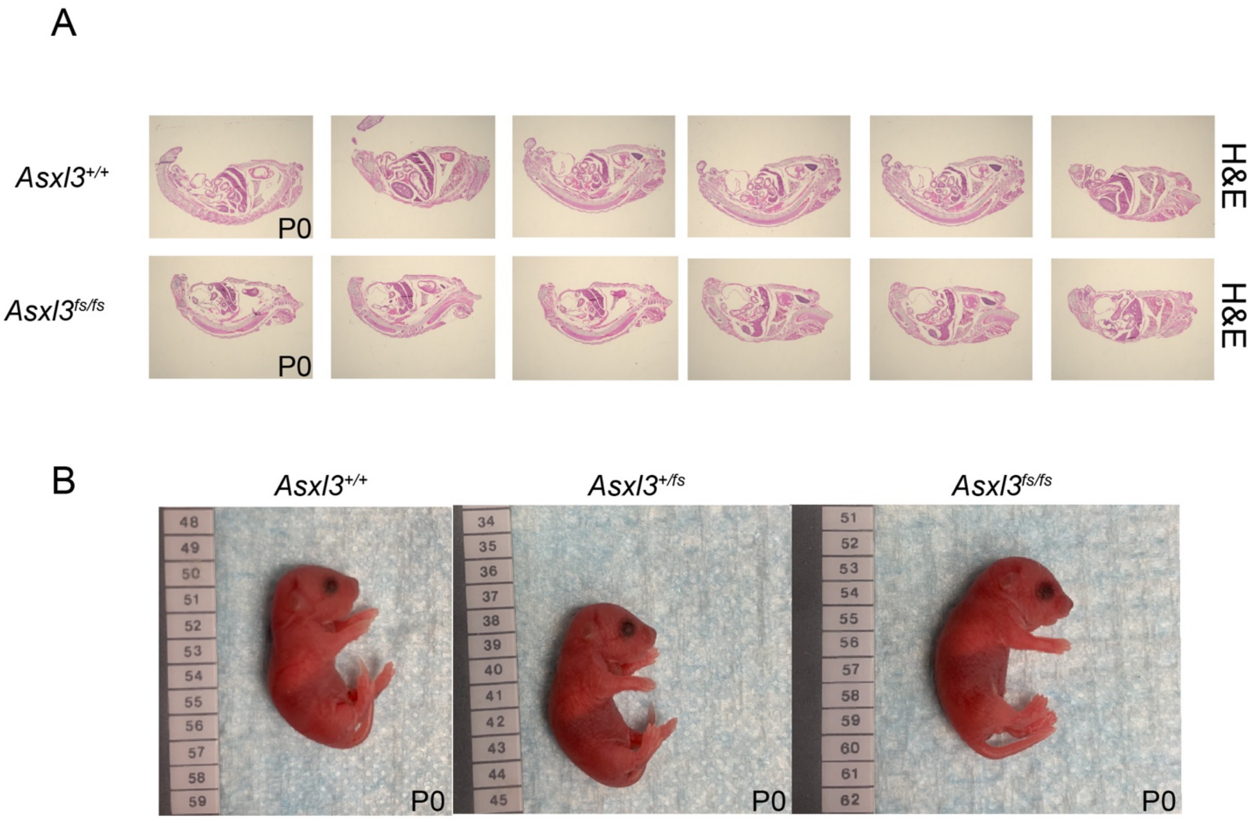

Supplemental Fig. 2.2. Gross anatomy of *Asxl3$^{fs/fs}$* mice A, Representative images of *Asxl3$^{+/+}$* and *Asxl3$^{fs/fs}$* P0.5 whole body transverse paraffin sections stained with H&E. **B.** Gross appearance of *Asxl3$^{+/+}$*, *Asxl3$^{+/fs}$*, and *Asxl3$^{fs/fs}$* live mice.

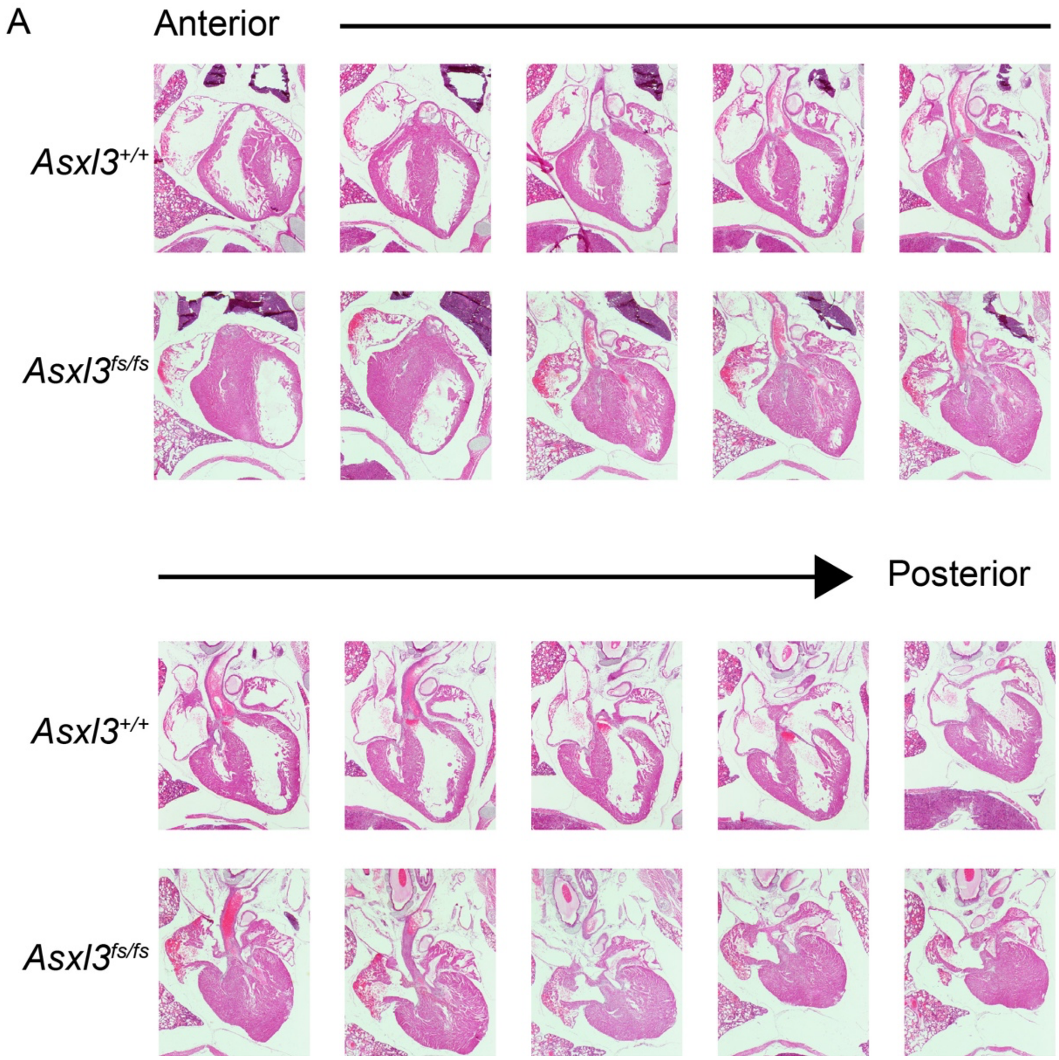

Supplemental Fig. 2.3. Ventricular hypoplasia phenotype in *Asxl3*$^{fs/fs}$ mice A, Serial coronal sections of hematoxylin and eosin stained hearts from P0.5 littermates. Compared with controls, *Asxl3*$^{fs/fs}$ mice exhibit ventricular hypoplasia throughout the anterior to posterior axis of the heart.

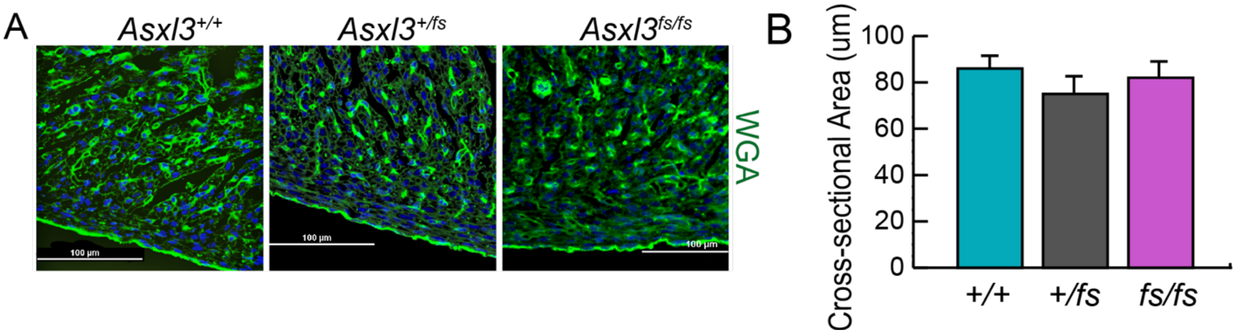

Supplemental Fig. 2.4. Cross sectional area of cardiomyocytes A, Representative images of *Asxl3*$^{+/+}$, *Asxl3*$^{+/fs}$, and *Asxl3*$^{fs/fs}$ P0.5 transverse heart sections stained with wheat germ agglutinin (WGA). **B,** Quantification of cardiomyocyte cross-sectional area.

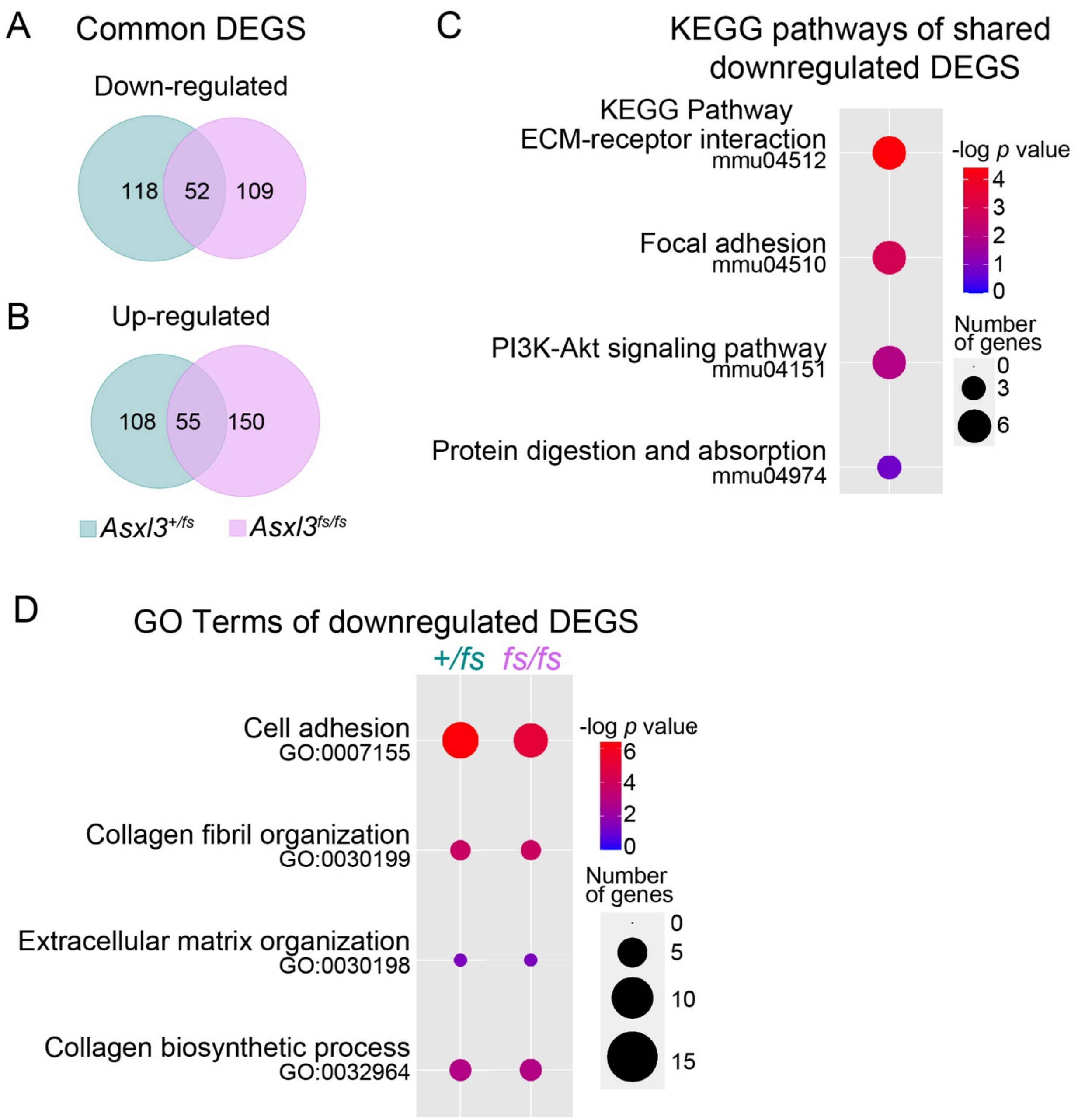

Supplemental Fig. 2.5. Differentially expressed genes shared by *Asxl3*$^{+/fs}$ and *Asxl3*$^{fs/fs}$ Venn diagrams comparing the significantly **A,** downregulated and **B,** upregulated genes (p-value > 0.05 and log fold change > 0.4) for *Asxl3*$^{+/fs}$ and *Asxl3*$^{fs/fs}$ E18.5 hearts. **C,** KEGG pathway enrichment analysis for shared *Asxl3*$^{+/fs}$ and *Asxl3*$^{fs/fs}$ downregulated genes. The top 4 KEGG pathways are shown. The size of each dot represents the gene number and the shading represents the -log$_{10}$ p-value. **D,** Common Gene Ontology terms shared between *Asxl3*$^{+/fs}$ and *Asxl3*$^{fs/fs}$ downregulated genes. The size of each dot represents the gene number and the shading represents the -log$_{10}$ p-value.

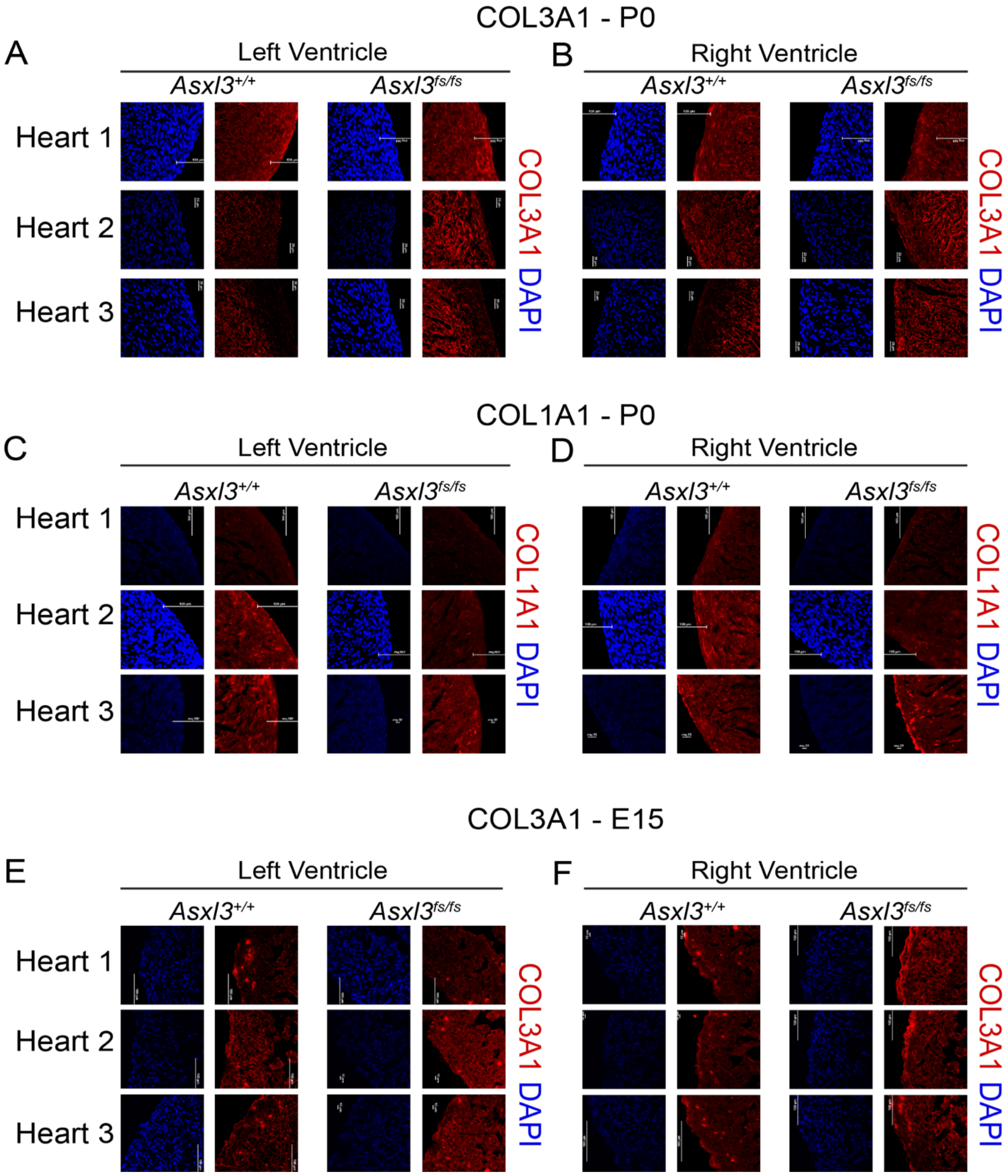

Supplemental Fig. 2.6. Collagen expression in the developing heart Representative images of *Asxl3*$^{+/+}$ and *Asxl3*$^{fs/fs}$ P0.5 **A,** left and **B,** right ventricles immunostained with COL3A1. Representative images of *Asxl3*$^{+/+}$ and *Asxl3*$^{fs/fs}$ P0.5 **C,** left and **D,** right ventricles immunostained with COL1A1. Representative images of *Asxl3*$^{+/+}$ and *Asxl3*$^{fs/fs}$ E15 **E,** left and **F,** right ventricles immunostained with COL3A1.

Supplemental Fig. 2.7. Human embryonic stem cell line carrying compound heterozygous mutation of *ASXL3* A, Chromatogram from Sanger sequencing of the ASXL3$^{fs/fs}$ cell line identifying a compound heterozygous mutations (c.1393dupT; p.C465LfsX4/c.1390_1393del; p.E464AfsX19) in the *ASXL3*. **B**, Read density plots focusing on the last 4 exons (Exon 9 through Exon 12) of *ASXL3* from the single-cell RNA-sequencing data of the day 12 cardiac differentiation.

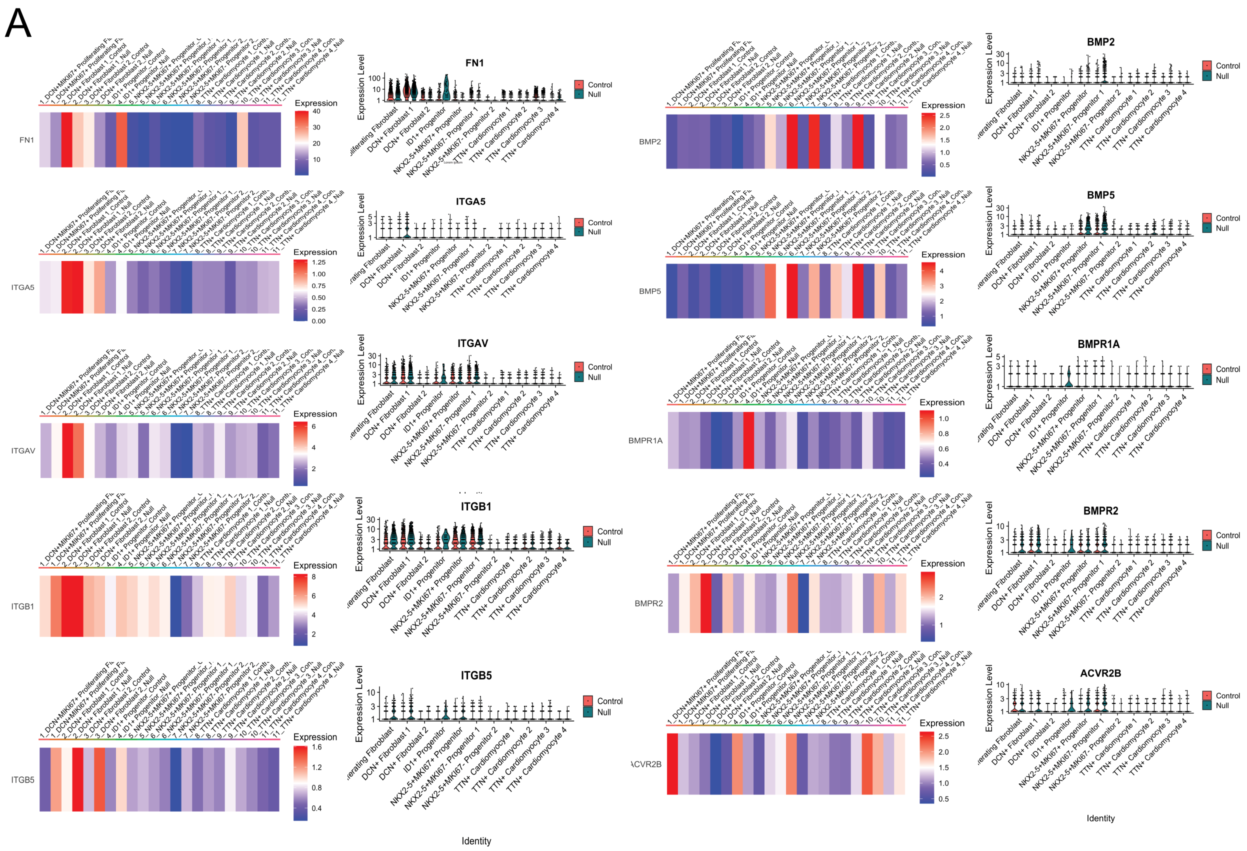

Supplemental Fig. 2.8. Marker gene expression analysis A, Gene expression violin plots and heat maps of the genes shown in Fig. 2.7G in all clusters.

Chapter 3[3]

ASXL3 Controls Cortical Neuron Fate Specification Through Extrinsic Self-Renewal Pathways

ABSTRACT

During corticogenesis, transcription plasticity is fundamental to the restriction of neural progenitor cell (NPC) multipotency and production of cortical neuron heterogeneity. Human and mouse genetic studies have highlighted the role of Polycomb transcriptional regulation in this process. *ASXL3*, which encodes a component of the Polycomb repressive deubiquitination (PR-DUB) complex, has been identified as a high confidence autism spectrum disorder (ASD) risk gene. Genetic inactivation of *Asxl3,* in a mouse model that carries a clinically relevant *ASXL3* frameshift ($\mathit{Asxl3}^{fs}$*)* variant, disrupts lateral expansion of NPCs and delays cortical neuron differentiation. Single-cell RNA sequencing analysis implicates Notch signaling, which alters the composition of excitatory neurons and fidelity of cortical layer deposition. Our data provides a new link between extrinsic signaling cues and intrinsic epigenetic regulation that together control the timing of cell fate programs. Furthermore, transcriptomic analysis revealed dysregulation of other known ASD risk genes indicating that a convergent developmental pathway is affected. Collectively our work provides important insights about developmental mechanisms that contribute to ASD neuropathology.

---

[2] This chapter represents a submitted manuscript. McGrath BT, Wu P, Salvi S, Girgla N, Chen X, Zhu J, KC R, Tsan YC, Moccia A, Srivastava A, Zhou X, Bielas SL. ASXL3 controls cortical neuron fate specification through extrinsic self-renewal pathways. *Under Review*

INTRODUCTION

The cellular complexity of the neocortex is precisely orchestrated during development by the sequential generation of cortical neurons from a common pool of neural progenitor cells (NPCs) [1-8]. Progressive restriction of NPC multipotency, by highly defined gene expression patterns, determines the composition of excitatory cortical neurons distributed across the six-layers of the cerebral cortex. Chromatin organization and dynamic epigenomic regulation of histone modifications are required for the transcriptional plasticity that affords progressive restriction of NPC multipotency, while instilling mature cortical neuron fate on immature postmitotic neurons [9]. Genes that encode components of chromatin modification complexes comprise a prominent genetic etiology of developmental syndromes and autism spectrum disorders (ASD), further implicating an important role for chromatin biology in corticogenesis and neuron fate determination [10-12].

Polycomb group (PcG) complexes are a source of chromatin modifications that play an essential role in repressing gene expression to control development [13]. Much of our understanding of Polycomb transcriptional repression comes from characterization of Polycomb repressive complex 1 (PRC1) and Polycomb repressive complex 2 (PRC2). PRC1 monoubiquitylates histone H2A at lysine 119 (H2AUb1), and PRC2 mono-, di-, and tri-methylates histone H3 at lysine 27 (H3K27me1/2/3). Polycomb repressive deubiquitination complex (PR-DUB) is responsible for H2AUb1 deubiquitination, but is less well studied than PRC1 and PRC2 [14]. PRC1 and PRC2 loss-of-function studies support a role for PcG epigenetic repression in progressive restriction of NPC multipotency required for the full spectrum of mature cortical neuron production during corticogenesis [15, 16]. Human neurogenetic evidence suggest an important role for PR-DUB in brain development, with genes that encode PR-DUB complex components identified as the genetic basis of developmental disorders [17-21].

De novo dominant pathogenic variants in the PcG protein *ASXL3* (*Additional sex comb-like 3)* were identified as the genetic basis of Bainbridge-Ropers syndrome and ASD [19].

H2AUb1 dysregulation is a key feature of ASXL3 molecular pathology and re-distribution of genome wide H2AUb1 is accompanied by altered transcriptional profiles [17]. ASXL3 expression is highest in the brain during the first 24 weeks of gestation (Brainspan, Allen Brain Institute), a period of cortical development characterized by rapid NPC proliferation, birth of postmitotic neurons, and specification of cortical neuron fates [22, 23]. The impact of ASXL3-dependent H2AUb1 deubiquitination on neural development has not been previously described.

Here we investigate the role of ASXL3 in modulating transcriptional programs that contribute to the neuronal diversity of the cortex. We created an *Asxl3* mouse model carrying a clinically relevant frameshift allele ($Asxl3^{fs/fs}$). We detect elevated levels of H2AUb1, differential gene expression, and a cortical neuron fate defect that opposes the cortical phenotype described for conditional deletion of Ring1b, the catalytic component of PRC1 [15]. Characterization of cellular composition by single-cell RNA sequencing (scRNA-seq) at three developmental stages depicted an increase in $Asxl3^{fs/fs}$ neural progenitors, which was validated by immunohistochemistry and attributed to expansion of ventricular radial glia consistent with altered lateral expansion. Transcriptomic analysis implicates perturbations to extrinsic signaling pathways that disrupt the balance of NPC proliferation and differentiation. Transcriptional pathways are enriched with differentially expressed genes (DEGs) that converge on chromatin biology and proliferation at embryonic day (E) 13.5 and E14.5, and evolved to implicate synaptic regulation at birth. Across cortical development, ASD risk genes are represented in DEGs, implicating a convergence of pathogenic mechanisms among chromatin etiologies of ASD.

RESULTS

Asxl3$^{fs/fs}$ mice display multiple defects of nervous system development

To investigate the role of *Asxl3* in brain development, we generated a clinically relevant *Asxl3 c.990_992delCA* frameshift allele (fs) in mouse exon 12 using CRISPR/Cas9 genome-editing. *Asxl3* exhibits low, but persistent expression in developing mouse cortex starting as early as E10.5 [24] (Supplemental Fig. 3.1). *Asxl3*$^{fs/fs}$ mRNA is also detected in developing cortical tissue, but full length ASXL3 protein was not detected by western blot (Fig. 3.1A and Supplemental Fig. 3.1). Loss of ASXL3 is accompanied by a 3-fold increase of genome-wide H2AUb1 in the E13.5 cerebral cortex (Fig. 3.1B, C). Hetero- and homo-zygous *Asxl3* frameshift mice are born at Mendelian ratios. *Asxl3*$^{+/fs}$ mice are indistinguishable from *Asxl3*$^{+/+}$ at birth and breed normally. However, homozygous *Asxl3*$^{fs/fs}$ are perinatal lethal, with a majority of *Asxl3*$^{fs/fs}$ pups dying within the first week of life [25]. Multiple organ systems, including the heart, brain and skeleton are affected in *Asxl3*$^{fs/fs}$ mice. Hypoplastic heart ventricles is the predicted cause of perinatal death of *Asxl3*$^{fs/fs}$ animals [25]. *Asxl3*$^{fs/fs}$ mice exhibit a distinguished posture at birth with a curved back and drooping forelimbs (Fig. 3.1D). Alizarin red and Alcian blue skeletal survey revealed a partially penetrant cervical rib in *Asxl3*$^{fs/fs}$ mice consistent with a homeotic transformation attributed to ectopic *Hox* gene expression, but ruled out kyphosis due to axial skeletal abnormalities [25]. Such posture has been observed in transgenic mouse models that disrupt neuromuscular axis elements, including upper motor neurons, corticospinal tracts, lower motor neurons and/or the neuromuscular junction [26].

Genetic disruption of individual PcG components give rise to a full spectrum of cortical size and cytoarchitectural changes [27]. *Asxl3*$^{fs/fs}$ cortical surface area and telencephalic hemisphere length were evaluated relative to control littermates. At P0, *Asxl3*$^{fs/fs}$ cortical surface area is 87% of *Asxl3*$^{+/+}$ littermates, while hemispheric length is not significantly shorter (Fig. 3.1E, F and Supplemental Fig. 3.1). Gross structural defects in cortical anatomy or commissure formation were not observed in a series of matched coronal and sagittal sections of *Asxl3*$^{fs/fs}$ and

Asxl3$^{+/+}$ P0.5 paraffin fixed brains (Fig. 3.1G and Supplemental Fig. 3.1). Sagittal sections through the cerebellar hemispheres reveal shallower fissures and smaller lobules in *Asxl3*$^{fs/fs}$ versus *Asxl3*$^{+/+}$ P2 littermates consistent with a delay in cerebellar development (Fig. 3.1H). *Asxl3*$^{fs/fs}$ cortices lack distinct boundaries between cortical layers in cresyl violet stained sections (Fig. 3.1G). To explore this phenotype, cortical layers (L) were evaluated by immunohistochemistry (IHC) using markers of mature neuron subtypes, including TBR1, BCL11B, and SATB2 (Fig. 3.1J and Supplemental Fig. 3.2). A >20% reduction of BCL11B labeled L5 neurons was quantified in the P0.5 cortex of *Asxl3*$^{fs/fs}$ mice relative to *Asxl3*$^{+/+}$ controls (Fig. 3.1I). This phenotype does not correlate to a corresponding change in the number of L6 TBR1 and/or L2-4 SATB2 cortical neurons.

Lateral expansion generates increased NPCs in Asxl3$^{fs/fs}$ *cortex*

During cortical development, NPCs sequentially give rise to distinct cortical neuron subtypes. To characterize the developmental source of P0.5 cortical neuron composition changes, scRNA-seq using Seq-Well was performed on cortices from E13.5 and E14.5 littermates. NPCs at these developmental time points give rise to L5 neurons. In total, 17 cortices were processed across these two timepoints (Supplemental Fig. 3.3). Following quality control steps, data from *Asxl3*$^{+/+}$ and *Asxl3*$^{fs/fs}$ samples at E13.5 and E14.5 were integrated and analyzed using Seurat [28]. Standard quality control features for brain based single cell transcriptomics and Seq-Well studies were used (Supplemental Fig. 3.3) [29-31] Clustering was not driven by experimental batch or individual samples (Supplemental Fig. 3.4) indicating consistent transcriptional signatures for individual cell types between animals. After performing dimensionality reduction and unsupervised clustering with uniform manifold approximation and projection (UMAP) we identified unique cell populations for each developmental timepoint (Supplemental Fig. 3.4). 46,920 E13.5 and 24,963 E14.5 cortical cells were retained that span twelve and fifteen clusters respectively (Supplemental Fig. 3.3 and Fig. 3.4). *Asxl3*$^{+/+}$ and *Asxl3*$^{fs/fs}$

cells were represented in all clusters (Supplemental Fig. 3.4). Cluster cell-type identities were manually annotated based on cluster-specific molecular markers as defined by previous studies [29, 30, 32]. We confirmed our annotation by aligning our *Asxl3*$^{+/+}$ E14.5 dataset with published E14.5 mouse brain scRNA-seq data [29]. Cluster assignments between the two datasets were closely matched, with little representation of cell types outside our dissection perimeter (Supplemental Fig. 3.5). This highlights the reproducibility of scRNA-seq between studies and the robustness of our data to characterize developmental defects.

Following cell-type annotation, we compiled transcriptomic data from clusters which contribute to excitatory lineages. Unsupervised clustering of data from this subset of cells was performed and clusters annotated (Fig. 3.2). At E13.5, eleven clusters were identified corresponding to known excitatory lineage cell types, including seven radial glia cell (RGC), a differentiating radial glia cell (dRGC), an intermediate progenitor (IP), a migrating neuron, and two L5-6 excitatory neuron (DL neuron) clusters (Fig. 3.2B). At E14.5, ten clusters were defined that included four RGC, a dRGC, two IP, a migrating neuron, and three DL neuron populations (Fig. 3.2E). Consistent with scRNA-seq data from developing human cortex, the clustering resembled the predicted developmental trajectory with RGCs transitioning to IPs then migrating neurons and finally DL neurons (Fig. 3.2E) [30]. We next examined the distribution of canonical marker genes that define cells at different stages of neurogenesis (Fig. 3.2G, H and Supplemental Fig. 3.6). The numerous RGC populations (Clusters E13-0, 13-1, 13-2, 13-3, 13-4, 13-5, 13-6, 14-0, 14-1, 14-2, 14-3) express a combination of cell cycle genes like *MKi67*, *Aspm*, *Lig1* and RGC transcription factors like *Pax6* and *Sox2*. We observed that dRGC (Clusters E13-7, 14-4) co-express markers of the other major cell types (RGC, IP, migrating neuron, DL neuron) at a reduced level. Similar transitory cells have been described in transcriptomic studies of developing mouse and human cortex [30, 33, 34]. IP clusters (Clusters E13-8,14-5,14-6) are marked by *Eomes*. Migrating neurons express a combination of general neuronal markers *Neurod2*, *Neurod6*, and axon guidance genes *Rnd2*, *Cntn2*, and *Robo2*. Among L5-6 excitatory neuron clusters, expression of transcription factors that demark deep and upper layer excitatory neurons was noted, such as *Sox5*, *Tbr1*, *Bcl11b*, *Bcl11a*, *Fezf2*, *Satb2*, and *Pou3f1*.

While *Asxl3*$^{fs/fs}$ and *Asxl3*$^{+/+}$ cells are distributed across all clusters at E13.5, the density of *Asxl3*$^{fs/fs}$ cells are significantly enriched in the region of UMAP space that overlaps with cluster E13-6 (Fig. 3.2C and Supplemental Fig. 3.4C). Cells in E13-6 have the transcriptional characteristics of a transition cell type, uniformly expressing markers of RGC and other major cell types at low levels (Fig. 3.2G). The position of cluster E13-6 in UMAP space suggest the cluster is composed of RGC cells differentiating to IPs and/or immature postmitotic migrating neurons. These findings are consistent with a model where progenitors exhibit a permissive transcriptional status that supports gradual differentiation to excitatory linage fates, independent of a direct or indirect path through IPs [35, 36]. At E14.5, all clusters were populated by *Asxl3*$^{fs/fs}$ and *Asxl3*$^{+/+}$ cells, without genotype-dependent enrichment in one or more cell-specific clusters (Fig. 3.2E and Supplemental Fig. 3.4B).

To assess changes in *Asxl3*$^{fs/fs}$ cortical cell composition, the overall proportions of developmental cell classes were calculated at E13.5 and E14.5. For this analysis cortical cells were grouped into five classes, namely RGC, dRGC, IP, Migrating neurons, and DL neurons. When compared to *Asxl3*$^{+/+}$, RGCs are significantly increased at E13.5 in *Asxl3*$^{fs/fs}$ cortex, with a corresponding decrease in more mature cell types (Fig. 3.2I and Supplemental Fig. 3.4F). A day later at E14.5, the E13.5 increased RGCs has transitioned to include more dRGCs and fewer IPs and migrating neurons in *Asxl3*$^{fs/fs}$ cortex (Fig. 3.2J and Supplemental Fig. 3.4E). This change implicates dysregulation of RGC proliferation or differentiation dynamics in *Asxl3*$^{fs/fs}$ developing cortex.

To characterize the developmental mechanism that accounts for *Asxl3*$^{fs/fs}$ cellular composition changes*,* we immunostained E14.5 cortical tissue for SOX2 and EOMES, to evaluate RGCs and IPs (Fig. 3.2K, I). Altered proliferation dynamics can alter NPC niche size by modulating ventricular (VZ)/subventricular (SVZ) zone thickness (radial expansion) or ventricular zone length (lateral expansion). Both radial and lateral VZ changes were quantified. To evaluate VZ/SVZ thickness, the number of SOX2+ RGCs and EOMES+ IPs in a single bin that spans the cortical thickness was quantified at medial, medial/lateral and lateral regions of the neocortex (Fig. 3.2K). A small but significant radial expansion of SOX2+ RGCs was detected in the lateral neocortex and a decrease in EOMES+ IPs was identified in the medial and medial/lateral neocortex (Fig. 3.2M,N and Supplemental Fig. 3.7). These changes would not entirely account for *Asxl3*$^{fs/fs}$ progenitor increase detected by scRNA-seq. Lateral expansion was assessed by measuring the length of the lateral ventricular/VZ boundary that corresponds to the apical border of the VZ. The length of the *Asxl3*$^{fs/fs}$ VZ was significantly longer along all rostral to caudal sections measured (Fig. 3.2O and Supplemental Fig. 3.7). Therefore, *Asxl3*$^{fs/fs}$ cortical cell composition changes detected by scRNA-seq can largely be attributed to lateral expansion of VZ RGCs. Similar phenotypes have been observed in mouse models that disrupt signaling pathways critical for balancing NPC maintenance and differentiation [37-39].

Deep layer cortical neuron differentiation delayed in Asxl3*$^{fs/fs}$ *cortex

Corticogenesis relies on an exquisite balance between RGC expansion and neuronal differentiation that generates the full complement of mature cortical neuron subtypes. The embryonic increase in *Asxl3*$^{fs/fs}$ progenitors suggests the balance of this stereotypic process is disrupted. Pseudotemporal analysis was performed using Monocle 3 to reconstruct and evaluate the differentiation process of E13.5 and E14.5 corticogenesis (Fig. 3.3A-F) [40]. At both time points, pseudotime ordering of cell types mirrored *in vivo* corticogenesis. RGCs represent the earliest pseudotime stages of differentiation followed by dRGCs, IP, Migrating neurons, and DL excitatory neurons (Fig. 3.3A, D and Supplemental Fig. 3.8). We then constructed individual trajectories for *Asxl3*$^{+/+}$ and *Asxl3*$^{fs/fs}$ samples to compare genotypic pseudotime differentiation outcomes (Fig. 3.3B, E). Again, at E13.5 an *Asxl3*$^{fs/fs}$ increase in RGCs and corresponding decrease in more mature cell types was noted, based on a quantitative change in the amplitude, or cell density, of overlapping pseudotime peaks. This difference in pseudotime landscape is consistent with RGC multipotency persistence at the expense of neurogenic divisions. A genotypic dependent change in the position of peaks across pseudotime, consistent with a change in the timing of differentiation was not observed at E13.5 (Fig. 3.3B-C). E14.5 analysis revealed *Asxl3*$^{fs/fs}$ changes in amplitude and distribution of cell type-specific peaks. An increase in progenitors persists, but is now distributed across RGC, dRGC and IP cell types (Fig. 3.3E, F). However, progenitor persistence now correlates with a novel *Asxl3*$^{fs/fs}$ peak detected between pseudotime differentiation position 20-30. The peak exhibits unique spacing relative to *Asxl3*$^{+/+}$ peaks and is composed of migrating neurons and DL excitatory neurons, consistent with delayed differentiation of a subset of *Asxl3*$^{fs/fs}$ deep layer cortical neurons (Fig. 3.3E, F). Collectively, the analysis supports a model where persistence of RGC self-renewing proliferation at E13.5 manifests in delayed differentiation of a population of excitatory neurons evident at E14.5.

To assess the relationship of progenitor expansion on neuron differentiation, E13.5 or E14.5 time-pregnant dames were administered EdU and sacrificed at P0.5. The majority of EdU labeled cells at E13.5 were distributed across deep cortical layers, with a comparable distribution in both genotypes. No change in the percentage of EdU labeled or EdU/BCL11B double-labeled cells at E13.5 was quantified (Fig. 3.3G, H). At E14.5, the distribution of EdU labeled cells included upper cortical layers in *Asxl3*$^{+/+}$ littermates, with few cells labeled below BCL11B L5 neurons. *Asxl3*$^{fs/fs}$ EdU labeled cells exhibit greater distribution across cortical layers, including deep layers and a reduction in the percentage of EdU/BCL11B double-labeled cells was quantified in *Asxl3*$^{fs/fs}$ cortex, consistent with a delay in cortical neuron differentiation.

Altered extrinsic signaling disrupted in Asxl3$^{fs/fs}$ *corticogenesis*

To uncover the cell and molecular biology impacted by *Asxl3*$^{fs/fs}$ transcriptional changes and that may account for the corticogenesis defects, Gene Ontology (GO) analysis of E13.5 and E14.5 clusters was performed. Corresponding E13.5 and E14.5 *Asxl3*$^{fs/fs}$ DEGs were enriched in

GO terms implicating extrinsic signaling pathways, including Notch, Wnt, and Hippo (Fig. 3.4A). Enriched DEGs of note include *Hes1*, *Hes5*, *Notch1, Notch2, Dll1, Wnt5a, Wnt7b, Fzd1, Fzd4, Yap1, Tead1, Tead2*. Activities of these extrinsic signaling pathways have been demonstrated to act on NPCs to direct the balance between NPC proliferation and differentiation [37, 39, 41, 42]. Mouse models of constitutive overexpression or persistent activity have demonstrated cross talk between these signaling pathways during cortical development [37, 41].

DEGs in the Notch signaling pathway were used to investigate how coordination of temporally defined cell-specific transcription cascades are dysregulated to contribute to *Asxl3*$^{fs/fs}$ corticogenesis defects. Notch function is mediated through cell-cell interactions of neighboring cells (Fig. 3.4B). Expression of a transmembrane ligand (delta or jagged) in one cell, binds a Notch receptor on an opposing cell. A series of cleavage events allows the Notch intracellular domain (NICD) to translocate into the nucleus. Intranuclear NICD initiates transcription of bHLH transcription factors *Hes1/5* that inhibit neuronal differentiation by repressing expression of proneural bHLH *Neurog2*. In mice, overexpression of N1ICD, *Hes1* or *Hes5* in the developing cortex induces lateral expansion of NPCs [37, 38, 43]. N1ICD ChIP-seq and transcriptomic analysis of the N1ICD overexpression mouse cortex identified direct and downstream targets of N1ICD [37]. These targets were intersected with E13.5 and E14.5 individual cluster transcriptional changes which revealed enrichment for direct and downstream N1ICD targets amongst the *Asxl3*$^{fs/fs}$ DEGs (Fig. 3.4C, D).

Significant *Hes1* and *Hes5* differential overexpression in E13.5 RGC clusters and phenocopy between *Asxl3*$^{fs/fs}$ and *Hes1* and *Hes5* overexpression mouse models implicate disruption of Notch transcription factor coordination as a molecular driver of early *Asxl3*$^{fs/fs}$ cortical defects (Fig. 3.4C, D). Supporting this observation, Notch DEGs that regulate *Hes1* and *Hes5* expression were detected across E13.5 clusters, while few downstream targets of HES1/5 were among the DEGs identified (Fig. 3.4E). In line with disruption of coordinated Notch signaling, at E14.5 fewer regulators of *Hes* expression were differentially expressed in RGCs, *Hes1/5* expression was largely normalized, while an increase in downstream targets of *Hes1/5* were enriched among the DEGs (Fig. 3.4F). If we integrate the data from these two time points, it implicates a molecular mechanism where upregulation of *Hes* genes at E13.5 favors retention of multipotent RGC fate through a mechanism of lateral expansion. By E14.5 downstream targets of HES1/5 downregulate, such as *Neurog2* which participates in a negative feedback loop with the *Hes* genes in Notch signaling (Fig. 3.4B). These results would support a shift in the balance towards self-renewing progenitor proliferation and away from neurogenesis or neuronal differentiation.

Alterations in Asxl3$^{fs/fs}$ excitatory neuron composition

To characterize P0.5 cortical neuron composition by single cell transcriptomics, the P0.5 cortex was micro-dissected from brain stem, olfactory bulbs and ventral brain structures (Fig. 3.5A). scRNA-seq was performed on 23,511 cells from four *Asxl3*$^{+/+}$ and 38,672 cells from five *Asxl3*$^{fs/fs}$ cerebral cortices. Cells clustered into 21 unique cell populations and were annotated as described for embryonic timepoints (Supplemental Fig. 3.3). The cell populations identified were correlated to known major cell-types present in the P0.5 cortex, including subtypes of neural progenitors, intermediate progenitors, excitatory neurons and interneurons that are derived from ventral brain structures and tangentially migrate into the cortex (Supplemental Fig. 3.4). Comparable clusters were detected in both genotypes (Fig. 3.5C and Supplemental Fig. 3.4A). *Asxl3*$^{+/+}$ P0.5 data aligned with Loo et al. 2019 [29] P0 cortical scRNA-seq exhibited comparable clusters with minimal detection of cells from the striatum or ganglionic eminence, which were removed during dissection (Supplemental Fig. 3.5). This indicates the reproducibility of scRNA-seq between studies and the robustness of our data to characterize cortical neuron composition changes between *Asxl3*$^{+/+}$ and *Asxl3*$^{fs/fs}$ samples.

To assess the excitatory neuron composition, transcriptomic data from excitatory neuron lineages was isolated from total cortical cell data (Fig. 3.5A). Comparable clusters were detected in both genotypes when clustered independently and in aggregate (Fig. 3.5C and data not shown). Eleven distinct clusters were annotated corresponding to IPs, Migrating neurons, and cortical pyramidal neurons from upper and deep layers, further classified as subcerebral projection neurons (SCPN), corticothalamic projection neurons (CThPN) and callosal projection neurons (CPN). Layer 5/6 deep layer CPNs (dCPN) were present in cluster P0-2 and P0-7. Layer 2-4 upper layer CPNs (uCPN) were in P0-0, P0-3, P0-4, P0-5, P0-8. Several marker genes for these CPN clusters have regional-specific expression including *Lhx2* (caudo-rostral), *Cbln2* (rostro-caudal), *Crym* (caudo-rostral), *Dkk3* (visual cortex), *Epha5* (somatosensory cortex), *Lmo4* (sensory areas), Bhlhb22 (Sensory areas) (Fig. 3.5F) [44]. Genes known to have subtype specific expression in CThPN and ScPN were enriched in clusters P0-6 and P0-9 respectfully (Fig. 3.5F and Supplemental Fig. 3.5).

The ratio of broad cell classes were calculated for *Asxl3*$^{+/+}$ and *Asxl3*$^{fs/fs}$ samples to determine the cortical composition of cells from excitatory lineages. Overall, deep layer cortical neurons classes exhibit the largest genotypic differences in cortical composition changes that diminished in upper layer neuron subtypes. In *Asxl3*$^{fs/fs}$ samples a two-fold increase in CThPNs coincides with a 30% increase in SCPNs and switches to a reduction in dCPNs (15% reduction) and uCPNs (6% reduction) relative to control (Fig. 3.5E). This finding is consistent with an early disruption to the timing of cortical neuron differentiation.

We evaluated the spatial distribution of *Asxl3*$^{+/+}$ and *Asxl3*$^{fs/fs}$ cells for individual combined excitatory clusters by employing Tangram (Fig. 3.5G and Supplemental Fig. 3.9) [45, 46]. Tangram maps cells identified through scRNA-seq by aligning the data with a reference spatial dataset, in our case the STARmap spatial dataset of the mouse visual cortex [46]. *Asxl3*$^{+/+}$ and *Asxl3*$^{fs/fs}$ P0.5 scRNA-seq profiles were mapped based on 166 training genes present in both STARmap and our data. Of note, cell type distributions of excitatory neuron classes do not exhibit consistent layer-specific spatial patterns. CThPNs exhibit the greatest fidelity to the localized L6 spatial distribution in deep layers. Patterns of SCPNs, dCPNs and uCPNs distribution are less specific, with cells roughly distributed throughout upper and deep layers. These excitatory neuron classes were distinguished based on the percentage of cells mapped in L5-6 versus L2-4 (SCPN L6:34%. L5:56%. L2/4:9%; dCPN L6:32%, L:50%, L2/4:15%; uCPN L6:31%, L5:44%, L2/4:19%). This distribution is consistent with growing literature implicating a greater contribution of shared transcriptional profiles along the continuum of excitatory neuron differentiation as fate is established [36, 47].

ASXL3 disrupts differentiation of deep layer neurons

The P0.5 pseudotime differentiation trajectory of *Asxl3*$^{+/+}$ and *Asxl3*$^{fs/fs}$ cortical neuron subtypes was assessed as described for embryonic timepoints. The fundamental steps of cortical neuron differentiation are captured in this analysis, with undifferentiated IPs preceding Migrating neurons and terminally differentiated classes of excitatory neurons (Fig. 3.6A, B). The developmental relationship between cortical neuron subtypes along the pseudotime axis reflects the chronological acquisition of terminal fate. As such, early born L6 CThPN represent the most mature, or the terminus of differentiation and successive classes of later fated cortical neuron classes, SCPN, dCPN, uCPN, are correctly organized along the axis progressively closer to the immature cell types (Fig. 3.6C and Supplemental Fig. 3.9). This fidelity to the developmental process of corticogenesis allows differences in the individual genotypic trajectories to be identified. Most prominent among them are the differential *Asxl3*$^{fs/fs}$ amplitude peak increase between pseudotime position 25-35 and the corresponding reduced *Asxl3*$^{fs/fs}$ amplitude peak between differentiation position 15-25 (Fig. 3.6A).

Pseudotime trajectories for individual cortical neuronal subtypes were generated to identify the contribution of individual neuron classes to genotypic differences in differential peak dynamics of the combined data (Fig. 3.6C). The independent trajectories of terminally differentiated neuron subtypes do not follow a discrete tip-to-tail order along the pseudotime axis and instead exhibit overlapping distribution. The relative distribution along pseudotime is positively correlated to timing of terminal fate acquisition, with the uCPN L2-4 trajectory encompassing the largest portion of pseudotime (10-50), followed by dCPN (15-50) and SCPN (25-45), with CThPN L6 sharing the smallest portion of the pseudotime axis (30-45) (Fig. 3.6C). Several genotypic differences in uCPN, SCPN and dCPN classes of neurons contribute to the *Asxl3*$^{fs/fs}$ amplitude increase between 25-35. For *Asxl3*$^{fs/fs}$ uCPN within this pseudotime interval, we find a differential increase in peak amplitude compared to control. While in the SCPN and dCPN individual trajectories, novel asynchronous *Asxl3*$^{fs/fs}$ peaks were detected between the pseudotime 25-35 interval, that do not correspond to smaller *Asxl3*$^{+/+}$ peaks of the same periodicity across pseudotime (Fig. 3.6C). The unique P0.5 *Asxl3*$^{fs/fs}$ dCPN and SCPN peaks corresponds to the shift in E14.5 peak periodicity across pseudotime differentiation, further implicating delayed differentiation and altered mature excitatory neuron composition in *Asxl3*$^{fs/fs}$ cortex.

To characterize the transcriptional differences underling these altered fate trajectories, the DeCoN corticogenesis transcriptomic resource was used to compile modules of proneural genes which inform CThPN, SCPN and CPN fate acquisition (Table S2) [48]. Differential module expression was assessed for all clusters combined, as well as clusters that broadly comprise deep layer neurons (CThPN; P0-6, SCPN; P0-9 & dCPN; P0-2, P0-7) and upper layer uCPN (P0-0, P0-3, P0-4, P0-5, P0-8) clusters (Fig. 3.6D). SCPN module expression was significantly increased in *Asxl3*$^{fs/fs}$ samples for each cluster class evaluated (adjusted *p*=0.009 comprehensive clusters; *p*=0.030 deep layer clusters; *p*=0.048 uCPN clusters, linear mixed models). Expression of the CThPN module was increased in all clusters (adjusted *p*=0.002) and deep layer clusters (adjusted *p*=0.028) (Fig. 3.6D), while the CPN module was not significantly differentially regulated in any of the cluster groups.

We identified the differentially expressed genes for clusters P0-9, P0-7 and P0-2, to explore the *Asxl3*$^{fs/fs}$ transcriptomic changes that drive asynchronous SCPN (cluster P0-9) and dCPN (cluster P0-7 & cluster P0-2) peaks in individual neuronal subtype trajectories. DEGs associated with asynchronous SCPN and dCPN pseudotime differentiation included *Bhlhe22, Stmn2, Fezf2, Ldb2, Tshz2, Crym*, and *Cbln2* for SCPN and *Plxnd1, Robo2, Ptn, Runx1t1, Ssbp2, Shisa6, Nr2f2, Nr4A2, Myt1l* for dCPN (Fig. 3.6E-G). Dysregulation of these genes which drive identity and specification of excitatory lineages, implicates that transcriptomics were impacted by delayed timing of cortical neuron differentiation during *Asxl3*$^{fs/fs}$ corticogenesis.

ASD genes differentially expressed in Asxl3*$^{fs/fs}$ *cortex

Large scale human genetic studies have identified hundreds of ASD risk genes, *de novo* mono-allelic frameshift variants in *ASXL3* among them [10-12]. Differential expression of other candidate ASD risk genes has repeatedly been observed in transcriptomic studies of human and mouse ASD neuropathology [32, 49-54]. To identify ASD biology implicated by and shared with biallelic *Asxl3*$^{fs/fs}$ molecular pathology, we identified ASD genes differentially expressed in *Asxl3*$^{fs/fs}$ transcriptomics. E13.5, E14.5, and P0.5 cluster specific DEGs were intersected with the SFARI ASD gene set, and further partitioned based on high-confidence classification (hcASD) (Fig. 3.7) [10]. Greater than 12% of all DEGs at each time point were ASD risk genes, which were found to be up- and down-regulated, in a developmental and cell-type defined manner (Fig. 3.7A-C). At E13.5 *Asxl3*$^{fs/fs}$ DEGs are predominantly down-regulated, while at E14.5 and P0.5 differential expression is more equally up- and down-regulated. This is consistent with ASXL3-dependent role in ASD gene expression and provides further evidence for convergence of ASD risk genes on a common molecular mechanism.

Genes that encode proteins involved in chromatin regulation, transcriptional regulation and synaptic signaling have been identified as the genetic basis of ASD [12, 55]. With little evidence of functional overlap between ASD genes, a common molecular pathway is not clear. To investigate functional overlap between DEGs, GO analysis of ASD DEGs at individual developmental time points was performed. Top GO terms identified at E13.5 highlight the function of ASD chromatin and transcriptional regulator genes early in development (Fig. 3.7D). At E14.5

GO terms reflective of synaptic function and chromatin biology are enriched (Fig. 3.7D). By P0.5, GO terms associated with synaptic function are significantly enriched. These results implicate molecular synergy during development where chromatin genes are required for early stages of corticogenesis, that ultimately determine synaptic functions at later stages (Fig. 3.7D). Future experiments will be required to determine if chromatin genes such as *Asxl3* impact synaptic function by directly modulating synaptic genes or indirectly by initiating defects in corticogenesis that disrupt synaptic formation and function. Understanding the convergence of ASD risk genes could provide opportunities to develop targeted therapeutic approaches.

DISCUSSION

Polycomb transcriptional regulation is critical for organ development and cell fate specification. Evaluation of an *Asxl3* mouse model revealed a critical role in cortical development. The emerging pathogenic model based on analysis of multiple cell types, at sequential developmental timepoints, implicates overactivation of Notch signaling that alters NPCs proliferation and timing of differentiation. These early developmental defects lead to altered composition of excitatory neurons with aberrant expression of proneural genes responsible for layer specificity at later timepoints. Across cortical development, dysregulated genes were enriched for high confidence ASD risk genes, implicating a convergent pathological mechanism. Together our findings underscore the importance of ASXL3 in Polycomb transcriptional repression during development and provide insight into developmental mechanisms altered by ASD risk genes.

Polycomb transcriptional repression required for corticogenesis

The role of H2AUb1 in Polycomb transcriptional repression remains poorly understood compared to other histone modifications. Pathogenic variants in genes which encode individual components of both PRC1 and PR-DUB are the genetic basis for a growing number of neurodevelopmental disorders, highlighting the importance for dynamic exchange of H2A ubiquitination in neural development [18, 56, 57]. An ASXL3-dependent developmental and transcriptomic disruption of excitatory neuron lineage differentiation and fate was identified in the *Asxl3* frameshift mouse model, with IHC revealing a 25% reduction of BCL11B L5 neurons (Fig. 3.1). This stands in contrast to a 30% increase in BCL11B cells described in the cortex after conditional knockout of *Ring1b*, the enzymatic component of PRC1 [15]. The opposing lamination defects of these two mouse models mirrors the antagonistic activity of PRC1 and PR-DUB, further implicating a role for dynamic H2AUb1 regulation in NPC fate specification. Future studies need to determine targets of PR-DUB complexes that allow for dynamic transcriptional control of proneural genes.

Extrinsic signaling pathways coordinate balance of self-renewal & differentiation

During corticogenesis NPCs undergo symmetric self-renewing and asymmetric neurogenic mitotic events. Extrinsic signaling pathways, including Notch, Wnt, and Hippo, are important for directing the self-renewal and differentiation behavior of NPCs. Overactivation of Notch or Wnt signaling or inactivation of Hippo signaling during neurogenesis shift NPCs toward self-renewal and away from neurogenic proliferation [37, 39, 41, 42]. A commonly observed phenotype in these mouse models is lateral expansion of RGCs and increased VZ perimeter, without a corresponding change in brain size or cortical thickness, similar to the phenotypes observed in *Asxl3*$^{fs/fs}$ brain development [37, 39, 41, 42]. Notably, the extent of lateral expansion was shown to be dose-dependent implicating a critical role for ASXL3 dependent transcriptional regulation of extrinsic signaling pathways as *Asxl3*$^{fs/fs}$ transcriptomic changes implicated their dysregulation at an early stage of neurogenesis [37, 41, 58].

The N1ICD directly regulates expression of WNT and Hippo signaling pathways components, allowing Notch to facilitate pathway crosstalk in NPCs [37]. Consistent with altered Notch signaling, *Hes1* and *Hes5* are up-regulated in *Asxl3*$^{fs/fs}$ mice. These transcription factors are at the nexus of the Notch signaling pathway during corticogenesis, required for inhibiting neuronal differentiation and promoting maintenance of NPC multipotency [59-62] Phenocopy between *Asxl3*$^{fs/fs}$ and the transgenic *Hes1*- and *Hes5*-overexpression mouse models, implicates a prominent role for Notch signaling through HES1/HES5 in *Asxl3*$^{fs/fs}$ neuropathology [38, 43]. In both models, *Hes1* or *Hes5* overexpression results in lateral expansion of VZ RGC progenitors and altered emergence of excitatory fated cortical neurons. HES1 and HES5 maintain NPCs multipotency by repressing *Ngn2*, which induces neurogenesis. Using the cell-type and temporal resolutions of Asxl3$^{fs/fs}$ transcriptomic data, the overexpression of HES1 and HES5 in *Asxl3*$^{fs/fs}$

RGCs at E13.5 was correlated to differential expression of proneural genes, including down-regulation of *Ngn2* in *Asxl3*$^{fs/fs}$ differentiating cell types at E14.5 [38, 43]. Ultimately, the developmental impact on corticogenesis can be summarized into a model where NPC self-renewal alters the length of neurogenesis through lateral inhibition which affects the fate of excitatory neuron and cytoarchitectural cortical layer deposition [38, 43].

Single-cell transcriptomic view of cortiocogenesis

Histology based analysis of corticogenesis has identified individual proneural genes critical for generation and differentiation of distinct cortical neuron subtypes [63-67]. Generating the complement of mature cortical neuron subtypes from multipotent NPCs requires cell-intrinsic and dynamic chromatin modifications that play important roles in defining transcriptional plasticity and cell identities. Distinguishing the transcriptomic diversity of individual cells in a developing organ requires single-cell resolution. The challenge moving forward is to correlate single-cell transcriptomic characterization of normal and pathogenic corticogenesis with decades of knowledge generated by investigating corticogenesis in single-gene mouse models using a limited selection of histological markers. This correlation is less complicated at earlier embryonic timepoints when cortical tissue is largely composed of RGCs and IPs expressing consistent marker genes that modulate minimally during corticogenesis. At later stages of corticogenesis, transcriptional programs of excitatory lineages diverge in the post-mitotic neurons as cortical neurons separate into increasingly partitioned cell populations.

Due to the relatively low heterogeneity of E13.5 and E14.5 cortical tissue, we observed high correlation between scRNA-seq data and tissue analysis with immunohistochemistry. While the ratio of progenitors detected with scRNA-seq decreased between E13.5 and E14.5, the progenitor marker genes were consistent between stages and were robustly distinguished from terminal neuronal subtypes. The conformity between these two techniques allowed us to predict the *Asxl3*$^{fs/fs}$ developmental mechanisms based on the transcriptomics. Subsequent evaluation of the cell-specific transcriptomics *in vivo* identified important molecular mechanisms of early *Asxl3*$^{fs/fs}$ neuropathology.

Greater diversity of terminally differentiated neuronal subtypes at P0.5 complicates correlating the scRNA-seq data with immunohistochemistry. Since we detect a reduction in BCL11B L5 neurons with immunohistochemistry, we predicted that our scRNA transcriptomic analysis would directly translate into a reduction of SCPN neurons. Instead, we observe a significant shift in the proportions of all neuronal subtypes in *Asxl3*$^{fs/fs}$, consistent with a transcriptional shift in cell lineage profiles that transform their terminal fate. This interpretation is supported by the divergent P0.5 *Asxl3*$^{+/+}$ and *Asxl3*$^{fs/fs}$ pseudotime differentiation peaks. The upregulation of CThPN and SCPN cell lineage profiles resembles transcriptional alterations attributed to Polycomb transcriptional regulation that result in fate transformations [16, 36]. In addition, the dCPN and SCPN DEGs we detect for individual trajectories include proneural genes known to govern the acquisition of cell identity. These data are consistent with cortical neuron fate changes in *Asxl3*$^{fs/fs}$ samples that acquire a hybrid transcriptional profile, which may allow these cells to associate with clusters across the SPCN, dCPN and uCPN classes. The broad distribution of dCPN and uCPN classes of neurons mapped to a spatial reconstruction of the visual cortex may reflect the current nuances in the annotation of cortical classes of cells by transcriptional profile, as opposed to detection of protein expression with immunohistochemistry. In summary, a reduction in BCL11B L5 neurons is detected by IHC in *Asxl3*$^{fs/fs}$ cortex, without a change in L5 cell density. This suggests these cells are replaced by another neuron type or an undefined hybrid fate that may reflect overlapping expression of CThPN and SCPN proneural genes based on transcriptomic data.

Molecular synergy of ASD neuropathology

Our data linking early defects in *Asxl3*$^{fs/fs}$ cortical neurogenesis to altered timing of cortical neuron subtypes is pertinent in the context of human ASD genetics and *in vitro* models that predicted pathogenic mechanisms that impinge on neurogenesis [54, 68-74]. Recently, neural fated tissue differentiated from human pluripotent stem cells (hPSCs) carrying pathogenic variants in hcASD genes were tested for neurogenesis competency. Consistent with the *Asxl3*$^{fs/fs}$ neuropathology, the cellular progeny of *ASXL3* hPSC lines fell into a subclass of ASD risk genes that are hyporesponsive to WNT and exhibit decreased neuronal output with an enrichment for NPCs [68]. In the same phenotypic class of ASD risk genes were the chromatin associated genes *ASH1L*, *KDM5B*, *CHD2* and *KMT2C* that have a documented role in impacting Polycomb transcriptional regulation and implicate novel molecular mechanisms of ASD yet to be explored in animal models. Conversely, neurogenesis defects which result in increased neurogenesis at the expense of SOX2 progenitors were observed in *Bcl6* gain-of-function mouse model that were in part due to dysregulation of extrinsic signaling pathways. BCL6, a transcriptional repressor that interacts with the PRC1.1 component, BCOR, that modulates H2AUb1 [75]. Together these findings demonstrate that dynamic Polycomb transcriptional repression is essential for balancing progenitor expansion and differentiation of NPC.

ASD neuropathology is attributed to mid-gestation neurogenesis defects in the prefrontal cortex and excitatory/inhibitory (E/I) imbalance of the cortical microcircuit [76-78]. *Asxl3*$^{fs/fs}$ neuropathology provides evidence for how pathogenic variants in chromatin genes which disrupt development could damage synaptic function and the balance of cortical microcircuit activity. Such imbalance could be initiated due to a change in the composition of mature cortical subtypes. The shift in the focus of GO terms from chromatin and transcriptional regulation at E13.5 to greater enrichment in synaptic function terms at P0.5 support this interpretation. Precluding direct differential expression of synaptic genes by chromatin based genetic etiologies of ASD, *in vivo* studies have demonstrated that even subtle developmental alterations in circuit composition can result in disproportionally large functional effects on the mature circuit [79-81].

METHODS

Animals

All experiments were performed in accordance with animal protocols approved by the Unit for Laboratory Animal Medicine (ULAM), University of Michigan. The *Asxl3*^{fs} mice line was generated by cloning sgRNAs that target a region in exon 12 into a pX330 vector. The vectors were microinjected into fertilized eggs before being transferred into pseudopregnant C57BL/6 X DBA/2 F1 females. Topo cloning and sanger sequencing were used to detect a unique frameshift *Asxl3* allele. *Asxl3*$^{+/fs}$ mice were maintained on a C57BL/6 background. Heterozygous breeding was used for experiments with E0.5 established as the day of vaginal plug.

Western Blot Analysis

Whole brains from E13 *Asxl3*$^{+/+}$ and *Asxl3*$^{fs/fs}$ mice were homogenized in RIPA buffer supplemented with protease inhibitor cocktail and phosphatase inhibitor cocktail 3 obtained from Sigma-Aldrich (P8340 and P0044; St Louis, MO, USA). Protein levels were normalized after BCA analysis (Pierce). Cell lysates were separated using electrophoresis on 4-20% SDS-polyacrylamide gels and transferred to PVDF membrane (Millipore, Billerica, MA, USA). For western blot, after the transfer, the PVDF membrane was blocked with 5% milk and incubated with following antibodies overnight. Primary antibodies used were: anti-ASXL3 (Bielas Lab, 1:200), anti-ubiquityl-Histone H2A (Cell Signaling Technology, 8240, 1:2000), anti-Histone H3 (Abcam, Ab10543, 1:5000). Donkey anti-rabbit HRP-conjugated (Cytiva, NA9340V, 1:5000) and goat anti-mouse HRP-conjugated (Invitrogen, 32430, 1:10000) were used for 1h incubation at room temperature. Antibody incubation and chemiluminescence detection were performed according to manufacturer’s instruction [ThermoFisher Scientific, Waltham, MA, USA, cat no. 34095].

Immunohistochemistry and cell counting

Brains were dissected and removed from mice at E13.5, E14.5, or P0.5 and then kept in 4% PFA at 4°C overnight. Brains were cryopreserved by submersion in 20% then 30% sucrose solutions. After embedding in OCT cryosectioning media (Tissue-Tek, Torrance, CA), brains were cryosectioned at 13 μm. Sections were incubated with PBS for 15 min to wash away OCT. For antibodies that required antigen retrieval, cryosections were heated in 10 mM Sodium citrate for 20 minutes at 95°C followed by incubation at room temperature for 20 minutes. Incubation with a normal donkey serum blocking buffer [5% NDS (Jackson ImmunoResearch), 0.1% Triton X-100, 5% BSA]. was performed for 1 hour. Sections were stained with primary antibodies in blocking buffer at 4℃ overnight, washed with PBS, and stained with secondary antibodies at room temperature for 1 hour. Slides were washed with PBS, incubated with DAPI for 5 minutes and cover-slipped with MOWIOL. Images were acquired with a Nikon A1 microscope and processed with LAS X software. Cells were counted using ImageJ. The following antibodies and dilutions were used: SOX2 (Neuromics, GT15098, 1:500), CTIP2 (Abcam, ab18465, 1:500), TBR1 (Abcam, ab31940, 1:200), SATB2 (Abcam, ab51502, 1:100), CUX1 (Santa Cruz, sc-13024, 1:150), pH3 (Abcam, ab10543, 1:250), EOMES (Abcam, ab23345, 1:400). AlexaFluor-conjugated secondaries were: donkey anti-rabbit 647 (Invitrogen, A31573, 1:400), anti-rabbit 555 (Invitrogen, A31572, 1:400), donkey anti-mouse 555 (Invitrogen, A31570, 1:400), donkey anti-mouse 647 (Invitrogen, A31571, 1:400), donkey anti-goat 555 (Abcam, ab150154, 1:400), donkey anti-goat 488 (Invitrogen, A-11055, 1:400).

EdU Birthdate analysis

Time pregnant dames were injected with EdU (20 mg/kg) at embryonic day 13.5 or 14.5 (E13.5 or E14.5). At P0.5, brains were dissected and removed from EdU injected pups and kept in 4% PFA at 4℃ overnight. EdU was labeled and detected in Cryosections with the Click-IT EdU imaging kit (Invitrogen, Carlsbad, CA) according to the manufacturer’s instructions. After sections were incubated with Click-IT reaction cocktail, they were washed with normal donkey serum blocking buffer. Then, additional antibody staining was performed.

Cresyl Violet

Brains were dissected and removed from mice at P0.5 then kept in 4% PFA overnight. Brains were dehydrated in a series of ethanol washes and embedded in paraffin with a paraffin tissue processor. 6 µm microtome sections were dewaxed in xylene, rehydrated in ethanol, stained with 0.5% cresyl violet, dehydrated with ethanol and cleared with xylene.

Collection of cells for single-cell RNA sequencing

The cerebral cortices from E13.5, E14.5 or P0.5 brains were dissected in Earl's balanced salt solution (EBSS). Isolated cortices were incubated with papain (Worthington Biochemical Corporation), 5.5mM L-cysteine-HCL, 1.1 mM EDTA, and 100 mg/ml DNase I in O_2:CO_2 equilibrated EBSS for 8 minutes at 37℃. Samples were titrated with flame tipped glass pipettes and centrifuged at 800 RCF for 5 minutes. Cells were resuspended with ovomucoid protease inhibitor (Worthington Biochemical Corporation) and 50 mg/ml DNase I in O_2:CO_2 equilibrated EBSS and passed through a 70 micron cell strainer. Cells were centrifuged at 200 RCF for 5 minutes over a gradient of ovomucoid protease inhibitor and cells were resuspended in N2/B27 media. Cells were counted and checked for viability using a Luna automated cell counter before loading onto a Seq-Well platform.

Seq-Well Single Cell RNA-sequencing

Seq-Well was performed as described [31, 82]. Briefly, functionalized Seq-Well arrays, containing 90,000 picowells, were loaded with barcoded beads (ChemeGenes, Wilmington, MA). 20,000 cells were loaded onto the arrays and incubated for 15 minutes. To remove residual BSA and excess cells, arrays were washed with PBS. Functionalized membranes were applied to the top of arrays, sealed in an Agilent clamp, and incubated at 37 for 45 minutes. Sealed arrays were incubated in a lysis buffer (5M guanidine thiocynate, 1mM EDTA, 0.5% sarkosyl, 1% BME) for 20 minutes followed by a 45 minute incubation with hybridization buffer (2M NaCl, 1X PBS, 8% PEG8000). Beads were removed from arrays by centrifuging at 2000xg for 5 minutes in wash buffer (2M NaCl, 3mM $MgCl_2$, 20mM Tris-HCl pH 8.0, 8% PEG8000). To perform reverse transcription beads were incubated with the Maxima Reverse Transcriptase (Thermo Scientific) for 30 minutes at room temperature followed by overnight incubation at 52℃. Reactions were treated with Exonuclease 1 (New England Biolabs, M0293S) for 45 minutes at 37℃. Whole transcriptome amplification was performed using the 2X KAPA Hifi Hotstart Readymix (KAPA Biosystems, KK-2602). Beads were split to 1,500-2,000 per reaction and run under the following conditions 4 Cycles (98℃, 20s; 65℃, 45s; 72℃, 3m) 12 Cycles (98℃, 20s; 67℃, 20s; 72℃, 3m) final extension (72℃, 3m, 4℃, hold). Products were purified with Ampure SPRI beads (Beckman Coulter, A63881) at a 0.6X volumetric ratio then a 1.0X volumetric ratio. Libraries were prepared using the Nextera XT kit (illumina) and libraries were sequenced on an Illumina NextSeq 75 cycle instrument.

scRNA-seq data processing

Sequencing reads were processed into a digital gene expression matrix using Drop-seq software as described [83]. FASTQ files were converted into bam files before being tagged with cell and molecular barcodes and trimmed. After converting back to FASTQs, reads were aligned to mm10 with STAR. BAM files are then sorted, merged, and tagged with gene exons. Bead synthesis errors were corrected as described and digital gene expression matrices were generated. We excluded the poor-quality cells in the gene-cell data matrix using the Seurat package (v3.1.2) for the samples (E13.5: n=8, E14.5: n=9 and P0.5: n=9). For downstream analysis cells with fewer than 300 detectable genes, greater than 5,000 genes or greater than 10% mitochondrial genes were removed. Genes that were detected in less than 5 cells were removed. To remove blood cells from our data we visualized the raw count of hemoglobin genes (*Hbb-bh1*, *Hba-a2*, *Alas2*, *Hbb-y*, *Hbb-bs*, *Fam46c*, *Hbb-bt*, *Hba-a1*, *Hmbs*, *Fech*, *Slc25a37*) using violin plots to set a threshold for filtering blood cells. We excluded the cells that expressed more than these predetermined thresholds for further analysis. We normalized the data in each sample for each cell by dividing the total counts for that cell and multiplied by 10,000. This is then natural-log transformed using log10(p). After this normalization step, we selected genes showing a dispersion (variance/mean expression) larger than two standard deviations away from the expected dispersion as variable genes using the Seurat (v3.1.2) function “FindVariableGenes” for each sample. In this way, there are 2000 significant genes which were identified using variance stabilizing transformation for each sample in different stages. We then used these most informative genes for sample alignment for each stage. We integrated all the samples in each stage by using the FindIntegrationAnchors and IntegrateData functions of Seurat (v3.1.2). We performed this alignment as described and implemented in Seurat tutorial (v3.1.2). After we integrated the datasets for each stage, we scaled and centered the data for each stage.

Dimensionality reduction, cisualization and clustering

We used the Seurat package (v3.1.2) to perform dimensionality reduction. We used the integrated and normalized data as the input to the RunPCA function of Seurat (v3.1.2) in order to compute the first 100 PCs. After that, we used the elbow algorithm to find the optimal number of PCs to construct Uniform Manifold Approximation and Projection (UMAP) plots. Visualizations in a two-dimensional space were done using RunUMAP and RunTSNE function of Seurat (v3.1.2) for the integrated data using previous dimensional reduction data and predetermined best PC number. We performed a graph-based clustering approach using FindNeighbors and FindClusters functions of Seurat (v3.1.2). We clustered the cells based on modularity optimization technique: Louvain algorithm with resolution parameter 0.5 and partitioned the graph constructed before into communities. We then collected cluster marker genes using the Wilcoxon rank-sum test between the cells in a single cluster and all other cells with log fold change threshold of 0.2. To assign identities to clusters, we cross-referenced the marker genes with previously described cortical cells [29, 30, 47]. The expression of cell type markers was visualized using the FeaturePlot function in Seurat. After we determined the identity of excitatory and non-excitatory cortical cells, we extracted the cell types that contribute to the excitatory cells and redid the clustering for this subset.

Alignment with Loo et al. 2019

We mapped our dataset to the Loo et al. 2019 [29] E14.5 and P0 cortices using label transferring features from Seurat (v3.1.2). We leveraged the cell type labels provided by Loo et al. 2019 as the reference and projected our cells onto the reference using FindTransferAnchors and TransferData function from Seurat. We obtained the classification scores which depicts the level of cell type prediction for the query cells and assigned the reference labels to the query cells based on the highest prediction score. For our excitatory neuron lineage analysis, we filtered out cells that do not contribute to this lineage after we projected the reference labels on our dataset. P0 filtered cells included: Astrocytes (10-P, 13-P), Choroid Plexus (20-P), Endothelial (17-P, 21-P), Ganglionic Eminence (9-P), Interneurons (5-P,14-P, 11-P, 6-P), Layer 1 (19-P), Microglia (22-P), Oligodendrocytes (16-P), Striatal neurons (3-P, 7-P). E14.5 filtered cells included: Choroid Plexus (22-E), Endothelial (18-E), Ganglionic Eminence (6-E), Interneurons (1-E, 12-E), Microglia (20-E), Cortical Hem RGC (21-E), Striatal neurons (16-E, 9-E), Thalamic (19-E). We visualized the query transferred labels on the UMAP plots using DimPlot function from Seurat.

Differential expression analysis and enrichment analysis

We used the Wilcoxon rank-sum test to conduct the DE analysis between *Asxl3*$^{+/+}$ and *Asxl3*$^{fs/fs}$ samples for each stage in the alignment data. To investigate the overlap of ASD risk genes with DEGs within individual clusters, we overlapped the combined list of DEGs at each timepoint with genes listed in the SFARI database (https://gene.sfari.org/, 02-11-2020 release). We combined all the significant genes from the DE analysis between *Asxl3*$^{+/+}$ and *Asxl3*$^{fs/fs}$ samples for each stage in the alignment data across different clusters. We used the 'EnhancedVolcano' R package to visualize ASD associated DEGs with a log fold change greater than 0.05 and p-value less than 10e^{-5}. To investigate the overlap of Notch target genes, we evaluated the enrichment of direct and indirect N1ICD targets identified by Li et al. 2012 [37] by conducting a Fisher's exact test on the 2x2 enrichment table (DAVID). We utilized the cluster specific DE gene list and compared it to the direct and indirect N1ICD gene lists to collect the 2x2 enrichment table which was then evaluated by the two-sided Fisher exact test. We used the p-value collected from Fisher exact test and the number of genes that are contained in the gene list in each cluster to visualize the enrichment results on each cluster across different stages.

Functional enrichment analysis

We used lists of significant genes from differential expression analysis across genotypes to identify enriched biological pathways using the Database for Annotation, Visualization and Integrated Discovery (DAVID) v6.8, an online program uses a modified Fisher's exact test (EASE score) to examine the significance of gene-term enrichment. Gene names were first mapped into Entrez ID through genome wide annotation for mouse by R package 'org.Mm.eg.db'. KEGG pathway, UniProt keywords and Gene Ontology (GO) were chosen for three different options of annotation categories. Terms were filtered using a threshold of Bonferroni corrected p-value smaller than 0.05. GO terms including molecular function, cellular component and biological process were also used for DAVID functional annotation clustering, with default classification stringency.

Module score

To investigate the differential expression pattern of cortical neuron subtype modules, we used the gene list from Molyneaux et al. 2015 and utilized the 'AddModuleScore' function using the Seurat package (v3.1.2). For CThPN we used genes in cluster 6 and 9, for SCPN we used genes in cluster 16, and for CPN we used genes in cluster 0, 5, and 15. For each module, the average gene expression level was calculated and was compared to the control genes for each cell. Moreover, we used a linear mixed-effect model to evaluate the module expression differences between *Asxl3*$^{+/+}$ and *Asxl3*$^{fs/fs}$. Specifically, we treated the module scores as the output for each cell, genotype as the predictor variable with the sample identity being the random intercept to account for the batch effect. We applied the ANOVA test to calculate the p-values which are then adjusted across modules using the Benjamini-Hochberg correction.

Spatial Distribution

To learn the spatial structure of P0 data, we used Tangram [45] and aligned our data with STARMap dataset [46] (1127 cells and 166 genes). We manually assigned the spatial clusters to the cells based on the neuronal layer specific genes and used the ‘shiny’ package to label the cells. We then extracted the common genes among our data and the STARMap data and obtained the cell-by-coordinates structure matrix where it gives the probability for cell to be in coordinates. The matrix was then multiplied by the one hot encoding matrix of cell types in our data, and we visualized the mapping results using the ‘ggplot2’ package.

Pseudotime analysis

For neuronal cells identified using two levels of clustering in each stage, we used Monocle 3 to conduct single-cell pseudotime analysis [84]. First, we performed principal components analysis on gene expression data to capture the variation and removed batch effects using mutual nearest neighbor alignment. UMAP was then used for dimensionality reduction and visualization, setting the number of neighbors to 50. We then created a curvilinear trajectory using the function ‘learn graph’ and ordered the cells with progenitors (in E13.5 and E14.5) or intermediate progenitors (in P0) constrained as starting points. The 2-D visualization of trajectory was conducted using default function ‘plot cell’ in Monocle 3 and the comparison of pseudotime information between genotypes was shown using density plot and histogram by ggplot2.

REFERENCES

1. Greig, L.C., et al., *Molecular logic of neocortical projection neuron specification, development and diversity.* Nat Rev Neurosci, 2013. **14**(11): p. 755-69.
2. Desai, A.R. and S.K. McConnell, *Progressive restriction in fate potential by neural progenitors during cerebral cortical development.* Development, 2000. **127**(13): p. 2863-72.
3. McConnell, S.K., *Constructing the cerebral cortex: neurogenesis and fate determination.* Neuron, 1995. **15**(4): p. 761-8.
4. McConnell, S.K. and C.E. Kaznowski, *Cell cycle dependence of laminar determination in developing neocortex.* Science, 1991. **254**(5029): p. 282-5.
5. Leone, D.P., et al., *The determination of projection neuron identity in the developing cerebral cortex.* Curr Opin Neurobiol, 2008. **18**(1): p. 28-35.
6. Luskin, M.B., A.L. Pearlman, and J.R. Sanes, *Cell lineage in the cerebral cortex of the mouse studied in vivo and in vitro with a recombinant retrovirus.* Neuron, 1988. **1**(8): p. 635-47.
7. Shen, Q., et al., *The timing of cortical neurogenesis is encoded within lineages of individual progenitor cells.* Nat Neurosci, 2006. **9**(6): p. 743-51.
8. Walsh, C. and C.L. Cepko, *Clonally related cortical cells show several migration patterns.* Science, 1988. **241**(4871): p. 1342-5.
9. Hirabayashi, Y. and Y. Gotoh, *Epigenetic control of neural precursor cell fate during development.* Nat Rev Neurosci, 2010. **11**(6): p. 377-88.
10. Satterstrom, F.K., et al., *Large-Scale Exome Sequencing Study Implicates Both Developmental and Functional Changes in the Neurobiology of Autism.* Cell, 2020. **180**(3): p. 568-584 e23.
11. De Rubeis, S., et al., *Synaptic, transcriptional and chromatin genes disrupted in autism.* Nature, 2014. **515**(7526): p. 209-15.
12. Iossifov, I., et al., *The contribution of de novo coding mutations to autism spectrum disorder.* Nature, 2014. **515**(7526): p. 216-21.
13. Schuettengruber, B., et al., *Genome Regulation by Polycomb and Trithorax: 70 Years and Counting.* Cell, 2017. **171**(1): p. 34-57.
14. Barbour, H., et al., *Polycomb group-mediated histone H2A monoubiquitination in epigenome regulation and nuclear processes.* Nat Commun, 2020. **11**(1): p. 5947.
15. Morimoto-Suzki, N., et al., *The polycomb component Ring1B regulates the timed termination of subcerebral projection neuron production during mouse neocortical development.* Development, 2014. **141**(22): p. 4343-53.
16. Pereira, J.D., et al., *Ezh2, the histone methyltransferase of PRC2, regulates the balance between self-renewal and differentiation in the cerebral cortex.* Proc Natl Acad Sci U S A, 2010. **107**(36): p. 15957-62.
17. Srivastava, A., et al., *De novo dominant ASXL3 mutations alter H2A deubiquitination and transcription in Bainbridge-Ropers syndrome.* Hum Mol Genet, 2016. **25**(3): p. 597-608.
18. Srivastava, A., B. McGrath, and S.L. Bielas, *Histone H2A Monoubiquitination in Neurodevelopmental Disorders.* Trends Genet, 2017. **33**(8): p. 566-578.
19. Bainbridge, M.N., et al., *De novo truncating mutations in ASXL3 are associated with a novel clinical phenotype with similarities to Bohring-Opitz syndrome.* Genome Med, 2013. **5**(2): p. 11.
20. Hoischen, A., et al., *De novo nonsense mutations in ASXL1 cause Bohring-Opitz syndrome.* Nat Genet, 2011. **43**(8): p. 729-31.
21. Shashi, V., et al., *De Novo Truncating Variants in ASXL2 Are Associated with a Unique and Recognizable Clinical Phenotype.* Am J Hum Genet, 2017. **100**(1): p. 179.

22. Hansen, D.V., et al., *Neurogenic radial glia in the outer subventricular zone of human neocortex.* Nature, 2010. **464**(7288): p. 554-561.
23. Silbereis, J.C., et al., *The Cellular and Molecular Landscapes of the Developing Human Central Nervous System.* Neuron, 2016. **89**(2): p. 248-68.
24. La Manno, G., et al., *Molecular architecture of the developing mouse brain.* bioRxiv, 2020: p. 2020.07.02.184051.
25. McGrath, B., et al., *Aberrant extracellular matrix and cardiac development in models lacking the PR-DUB component ASXL3.* Submitted, 2021.
26. Turgeon, B. and S. Meloche, *Interpreting neonatal lethal phenotypes in mouse mutants: insights into gene function and human diseases.* Physiol Rev, 2009. **89**(1): p. 1-26.
27. Tsuboi, M., Y. Hirabayashi, and Y. Gotoh, *Diverse gene regulatory mechanisms mediated by Polycomb group proteins during neural development.* Curr Opin Neurobiol, 2019. **59**: p. 164-173.
28. Stuart, T., et al., *Comprehensive Integration of Single-Cell Data.* Cell, 2019. **177**(7): p. 1888-1902 e21.
29. Loo, L., et al., *Single-cell transcriptomic analysis of mouse neocortical development.* Nat Commun, 2019. **10**(1): p. 134.
30. Polioudakis, D., et al., *A Single-Cell Transcriptomic Atlas of Human Neocortical Development during Mid-gestation.* Neuron, 2019. **103**(5): p. 785-801 e8.
31. Hughes, T.K., et al., *Second-Strand Synthesis-Based Massively Parallel scRNA-Seq Reveals Cellular States and Molecular Features of Human Inflammatory Skin Pathologies.* Immunity, 2020. **53**(4): p. 878-894 e7.
32. Velmeshev, D., et al., *Single-cell genomics identifies cell type-specific molecular changes in autism.* Science, 2019. **364**(6441): p. 685-689.
33. Zahr, S.K., et al., *A Translational Repression Complex in Developing Mammalian Neural Stem Cells that Regulates Neuronal Specification.* Neuron, 2018. **97**(3): p. 520-537 e6.
34. Zhong, S., et al., *A single-cell RNA-seq survey of the developmental landscape of the human prefrontal cortex.* Nature, 2018. **555**(7697): p. 524-528.
35. Yuzwa, S.A., et al., *Developmental Emergence of Adult Neural Stem Cells as Revealed by Single-Cell Transcriptional Profiling.* Cell Rep, 2017. **21**(13): p. 3970-3986.
36. Telley, L., et al., *Temporal patterning of apical progenitors and their daughter neurons in the developing neocortex.* Science, 2019. **364**(6440).
37. Li, Y., et al., *Genome-wide analysis of N1ICD/RBPJ targets in vivo reveals direct transcriptional regulation of Wnt, SHH, and hippo pathway effectors by Notch1.* Stem Cells, 2012. **30**(4): p. 741-52.
38. Bansod, S., R. Kageyama, and T. Ohtsuka, *Hes5 regulates the transition timing of neurogenesis and gliogenesis in mammalian neocortical development.* Development, 2017. **144**(17): p. 3156-3167.
39. Chenn, A. and C.A. Walsh, *Regulation of cerebral cortical size by control of cell cycle exit in neural precursors.* Science, 2002. **297**(5580): p. 365-9.
40. Cao, J., et al., *The single-cell transcriptional landscape of mammalian organogenesis.* Nature, 2019. **566**(7745): p. 496-502.
41. Kim, W.Y., et al., *GSK-3 is a master regulator of neural progenitor homeostasis.* Nat Neurosci, 2009. **12**(11): p. 1390-7.
42. Lavado, A., et al., *The Hippo Pathway Prevents YAP/TAZ-Driven Hypertranscription and Controls Neural Progenitor Number.* Dev Cell, 2018. **47**(5): p. 576-591 e8.
43. Ohtsuka, T. and R. Kageyama, *Hes1 overexpression leads to expansion of embryonic neural stem cell pool and stem cell reservoir in the postnatal brain.* Development, 2021. **148**(4).
44. Cadwell, C.R., et al., *Development and Arealization of the Cerebral Cortex.* Neuron, 2019. **103**(6): p. 980-1004.

45. Biancalani, T., et al., *Deep learning and alignment of spatially-resolved whole transcriptomes of single cells in the mouse brain with Tangram.* bioRxiv, 2020: p. 2020.08.29.272831.
46. Wang, X., et al., *Three-dimensional intact-tissue sequencing of single-cell transcriptional states.* Science, 2018. **361**(6400).
47. Di Bella, D.J., et al., *Molecular Logic of Cellular Diversification in the Mammalian Cerebral Cortex.* bioRxiv, 2020: p. 2020.07.02.185439.
48. Molyneaux, B.J., et al., *DeCoN: genome-wide analysis of in vivo transcriptional dynamics during pyramidal neuron fate selection in neocortex.* Neuron, 2015. **85**(2): p. 275-288.
49. Araujo, D.J., et al., *Foxp1 in Forebrain Pyramidal Neurons Controls Gene Expression Required for Spatial Learning and Synaptic Plasticity.* J Neurosci, 2017. **37**(45): p. 10917-10931.
50. Celen, C., et al., *Arid1b haploinsufficient mice reveal neuropsychiatric phenotypes and reversible causes of growth impairment.* Elife, 2017. **6**.
51. Gompers, A.L., et al., *Germline Chd8 haploinsufficiency alters brain development in mouse.* Nat Neurosci, 2017. **20**(8): p. 1062-1073.
52. Jin, X., et al., *In vivo Perturb-Seq reveals neuronal and glial abnormalities associated with autism risk genes.* Science, 2020. **370**(6520).
53. Duan, W., et al., *Integrated Transcriptome Analyses Revealed Key Target Genes in Mouse Models of Autism.* Autism Res, 2020. **13**(3): p. 352-368.
54. Durak, O., et al., *Chd8 mediates cortical neurogenesis via transcriptional regulation of cell cycle and Wnt signaling.* Nat Neurosci, 2016. **19**(11): p. 1477-1488.
55. Quesnel-Vallieres, M., et al., *Autism spectrum disorder: insights into convergent mechanisms from transcriptomics.* Nat Rev Genet, 2019. **20**(1): p. 51-63.
56. Pierce, S.B., et al., *De novo mutation in RING1 with epigenetic effects on neurodevelopment.* Proc Natl Acad Sci U S A, 2018. **115**(7): p. 1558-1563.
57. Turnpenny, P.D., et al., *Missense Mutations of the Pro65 Residue of PCGF2 Cause a Recognizable Syndrome Associated with Craniofacial, Neurological, Cardiovascular, and Skeletal Features.* Am J Hum Genet, 2018. **103**(5): p. 786-793.
58. Bonnefont, J., et al., *Cortical Neurogenesis Requires Bcl6-Mediated Transcriptional Repression of Multiple Self-Renewal-Promoting Extrinsic Pathways.* Neuron, 2019. **103**(6): p. 1096-1108 e4.
59. Ohtsuka, T., et al., *Roles of the basic helix-loop-helix genes Hes1 and Hes5 in expansion of neural stem cells of the developing brain.* J Biol Chem, 2001. **276**(32): p. 30467-74.
60. Ohtsuka, T., et al., *Hes1 and Hes5 as notch effectors in mammalian neuronal differentiation.* EMBO J, 1999. **18**(8): p. 2196-207.
61. Ishibashi, M., et al., *Targeted disruption of mammalian hairy and Enhancer of split homolog-1 (HES-1) leads to up-regulation of neural helix-loop-helix factors, premature neurogenesis, and severe neural tube defects.* Genes Dev, 1995. **9**(24): p. 3136-48.
62. Ishibashi, M., et al., *Persistent expression of helix-loop-helix factor HES-1 prevents mammalian neural differentiation in the central nervous system.* EMBO J, 1994. **13**(8): p. 1799-805.
63. Han, W., et al., *TBR1 directly represses Fezf2 to control the laminar origin and development of the corticospinal tract.* Proc Natl Acad Sci U S A, 2011. **108**(7): p. 3041-6.
64. McKenna, W.L., et al., *Tbr1 and Fezf2 regulate alternate corticofugal neuronal identities during neocortical development.* J Neurosci, 2011. **31**(2): p. 549-64.
65. Chen, B., et al., *The Fezf2-Ctip2 genetic pathway regulates the fate choice of subcortical projection neurons in the developing cerebral cortex.* Proc Natl Acad Sci U S A, 2008. **105**(32): p. 11382-7.

66. Bedogni, F., et al., *Tbr1 regulates regional and laminar identity of postmitotic neurons in developing neocortex.* Proc Natl Acad Sci U S A, 2010. **107**(29): p. 13129-34.
67. Alcamo, E.A., et al., *Satb2 regulates callosal projection neuron identity in the developing cerebral cortex.* Neuron, 2008. **57**(3): p. 364-77.
68. Cederquist, G.Y., et al., *A Multiplex Human Pluripotent Stem Cell Platform Defines Molecular and Functional Subclasses of Autism-Related Genes.* Cell Stem Cell, 2020. **27**(1): p. 35-49 e6.
69. Adhya, D., et al., *Atypical Neurogenesis in Induced Pluripotent Stem Cells From Autistic Individuals.* Biol Psychiatry, 2021. **89**(5): p. 486-496.
70. Lalli, M.A., et al., *High-throughput single-cell functional elucidation of neurodevelopmental disease-associated genes reveals convergent mechanisms altering neuronal differentiation.* Genome Res, 2020. **30**(9): p. 1317-1331.
71. Lennox, A.L., et al., *Pathogenic DDX3X Mutations Impair RNA Metabolism and Neurogenesis during Fetal Cortical Development.* Neuron, 2020. **106**(3): p. 404-420 e8.
72. Marchetto, M.C., et al., *Altered proliferation and networks in neural cells derived from idiopathic autistic individuals.* Mol Psychiatry, 2017. **22**(6): p. 820-835.
73. Mariani, J., et al., *FOXG1-Dependent Dysregulation of GABA/Glutamate Neuron Differentiation in Autism Spectrum Disorders.* Cell, 2015. **162**(2): p. 375-90.
74. Zhang, Y., et al., *Genetic evidence of gender difference in autism spectrum disorder supports the female-protective effect.* Transl Psychiatry, 2020. **10**(1): p. 4.
75. Gearhart, M.D., et al., *Polycomb group and SCF ubiquitin ligases are found in a novel BCOR complex that is recruited to BCL6 targets.* Mol Cell Biol, 2006. **26**(18): p. 6880-9.
76. Dani, V.S., et al., *Reduced cortical activity due to a shift in the balance between excitation and inhibition in a mouse model of Rett syndrome.* Proc Natl Acad Sci U S A, 2005. **102**(35): p. 12560-5.
77. Gogolla, N., et al., *Common circuit defect of excitatory-inhibitory balance in mouse models of autism.* J Neurodev Disord, 2009. **1**(2): p. 172-81.
78. Rubenstein, J.L. and M.M. Merzenich, *Model of autism: increased ratio of excitation/inhibition in key neural systems.* Genes Brain Behav, 2003. **2**(5): p. 255-67.
79. Bocchi, R., et al., *Perturbed Wnt signaling leads to neuronal migration delay, altered interhemispheric connections and impaired social behavior.* Nat Commun, 2017. **8**(1): p. 1158.
80. Lodato, S., et al., *Excitatory projection neuron subtypes control the distribution of local inhibitory interneurons in the cerebral cortex.* Neuron, 2011. **69**(4): p. 763-79.
81. Lodato, S., et al., *Loss of COUP-TFI alters the balance between caudal ganglionic eminence- and medial ganglionic eminence-derived cortical interneurons and results in resistance to epilepsy.* J Neurosci, 2011. **31**(12): p. 4650-62.
82. Aicher, T.P., et al., *Seq-Well: A Sample-Efficient, Portable Picowell Platform for Massively Parallel Single-Cell RNA Sequencing.* Methods Mol Biol, 2019. **1979**: p. 111-132.
83. Macosko, E.Z., et al., *Highly Parallel Genome-wide Expression Profiling of Individual Cells Using Nanoliter Droplets.* Cell, 2015. **161**(5): p. 1202-1214.
84. Trapnell, C., et al., *The dynamics and regulators of cell fate decisions are revealed by pseudotemporal ordering of single cells.* Nat Biotechnol, 2014. **32**(4): p. 381-386.

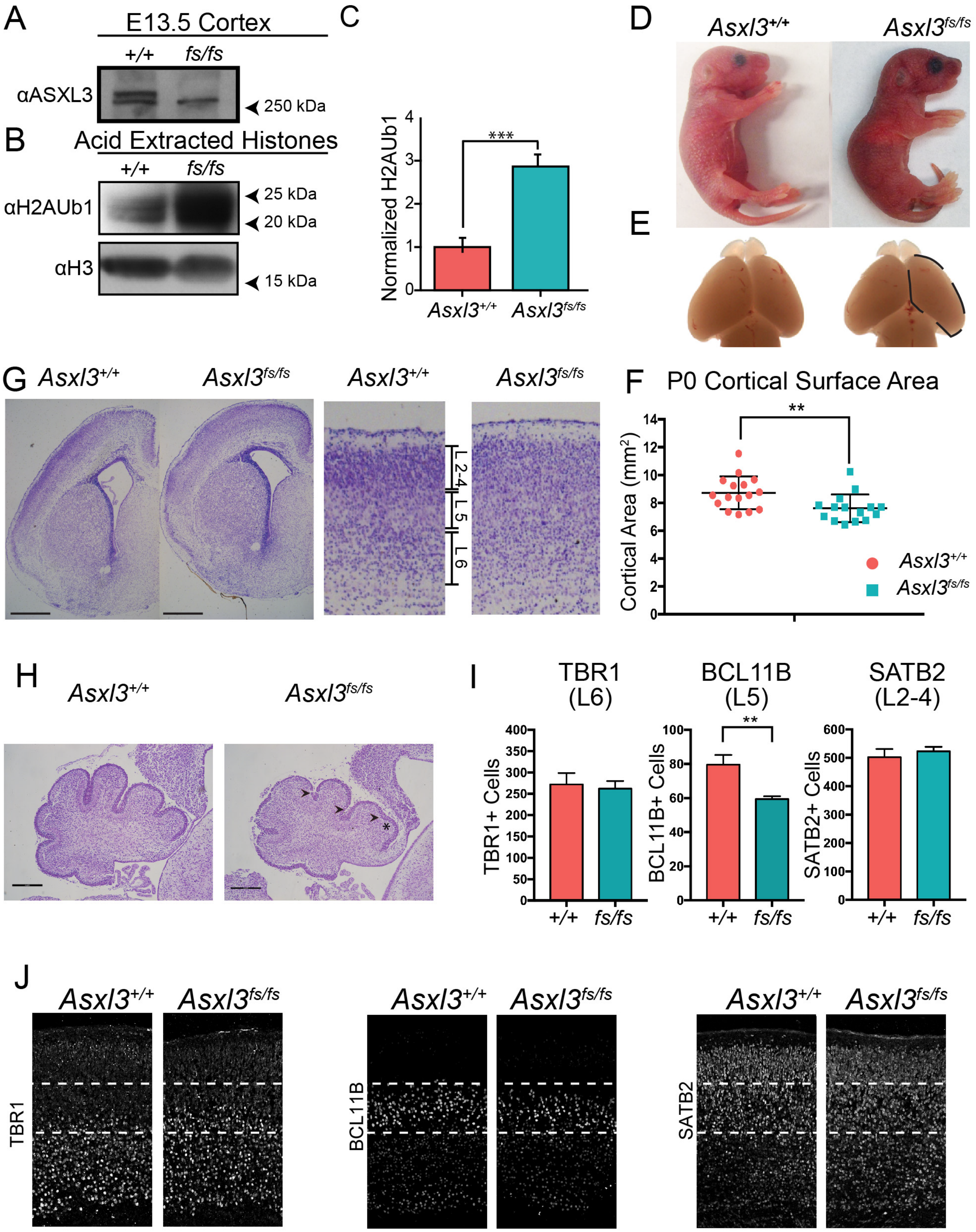
A
E13.5 Cortex
+/+
fs/fs
αASXL3
250 kDa
B
Acid Extracted Histones
+/+
fs/fs
αH2AUb1
25 kDa
20 kDa
αH3
15 kDa
C
Normalized H2AUb1
0
1
2
3
4
***
Asxl3+/+
Asxl3fs/fs
D
Asxl3+/+
Asxl3fs/fs
E
G
Asxl3+/+
Asxl3fs/fs
Asxl3+/+
Asxl3fs/fs
L 2-4
L 5
L 6
F
P0 Cortical Surface Area
Cortical Area (mm²)
0
2
4
6
8
10
12
14
**
Asxl3+/+
Asxl3fs/fs
H
Asxl3+/+
Asxl3fs/fs
*
I
TBR1 (L6)
TBR1+ Cells
0
50
100
150
200
250
300
350
400
+/+
fs/fs
BCL11B (L5)
BCL11B+ Cells
0
20
40
60
80
100
**
+/+
fs/fs
SATB2 (L2-4)
SATB2+ Cells
0
100
200
300
400
500
600
+/+
fs/fs
J
Asxl3+/+
Asxl3fs/fs
TBR1
Asxl3+/+
Asxl3fs/fs
BCL11B
Asxl3+/+
Asxl3fs/fs
SATB2

Fig. 3.1. Loss of *Asxl3* disrupts cerebral cortex and cerebellum morphology A, Lysates from E13.5 *Asxl3*$^{+/+}$ and *Asxl3*$^{fs/fs}$ cortices immunoblotted for full length ASXL3. **B,** Acid extracted histones from E13.5 *Asxl3*$^{+/+}$ and *Asxl3*$^{fs/fs}$ E13.5 cortices immunoblotted for H2AUb1 and histone H3. **C,** Quantification of H2AUb1 levels relative to H3 in *Asxl3*$^{+/+}$ (*n*=3) and *Asxl3*$^{fs/fs}$ (*n*=3) E13.5 cortices.****p*<0.001 using two-tailed unpaired Student's *t* test. Values are displayed as mean ± SEM. **D,** Appearance of curved back and drooping forelimbs in P0.5 *Asxl3*$^{fs/fs}$ mice. **E,** Representative images and **F,** quantification of P0.5 cortical surface area, marked by a black dashed line, for *Asxl3*$^{+/+}$ (*n*=16) and *Asxl3*$^{fs/fs}$ (*n*=15) mice. *p*=0.009 using two-tailed unpaired Student's *t* test. Values are displayed as mean±SEM. **G,** Cresyl violet staining of *Asxl3*$^{+/+}$ vs *Asxl3*$^{fs/fs}$ P0.5 cerebral cortex. Whole hemisphere (left) and magnification of the cortex (right). Scale bar, 500 μm. **H,** Sagittal P2 cerebellar sections stained with cresyl violet. *Asxl3*$^{fs/fs}$ cerebellums have shallower fissures (arrowheads) and smaller lobules (asterisk). Scale bar, 500 μm. **I,** Quantification of the number of neurons expressing TBR1, BCL11B, or SATB2 in *Asxl3*$^{+/+}$ (*n*=4, *n*=8, *n*=3) and *Asx3*$^{fs/fs}$ (*n*=4, *n*=8, *n*=3) cortices. *p*=0.76 (TBR1), *p*=0.004 (BCL11B), *p*=0.57 (SATB2) using two-tailed unpaired Student's *t* test. **J,** Immunohistochemistry of *Asxl3*$^{+/+}$ versus *Asx3*$^{fs/fs}$ P0.5 coronal cortical sections using layer-specific markers TBR1 (layer 6), BCL11B (layer 5), and SATB2 (layer 2-4).

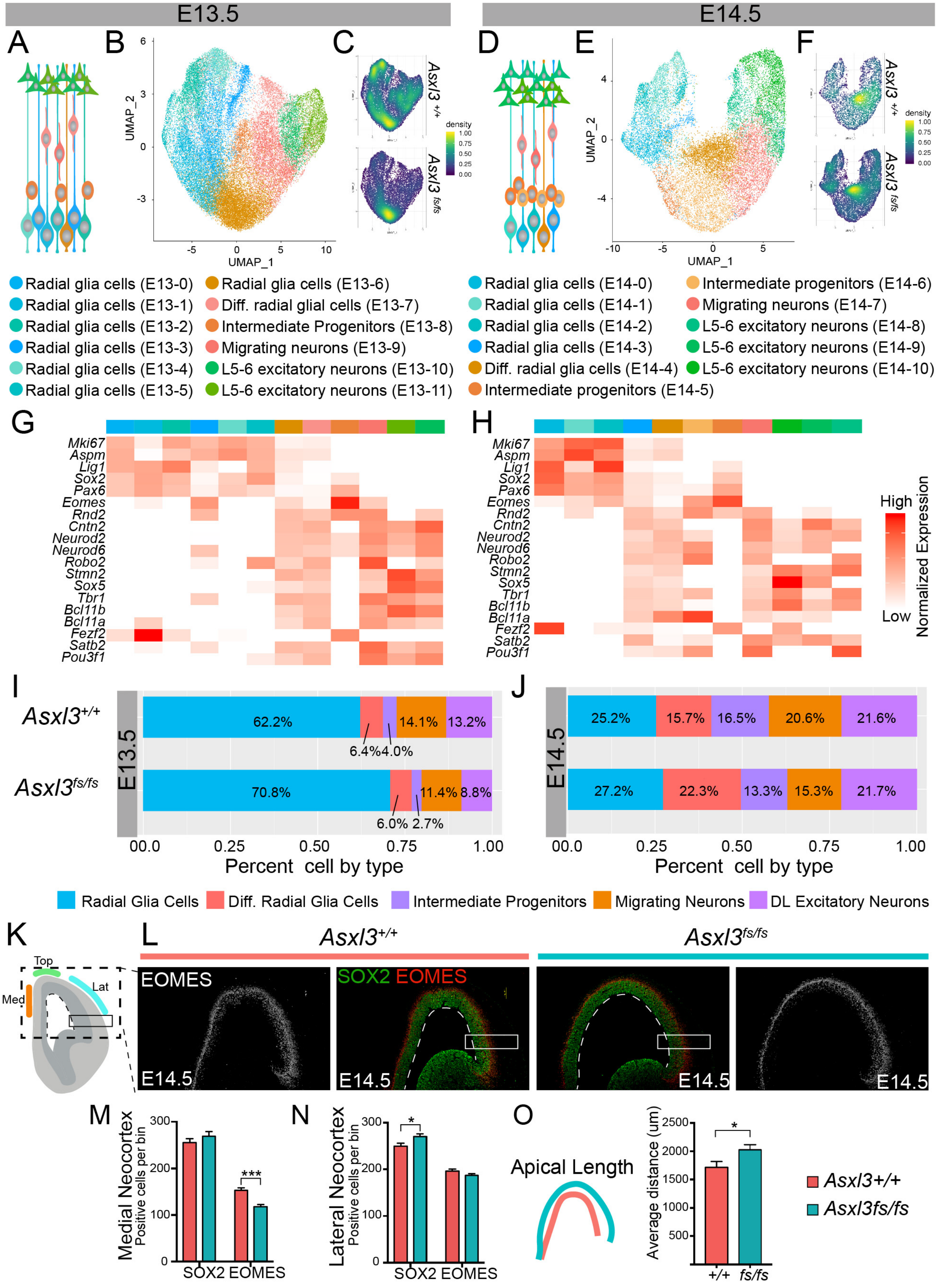
E13.5
E14.5
A
B
C
D
E
F
UMAP_2
UMAP_1
Asxl3 +/+
Asxl3 fs/fs
density
1.00
0.75
0.50
0.25
0.00
Radial glia cells (E13-0)
Radial glia cells (E13-1)
Radial glia cells (E13-2)
Radial glia cells (E13-3)
Radial glia cells (E13-4)
Radial glia cells (E13-5)
Radial glia cells (E13-6)
Diff. radial glial cells (E13-7)
Intermediate Progenitors (E13-8)
Migrating neurons (E13-9)
L5-6 excitatory neurons (E13-10)
L5-6 excitatory neurons (E13-11)
Radial glia cells (E14-0)
Radial glia cells (E14-1)
Radial glia cells (E14-2)
Radial glia cells (E14-3)
Diff. radial glia cells (E14-4)
Intermediate progenitors (E14-5)
Intermediate progenitors (E14-6)
Migrating neurons (E14-7)
L5-6 excitatory neurons (E14-8)
L5-6 excitatory neurons (E14-9)
L5-6 excitatory neurons (E14-10)
G
H
Mki67
Aspm
Lig1
Sox2
Pax6
Eomes
Rnd2
Cntn2
Neurod2
Neurod6
Robo2
Stmn2
Sox5
Tbr1
Bcl11b
Bcl11a
Fezf2
Satb2
Pou3f1
High
Low
Normalized Expression
I
J
Asxl3+/+
Asxl3fs/fs
E13.5
E14.5
62.2%
6.4%
4.0%
14.1%
13.2%
70.8%
6.0%
2.7%
11.4%
8.8%
25.2%
15.7%
16.5%
20.6%
21.6%
27.2%
22.3%
13.3%
15.3%
21.7%
00.0
0.25
0.50
0.75
1.00
Percent cell by type
Radial Glia Cells
Diff. Radial Glia Cells
Intermediate Progenitors
Migrating Neurons
DL Excitatory Neurons
K
Top
Med
Lat
L
Asxl3+/+
Asxl3fs/fs
EOMES
SOX2 EOMES
E14.5
M
Medial Neocortex
Positive cells per bin
300
200
100
0
***
SOX2 EOMES
N
Lateral Neocortex
Positive cells per bin
*
O
Apical Length
Average distance (um)
2500
2000
1500
1000
500
+/+
fs/fs
Asxl3+/+
Asxl3fs/fs

Fig. 3.2. Neural progenitor cells expansion in *Asxl3*$^{fs/fs}$ cortex A, Depiction of E13.5 cortical excitatory neurons. **B,** Unsupervised clustering of E13.5 excitatory neurons collected from *Asxl3*$^{+/+}$ (26,780 cells; *n*=5) and *Asx3*$^{fs/fs}$ (25,144 cells; *n*=3) mice color coded by cell type and represented on a UMAP. **C,** Distribution of *Asxl3*$^{+/+}$ (top) and *Asx3*$^{fs/fs}$ (bottom) cells across populations in the E13.5 UMAP. **D,** Depiction of E14.5 cortical excitatory neurons. **E,** Unsupervised clustering of E14.5 excitatory neurons collected from *Asxl3*$^{+/+}$ (8,261 cells; *n*=5) and *Asx3*$^{fs/fs}$ (22,075 cells; *n*=7) mice color coded by cell type and represented on a UMAP. **F,** Distribution of *Asxl3*$^{+/+}$ (top) and *Asx3*$^{fs/fs}$ (bottom) cells across populations in the E14.5 UMAP. The UMAPs in C and F are colored by density with yellow indicating a high density and blue a low density. Heatmap showing normalized expression of key marker genes expressed in **G**, E13.5 and **H**, E14.5, cortices. Comparison of the proportion of developmental cell classes detected in the *Asxl3*$^{+/+}$ and *Asx3*$^{fs/fs}$ datasets at **I**, E13.5, and **J**, E14.5. Developmental cell classes include radial glia cells (RGC E13.5 *p*=6.3e^{-79} , E14.5 *p*=0.02), differentiating radial glia cells (dRGC E13.5 *p*=0.1 , E14.5 *p*=1.7e^{-72}), intermediate progenitors (IP E13.5 *p*=8.1e^{-12}, E14.5 *p*=2.8e^{-09}), migrating neurons (E13.5 *p*=4.2e^{-16}, E14.5 *p*=2.6e^{-20}), and deep layer excitatory neurons (E13.5 *p*=3.6e^{-46}, E14.5 *p*=0.82). P values were generated using a two proportion Z test. **K,** Schematic illustrating quantifications collected from immunostained coronal sections of the cortex. SOX2 and EOMES positive cells were counted in bins (black boxes) throughout the medial, top, and lateral neocortex. Apical length (white dashed line) was measured throughout serial sections. **L,** Immunohistochemical staining of *Asxl3*$^{+/+}$ (left) and *Asx3*$^{fs/fs}$ (right) E14.5 coronal cortical sections with SOX2 (Green) and EOMES (grey, red). White boxes denote regions of quantification. White dashed line marks the apical length. Quantification of the number of cells expressing SOX2 or EOMES in the **M,** medial, or **N,** lateral neocortex in *Asxl3*$^{+/+}$ (*n*=6) and *Asx3*$^{fs/fs}$ (*n*=6) mice. M, *p*=0.3 (SOX2), *p*=1.3x10^{-6} (EOMES). N, *p*=0.02 (SOX2), *p*=0.11 (EOMES) using two-tailed unpaired Student's *t* test. **O,** Quantification of the apical length of E14.5 *Asxl3*$^{+/+}$ (*n*=8) and *Asx3*$^{fs/fs}$ (*n*=8) littermate cortices. *p*=0.038 using two-tailed unpaired Student's *t* test. In M-N values are displayed as mean ± SEM.

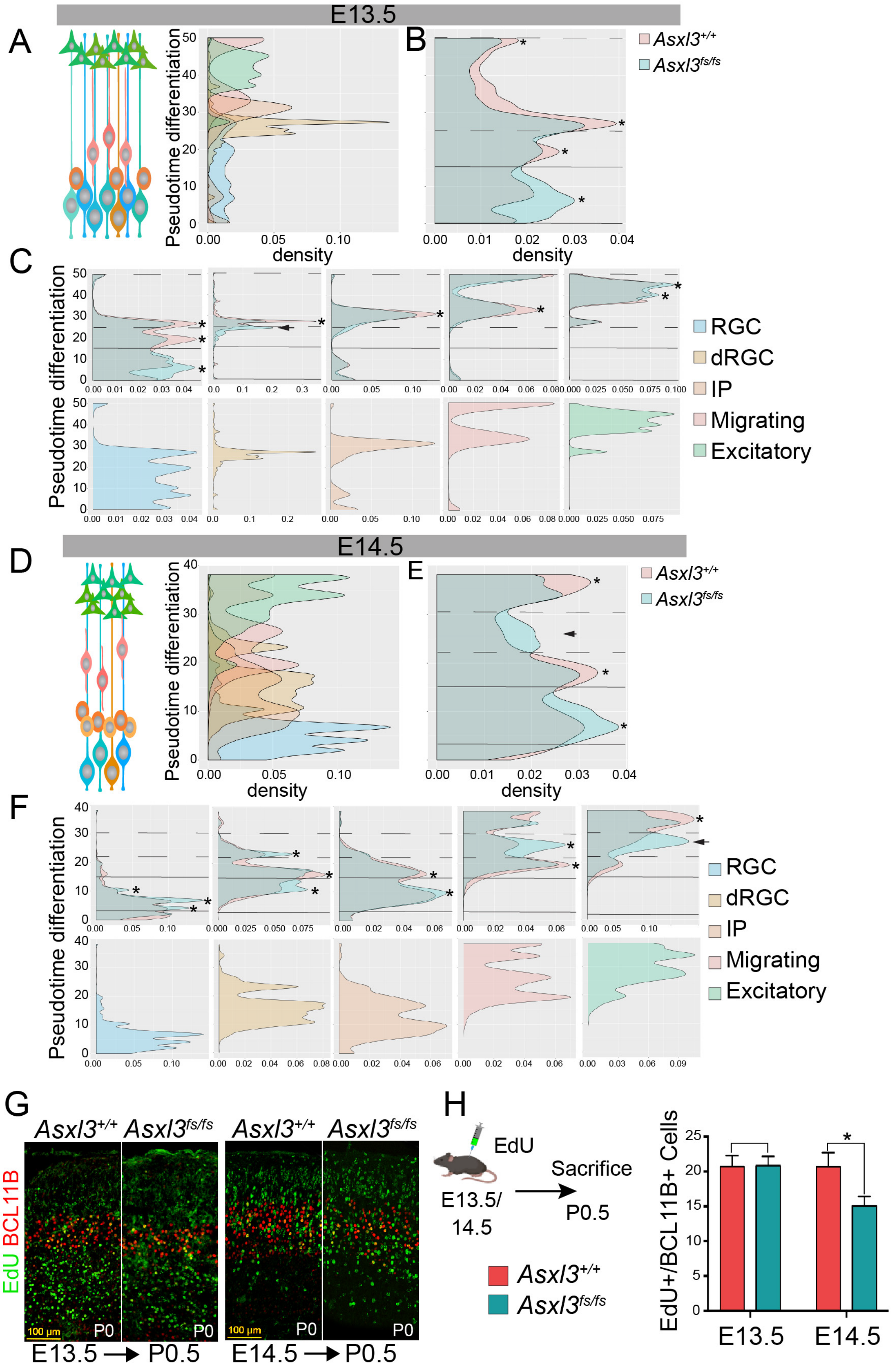
E13.5
A
B
C
Pseudotime differentiation
density
Asxl3+/+
Asxl3fs/fs
RGC
dRGC
IP
Migrating
Excitatory
E14.5
D
E
F
G
Asxl3+/+ Asxl3fs/fs Asxl3+/+ Asxl3fs/fs
EdU BCL11B
100 µm
P0
E13.5 → P0.5
E14.5 → P0.5
H
EdU
E13.5/ 14.5
Sacrifice
P0.5
EdU+/BCL11B+ Cells
E13.5
E14.5
*

Fig. 3.3. *Asxl3*$^{fs/fs}$ cortices show altered timing of neuronal differentiation A, Histograms displaying number of E13.5 cells ordered along pseudotime colored by cell type. **B,** E13.5 pseudotime histogram colored by genotype (*Asxl3*$^{+/+}$, red; *Asxl3*$^{fs/fs}$, blue). **C,** Individual E13.5 pseudotime histograms of RGC, dRGC, IP, Migrating neurons, and DL excitatory neurons. **D,** Histograms of the number of E14.5 cells ordered along pseudotime colored by cell type. **E,** E14.5 pseudotime histogram colored by genotype (*Asxl3*$^{+/+}$, red; *Asxl3*$^{fs/fs}$, blue). **F,** Individual E14.5 pseudotime histograms of RGC, dRGC, IP, Migrating neurons, and DL excitatory neurons. An asterisk indicates peaks with changes in amplitude and arrowheads indicate peaks with a shift in pseudotime. Birthdating analysis was performed at E13.5 and E14.5. EdU was injected at either E13.5 or E14.5 and then labeled brains were collected at P0.5. **G,** Representative P0.5 *Asxl3*$^{+/+}$ and *Asxl3*$^{fs/fs}$ cortical sections after EdU detection and immunostained with BCL11B. The left panel shows sections from animals injected with EdU at E13.5 and the right shows E14.5. **H,** Quantification of EdU+/BCL11B+ cells in E13.5 injected cortices (p=0.947) and E14.5 (p=0.018) using two-tailed unpaired Student's t test. values are displayed as mean ± SEM.

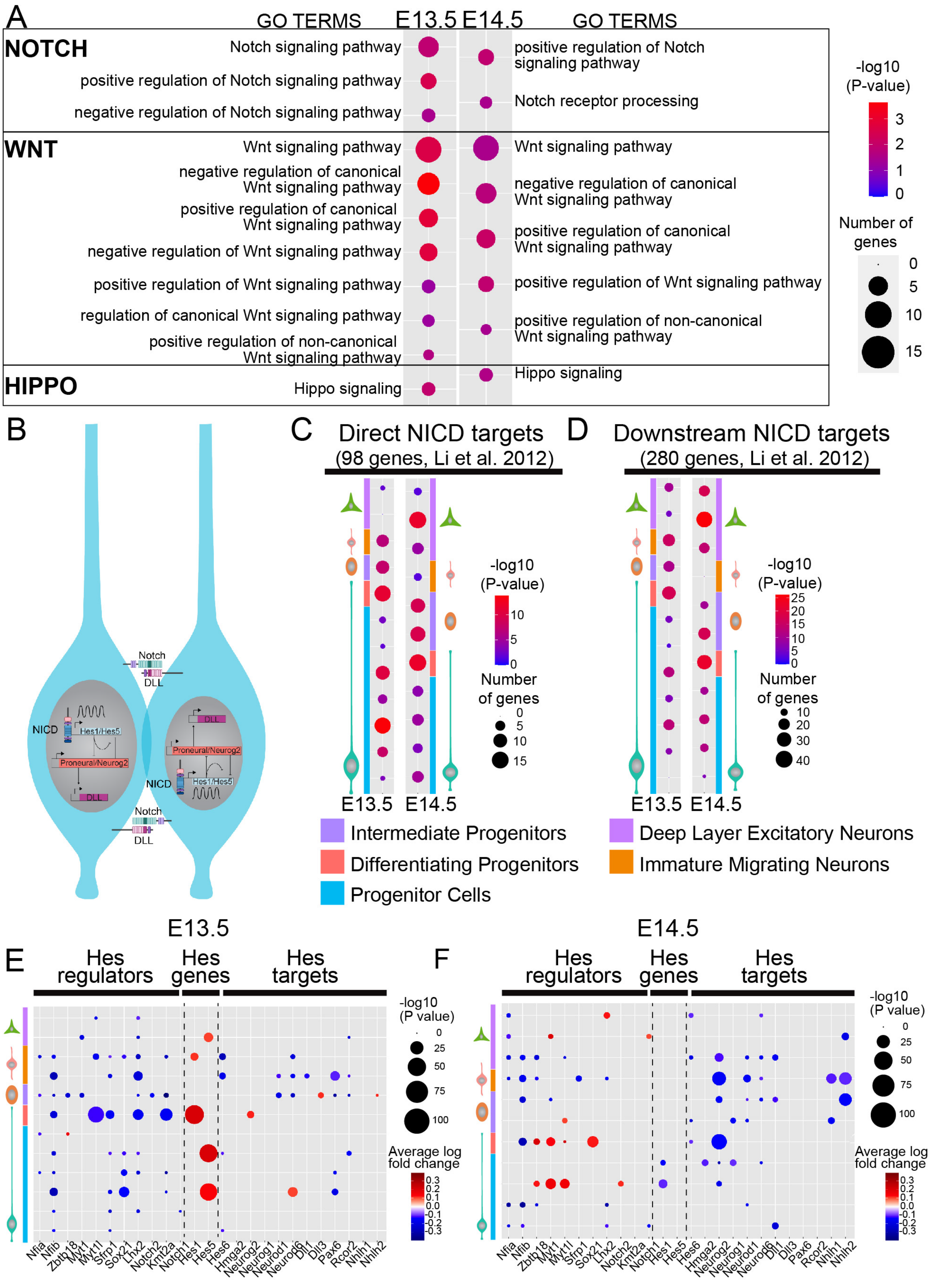
A
GO TERMS
E13.5
E14.5
GO TERMS
NOTCH
Notch signaling pathway
positive regulation of Notch signaling pathway
negative regulation of Notch signaling pathway
positive regulation of Notch signaling pathway
Notch receptor processing
WNT
Wnt signaling pathway
negative regulation of canonical Wnt signaling pathway
positive regulation of canonical Wnt signaling pathway
negative regulation of Wnt signaling pathway
positive regulation of Wnt signaling pathway
regulation of canonical Wnt signaling pathway
positive regulation of non-canonical Wnt signaling pathway
Wnt signaling pathway
negative regulation of canonical Wnt signaling pathway
positive regulation of canonical Wnt signaling pathway
positive regulation of Wnt signaling pathway
positive regulation of non-canonical Wnt signaling pathway
HIPPO
Hippo signaling
Hippo signaling
-log10 (P-value)
3
2
1
0
Number of genes
0
5
10
15
B
Notch
DLL
NICD
Hes1/Hes5
Proneural/Neurog2
DLL
DLL
Proneural/Neurog2
NICD
Hes1/Hes5
Notch
DLL
C
Direct NICD targets
(98 genes, Li et al. 2012)
E13.5
E14.5
-log10 (P-value)
10
5
0
Number of genes
0
5
10
15
D
Downstream NICD targets
(280 genes, Li et al. 2012)
E13.5
E14.5
-log10 (P-value)
25
20
15
10
5
0
Number of genes
10
20
30
40
Intermediate Progenitors
Differentiating Progenitors
Progenitor Cells
Deep Layer Excitatory Neurons
Immature Migrating Neurons
E13.5
E
Hes regulators
Hes genes
Hes targets
-log10 (P value)
0
25
50
75
100
Average log fold change
0.3
0.2
0.1
0.0
-0.1
-0.2
-0.3
Nfia
Nfib
Zbtb18
Myt1
Myt1l
Sfrp1
Sox21
Lhx2
Notch2
Kmt2a
Notch1
Hes1
Hes5
Hes6
Hmga2
Neurog2
Neurog1
Neurod1
Neurod6
Dll1
Dll3
Pax6
Rcor2
Nhlh1
Nhlh2
E14.5
F
Hes regulators
Hes genes
Hes targets
-log10 (P value)
0
25
50
75
100
Average log fold change
0.3
0.2
0.1
0.0
-0.1
-0.2
-0.3
Nfia
Nfib
Zbtb18
Myt1
Myt1l
Sfrp1
Sox21
Lhx2
Notch2
Kmt2a
Notch1
Hes1
Hes5
Hes6
Hmga2
Neurog2
Neurog1
Neurod1
Neurod6
Dll1
Dll3
Pax6
Rcor2
Nhlh1
Nhlh2

Fig. 3.4. Extrinsic signaling pathways disrupted in *Asxl3*$^{fs/fs}$ developing cortex A, Gene ontology analysis showing statistically significant enrichment for dysregulated genes in E13.5 (left) and E14.5 (right) cortices. GO terms were enriched for Notch, Wnt, and Hippo genes. The size of each dot represents the gene number and the shading represents the -$\log_{10}$ *p*-value. **B,** Model of Notch signaling between neighboring RGC during neurogenesis to promote maintenance of progenitor multipotency. Binding of Notch ligands to the Notch receptors leads to a series of cleavage events and subsequent translocation of the NICD into the nucleus. Within the nucleus, the Notch intracellular domain (NICD) promotes the expression of *Hes1*/*Hes5.* In turn, HES1/HES5 repress *Neurog2* and other proneural genes that promote differentiation. Enrichment analysis for **C,** direct NICD and **D,** downstream NICD targets identified by Li et al. 2012 in our E13.5 and E14.5 differentially expressed genes. The size of each dot represents the number of genes and the shading represents the -$\log_{10}$ *p*-value. Each row represents enrichment of targets within DEGs from a single cluster. Results are grouped and colored by cell type. A Fisher's exact test was used to determine if the gene lists were enriched. Cell type specific expression changes of Hes regulators, Hes genes and Hes targets based on scRNA-seq from **E,** E13.5 and **F,** E14.5 *Asxl3*$^{fs/fs}$ relative to *Asxl3*$^{+/+}$. The size of each dot represents the -$\log_{10}$ *p*-value and the shading represents the average log fold change. Results are grouped and colored by cell type.

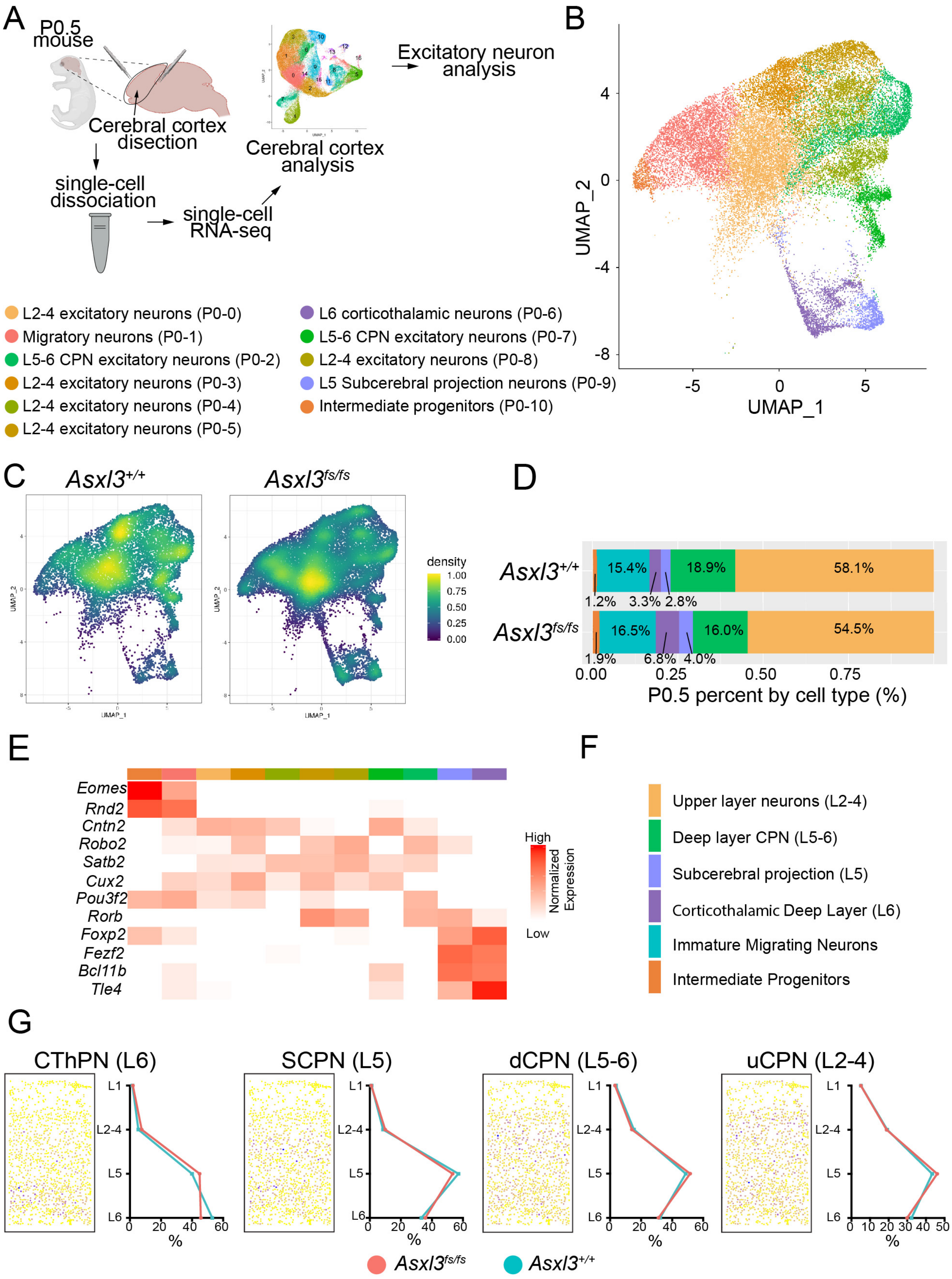
A
P0.5 mouse
Cerebral cortex disection
single-cell dissociation
single-cell RNA-seq
Cerebral cortex analysis
Excitatory neuron analysis
L2-4 excitatory neurons (P0-0)
Migratory neurons (P0-1)
L5-6 CPN excitatory neurons (P0-2)
L2-4 excitatory neurons (P0-3)
L2-4 excitatory neurons (P0-4)
L2-4 excitatory neurons (P0-5)
L6 corticothalamic neurons (P0-6)
L5-6 CPN excitatory neurons (P0-7)
L2-4 excitatory neurons (P0-8)
L5 Subcerebral projection neurons (P0-9)
Intermediate progenitors (P0-10)
B
UMAP_2
UMAP_1
4
0
-4
-8
-5
0
5
C
Asxl3+/+
Asxl3fs/fs
density
1.00
0.75
0.50
0.25
0.00
D
Asxl3+/+
15.4%
18.9%
58.1%
1.2%
3.3%
2.8%
Asxl3fs/fs
16.5%
16.0%
54.5%
1.9%
6.8%
4.0%
0.00
0.25
0.50
0.75
P0.5 percent by cell type (%)
E
Eomes
Rnd2
Cntn2
Robo2
Satb2
Cux2
Pou3f2
Rorb
Foxp2
Fezf2
Bcl11b
Tle4
High
Normalized Expression
Low
F
Upper layer neurons (L2-4)
Deep layer CPN (L5-6)
Subcerebral projection (L5)
Corticothalamic Deep Layer (L6)
Immature Migrating Neurons
Intermediate Progenitors
G
CThPN (L6)
SCPN (L5)
dCPN (L5-6)
uCPN (L2-4)
L1
L2-4
L5
L6
0
20
40
60
%
0
10
20
30
40
50
Asxl3fs/fs
Asxl3+/+

Fig. 3.5. Excitatory cortical neuron composition altered in *Asxl3*$^{fs/fs}$ cortex A, Experimental procedure schematic depicting dissection of P0.5 cortex, single cell dissociation, scRNA-seq, and bioinformatic enrichment of excitatory neurons. **B,** Unsupervised clustering of P0.5 excitatory neurons collected from *Asxl3*$^{+/+}$ (31,798 cells; *n*=4) and *Asx3*$^{fs/fs}$ (44,384 cells; *n*=6) mice color coded by cluster and represented on a UMAP. Cell type annotations are located to the right. **C,** Distribution of *Asxl3*$^{+/+}$ (top) and *Asx3*$^{fs/fs}$ (bottom) cells across populations in the UMAP. The UMAP is colored by density with yellow indicating a high density and blue a low density. **D,** Comparison of the proportion of major cell types detected in the *Asxl3*$^{+/+}$ and *Asx3*$^{fs/fs}$ datasets. IP p=3.7e^{-06}, Migrating p=0.01, CThPN p=5.2e^{-37}, SCPN p=8.9e^{-08}, dCPN p=7.7e^{-11}, uCPN p=1.4e^{-09} using a two proportion Z test. **E,** Heatmap showing normalized expression of key marker genes expressed in P0.5 cortices. **F,** Major cell types and corresponding color code **G,** Left: mapping of our single cell gene expression data onto STARmap spatial gene expression data (Wang et al. 2018) using Tangram (Biancalani et al. 2020). Dots colored by the probability of our cell type mapping to the STARmap cell type (blue high probability, yellow low probability). Right: distribution of cells mapping to spatial gene expression data for CThPN, SCPN, dCPN, and uCPN.

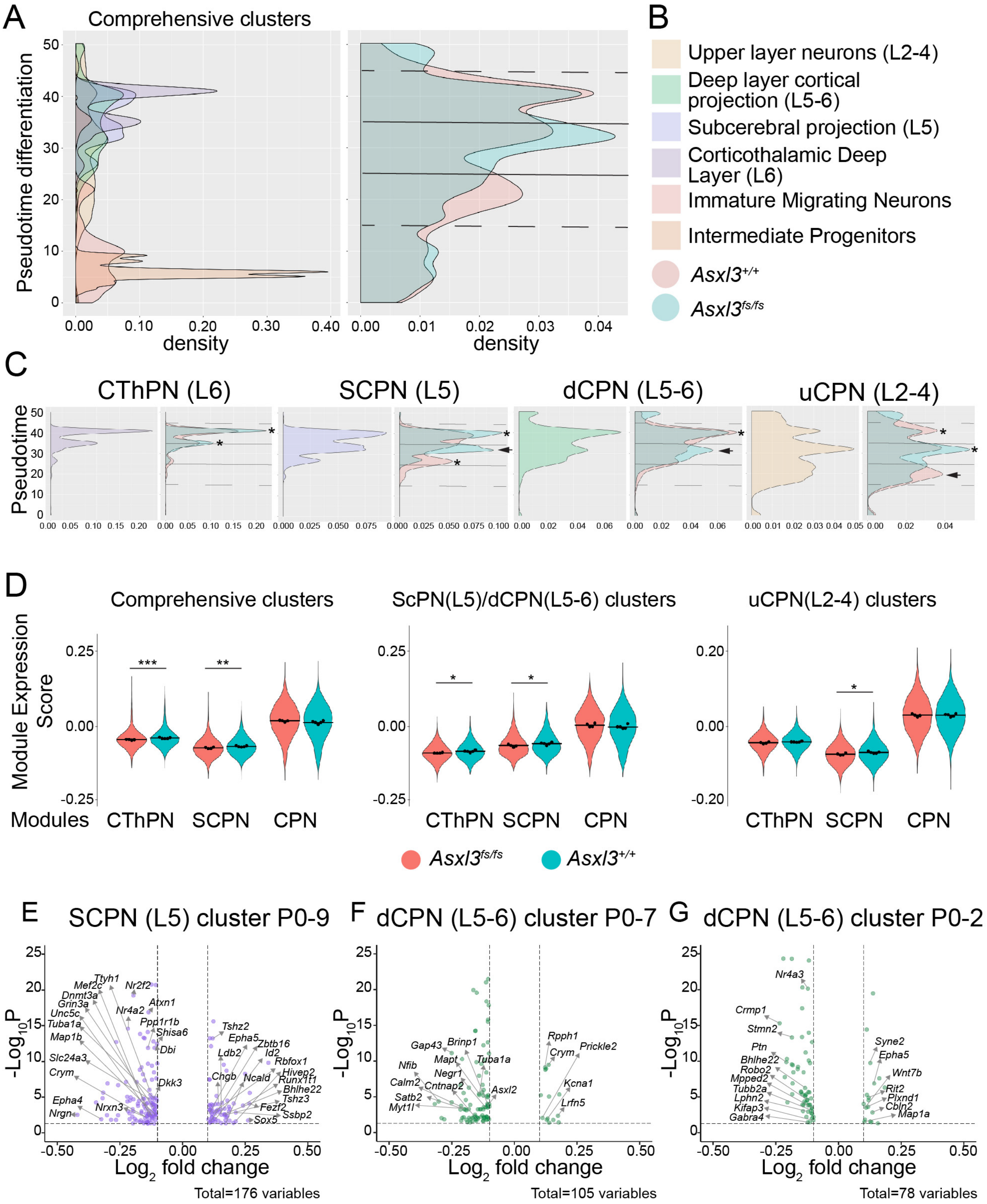
A
Comprehensive clusters
Pseudotime differentiation
density
B
Upper layer neurons (L2-4)
Deep layer cortical projection (L5-6)
Subcerebral projection (L5)
Corticothalamic Deep Layer (L6)
Immature Migrating Neurons
Intermediate Progenitors
Asxl3+/+
Asxl3fs/fs
C
CThPN (L6)
SCPN (L5)
dCPN (L5-6)
uCPN (L2-4)
Pseudotime
D
Comprehensive clusters
ScPN(L5)/dCPN(L5-6) clusters
uCPN(L2-4) clusters
Module Expression Score
Modules
CThPN
SCPN
CPN
Asxl3fs/fs
Asxl3+/+
E
SCPN (L5) cluster P0-9
F
dCPN (L5-6) cluster P0-7
G
dCPN (L5-6) cluster P0-2
-Log10P
Log2 fold change
Total=176 variables
Total=105 variables
Total=78 variables
Ttyh1
Mef2c
Nr2f2
Dnmt3a
Atxn1
Grin3a
Nr4a2
Unc5c
Ppp1r1b
Tuba1a
Shisa6
Map1b
Dbi
Slc24a3
Crym
Dkk3
Epha4
Nrgn
Nrxn3
Tshz2
Epha5
Zbtb16
Ldb2
Id2
Rbfox1
Hivep2
Chgb
Ncald
Runx1t1
Bhlhe22
Tshz3
Fezf2
Ssbp2
Sox5
Gap43
Brinp1
Mapt
Tuba1a
Nfib
Negr1
Calm2
Cntnap2
Asxl2
Satb2
Myt1l
Rpph1
Prickle2
Crym
Kcna1
Lrfn5
Nr4a3
Crmp1
Stmn2
Ptn
Bhlhe22
Robo2
Mpped2
Tubb2a
Lphn2
Kifap3
Gabra4
Syne2
Epha5
Wnt7b
Rit2
Plxnd1
Cbln2
Map1a

Fig. 3.6. Timing of deep layer neuron differentiation disrupted in *Asxl3*$^{fs/fs}$ cortical development A, Histograms of the number of P0.5 cells ordered along pseudotime colored by cell type (left) and colored by genotype (right: *Asxl3*$^{+/+}$, red; *Asxl3*$^{fs/fs}$, blue). **B,** Major cell types and corresponding color code **C,** Individual P0.5 pseudotime histograms of CThPN, SCPN, dCPN, and uCPN. An asterisk indicates peaks with changes in amplitude and arrowheads indicate peaks with a shift in pseudotime. **D,** Violinplots showing module scores for CThPN, SCPN, and CPN gene modules identified by Molyneaux et al. 2015. Module scores were calculated for comprehensive clusters (CThPN, SCPN, dCPN, uCPN), layer 5 neurons (SCPN, dCPN), and upper layer neurons (uCPN). Volcanoplots showing differentially expressed genes identified for **E,** Cluster P0-9 SCPN, **F,** Cluster P0-7 dCPN, and **G,** Cluster P0-2 dCPN.

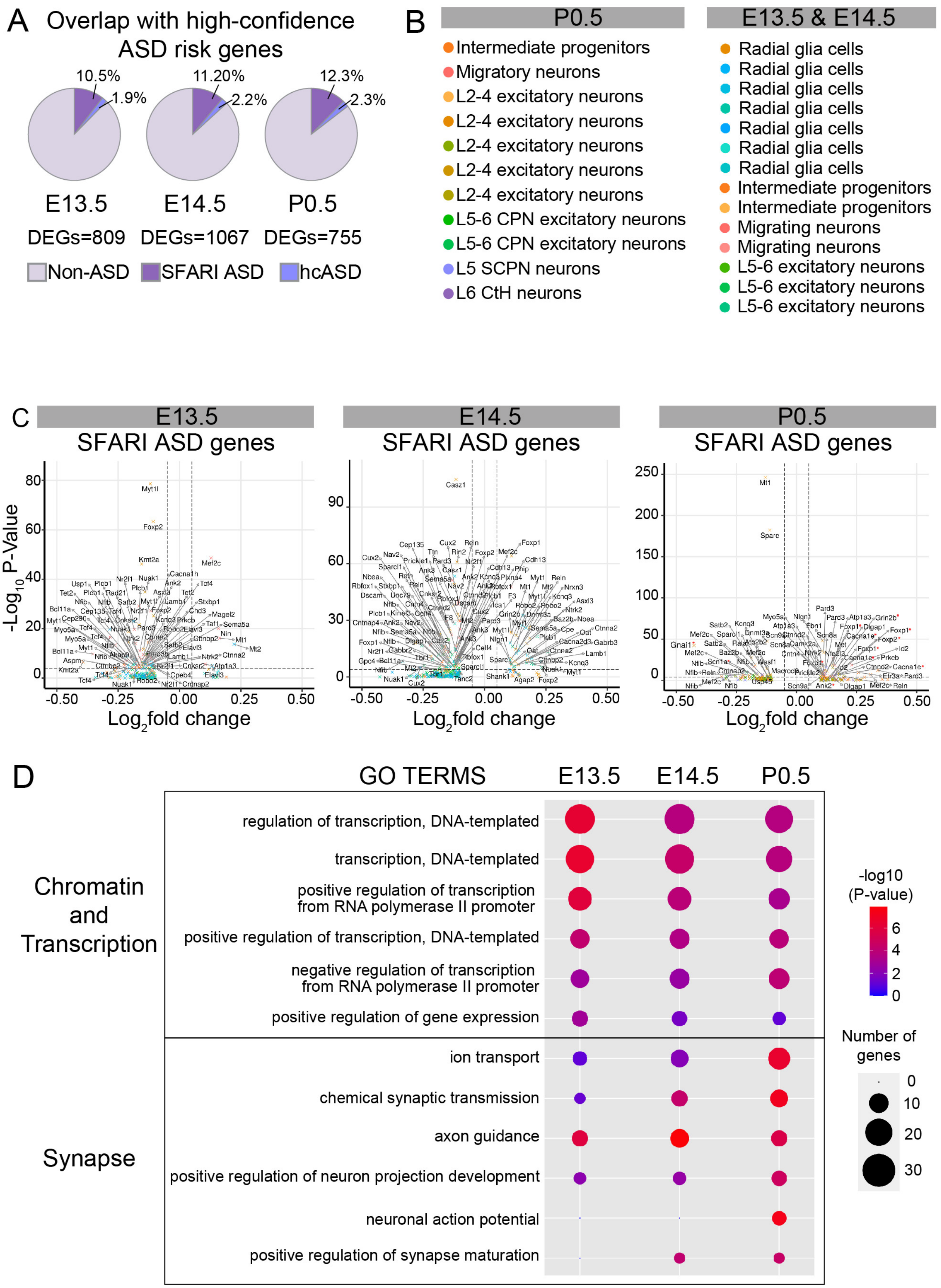
A
Overlap with high-confidence ASD risk genes
10.5%
1.9%
11.20%
2.2%
12.3%
2.3%
E13.5
E14.5
P0.5
DEGs=809
DEGs=1067
DEGs=755
Non-ASD
SFARI ASD
hcASD
B
P0.5
Intermediate progenitors
Migratory neurons
L2-4 excitatory neurons
L2-4 excitatory neurons
L2-4 excitatory neurons
L2-4 excitatory neurons
L2-4 excitatory neurons
L5-6 CPN excitatory neurons
L5-6 CPN excitatory neurons
L5 SCPN neurons
L6 CtH neurons
E13.5 & E14.5
Radial glia cells
Radial glia cells
Radial glia cells
Radial glia cells
Radial glia cells
Radial glia cells
Radial glia cells
Intermediate progenitors
Intermediate progenitors
Migrating neurons
Migrating neurons
L5-6 excitatory neurons
L5-6 excitatory neurons
L5-6 excitatory neurons
C
E13.5
SFARI ASD genes
E14.5
SFARI ASD genes
P0.5
SFARI ASD genes
-Log$_{10}$ P-Value
Log$_2$fold change
-0.50
-0.25
0.00
0.25
0.50
0
20
40
60
80
30
60
90
50
100
150
200
250
Myt1l
Foxp2
Kmt2a
Mef2c
Casz1
Mt1
Sparc
D
GO TERMS
E13.5
E14.5
P0.5
Chromatin and Transcription
regulation of transcription, DNA-templated
transcription, DNA-templated
positive regulation of transcription from RNA polymerase II promoter
positive regulation of transcription, DNA-templated
negative regulation of transcription from RNA polymerase II promoter
positive regulation of gene expression
Synapse
ion transport
chemical synaptic transmission
axon guidance
positive regulation of neuron projection development
neuronal action potential
positive regulation of synapse maturation
-log10 (P-value)
6
4
2
0
Number of genes
0
10
20
30

Fig. 3.7. Enrichment of ASD risk genes A, The pie chart illustrates the percentage of SFARI ASD genes amongst our P0.5, E14.5, and E13.5 differentially expressed genes. **B,** Cell type annotations and color codes used for volcano plots in C. **C,** Volcano plots for differentially expressed SFARI ASD genes in E13.5, E14.5, and P0.5 excitatory cells. Genes with a *p*-value < 0.05 and log fold change > 0.1 are displayed and colored by the cell type they are dysregulated in. **D,** Gene ontology analysis showing statistically significant enrichment for dysregulated ASD genes in the E13.5, E14.5, and P0.5 cortex from C. At early timepoints GO terms were enriched for chromatin ASD genes. At later timepoints GO terms were enriched for synaptic ASD genes. The size of each dot represents the number of genes and the shading represents the $-\log_{10}$ *p*-value.

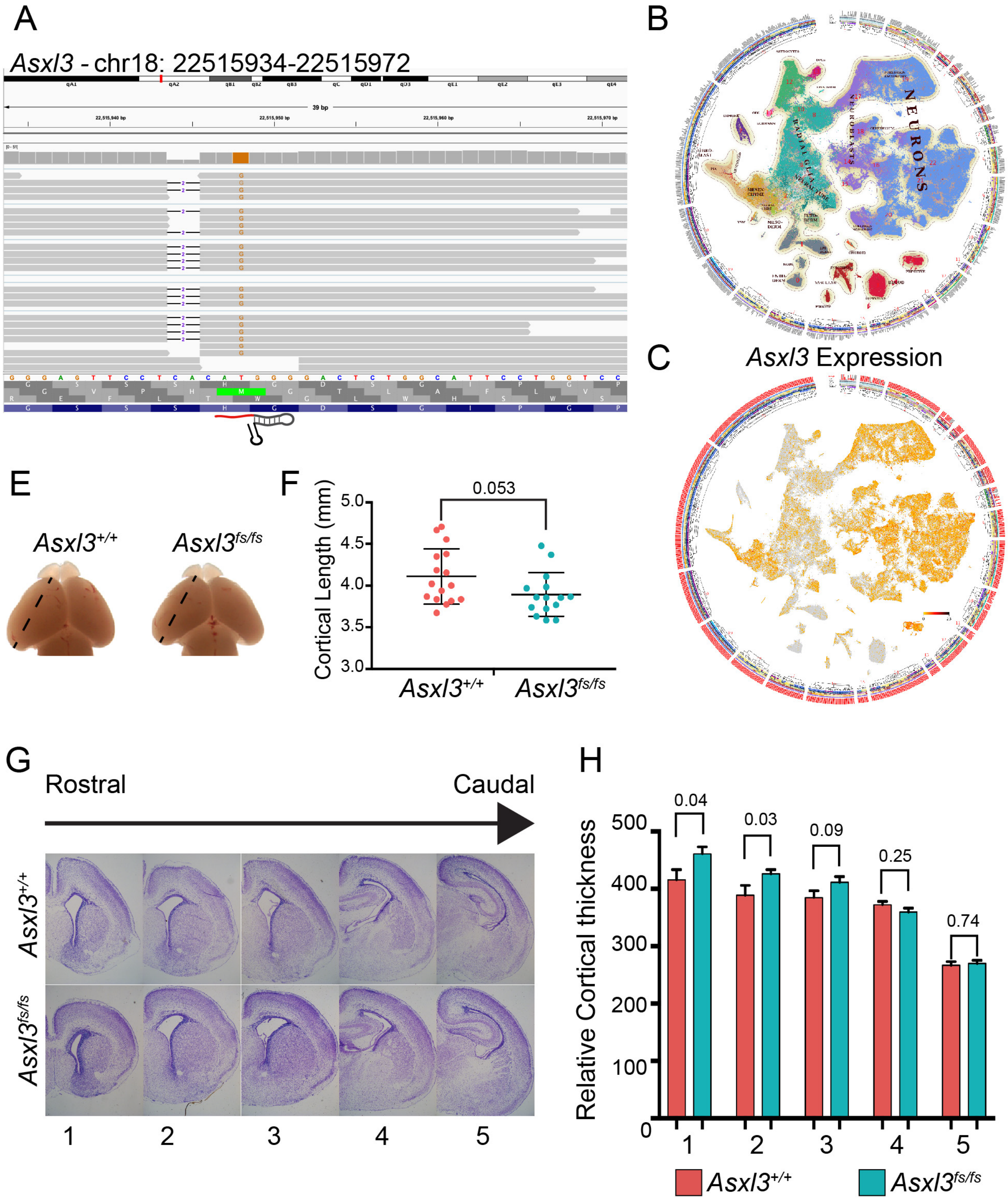
A
Asxl3 - chr18: 22515934-22515972
39 bp
B
NEURONS
NEUROBLASTS
RADIAL GLIA
C
Asxl3 Expression
E
Asxl3+/+
Asxl3fs/fs
F
0.053
Cortical Length (mm)
5.0
4.5
4.0
3.5
3.0
Asxl3+/+
Asxl3fs/fs
G
Rostral
Caudal
Asxl3+/+
Asxl3fs/fs
1
2
3
4
5
H
0.04
0.03
0.09
0.25
0.74
Relative Cortical thickness
500
400
300
200
100
0
1
2
3
4
5
Asxl3+/+
Asxl3fs/fs

Supplemental Fig. 3.1. Cortical thickness and length unaffected in *Asxl3*$^{fs/fs}$ A, IGV viewer window of *Asxl3* that shows the detection of *Asxl3*^{fs} mRNA in our P0.5 scRNA-seq. **B,** Wheel plots showing scRNA-seq data using t-SNE embedding (La Manno et al. 2020) (http://mousebrain.org). Clusters are colored by major classes. **C,** Expression of *Asxl3* overlaid on the t-SNE plot in B. **E,** Representative images and **F,** quantification of P0.5 cortical length, marked by a black dashed line, for *Asxl3*$^{+/+}$ (*n*=16) and *Asxl3*$^{fs/fs}$ (*n*=15) mice. *p*=0.053 using two-tailed unpaired Student's *t* test. **G,** Serial coronal sections of P0.5 brains stained with cresyl violet. Comparable *Asxl3*$^{+/+}$ (top) and *Asxl3*$^{fs/fs}$ (bottom) sections from rostral to caudal regions were compared. **H,** Quantification of cortical thickness in equivalent areas of control and homozygous frameshift cortices (1: *p*=0.24, 2: *p*=0.29, 3: *p*=0.09, 4: *p*=0.17, 5: *p*=0.59 using two-tailed unpaired Student's *t* test). All values are displayed as mean±SEM.

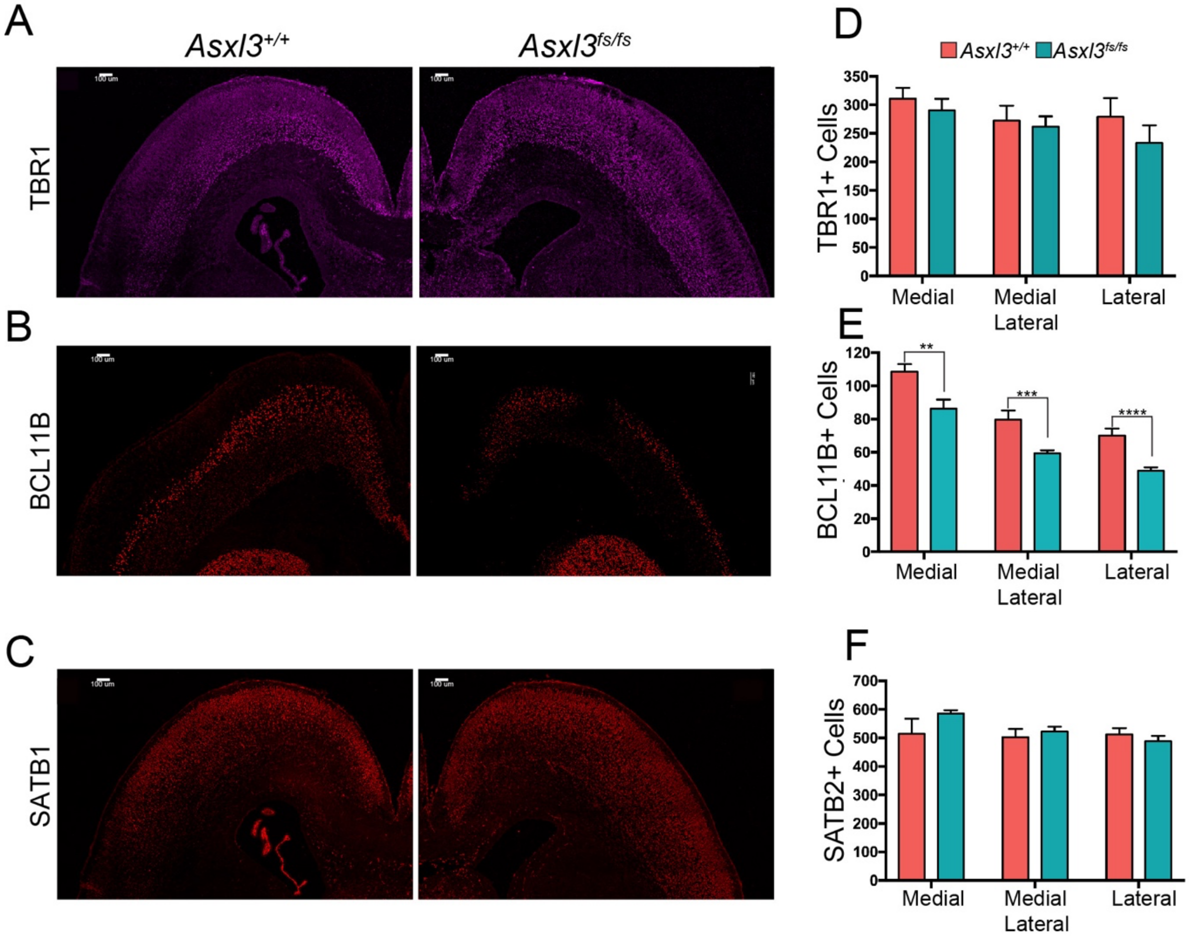

Supplemental Fig. 3.2. Excitatory neuron cortical composition in *Asxl3*$^{fs/fs}$ mouse model Large scale images displaying immunostaining of *Asxl3*$^{+/+}$ versus *Asx3*$^{fs/fs}$ P0.5 coronal cortical sections with layer-specific markers **A,** TBR1 (layer 6), **B,** BCL11B (layer 5), and **C,** SATB2 (layer 2-4). Quantification of the number of neurons expressing **D,** TBR1, **E,** BCL11B, or **F,** SATB2 in *Asxl3*$^{+/+}$ (n=4, n=8, n=3) and *Asx3*$^{fs/fs}$ (n=4, n=8, n=3) cortices. Equal-sized bins were used to quantify cells across medial, medial/lateral, and lateral regions. TBR1 (m: p=0.49, m/l: p=0.76, l: p=0.35) BCL11B (m: $p=7.7\text{x}10^{-3}$, m/l: $p=4.3\text{x}10^{-3}$, l: $p=5.3\text{x}10^{-4}$), SATB2 (m: p=0.26, m/l: p=0.57, l: p=0.45) using two-tailed unpaired Student's t test. Scale bars, 100 um. **$p<0.01$, ***$p<0.005$, ****$p<0.001$. All values are displayed as mean±SEM.

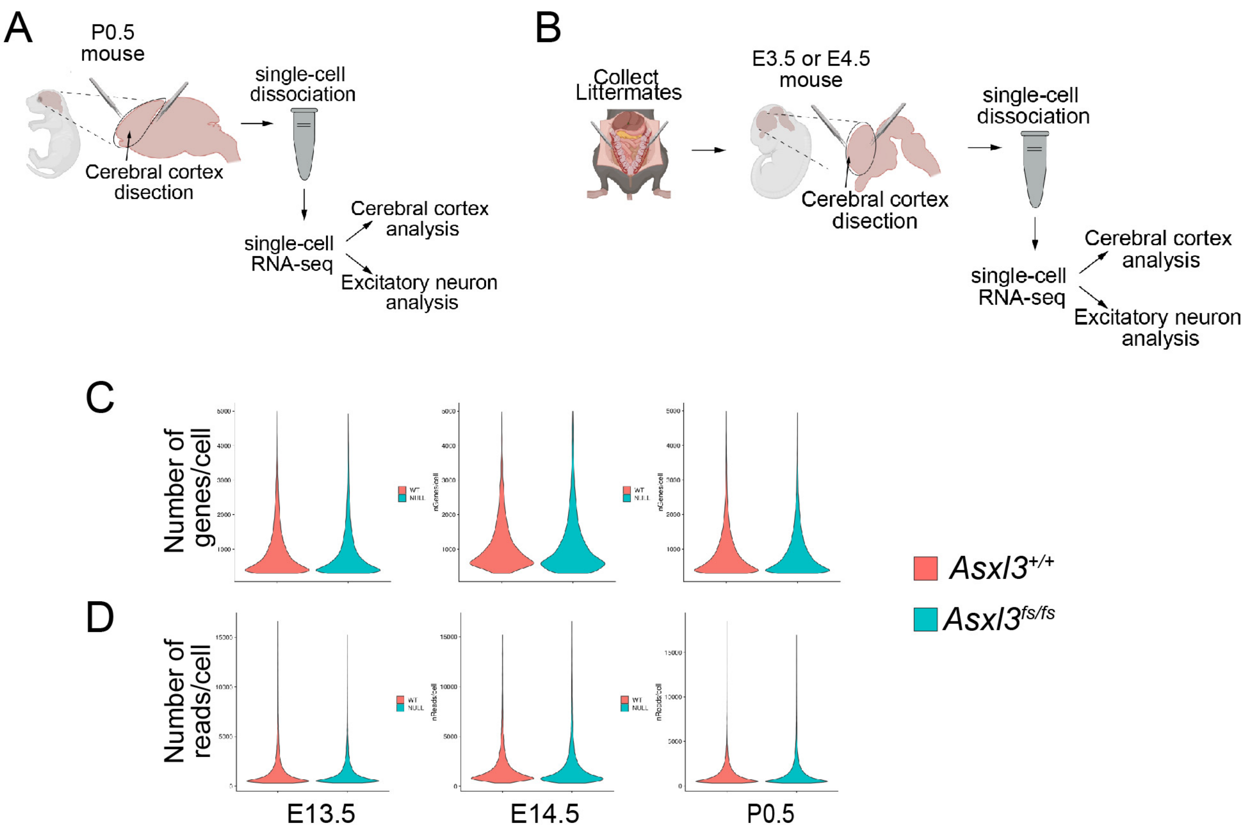

F

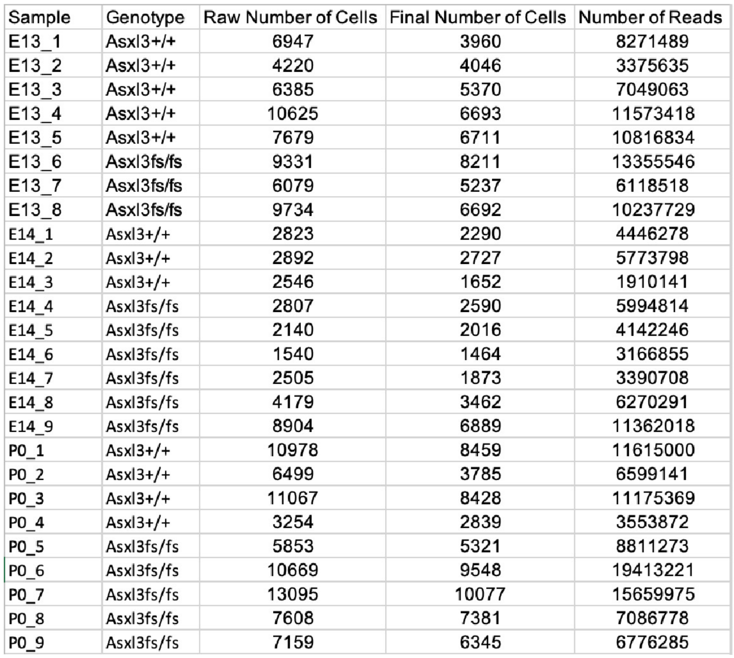

Sample	Genotype	Raw Number of Cells	Final Number of Cells	Number of Reads
E13_1	Asxl3+/+	6947	3960	8271489
E13_2	Asxl3+/+	4220	4046	3375635
E13_3	Asxl3+/+	6385	5370	7049063
E13_4	Asxl3+/+	10625	6693	11573418
E13_5	Asxl3+/+	7679	6711	10816834
E13_6	Asxl3fs/fs	9331	8211	13355546
E13_7	Asxl3fs/fs	6079	5237	6118518
E13_8	Asxl3fs/fs	9734	6692	10237729
E14_1	Asxl3+/+	2823	2290	4446278
E14_2	Asxl3+/+	2892	2727	5773798
E14_3	Asxl3+/+	2546	1652	1910141
E14_4	Asxl3fs/fs	2807	2590	5994814
E14_5	Asxl3fs/fs	2140	2016	4142246
E14_6	Asxl3fs/fs	1540	1464	3166855
E14_7	Asxl3fs/fs	2505	1873	3390708
E14_8	Asxl3fs/fs	4179	3462	6270291
E14_9	Asxl3fs/fs	8904	6889	11362018
P0_1	Asxl3+/+	10978	8459	11615000
P0_2	Asxl3+/+	6499	3785	6599141
P0_3	Asxl3+/+	11067	8428	11175369
P0_4	Asxl3+/+	3254	2839	3553872
P0_5	Asxl3fs/fs	5853	5321	8811273
P0_6	Asxl3fs/fs	10669	9548	19413221
P0_7	Asxl3fs/fs	13095	10077	15659975
P0_8	Asxl3fs/fs	7608	7381	7086778
P0_9	Asxl3fs/fs	7159	6345	6776285

E

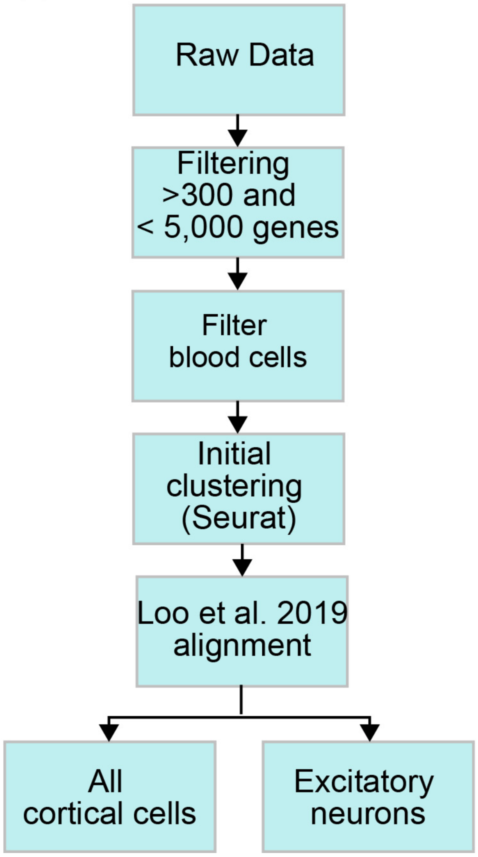

Supplemental Fig. 3.3. Workflow and QC for scRNA-seq of cortical tissue Illustration of the **A,** P0.5 and **B,** E13.5/14.5 cortical dissections. Single cell dissociations were loaded onto the SEQ-Well platform and prepped for RNA sequencing. After cell annotation, excitatory neurons were bioinformatically enriched for analysis. Violin plots showing the distribution of per cell **C,** gene and **D,** reads detection at E13.5, E14.5 and P0.5 for *Asxl3*$^{+/+}$ and *Asxl3*$^{fs/fs}$ samples. **E,** Schematic overview of our scRNA-seq analysis pipeline. Cells with fewer than 300 or more than 5,000 genes detected were removed. As were cells expressing blood cell genes. After unsupervised clustering with Seurat, excitatory neurons were selected for further analysis. **F,** Table listing the sample, cell number, number of filtered cells and number of reads for E13.5, E14.5 and P0.5 sets.

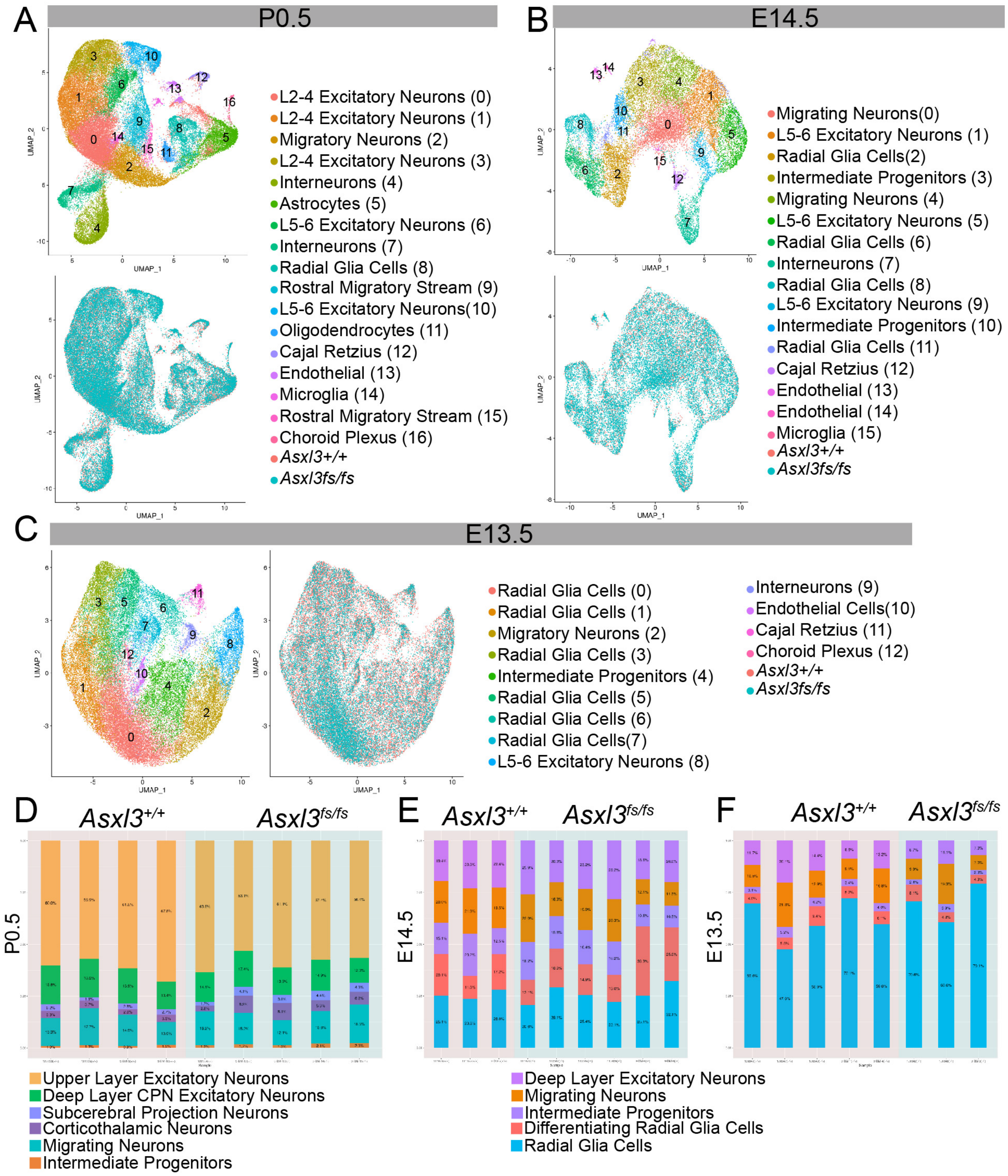
A
P0.5
L2-4 Excitatory Neurons (0)
L2-4 Excitatory Neurons (1)
Migratory Neurons (2)
L2-4 Excitatory Neurons (3)
Interneurons (4)
Astrocytes (5)
L5-6 Excitatory Neurons (6)
Interneurons (7)
Radial Glia Cells (8)
Rostral Migratory Stream (9)
L5-6 Excitatory Neurons(10)
Oligodendrocytes (11)
Cajal Retzius (12)
Endothelial (13)
Microglia (14)
Rostral Migratory Stream (15)
Choroid Plexus (16)
Asxl3+/+
Asxl3fs/fs
UMAP_1
UMAP_2
B
E14.5
Migrating Neurons(0)
L5-6 Excitatory Neurons (1)
Radial Glia Cells(2)
Intermediate Progenitors (3)
Migrating Neurons (4)
L5-6 Excitatory Neurons (5)
Radial Glia Cells (6)
Interneurons (7)
Radial Glia Cells (8)
L5-6 Excitatory Neurons (9)
Intermediate Progenitors (10)
Radial Glia Cells (11)
Cajal Retzius (12)
Endothelial (13)
Endothelial (14)
Microglia (15)
Asxl3+/+
Asxl3fs/fs
C
E13.5
Radial Glia Cells (0)
Radial Glia Cells (1)
Migratory Neurons (2)
Radial Glia Cells (3)
Intermediate Progenitors (4)
Radial Glia Cells (5)
Radial Glia Cells (6)
Radial Glia Cells(7)
L5-6 Excitatory Neurons (8)
Interneurons (9)
Endothelial Cells(10)
Cajal Retzius (11)
Choroid Plexus (12)
Asxl3+/+
Asxl3fs/fs
D
Asxl3+/+
Asxl3fs/fs
P0.5
E
Asxl3+/+
Asxl3fs/fs
E14.5
F
Asxl3+/+
Asxl3fs/fs
E13.5
Sample
Upper Layer Excitatory Neurons
Deep Layer CPN Excitatory Neurons
Subcerebral Projection Neurons
Corticothalamic Neurons
Migrating Neurons
Intermediate Progenitors
Deep Layer Excitatory Neurons
Migrating Neurons
Intermediate Progenitors
Differentiating Radial Glia Cells
Radial Glia Cells

Supplemental Fig. 3.4. Cortical cell types profiled with Seq-Well A, Unsupervised clustering of P0.5 cells collected from *Asxl3*$^{+/+}$ (23,511 cells; *n*=4) and *Asx3*$^{fs/fs}$ (44,384 cells; *n*=6) samples after removal of blood cells. Top UMAP color coded by cell type and bottom UMAP colored by genotype with *Asxl3*$^{+/+}$ colored red and *Asxl3*$^{fs/fs}$ colored blue. Cell type annotations are located to the right. **B,** Unsupervised clustering of E14.5 cells collected from *Asxl3*$^{+/+}$ (6,669 cells; *n*=5) and *Asx3*$^{fs/fs}$ (18,294 cells; *n*=7) samples after removal of blood cells. Top UMAP color coded by cell type and bottom UMAP colored by genotype with *Asxl3*$^{+/+}$ colored red and *Asxl3*$^{fs/fs}$ colored blue. Cell type annotations are located to the right. **C,** Unsupervised clustering of E13.5 cells collected from *Asxl3*$^{+/+}$ (26,780 cells; *n*=5) and *Asx3*$^{fs/fs}$ (20,140 cells; *n*=3) samples after removal of blood cells. Left UMAP color coded by cell type and right UMAP colored by genotype with *Asxl3*$^{+/+}$ colored red and *Asxl3*$^{fs/fs}$ colored blue. Cell type annotations are located to the right. Stacked barplots depicting distribution of detected excitatory cell types within each sample at **D,** P0.5 (left), **E,** E14.5 (center), **F,** E13.5 (right). Barplots are organized by genotype with *Asxl3*$^{+/+}$ samples on a red background and *Asxl3*$^{fs/fs}$ on a blue background.

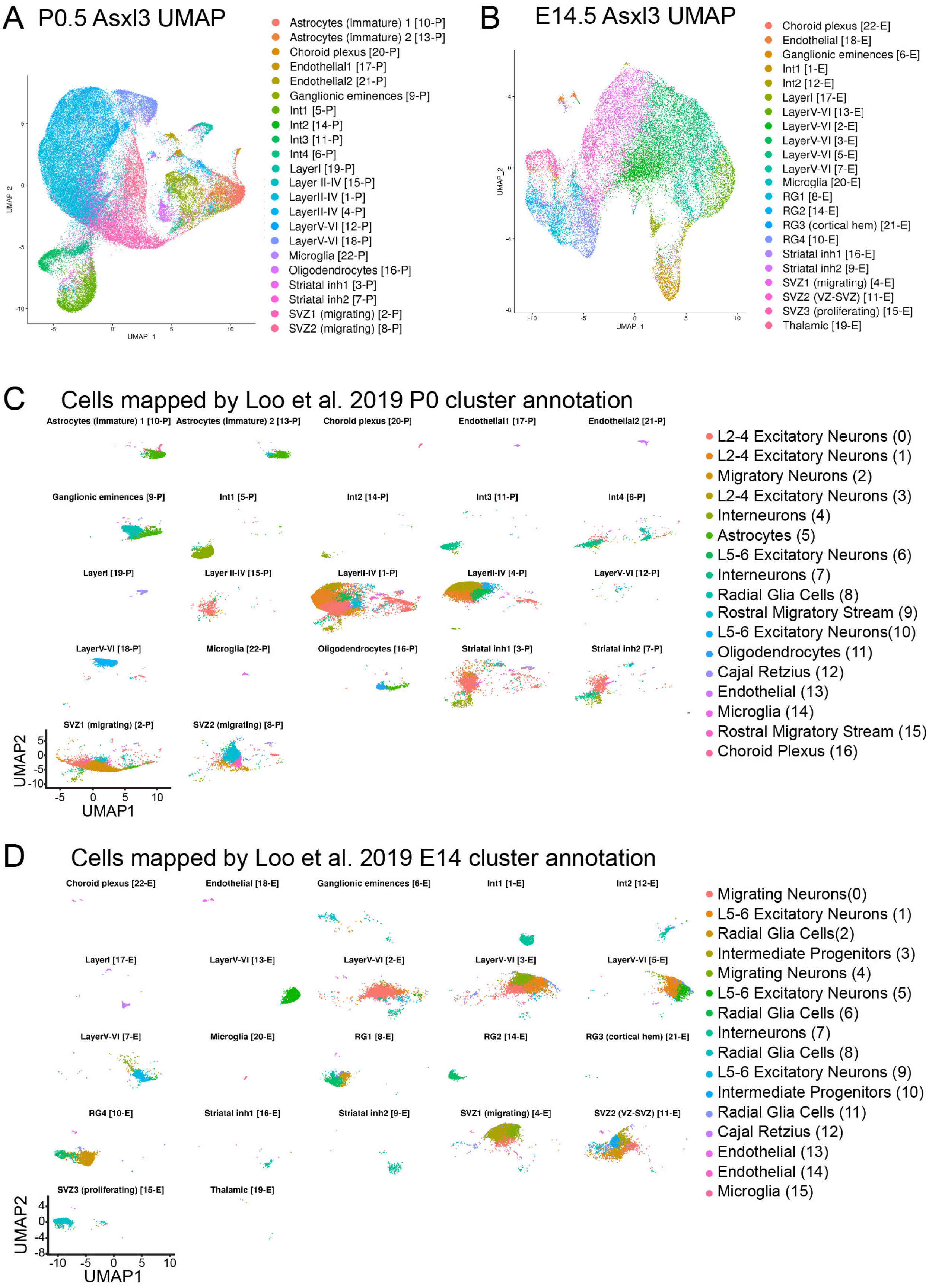
A P0.5 Asxl3 UMAP
UMAP_2
UMAP_1
Astrocytes (immature) 1 [10-P]
Astrocytes (immature) 2 [13-P]
Choroid plexus [20-P]
Endothelial1 [17-P]
Endothelial2 [21-P]
Ganglionic eminences [9-P]
Int1 [5-P]
Int2 [14-P]
Int3 [11-P]
Int4 [6-P]
LayerI [19-P]
Layer II-IV [15-P]
LayerII-IV [1-P]
LayerII-IV [4-P]
LayerV-VI [12-P]
LayerV-VI [18-P]
Microglia [22-P]
Oligodendrocytes [16-P]
Striatal inh1 [3-P]
Striatal inh2 [7-P]
SVZ1 (migrating) [2-P]
SVZ2 (migrating) [8-P]
B E14.5 Asxl3 UMAP
UMAP_2
UMAP_1
Choroid plexus [22-E]
Endothelial [18-E]
Ganglionic eminences [6-E]
Int1 [1-E]
Int2 [12-E]
LayerI [17-E]
LayerV-VI [13-E]
LayerV-VI [2-E]
LayerV-VI [3-E]
LayerV-VI [5-E]
LayerV-VI [7-E]
Microglia [20-E]
RG1 [8-E]
RG2 [14-E]
RG3 (cortical hem) [21-E]
RG4 [10-E]
Striatal inh1 [16-E]
Striatal inh2 [9-E]
SVZ1 (migrating) [4-E]
SVZ2 (VZ-SVZ) [11-E]
SVZ3 (proliferating) [15-E]
Thalamic [19-E]
C Cells mapped by Loo et al. 2019 P0 cluster annotation
Astrocytes (immature) 1 [10-P]
Astrocytes (immature) 2 [13-P]
Choroid plexus [20-P]
Endothelial1 [17-P]
Endothelial2 [21-P]
Ganglionic eminences [9-P]
Int1 [5-P]
Int2 [14-P]
Int3 [11-P]
Int4 [6-P]
LayerI [19-P]
Layer II-IV [15-P]
LayerII-IV [1-P]
LayerII-IV [4-P]
LayerV-VI [12-P]
LayerV-VI [18-P]
Microglia [22-P]
Oligodendrocytes [16-P]
Striatal inh1 [3-P]
Striatal inh2 [7-P]
SVZ1 (migrating) [2-P]
SVZ2 (migrating) [8-P]
UMAP2
5
0
-5
-10
-5
0
5
10
UMAP1
L2-4 Excitatory Neurons (0)
L2-4 Excitatory Neurons (1)
Migratory Neurons (2)
L2-4 Excitatory Neurons (3)
Interneurons (4)
Astrocytes (5)
L5-6 Excitatory Neurons (6)
Interneurons (7)
Radial Glia Cells (8)
Rostral Migratory Stream (9)
L5-6 Excitatory Neurons(10)
Oligodendrocytes (11)
Cajal Retzius (12)
Endothelial (13)
Microglia (14)
Rostral Migratory Stream (15)
Choroid Plexus (16)
D Cells mapped by Loo et al. 2019 E14 cluster annotation
Choroid plexus [22-E]
Endothelial [18-E]
Ganglionic eminences [6-E]
Int1 [1-E]
Int2 [12-E]
LayerI [17-E]
LayerV-VI [13-E]
LayerV-VI [2-E]
LayerV-VI [3-E]
LayerV-VI [5-E]
LayerV-VI [7-E]
Microglia [20-E]
RG1 [8-E]
RG2 [14-E]
RG3 (cortical hem) [21-E]
RG4 [10-E]
Striatal inh1 [16-E]
Striatal inh2 [9-E]
SVZ1 (migrating) [4-E]
SVZ2 (VZ-SVZ) [11-E]
SVZ3 (proliferating) [15-E]
Thalamic [19-E]
UMAP2
4
0
-4
-8
-10
-5
0
5
10
UMAP1
Migrating Neurons(0)
L5-6 Excitatory Neurons (1)
Radial Glia Cells(2)
Intermediate Progenitors (3)
Migrating Neurons (4)
L5-6 Excitatory Neurons (5)
Radial Glia Cells (6)
Interneurons (7)
Radial Glia Cells (8)
L5-6 Excitatory Neurons (9)
Intermediate Progenitors (10)
Radial Glia Cells (11)
Cajal Retzius (12)
Endothelial (13)
Endothelial (14)
Microglia (15)

Supplemental Fig. 3.5. Alignment of *Asxl3* datasets with E14.5 and P0 Loo et. al 2019 open source data UMAP of our **A,** P0.5 and **B,** E14.5 scRNA-seq data with colors and clustering assignment derived from Loo et al. 2019 P0.5 and E14.5 annotations. **C,** P0.5 and **D,** E14.5 UMAP plots displaying cells that align to previously published cell types detected in Loo et al. 2019 P0.5 and E14.5 datasets.

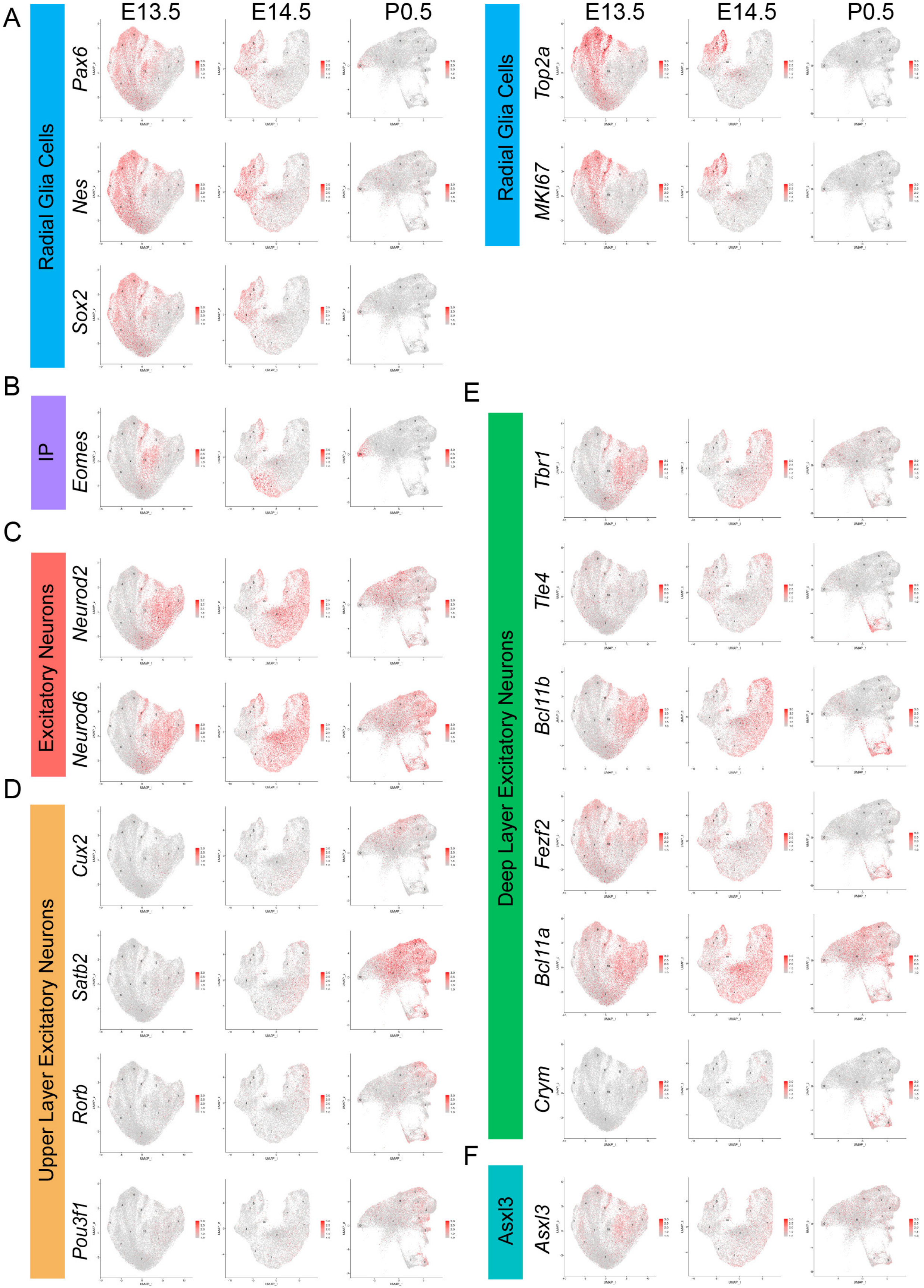
A
Radial Glia Cells
E13.5
E14.5
P0.5
Pax6
Nes
Sox2
Radial Glia Cells
E13.5
E14.5
P0.5
Top2a
MKI67
B
IP
Eomes
C
Excitatory Neurons
Neurod2
Neurod6
D
Upper Layer Excitatory Neurons
Cux2
Satb2
Rorb
Pou3f1
E
Deep Layer Excitatory Neurons
Tbr1
Tle4
Bcl11b
Fezf2
Bcl11a
Crym
F
Asxl3
Asxl3
UMAP_1
UMAP_2

Supplemental Fig. 3.6. Characterization of E13.5, E14.5, and P0.5 excitatory cell types E13.5, E14.5, and P0.5 feature plots showing the expression of known markers for **A,** radial glia cells, **B,** intermediate progenitors (IP), **C,** excitatory neurons, **D,** upper layer excitatory neurons, and **E,** deep layer excitatory neurons. **F,** E13.5, E14.5, and P0.5 feature plots showing the expression of *Asxl3*.

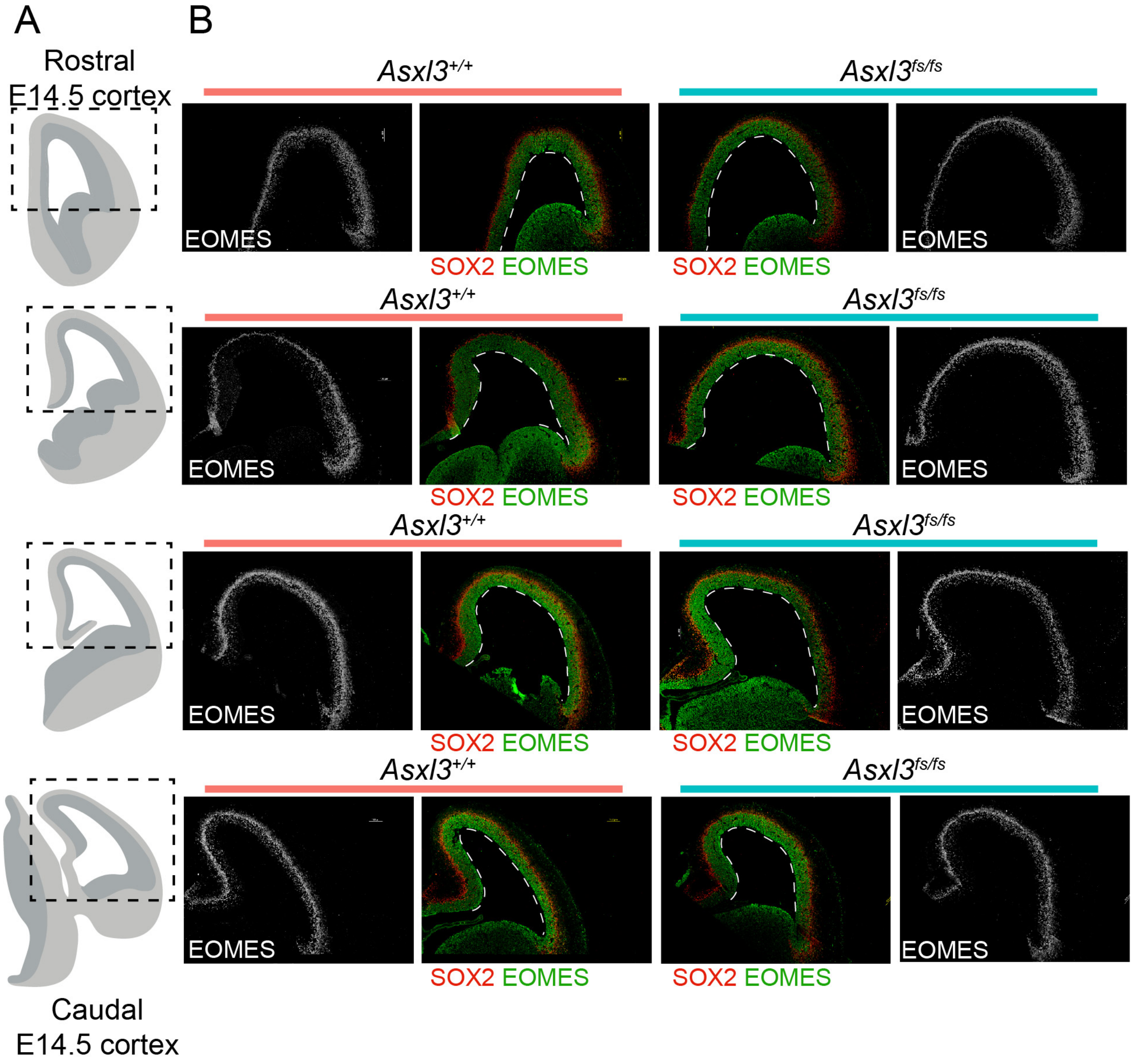
A
B
Rostral
E14.5 cortex
Asxl3+/+
Asxl3fs/fs
EOMES
SOX2 EOMES
Caudal
E14.5 cortex

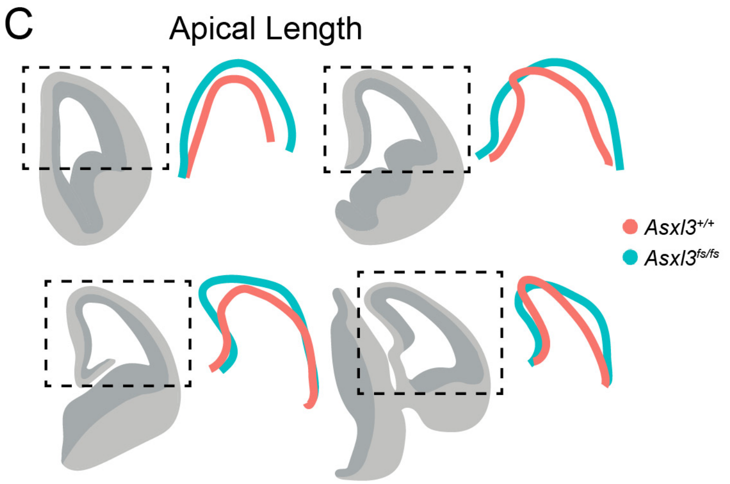
C
Apical Length
Asxl3+/+
Asxl3fs/fs

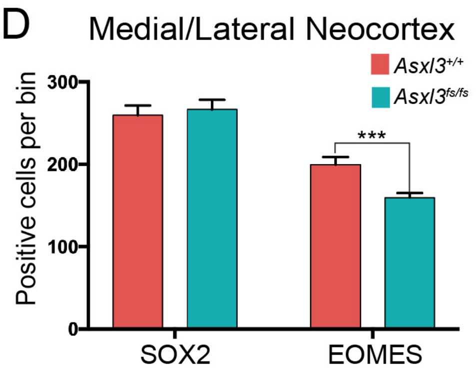
D
Medial/Lateral Neocortex
Asxl3+/+
Asxl3fs/fs
Positive cells per bin
300
200
100
0
***
SOX2
EOMES

Supplemental Fig. 3.7. Expansion of NPCs A, Schematic illustrating coronal sections of rostral to caudal neocortical regions used for immunohistochemistry and apical length quantification. **B,** Immunohistochemical staining of *Asxl3*$^{+/+}$ (left) and *Asx3*$^{fs/fs}$ (right) E14.5 coronal cortical sections with SOX2 (Green) and EOMES (grey, red) at different regions of the rostrocaudal axis. **C,** Comparison of *Asxl3*$^{+/+}$ (red) and *Asxl3*$^{fs/fs}$ (blue) apical lengths across the E14.5 neocortex. **D,** Quantification of the number of cells expressing SOX2 or EOMES in the medial/lateral neocortex in *Asxl3*$^{+/+}$ (n=6) and *Asx3*$^{fs/fs}$ (n=6) mice. p=0.699 (SOX2), p=1.8x10^{-4} (EOMES) using two-tailed unpaired Student's t test. *p<0.05, **p<0.01, ***p<0.001.

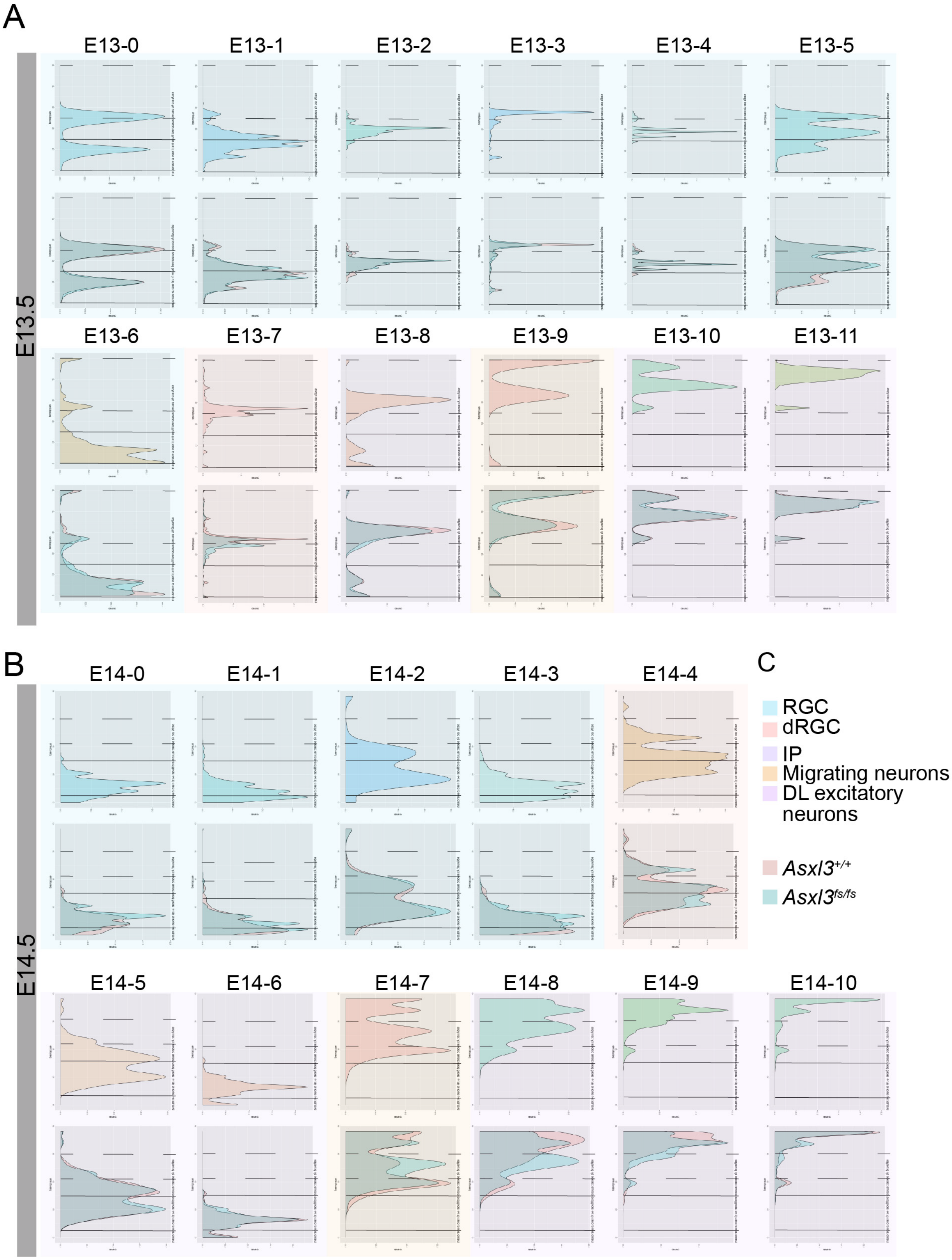
A
E13-0
E13-1
E13-2
E13-3
E13-4
E13-5
E13-6
E13-7
E13-8
E13-9
E13-10
E13-11
E13.5
B
E14-0
E14-1
E14-2
E14-3
E14-4
E14-5
E14-6
E14-7
E14-8
E14-9
E14-10
E14.5
C
RGC
dRGC
IP
Migrating neurons
DL excitatory neurons
Asxl3+/+
Asxl3fs/fs

Supplemental Fig. 3.8. E13.5 and E14.5 pseudotime analysis by cluster Monocle 3 pseudotime analysis showing the pseudotime histograms for individual **A,** E13.5 and **B,** E14.5 clusters. The top graph shows the psuedotime ordering for the entire cluster. The bottom graph is colored by genotype (Asxl3$^{+/+}$, red; Asxl3$^{fs/fs}$, blue). Pseudotime maps are grouped by cell types. **C,** Legend depicting the cell type colors.

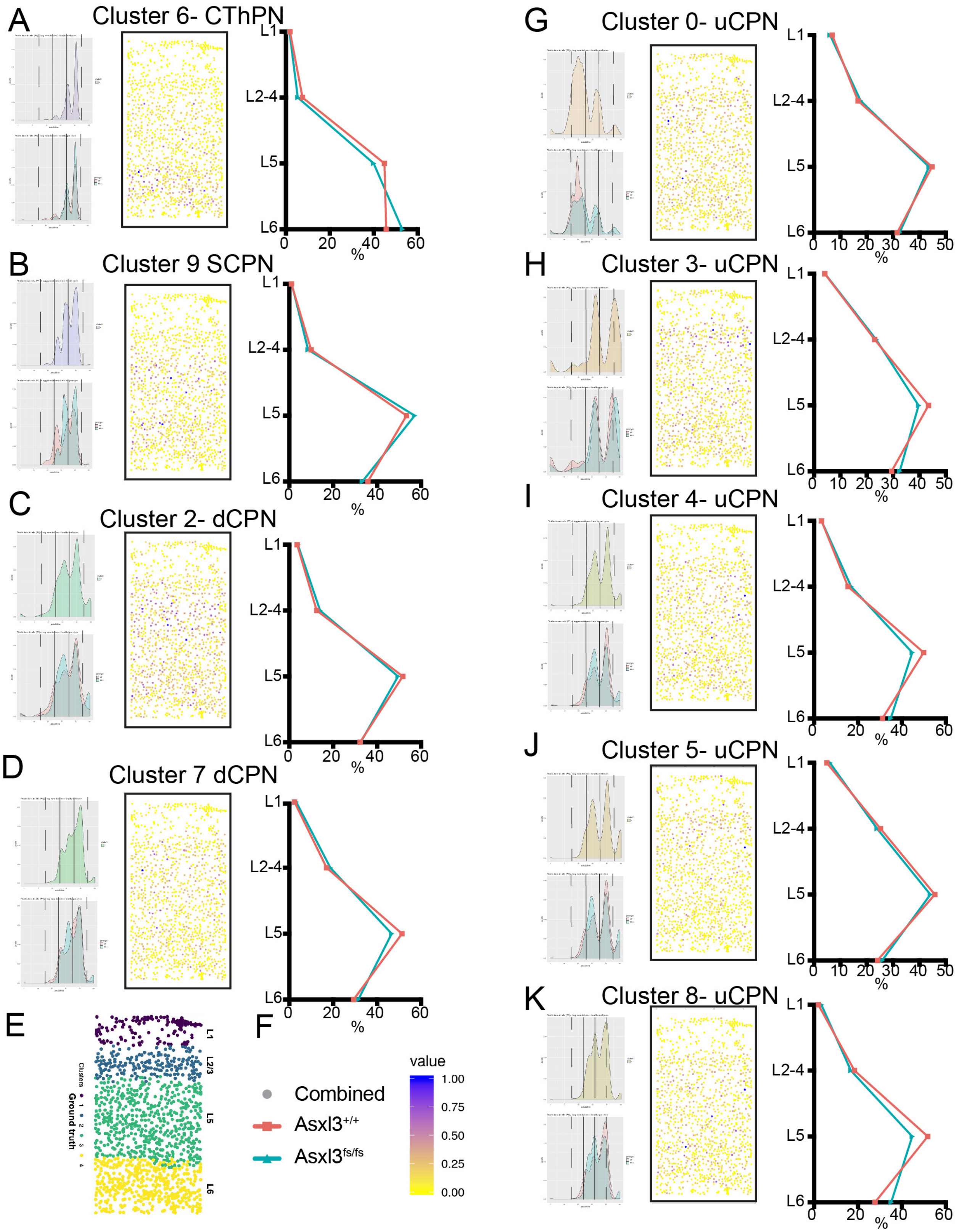
A
Cluster 6- CThPN
B
Cluster 9 SCPN
C
Cluster 2- dCPN
D
Cluster 7 dCPN
E
F
G
Cluster 0- uCPN
H
Cluster 3- uCPN
I
Cluster 4- uCPN
J
Cluster 5- uCPN
K
Cluster 8- uCPN
L1
L2-4
L5
L6
0
10
20
30
40
50
60
%
L1
L2/3
L5
L6
Clusters
Ground truth
1
2
3
4
● Combined
Asxl3$^{+/+}$
Asxl3$^{fs/fs}$
value
1.00
0.75
0.50
0.25
0.00

Supplemental Fig. 3.9. Tangram mapping of P0.5 *Asxl3*$^{fs/fs}$ scRNA-seq data to STARmap spatial transcriptomic data Left: Monocle 3 pseudotime analysis showing the pseudotime histograms for individual P0.5 clusters identified by scRNA-seq. Middle: probabilistic mapping of our single cell gene expression data onto STARmap spatial gene expression data (Wang et al. 2018) using Tangram (Biancalani et al. 2020). Dots colored by the probability of our cell type mapping to the STARmap cell type (blue high probability, yellow low probability). Right: Distribution of cells mapping to spatial gene expression data for L6, L5, L2-4, and L1. Each analysis was performed for **A,** cluster P0-6 CThPN cells **B,** cluster P0-9 SCPN, **C,** cluster P0-2 dCPN, **D,** cluster P0-7 dCPN, **G,** Cluster P0-0 uCPN, **H,** Cluster P0-3 uCPN, **I,** Cluster P0-4 uCPN, **J,** Cluster P0-5 uCPN, **K,** Cluster P0-8 uCPN. Distributions are colored by genotype (*Asxl3*$^{+/+}$ red, *Asxl3*$^{fs/fs}$ blue). **E,** Spatial localization of cell types. **F,** Figure legend for corresponding plots and graphs.

Chapter 4

Conclusion

With major advances in DNA sequencing technologies, the genetic etiology of many diseases are being uncovered. Surprisingly, pathogenic variants in genes involved in chromatin regulation are being described as a genetic basis for an increasing number of diseases including cancer, neurodevelopmental disorders, congenital heart defects, and others. A myriad of pathogenic variants in these disease genes encoding chromatin proteins have been described, yet comparatively few have been functionally characterized. For my dissertation, I used human genetics as a tool to generate clinically relevant hypotheses and functionally validate pathogenic variants in *ASXL3.* My investigation of the *Asxl3*$^{fs/fs}$ mouse showed that loss of ASXL3 was responsible for elevated levels of H2AUb1. The increase in H2AUb1 was correlated with changes in progenitor behavior and fate specification during the development of multiple organ systems. Investigation of cardiac and neurodevelopmental defects suggest that ASXL3-dependent H2AUb1 is important for generating the transcriptional plasticity required for key cell fate decisions and important developmental processes during organogenesis.

Histone H2AUb1 regulatory axis in development

During early development, multipotent cells must restrict their fate in a highly regulated manner to ensure the production of the right mature cell types in the right locations. Chromatin plasticity and the dynamic addition and removal of chromatin marks is an important aspect of this fate specification process [1]. The balance between cell proliferation and cell fate determination is critical to forming organs with the right shape and size and the right cell composition [2]. PcG proteins have emerged as central players in epigenetic programming events during mammalian development [3]. Polycomb transcriptional repression plays a critical role in pluripotent stem cells to help suppress differentiation and maintain the potential to differentiate into specific lineages [4-9]. Dynamic chromatin modifications, like H2AUb1, play important roles in defining stem cell identities and plasticity. They contribute to the establishment and maintenance of chromatin states that allow for spatial and temporal regulation of transcription profiles [10]. Although Histone H2A mono-ubiquitination was discovered more than three decades ago, its function as a transcriptional regulator and epigenetic repressor remain poorly understood compared to other histone modifications. In Chapter 1, we discuss the human genetic evidence for H2AUb1 regulatory axis components which implicates an important role for this modification during the development of multiple organ systems. Pathogenic variants in components of Polycomb repressive complex 1 (PRC1), which catalyzes ubiquitination of H2A, are the genetic basis of autism spectrum disorder (ASD), intellectual disability (ID), primary microcephaly, Oculofaciocardiodental syndrome, and Lenz microphthalmia syndrome [11-16]. Conversely, mutations in components of the Polycomb repressive deubiquitination complex (PR-DUB), which deubiquitinates H2AUb1, are the genetic basis for ASD, Bohring-Opitz syndrome, and Bainbridge-Ropers syndrome (BRS) [17-23]. These human genetics findings highlight the important role for dynamic exchange of H2A ubiquitination in neurodevelopment and associated disorders [24]. Our findings that H2AUb1 levels are significantly increased upon loss of ASXL3 in multiple systems implicates it is a key molecular pathology associated with pathogenic variants. However, the role of histone H2A mono-ubiquitination remained undefined during development and, specifically, in the pathophysiology of *ASXL3* mutations [10, 25]. This important scientific question served as the basis of my thesis research.

The role of Asxl3 in heart development

In chapter 2, we discuss the role of ASXL3 in cardiac development by using a biallelic frameshift *Asxl3* mouse model and cardiac tissue differentiated from biallelic frameshift *ASXL3* human embryonic stem cell (hESC) lines. Our study was the first to describe hypoplastic right ventricles in an *Asxl3* mouse model. Single ventricle CHDs, including hypoplastic right heart syndrome (HRHS) and hypoplastic left heart syndrome (HLHS), occur in ~3.1-4.9 per 10,000 live births [26]. HLHS and HRHS are characterized by underdeveloped or malformed structures of a single ventricle. Several potential pathological mechanisms centered around blood flow or balance of proliferation and differentiation programs in the SVD heart have been suggested. The increased proliferation we observe in $Asxl3^{fs/fs}$ ventricles provides further evidence for the second model, but cannot rule out a role for hemodynamics as it was not assessed.

Our mouse and human transcriptomic studies implicate alterations in extracellular matrix (ECM) composition as the basis of these developmental defects. A growing number of human and mouse genetic studies of SVDs provide similar evidence suggestive of a common disrupted molecular pathway [27-32]. The extracellular matrix plays a central role in many processes throughout heart development including cell migration, cardiomyocyte proliferation, differentiation and maturation, chamber formation, and valve development. The spatial programs of cardiac organogenesis are modulated by a multitude of intracellular and extracellular cues transmitted via the extracellular matrix (ECM) [33]. Given this broad role of the ECM during cardiogenesis, systematic deletion of *Asxl3* at multiple developmental time points and cell types will be necessary to determine its precise developmental and molecular function in ECM regulation. Use of heart-field specific CRE lines should also be used to investigate the laterality of ventricular hypoplastic heart phenotypes and how altered ECM dynamics contribute to asymmetric expressivity. Additional ASXL3 and H2AUb1 genome-wide profiling studies will be important for resolving if altered differentiation of cardiac lineages initiates a cascade of ECM composition changes and cell-cell signaling defects, or if chromatin changes directly alter expression of ECM components.

This study highlights the importance of conducting analysis in multiple model systems. While alterations in extracellular matrix (ECM) composition contribute to the pathogenic mechanisms in both species, the distinct genetic and molecular details of each pathogenic mechanism are species-specific not a direct phenocopy. These findings highlight species similarities and differences that can be important for identifying therapeutic targets. Our heart analysis also speaks to the dosage-sensitivity of ASXL3 during development and sheds light on the partial penetrance of congenital heart defects associated with mono-genetic etiologies of ASD. These phenotypic outcomes provide further evidence for the importance of chromatin biology and Polycomb transcriptional repression in heart development.

Human genetic studies have identified chromatin genes as a growing genetic basis of congenital heart defects (CHDs) [34-36]. In particular CHD causing damaging de novo mutations are enriched in ASD-associated chromatin modifiers, suggesting a link between cardiac and neurodevelopment [34]. Notably, defects in ECM have been observed in other models investigating the role of chromatin genes in cardiac development. This suggests that cardiac ECM is vulnerable to genetic perturbations and/or a common pathogenic mechanism is shared between a subset of chromatin genes. Functional studies of these chromatin genes identified in CHD human genetic studies should be conducted to identify shared molecular and developmental phenotypes. This kind of work is important not only for expanding our understanding of early development, but also for providing potential targets for therapeutics for the patients with these disorders.

Fate specification and developmental mechanisms during neurodevelopment

During cortical development, neural progenitor cells (NPCs) produce mature neuronal subtypes in a defined temporal order [37]. This process occurs in an inside out fashion beginning with the production of layer 6, then layer 5, and finally layers 2-4. Mature cortical neurons in each layer display distinct morphologies, axonal projections, and gene expression patterns that defines their ultimate function [37]. How NPCs generate the neuronal diversity in the cerebral cortex required for proper function has been heavily debated. Early transplant and birth-dating studies indicate that NPCs progenitors gradually restrict their fate over the period of neurogenesis [38-40]. An alternative model suggests that there are distinct progenitors that produce restricted lineages [41, 42]. Consistent with emerging single cell studies of neurogenesis [43, 44], our scRNA profiles of NPCs at multiple developmental time points supports a progressive linear restrictive model [45]. We find that the progenitors at E13.5 and E14.5 are clustered by cell cycle and express broad progenitor programs suggesting that cortical neuron subtypes are sequentially generated through progressive lineage restriction of a common NPC [10, 39, 40, 46-54]. Thus, it remains unclear how exactly distinct neuron types emerge from a seemingly uniform pool of progenitor cells [55]. The mechanism of selective fate restriction and the control of timing during this process is not fully understood.

Prior research into the regulatory molecules that instruct mature cortical neuron fate has focused on individual proneural transcription factors (TFs). These studies have shown that a complex and mutually inhibitory proneural transcription factor cascade controls the fate of NPCs [47, 51, 53, 56-59]. These layer-defining transcription factors actively repress alternative fates while promoting the expression of transcriptional programs [37, 56, 60]. Therefore spatiotemporal regulation of this transcription circuitry is required by NPC for proper fate specification. These findings have shown that individual TFs, or networks of TFs alone are *insufficient* to account for dynamic gene regulation that precisely specifies the diverse fates of neurons descended from a single progenitor pool [61]. Our work provides another data point that suggests that chromatin regulation allows for spatial and temporal regulation of transcription profiles required for neurogenesis [10]. In the P0.5 *Asxl3*$^{fs/fs}$ cortex, we observe a loss of BCL11B+ layer 5 neurons that suggests altered expression of transcriptional programs that direct fate. In accordance with this, our developmental scRNA-seq results revealed dysregulation of proneural genes, including *Fezf2* and *Sox4*, that participate in the L5 regulatory network. Notably, Fezf2 and Sox4 loss-of-function mouse models display a similar reduction in BCL11B+ layer 5 neurons [53, 62]. Similar to other proneural fate specification genes, deletion or ectopic expression of Fezf2 or Sox4 causes a fate switch of neurons to an alternative identity [44, 60, 62, 63]. In these models, the absent BCL11B+ layer 5 neurons are replaced by cells expressing multiple genetic programs of distinct cell types [44]. In accordance with this, we detect cells aberrantly expressing layer specific genes of other subtypes in our P0.5 scRNA-seq data. In addition, pseudotime analysis revealed an *Asxl3*$^{fs/fs}$-specific shift in layer 5 neurons consistent with a change in the transcriptional program being expressed. Together these findings support the idea that misexpression of subtype-specific genes can result in transformations of neuronal identity.

We showed that loss of ASXL3 alters the behavior of progenitors and leads to changes in the timing of differentiation during early development. Our data provides a new link between extrinsic signaling cues and intrinsic epigenetic regulation that together control the timing of cell fate programs. The phenotypic and transcriptomic overlap of *Asxl3*$^{fs/fs}$ and Notch gain-of-function mouse models implicates a role for ASXL3-dependent Notch signaling. Recent high-throughput proteomic and biochemical analysis found that RING1 (Ring1a) and RNF2 (Ring1b) are interacting partners with the Notch intracellular domain (NICD) [64, 65]. This link between Notch and PRC1 is further strengthened by extensive overlap between NICD and PRC1 binding sites and the finding that inhibition of Notch signaling results in reduced recruitment of PRC1 components to target sites [65, 66]. Together this data suggests an interplay between the cell-intrinsically established Polycomb chromatin state and the cell-extrinsic Notch signal during transcriptional regulation. Future studies will need to investigate the molecular mechanism of this interaction during neurogenesis and how ASXL3 integrates these cues to inform cell decisions. This emerging interplay is being described for a growing number of ASD chromatin genes which disrupt the timing of neurogenesis [67-69]. Additional analysis will be important to understand how the extrinsic Notch signaling cues and intrinsic epigenetic regulation ultimately controls the timing of cell fate programs. In particular, how they coordinate broader neurogenic programs with the expression of fate specification programs during discrete temporal windows.

Convergence of autism models and implications for ASD comorbidities

Autism spectrum disorder (ASD) manifests as impairments in social communications and interactions as well as repetitive or restrictive behavior and commonly occurs with other clinical features termed co-morbidities [70]. Since the initial family and twin studies that demonstrated the large genetic contribution to ASD, hundreds of ASD associated genes have been identified [71-74]. ASD may present in vastly different ways, but it is thought that there is a common set of pathways and molecular players whose disruption can be linked to many of these disorders [75]. These common pathways are not yet known, and it is unclear how variants in so many genes with different functions can lead to similar phenotypes [76]. The genetic heterogeneity has made ASD difficult to study, and research thus far has failed to fully understand what contributes to some of the common phenotypes. Enrichment analysis revealed that pathogenic ASD variants commonly occur in chromatin, transcriptional, and synaptic genes [77-79]. This highlights a role for these cellular mechanisms in ASD biology, however it is unclear which developmental processes are controlled by these pathways and how dysregulation contributes to ASD pathogenesis.

Studies of post-mortem ASD tissues have uncovered cortical abnormalities with changes to mature neuron organization, neuron morphology and cortical connections implicating dysregulation of cortical development [80]. Co-expression of many ASD-risk genes peaks during mid-fetal stages of human neocortical development, further implicating a developmental basis of ASD neuropathology [81]. Assessment of ASD mouse models reveal disturbances in fundamental neocortical developmental processes including neurogenesis, neuronal migration, cortical lamination, neuronal morphogenesis and synaptogenesis [82]. Determining which ASD-risk genes affect the similar developmental processes will be critical for determining how distinct neurobiological mechanisms can lead to parallel social deficits or comorbidities.

ASXL3 has repeatedly emerged in large scale human genetic studies as a high confidence syndromic ASD risk gene with high effect size [78, 83]. Given its role as a chromatin regulator, we predicted that *Asxl3* might act as a hub gene and influence other known ASD risk genes. We hoped studying *Asxl3* would provide insights into how genetics contribute to ASD pathology and the shared pathogenic mechanism that links the functional gene groups. In humans, ASXL3 is highly expressed in the first 24 gestational weeks of the developing human brain, a spatiotemporal window of brain development significantly enriched for ASD genes [21, 81, 84]. Consistent with a function in neurogenesis we detect cortical expression of ASXL3 in the cortex during mouse neurodevelopment. To investigate the function of ASXL3 in neurodevelopment, we generated a mouse model with a two base-pair deletion in *Asxl3*, corresponding to homologous nucleotides classified as pathogenic *ASXL3* BRS/ASD variants.

Through our investigation of the *Asxl3*$^{fs/fs}$ mouse, we identified multiple developmental defects that shed light on neuropathological mechanisms underlying ASD. The cortical lamination defects we detect in *Asxl3*$^{fs/fs}$ mice support the altered cortical cytoarchitecture described in ASD post-mortem tissue. By performing a series of scRNA-seq experiments throughout corticogenesis, we identified abnormal NPC dynamics due to extrinsic signaling pathways that disrupt the developmental trajectory of mature neurons. In mice, modulation of the these signaling pathways result in altered cortical neuron production and ASD-like social deficits [82, 85-88]. A recent study found that altered developmental timing during neurogenesis is a shared feature of multiple human *in vitro* ASD models [89]. A separate analysis exploring the impact of *ASXL3*$^{fs/fs}$ on human neuronal differentiation found it caused decreased neuronal output and enrichment for NPCs [90]. This phenotype resembles the expansion of NPCs we detect in our *Asxl3*$^{fs/fs}$ mice and implicates a shared pathological mechanism between mouse and human models. Notably, in this study the other ASD risk genes that similarly caused a reduced neurogenic capacity were involved with Polycomb transcriptional repression [90]. Together with our data, this evidence suggests that Polycomb transcriptional repression is needed by NPCs to regulate the timing of differentiation and that there is potentially a unique disrupted mechanism that alters the neurogenic phase in a subset of ASD risk genes.

In agreement with Asxl3 acting as an ASD hub, we detect dysregulation of other known ASD risk genes at all three developmental time points profiled. This is a common transcriptional feature of several human and mouse ASD models [67, 91-96]. At the early developmental stages the dysregulated genes are associated with transcription and chromatin remodeling, while the DEGs at later stages are associated with synapse development and function. This provide insight into how molecular dysfunction at the chromatin level can affect developmental mechanisms which has downstream consequences on synaptic function/circuit formation and ultimately on behavior. Future studies, will need to determine if *Asxl3*$^{fs/fs}$ initiates a developmental defect that is compounding and results in synaptic dysfunction, or if it directly regulates synaptic genes.

The overlapping phenotypes in ASD mouse models we describe here provides evidence for a shared molecular mechanism. Exploring these common mechanisms of ASD will require systematic functional investigation of many ASD risk genes in multiple model systems to understand the distinct neuropathological mechanisms. Comparison of the convergent mouse data with the human phenotypes will be important to understand the conservation of molecular mechanisms during neurodevelopment. These studies will not only provide important insights about developmental mechanisms that contribute to ASD neuropathology, but also highlight potential therapeutic targets.

Genetic mechanisms contributing to clinical features and therapeutic implications

Genotype-phenotype correlation studies demonstrate that the number and severity of clinical features can vary substantially among patients with overlapping genetic etiology [75]. Substantial variability in the severity of BRS clinical features, exhibited by individuals with variants in *ASXL3*, suggests that deleterious variants may be acting by more than one pathogenic mechanism [108]. Irrespective of pathogenic *ASXL3* variant, BRS does not exhibit a consistent genotype-phenotype correlation, complicating genetic diagnosis and development of research models. While *de novo* germline truncating variants in

ASXL3 are often reported as pathogenic variants, missense variants in *ASXL3* do not exhibit the same fidelity to being pathogenic. From a research perspective, the diffuse *ASXL3*-BRS genotype-phenotype correlation warrants additional investigation into the pathogenic mechanisms of *ASXL3* variants, to account for haploinsufficiency, dominant-negative and toxic gain-of-function mechanisms of action in affected tissue. A myriad of pathogenic variants in these disease genes encoding chromatin proteins have been described, yet comparatively few have been functionally characterized. Here we investigated a single clinically relevant $Asxl3^{fs}$ allele during development. Comprehensive functional validation of pathogenic variants has the potential to make important basic science, translational, and therapeutically important discoveries. By systematically evaluating human genetics and epigenetics, therapeutic targets and new strategies for regeneration can be devised.

The options for therapeutic interventions, including CRISPR and ASO technologies are rapidly expanding and evolving. Mechanisms for safe delivery of nucleotide-based therapies are improving. Recent data suggests that some of the transcriptional and/or behavioral changes in mice are reversed by restoring expression or function of ASD risk genes in the adult brain [109]. Furthermore chromatin plasticity creates a potential for therapeutic targeting to reverse disease phenotypes. Realization of epigenetic therapies depends on a careful characterization of the genetic mechanism and spatiotemporal molecular pathology at the single-cell level. My work demonstrates that performing this analysis for multiple experimental conditions or developmental timepoints in clinically relevant tissues is critical to elucidate this dynamic chromatin biology.

Nonoverlapping roles for Asxl1/2/3 PR-DUB complexes during development

The PR-DUB complex is composed of an individual ASXL (additonal sex combs-like) family member (ASXL1, ASXL2 or ASXL3) and the ubiquitin C-terminal hydrolase BAP1. The ASXL protein functions as the mutually exclusive obligate regulatory subunits of the PR-DUB complex required to impart BAP1 histone H2A deubiquitination activity and target BAP1 DUB activity genome-wide [110, 111]. *De novo* dominant *ASXL1, ASXL2,* and *ASXL3* variants are the genetic basis of Bohring-Opitz syndrome, Sashi-Pena syndrome and Bainbridge-Ropers syndrome (BRS)/syndromic ASD respectively [18, 112, 113]. Consistent with the obligate role of ASXL proteins in PR-DUB, elevated genome-wide histone H2AK119Ub1 levels have been observed in primary tissues evaluated from individuals with ASXL3 variants [114]. Independent of overlapping molecular pathology, non-redundant functions are proposed for *ASXL* genes as ASXL-related disorders are differentiated by a subset of unique clinical features and somatic variants are associated with distinct tumor types. Large scale ASD genetic studies have identified recurrent predicted pathogenic variants in *ASXL3*, but not *ASXL1* or *ASXL2* [83]. ASXL3 exhibits elevated early/mid gestation brain expression, in line with the restricted temporal and spatial parameters ascribed to ASD, further predicting an important role for ASXL3 in cortical development and the developmental mechanisms predicted to be altered in ASD pathogenesis, including abnormal cortical layer cytoarchitecture composition and neuron organization.

FUTURE DIRECTIONS

Determine the functions of ASXL3-dependent H2AUb1 regulation in human models

Here we tested the effects of a single clinically relevant *Asxl3*^{fs} allele during mouse cortical development. Our data suggests that fate specification is altered due to deficits in NPC differentiation. Human cortical development has a longer window of differentiation plus additional progenitor niches. Interpreting our results within the context of human cortical development and pathogenic mechanisms highlights the need for *in vitro* models of human neurodevelopment. Until recently, investigating the neuropathology of human genetic findings was hindered by inaccessible affected tissue. Today, we can confirm our *in vivo* mouse findings, or identify novel human mechanisms of neuropathology, using established protocols to differentiate hESCs to NPCs and cerebral organoids [115-118]. We plan to test the conservation of *ASXL3* pathology and PR-DUB activity in human cerebral organoid models of neural development. We will determine the developmental mechanism of delayed neural differentiation of *ASXL3* mutant hESCs on formation of cortical neurons in cerebral organoids these experiments will provide insights into the developmental origin of the clinically relevant *ASXL3* phenotypes. This approach will allow us to explore human specific and shared epigenomic mechanisms of *ASXL3* pathology. By performing this analysis with NPCs from all *ASXL3* genotypes, we can connect the role of ASXL3 dosage with pathology. These findings and resources provide an exciting opportunity to investigate the molecular mechanisms and transriptional changes generated by reduced *ASXL3* andelevated H2AUb1 in a human in vitro model of neurodevelopment.

Role of dynamic H2AUb1 regulation during neural development

The H2A monoubiqutination regulatory axis is starting to be well characterized in embryonic stem cells (ESCs) [119-123]. These studies provide mechanistic details of its varied functions in ESCs, but investigation of H2AUb1 function in different cellular contexts and biological process remain to be resolved. My thesis sheds light on the regulatory axis during differentiation of multiple tissues. Existing research has not reached a consensus regarding the role of H2AUb1 in regulating gene transcription [121, 123-125]. Experiments with *Ring1B* knockdown, which functions in the PRC1 complex to add the ubiquitin mark to H2A, showed an opposing phenotype to *Asxl3*$^{\mathrm{fs/fs}}$, with increased BCL11B+ L5 neurons [126]. The increase in L5 neurons in *Ring1B* null mice and the decrease in L5 neurons in the *Asxl3* null mice were of roughly the same magnitude. The opposing lamination defects in *Ring1B* and *Asxl3* null mouse models support a role for H2AUb1 in neural differentiation and development. Some researchers claim that the enzymatic activity of RING1B is not necessary for proper embryonic development [124]. Yet, the *Ring1b* enzymatic null mice exhibited increased embryonic lethality and neurological defects, suggesting that *Ring1b* and proper regulation of H2A monoubiquitination is necessary for development. To investigate the role of H2AUb1-dependent PRC1 activity during neurogenesis, we have created a *Ring1a*$^{-/-}$;*Ring1b*$^{fl/I53A}$ line. We will use inducible Cre lines expressed in embryonic dorsal forebrain to leave a single catalytically inactive copy of PRC1 in the developing cortex. Using the same techniques described in chapter 3, we can determine how H2AUb1-dependent PRC1 activity affects the developmental, transcriptomic and epigenetic landscape of neurogenesis. Comparing the phenotypes to the Asxl3$^{\mathrm{fs/fs}}$ mouse should provide additional insights into disrupted developmental mechanisms and help identify targets of

H2AUb1 regulatory axis control. We predict this work will establish the importance of dynamic H2AUb1 in the maintenance and differentiation of NPCs.

H2AUb1 and ASXL3 genome-wide analysis

The molecular mechanism of H2AUb1 and the processes it regulates during normal development and disease remain largely unexplored. We discovered that H2AUb1 dysregulation is a key molecular pathology of *de novo* pathogenic *ASXL3* variants and that these chromatin changes are accompanied by altered transcriptional profiles in differentiated cells [114]. Consistent with these findings, we detect excess levels of global H2AUb1 in multiple developing tissues of *Asxl3*$^{fs/fs}$ mice. During neurogenesis, elevated H2AUB1 levels underlie altered NPC behavior and timing of differentiation. Our scRNA-seq analysis shed light on the impact of H2AUb1 accumulation on the epigenome which results in disrupted expression of signaling pathways and transcriptional networks that drive fate. However, the targets of H2AUb1 re-distribution across the genome and its mechanism at these sites is unclear. We hypothesize that excess H2AUb1 in NPCs alters the chromatin landscape and DNA accessibility required for expression of proneural genes critical fate determination.

Currently, we are profiling H2AUb1 across the genomes of E13.5 NPCs using CUT&RUN analysis, a low input alternative to ChIP-seq [127]. We hope to uncover the epigenomic mechanism of ASXL3-dependent H2AUb1 chromatin remodeling within NPCs necessary for fate determination. Determining epigenomic programs responsible for cell-type-specific phenotypes is complicated by the cellular heterogeneity of developing brain. CUT&RUN is a low input alternative ChIP-seq strategy with high signal to noise ratios, eliminating the need to pool many cortices from several pups. Differential genome-wide distribution of excess H2AUb1 in *Asxl3*$^{+/+}$ and *Asxl3*$^{fs/fs}$ NPCs will be mapped relative to functional elements, such as promoters and correlated to differentially expressed gene. Aberrant regulation of functionally relevant targets in distinct cell types will be molecularly and functionally validated in cell culture and *in vivo* models. We will integrate the scRNA-seq and CUT&RUN data to identify the epigenomic signature and direct targets of NPCs that contribute to NPC behavior and fate specification. This analysis will be important for determining if H2AUb1 directly regulates fate-specific genes or genes involved in extrinsic signaling pathways. Evidence also suggests that developmental remodeling of Polycomb marks at target loci regulates the timing of neurogenesis [126, 128]. Additional studies at other developmental time points will be essential to understand H2AUb1 temporal control and how this affects fate transitions. This work will reveal the chromatin mechanism of H2AUb1 and continue to uncover the role of epigenomics in specification of cortical neuron fate.

While the mammalian PR-DUB complex has been discussed as a single entity, human genetic and biochemical evidence suggests independent functions of ASXL1, ASXL2, and ASXL3 containing PR-DUB complexes [18, 111-113]. Currently, no genome-wide study for ASXL3-dependent deubiquitination activity in NPC and corticogenesis has been reported. We have generated an *Asxl3-V5* tagged mouse model to examine when and how ASXL3 affects expression of its targets. Using CUT&RUN analysis we will map the genomic binding-profile of ASXL3-V5 during neurogenesis. We can integrate this data with the H2AUb1 CUT&RUN data from *Asxl3*$^{fs/fs}$ NPCs to delineate the ASXL3-dependent chromatin distribution of H2AUb1. The analysis can uncover the ASXL3 DNA binding-motif and define developmentally important gene networks regulated by ASXL3-dependend H2AUb1 [129, 130]. Systematic evaluation of ASXL1/2/3 genomic distribution across multiple stages of development will be critical for defining specificity and overlap between the PR-DUB complexes. Differential distribution of ASXL family members may provide insight into the distinct BOS, SPS, and BRS neurodevelopmental clinical phenotypes.

Stage-specific requirements for Asxl3 during neurogenesis

The variability in phenotypic manifestation of pathogenic variants can depend on when in development and where in the nervous system the gene is operating. Given that our *Asxl3*^{fs} allele is a germline variant, it raises the question of what initially drives the pathogenic mechanism we detect and what processes are being disrupted. Our data strongly implicates a role for *Asxl3* in cortical neurons production during neurogenesis. However, it will be important to determine if the altered specification in *Asxl3*$^{fs/fs}$ represents a role for ASXL3 in (1) the sequential restriction of NPC multipotency, or (2) for establishing the mature L5 cortical neuron fate during differentiation of postmitotic neurons. With scRNA-seq, we detect early developmental changes in extrinsic signaling pathways and fate-specific genes that promote progenitor maintenance and alter differentiation. By P0.5 this leads to differential expression of axonal and synaptic genes. It is unclear from our *Asxl3*$^{fs/fs}$ mouse model if these transcriptional changes at P0.5 are caused by a developmental defect that's compounding and results in synaptic dysfunction, or if ASXL3 directly regulates synaptic genes. We have generated the *Asxl3* conditional mouse *Asxl3*$^{\text{flox/flox}}$ to systematically characterize deletions of *Asxl3* in distinct cell types and developmental timepoints. To define the stage- and cell type-dependent requirements for ASXL3 function, we will use tissue and cell-type specific inducible Cre lines expressed in embryonic dorsal forebrain. These comparative studies will enable us to elegantly dissect the cell type-dependent requirements for ASXL3 and potentially uncover novel therapeutic targets. Furthermore, the conditional *Asxl3* mouse will allow us to circumvent perinatal lethality to investigate defects in cerebellar development and to explore behavior phenotypes linked to *Asxl3*$^{fs/fs}$ neuropathology.

FINAL THOUGHTS

Overall, this work uncovers novel roles of the Histone H2A monoubiquitinaiton regulatory axis in the development of multiple organ systems. It highlights the importance of exploring the role of chromatin genes in clinically relevant organ systems. While Asxl3 dependent H2AUb1 influenced cell proliferation and cell fate determination in both cardiac and neural systems, the genes and processes it regulated were quite different. Our data provides insight into how insults to development can have downstream consequences that lead to pathogenic phenotypes. Not only is this work applicable to BRS patients and the search for potential therapeutics for BRS patients, but it also provides further insights into normal developmental process and creates a foundation for studying other developmental disorders.

REFERNCES:

1. Yadav, T., J.P. Quivy, and G. Almouzni, *Chromatin plasticity: A versatile landscape that underlies cell fate and identity.* Science, 2018. **361**(6409): p. 1332-1336.
2. Kobayashi, T. and R. Kageyama, *Expression dynamics and functions of Hes factors in development and diseases.* Curr Top Dev Biol, 2014. **110**: p. 263-83.
3. Di Croce, L. and K. Helin, *Transcriptional regulation by Polycomb group proteins.* Nat Struct Mol Biol, 2013. **20**(10): p. 1147-55.
4. Bernstein, B.E., et al., *A bivalent chromatin structure marks key developmental genes in embryonic stem cells.* Cell, 2006. **125**(2): p. 315-26.
5. Ezhkova, E., et al., *Ezh2 orchestrates gene expression for the stepwise differentiation of tissue-specific stem cells.* Cell, 2009. **136**(6): p. 1122-35.
6. Oguro, H., et al., *Poised lineage specification in multipotential hematopoietic stem and progenitor cells by the polycomb protein Bmi1.* Cell Stem Cell, 2010. **6**(3): p. 279-86.
7. Aloia, L., B. Di Stefano, and L. Di Croce, *Polycomb complexes in stem cells and embryonic development.* Development, 2013. **140**(12): p. 2525-34.
8. Piunti, A. and A. Shilatifard, *Epigenetic balance of gene expression by Polycomb and COMPASS families.* Science, 2016. **352**(6290): p. aad9780.
9. Tsuboi, M., Y. Hirabayashi, and Y. Gotoh, *Diverse gene regulatory mechanisms mediated by Polycomb group proteins during neural development.* Curr Opin Neurobiol, 2019. **59**: p. 164-173.
10. Corley, M. and K.L. Kroll, *The roles and regulation of Polycomb complexes in neural development.* Cell Tissue Res, 2015. **359**(1): p. 65-85.
11. Gao, Z., et al., *An AUTS2-Polycomb complex activates gene expression in the CNS.* Nature, 2014. **516**(7531): p. 349-54.
12. Awad, S., et al., *Mutation in PHC1 implicates chromatin remodeling in primary microcephaly pathogenesis.* Hum Mol Genet, 2013. **22**(11): p. 2200-13.
13. Ng, D., et al., *Oculofaciocardiodental and Lenz microphthalmia syndromes result from distinct classes of mutations in BCOR.* Nat Genet, 2004. **36**(4): p. 411-6.
14. Hilton, E., et al., *BCOR analysis in patients with OFCD and Lenz microphthalmia syndromes, mental retardation with ocular anomalies, and cardiac laterality defects.* Eur J Hum Genet, 2009. **17**(10): p. 1325-35.
15. Adorno, M., et al., *Usp16 contributes to somatic stem-cell defects in Down's syndrome.* Nature, 2013. **501**(7467): p. 380-4.
16. Pierce, S.B., et al., *De novo mutation in RING1 with epigenetic effects on neurodevelopment.* Proc Natl Acad Sci U S A, 2018. **115**(7): p. 1558-1563.
17. Hoischen, A., et al., *De novo nonsense mutations in ASXL1 cause Bohring-Opitz syndrome.* Nat Genet, 2011. **43**(8): p. 729-31.
18. Bainbridge, M.N., et al., *De novo truncating mutations in ASXL3 are associated with a novel clinical phenotype with similarities to Bohring-Opitz syndrome.* Genome Med, 2013. **5**(2): p. 11.
19. Srivastava, A., et al., *De novo dominant ASXL3 mutations alter H2A deubiquitination and transcription in Bainbridge-Ropers syndrome.* Hum Mol Genet, 2015.

20. Dinwiddie, D.L., et al., *De novo frameshift mutation in ASXL3 in a patient with global developmental delay, microcephaly, and craniofacial anomalies.* BMC Med Genomics, 2013. **6**: p. 32.
21. De Rubeis, S., et al., *Synaptic, transcriptional and chromatin genes disrupted in autism.* Nature, 2014. **515**(7526): p. 209-15.
22. Balasubramanian, M., et al., *Delineating the phenotypic spectrum of Bainbridge-Ropers syndrome: 12 new patients with de novo, heterozygous, loss-of-function mutations in ASXL3 and review of published literature.* J Med Genet, 2017.
23. Kuechler, A., et al., *Bainbridge-Ropers syndrome caused by loss-of-function variants in ASXL3: a recognizable condition.* Eur J Hum Genet, 2017. **25**(2): p. 183-191.
24. Srivastava, A., B. McGrath, and S.L. Bielas, *Histone H2A Monoubiquitination in Neurodevelopmental Disorders.* Trends Genet, 2017. **33**(8): p. 566-578.
25. Xie, W., et al., *Epigenomic analysis of multilineage differentiation of human embryonic stem cells.* Cell, 2013. **153**(5): p. 1134-48.
26. Garcia, A.M., J.T. Beatty, and S.J. Nakano, *Heart failure in single right ventricle congenital heart disease: physiological and molecular considerations.* Am J Physiol Heart Circ Physiol, 2020. **318**(4): p. H947-H965.
27. Grossfeld, P., et al., *Hypoplastic Left Heart Syndrome: A New Paradigm for an Old Disease?* J Cardiovasc Dev Dis, 2019. **6**(1).
28. Trivedi, C.M., et al., *Hopx and Hdac2 interact to modulate Gata4 acetylation and embryonic cardiac myocyte proliferation.* Dev Cell, 2010. **19**(3): p. 450-9.
29. Montgomery, R.L., et al., *Histone deacetylases 1 and 2 redundantly regulate cardiac morphogenesis, growth, and contractility.* Genes Dev, 2007. **21**(14): p. 1790-802.
30. Liu, X., et al., *The complex genetics of hypoplastic left heart syndrome.* Nat Genet, 2017. **49**(7): p. 1152-1159.
31. Gaber, N., et al., *Fetal reprogramming and senescence in hypoplastic left heart syndrome and in human pluripotent stem cells during cardiac differentiation.* Am J Pathol, 2013. **183**(3): p. 720-34.
32. Davies, B., et al., *Differences in extra-cellular matrix and myocyte homeostasis between the neonatal right ventricle in hypoplastic left heart syndrome and truncus arteriosus.* Eur J Cardiothorac Surg, 2008. **34**(4): p. 738-44.
33. Del Monte-Nieto, G., et al., *Basic Biology of Extracellular Matrix in the Cardiovascular System, Part 1/4: JACC Focus Seminar.* J Am Coll Cardiol, 2020. **75**(17): p. 2169-2188.
34. Jin, S.C., et al., *Contribution of rare inherited and de novo variants in 2,871 congenital heart disease probands.* Nat Genet, 2017. **49**(11): p. 1593-1601.
35. Zaidi, S., et al., *De novo mutations in histone-modifying genes in congenital heart disease.* Nature, 2013. **498**(7453): p. 220-3.
36. Homsy, J., et al., *De novo mutations in congenital heart disease with neurodevelopmental and other congenital anomalies.* Science, 2015. **350**(6265): p. 1262-6.
37. Greig, L.C., et al., *Molecular logic of neocortical projection neuron specification, development and diversity.* Nat Rev Neurosci, 2013. **14**(11): p. 755-69.

38. McConnell, S.K., *Migration and differentiation of cerebral cortical neurons after transplantation into the brains of ferrets.* Science, 1985. **229**(4719): p. 1268-71.
39. McConnell, S.K. and C.E. Kaznowski, *Cell cycle dependence of laminar determination in developing neocortex.* Science, 1991. **254**(5029): p. 282-5.
40. Desai, A.R. and S.K. McConnell, *Progressive restriction in fate potential by neural progenitors during cerebral cortical development.* Development, 2000. **127**(13): p. 2863-72.
41. Franco, S.J., et al., *Fate-restricted neural progenitors in the mammalian cerebral cortex.* Science, 2012. **337**(6095): p. 746-9.
42. Gil-Sanz, C., et al., *Lineage Tracing Using Cux2-Cre and Cux2-CreERT2 Mice.* Neuron, 2015. **86**(4): p. 1091-1099.
43. Telley, L., et al., *Temporal patterning of apical progenitors and their daughter neurons in the developing neocortex.* Science, 2019. **364**(6440).
44. Di Bella, D.J., et al., *Molecular Logic of Cellular Diversification in the Mammalian Cerebral Cortex.* bioRxiv, 2020: p. 2020.07.02.185439.
45. Dwyer, N.D., et al., *Neural Stem Cells to Cerebral Cortex: Emerging Mechanisms Regulating Progenitor Behavior and Productivity.* J Neurosci, 2016. **36**(45): p. 11394-11401.
46. McConnell, S.K., *Constructing the cerebral cortex: neurogenesis and fate determination.* Neuron, 1995. **15**(4): p. 761-8.
47. Leone, D.P., et al., *The determination of projection neuron identity in the developing cerebral cortex.* Curr Opin Neurobiol, 2008. **18**(1): p. 28-35.
48. Luskin, M.B., A.L. Pearlman, and J.R. Sanes, *Cell lineage in the cerebral cortex of the mouse studied in vivo and in vitro with a recombinant retrovirus.* Neuron, 1988. **1**(8): p. 635-47.
49. Shen, Q., et al., *The timing of cortical neurogenesis is encoded within lineages of individual progenitor cells.* Nat Neurosci, 2006. **9**(6): p. 743-51.
50. Walsh, C. and C.L. Cepko, *Clonally related cortical cells show several migration patterns.* Science, 1988. **241**(4871): p. 1342-5.
51. Han, W., et al., *TBR1 directly represses Fezf2 to control the laminar origin and development of the corticospinal tract.* Proc Natl Acad Sci U S A, 2011. **108**(7): p. 3041-6.
52. McKenna, W.L., et al., *Tbr1 and Fezf2 regulate alternate corticofugal neuronal identities during neocortical development.* J Neurosci, 2011. **31**(2): p. 549-64.
53. Molyneaux, B.J., et al., *Fezl is required for the birth and specification of corticospinal motor neurons.* Neuron, 2005. **47**(6): p. 817-31.
54. Chen, B., et al., *The Fezf2-Ctip2 genetic pathway regulates the fate choice of subcortical projection neurons in the developing cerebral cortex.* Proc Natl Acad Sci U S A, 2008. **105**(32): p. 11382-7.
55. Klingler, E., et al., *Mapping the molecular and cellular complexity of cortical malformations.* Science, 2021. **371**(6527).
56. Srinivasan, K., et al., *A network of genetic repression and derepression specifies projection fates in the developing neocortex.* Proc Natl Acad Sci U S A, 2012. **109**(47): p. 19071-8.

57. Bedogni, F., et al., *Tbr1 regulates regional and laminar identity of postmitotic neurons in developing neocortex.* Proc Natl Acad Sci U S A, 2010. **107**(29): p. 13129-34.
58. Alcamo, E.A., et al., *Satb2 regulates callosal projection neuron identity in the developing cerebral cortex.* Neuron, 2008. **57**(3): p. 364-77.
59. Kwan, K.Y., et al., *SOX5 postmitotically regulates migration, postmigratory differentiation, and projections of subplate and deep-layer neocortical neurons.* Proc Natl Acad Sci U S A, 2008. **105**(41): p. 16021-6.
60. Lodato, S., et al., *Gene co-regulation by Fezf2 selects neurotransmitter identity and connectivity of corticospinal neurons.* Nat Neurosci, 2014. **17**(8): p. 1046-54.
61. Molyneaux, B.J., et al., *Neuronal subtype specification in the cerebral cortex.* Nat Rev Neurosci, 2007. **8**(6): p. 427-37.
62. Shim, S., et al., *Cis-regulatory control of corticospinal system development and evolution.* Nature, 2012. **486**(7401): p. 74-9.
63. Lodato, S., et al., *Excitatory projection neuron subtypes control the distribution of local inhibitory interneurons in the cerebral cortex.* Neuron, 2011. **69**(4): p. 763-79.
64. Yatim, A., et al., *NOTCH1 nuclear interactome reveals key regulators of its transcriptional activity and oncogenic function.* Mol Cell, 2012. **48**(3): p. 445-58.
65. Doyen, C.M., et al., *NOTCH assembles a transcriptional repressive complex containing NuRD and PRC1 to repress genes involved in cell proliferation and differentiation.* bioRxiv, 2019: p. 513549.
66. Schwanbeck, R., et al., *The Notch signaling pathway: molecular basis of cell context dependency.* Eur J Cell Biol, 2011. **90**(6-7): p. 572-81.
67. Durak, O., et al., *Chd8 mediates cortical neurogenesis via transcriptional regulation of cell cycle and Wnt signaling.* Nat Neurosci, 2016. **19**(11): p. 1477-1488.
68. Tiberi, L., et al., *A BCL6/BCOR/SIRT1 complex triggers neurogenesis and suppresses medulloblastoma by repressing Sonic Hedgehog signaling.* Cancer Cell, 2014. **26**(6): p. 797-812.
69. Bonnefont, J., et al., *Cortical Neurogenesis Requires Bcl6-Mediated Transcriptional Repression of Multiple Self-Renewal-Promoting Extrinsic Pathways.* Neuron, 2019. **103**(6): p. 1096-1108 e4.
70. Lord, C., et al., *Autism spectrum disorder.* Nat Rev Dis Primers, 2020. **6**(1): p. 5.
71. Hallmayer, J., et al., *Genetic heritability and shared environmental factors among twin pairs with autism.* Arch Gen Psychiatry, 2011. **68**(11): p. 1095-102.
72. Sandin, S., et al., *The familial risk of autism.* JAMA, 2014. **311**(17): p. 1770-7.
73. Bailey, A., et al., *Autism as a strongly genetic disorder: evidence from a British twin study.* Psychol Med, 1995. **25**(1): p. 63-77.
74. Ronald, A. and R.A. Hoekstra, *Autism spectrum disorders and autistic traits: a decade of new twin studies.* Am J Med Genet B Neuropsychiatr Genet, 2011. **156B**(3): p. 255-74.
75. Parenti, I., et al., *Neurodevelopmental Disorders: From Genetics to Functional Pathways.* Trends Neurosci, 2020. **43**(8): p. 608-621.
76. Sullivan, P.F. and D.H. Geschwind, *Defining the Genetic, Genomic, Cellular, and Diagnostic Architectures of Psychiatric Disorders.* Cell, 2019. **177**(1): p. 162-183.

77. Iossifov, I., et al., *The contribution of de novo coding mutations to autism spectrum disorder.* Nature, 2014. **515**(7526): p. 216-21.
78. De Rubeis, S., et al., *Synaptic, transcriptional and chromatin genes disrupted in autism.* Nature, 2014. **515**(7526): p. 209-15.
79. Pinto, D., et al., *Convergence of genes and cellular pathways dysregulated in autism spectrum disorders.* Am J Hum Genet, 2014. **94**(5): p. 677-94.
80. Chen, J.A., et al., *The emerging picture of autism spectrum disorder: genetics and pathology.* Annu Rev Pathol, 2015. **10**: p. 111-44.
81. Willsey, A.J., et al., *Coexpression networks implicate human midfetal deep cortical projection neurons in the pathogenesis of autism.* Cell, 2013. **155**(5): p. 997-1007.
82. de la Torre-Ubieta, L., et al., *Advancing the understanding of autism disease mechanisms through genetics.* Nat Med, 2016. **22**(4): p. 345-61.
83. Satterstrom, F.K., et al., *Large-Scale Exome Sequencing Study Implicates Both Developmental and Functional Changes in the Neurobiology of Autism.* Cell, 2020. **180**(3): p. 568-584 e23.
84. Xu, X., et al., *Cell type-specific expression analysis to identify putative cellular mechanisms for neurogenetic disorders.* J Neurosci, 2014. **34**(4): p. 1420-31.
85. Lijam, N., et al., *Social interaction and sensorimotor gating abnormalities in mice lacking Dvl1.* Cell, 1997. **90**(5): p. 895-905.
86. Sowers, L.P., et al., *Disruption of the non-canonical Wnt gene PRICKLE2 leads to autism-like behaviors with evidence for hippocampal synaptic dysfunction.* Mol Psychiatry, 2013. **18**(10): p. 1077-89.
87. Fang, W.Q., et al., *Overproduction of upper-layer neurons in the neocortex leads to autism-like features in mice.* Cell Rep, 2014. **9**(5): p. 1635-1643.
88. Long, J.M., et al., *Expanded characterization of the social interaction abnormalities in mice lacking Dvl1.* Genes Brain Behav, 2004. **3**(1): p. 51-62.
89. Paulsen, B., et al., *Human brain organoids reveal accelerated development of cortical neuron classes as a shared feature of autism risk genes.* bioRxiv, 2020: p. 2020.11.10.376509.
90. Cederquist, G.Y., et al., *A Multiplex Human Pluripotent Stem Cell Platform Defines Molecular and Functional Subclasses of Autism-Related Genes.* Cell Stem Cell, 2020. **27**(1): p. 35-49 e6.
91. Araujo, D.J., et al., *Foxp1 in Forebrain Pyramidal Neurons Controls Gene Expression Required for Spatial Learning and Synaptic Plasticity.* J Neurosci, 2017. **37**(45): p. 10917-10931.
92. Celen, C., et al., *Arid1b haploinsufficient mice reveal neuropsychiatric phenotypes and reversible causes of growth impairment.* Elife, 2017. **6**.
93. Gompers, A.L., et al., *Germline Chd8 haploinsufficiency alters brain development in mouse.* Nat Neurosci, 2017. **20**(8): p. 1062-1073.
94. Velmeshev, D., et al., *Single-cell genomics identifies cell type-specific molecular changes in autism.* Science, 2019. **364**(6441): p. 685-689.
95. Jin, X., et al., *In vivo Perturb-Seq reveals neuronal and glial abnormalities associated with autism risk genes.* Science, 2020. **370**(6520).
96. Duan, W., et al., *Integrated Transcriptome Analyses Revealed Key Target Genes in Mouse Models of Autism.* Autism Res, 2020. **13**(3): p. 352-368.

97. Telley, L., et al., *Sequential transcriptional waves direct the differentiation of newborn neurons in the mouse neocortex.* Science, 2016. **351**(6280): p. 1443-6.
98. Wong, F.K., et al., *Pyramidal cell regulation of interneuron survival sculpts cortical networks.* Nature, 2018. **557**(7707): p. 668-673.
99. Lim, L., et al., *Development and Functional Diversification of Cortical Interneurons.* Neuron, 2018. **100**(2): p. 294-313.
100. Priya, R., et al., *Activity Regulates Cell Death within Cortical Interneurons through a Calcineurin-Dependent Mechanism.* Cell Rep, 2018. **22**(7): p. 1695-1709.
101. Anastasiades, P.G., et al., *GABAergic interneurons form transient layer-specific circuits in early postnatal neocortex.* Nat Commun, 2016. **7**: p. 10584.
102. Heyne, H.O., et al., *De novo variants in neurodevelopmental disorders with epilepsy.* Nat Genet, 2018. **50**(7): p. 1048-1053.
103. Myers, K.A., et al., *Childhood-onset generalized epilepsy in Bainbridge-Ropers syndrome.* Epilepsy Res, 2018. **140**: p. 166-170.
104. Verhoeven, W., et al., *Phenotypic characterization of an older adult male with late-onset epilepsy and a novel mutation in ASXL3 shows overlap with the associated Bainbridge-Ropers syndrome.* Neuropsychiatr Dis Treat, 2018. **14**: p. 867-870.
105. Nelson, S.B. and V. Valakh, *Excitatory/Inhibitory Balance and Circuit Homeostasis in Autism Spectrum Disorders.* Neuron, 2015. **87**(4): p. 684-98.
106. Rubenstein, J.L. and M.M. Merzenich, *Model of autism: increased ratio of excitation/inhibition in key neural systems.* Genes Brain Behav, 2003. **2**(5): p. 255-67.
107. Berg, A.T., S. Plioplys, and R. Tuchman, *Risk and correlates of autism spectrum disorder in children with epilepsy: a community-based study.* J Child Neurol, 2011. **26**(5): p. 540-7.
108. Balasubramanian, M. and S. Schirwani, *ASXL3-Related Disorder*, in *GeneReviews((R))*, M.P. Adam, et al., Editors. 1993: Seattle (WA).
109. Sullivan, J.M., S. De Rubeis, and A. Schaefer, *Convergence of spectrums: neuronal gene network states in autism spectrum disorder.* Curr Opin Neurobiol, 2019. **59**: p. 102-111.
110. Barbour, H., et al., *Polycomb group-mediated histone H2A monoubiquitination in epigenome regulation and nuclear processes.* Nat Commun, 2020. **11**(1): p. 5947.
111. Daou, S., et al., *The BAP1/ASXL2 Histone H2A Deubiquitinase Complex Regulates Cell Proliferation and Is Disrupted in Cancer.* J Biol Chem, 2015. **290**(48): p. 28643-63.
112. Shashi, V., et al., *De Novo Truncating Variants in ASXL2 Are Associated with a Unique and Recognizable Clinical Phenotype.* Am J Hum Genet, 2017. **100**(1): p. 179.
113. Hoischen, A., et al., *De novo nonsense mutations in ASXL1 cause Bohring-Opitz syndrome.* Nat Genet, 2011. **43**(8): p. 729-31.
114. Srivastava, A., et al., *De novo dominant ASXL3 mutations alter H2A deubiquitination and transcription in Bainbridge-Ropers syndrome.* Hum Mol Genet, 2016. **25**(3): p. 597-608.

115. Lancaster, M.A. and J.A. Knoblich, *Generation of cerebral organoids from human pluripotent stem cells.* Nat Protoc, 2014. **9**(10): p. 2329-40.
116. Mariani, J., et al., *Modeling human cortical development in vitro using induced pluripotent stem cells.* Proc Natl Acad Sci U S A, 2012. **109**(31): p. 12770-5.
117. Mariani, J., et al., *FOXG1-Dependent Dysregulation of GABA/Glutamate Neuron Differentiation in Autism Spectrum Disorders.* Cell, 2015. **162**(2): p. 375-90.
118. Shi, Y., P. Kirwan, and F.J. Livesey, *Directed differentiation of human pluripotent stem cells to cerebral cortex neurons and neural networks.* Nat Protoc, 2012. **7**(10): p. 1836-46.
119. Fursova, N.A., et al., *Synergy between Variant PRC1 Complexes Defines Polycomb-Mediated Gene Repression.* Mol Cell, 2019. **74**(5): p. 1020-1036 e8.
120. Fursova, N.A., et al., *BAP1 constrains pervasive H2AK119ub1 to control the transcriptional potential of the genome.* Genes Dev, 2021. **35**(9-10): p. 749-770.
121. Blackledge, N.P., et al., *PRC1 Catalytic Activity Is Central to Polycomb System Function.* Mol Cell, 2020. **77**(4): p. 857-874 e9.
122. Scelfo, A., et al., *Functional Landscape of PCGF Proteins Reveals Both RING1A/B-Dependent-and RING1A/B-Independent-Specific Activities.* Mol Cell, 2019. **74**(5): p. 1037-1052 e7.
123. Tamburri, S., et al., *Histone H2AK119 Mono-Ubiquitination Is Essential for Polycomb-Mediated Transcriptional Repression.* Mol Cell, 2020. **77**(4): p. 840-856 e5.
124. Illingworth, R.S., et al., *The E3 ubiquitin ligase activity of RING1B is not essential for early mouse development.* Genes Dev, 2015. **29**(18): p. 1897-902.
125. Kundu, S., et al., *Polycomb Repressive Complex 1 Generates Discrete Compacted Domains that Change during Differentiation.* Mol Cell, 2017. **65**(3): p. 432-446.e5.
126. Morimoto-Suzki, N., et al., *The polycomb component Ring1B regulates the timed termination of subcerebral projection neuron production during mouse neocortical development.* Development, 2014. **141**(22): p. 4343-53.
127. Skene, P.J. and S. Henikoff, *An efficient targeted nuclease strategy for high-resolution mapping of DNA binding sites.* Elife, 2017. **6**.
128. Pereira, J.D., et al., *Ezh2, the histone methyltransferase of PRC2, regulates the balance between self-renewal and differentiation in the cerebral cortex.* Proc Natl Acad Sci U S A, 2010. **107**(36): p. 15957-62.
129. Ben-David, E. and S. Shifman, *Combined analysis of exome sequencing points toward a major role for transcription regulation during brain development in autism.* Mol Psychiatry, 2013. **18**(10): p. 1054-6.
130. Xu, H., et al., *Construction and validation of a regulatory network for pluripotency and self-renewal of mouse embryonic stem cells.* PLoS Comput Biol, 2014. **10**(8): p. e1003777.